Imperial College London
Department of Materials

Medium Mn Steels

Thomas Kwok Wei Jie

Submitted in part fulfilment of the requirements
for the degree of Doctor of Philosophy at
Imperial College London, June 2022

I, Thomas Kwok Wei Jie, declare that this thesis and associated research are my own original work. All sources of information derived from literature and collaborative efforts have been appropriately indicated, referenced and acknowledged.

Abstract

Medium Mn steels containing 4-12 wt% Mn are a relatively new class of steels which has gained significant research attention over the past decade. These steels are typically duplex (austenite+ferrite) and can be processed in various ways to produce different microstructure variants. Additional Twinning Induced Plasticity (TWIP) and/or Transformation Induced Plasticity (TRIP) effects can also be enabled in the austenite phase. Medium Mn steels therefore have great flexibility in design and can be processed to exhibit a large range of tensile properties.

This thesis describes the alloy development journey to develop novel TWIP-assisted medium Mn steels with high strength and high ductility. The aim was to produce industrially scalable medium Mn steels compared to high Mn TWIP steels (16-30 wt% Mn) which faced many problems during industrial trials due to the high Mn content. Various tools such as Thermo-Calc were used to guide an iterative alloy design process that involved vacuum arc melting, hot rolling, tensile testing and electron microscopy. Findings from each alloy would then be used to guide the next iteration. As a result, a series of novel medium Mn steels with decreasing Mn contents and different strain hardening mechanisms have been developed. It is hoped that the relationships between composition, processing and tensile properties established in this work will continue to guide future medium Mn steel development.

In Chapter 3, a novel medium Mn steel with 8 wt% Mn was produced that displayed both TWIP and TRIP effects. Cold rolling was investigated as a means to improve strength. It was observed that cold rolling introduced a larger density of twins and therefore twin intersections into the microstructure compared to uniaxial tension. It was postulated that the higher density of twin intersections which can act as α'-martensite nucleation sites led to an enhanced TRIP response in the cold rolled samples, improving strain hardenability while retaining a signifcant amount of ductility ($\sim 30\%$). Chapter 4 describes a scaling up study on the same steel. It was found that after a standard slab reheating cycle of 1250 °C for 2 h, some δ-ferrite remained untransformed but the matrix was mostly compositionally homogeneous, even in Mn. When thermomechanically processed, the δ-ferrite was observed to form stringers, resulting in a slight loss in yield and tensile strength but the strain hardening behaviour was preserved.

Finally, the relative effects of TWIP and TRIP were investigated in chapter 5. A new medium Mn steel with 5 wt% Mn was developed and processed differently to produce two microstructure types (lamellar and mixed equiaxed+lamellar). Electron microscopy on interrupted tensile specimens showed different twinning kinetics but a similar α'-martensite nucleation and growth mechanism between the two microstructure variants. However, constitutive modelling of their strain hardening rate curves showed that the contribution to strength from twinning was insignificant compared to the TRIP effect, questioning the relevance of the TWIP effect in medium Mn steels.

Acknowledgements

Sir Isaac Newton once wrote: If I have seen further it is by standing on the shoulders of giants. Likewise, this PhD would not have been possible without the integral support from so many who have shown me the way.

First and foremost, I have to thank Professor David Dye for the opportunity to embark on this PhD and for all the advice, encouragement and support rendered during all these years. Your maverick attitude towards life and ever-flowing fountain of ideas are just some of your quirks that have left a lasting impression. Secondly I would like to thank the good people at A*STAR Graduate Academy for the provision of a PhD studentship and ensuring I was well taken care of.

Through the PhD, I am truly honoured to have been taken under the wings of several amazing postdocs, each having taught me both important scientific and life skills. Mezan, you have taught me diligence. Ioannis, you have taught me patience and Xin, you have taught me to be bold. To my greatest mentors, I am grateful to the three of you. I would also like to thank the company of my fellow metal bashers for all their little tips and tricks, crosswords, office banter, trips to the pub and surviving the pandemic together. And so, a big thank you to Vas, Sudha, Sandy, Abi, Claire, Lucy, Chris, Felicity, Yitong, Sam, Tom, Hannah, Gary and Rory.

Special thanks to Ben Wood for being patient with all my pestering around the lab, fixing things that I may or may not have broken and teaching me how not to break them again. I also have to thank Mahmoud and Cati for their help with electron microscopy.

I would like to thank my collaborators for fruitful discussions and lending me their invaluable skills. To the steel gurus Dr Carl Slater and Professor Claire Davis, thank you for showing me the industrial and practical side of steel research. To Dr Gong Peng, your TEM wizardry never fails to inspire and thank you for showing me what a working Tenupol is meant to do.

Finally, I would like to thank my parents and wider family for their unwavering support, especially my grandmother who had absolutely no clue as to what I was doing but could not be any prouder of me. And to my wife Tammy, you have always been my rock and pillar, my light during the darkest night. Thank you for your unconditional love and for always believing in me. This PhD would have been impossible without you.

To my wife, my grandmother and all who never doubted.

The major difference between a thing that might go wrong
and a thing that cannot possibly go wrong
is that when a thing that cannot possibly go wrong goes wrong
it usually turns out to be impossible to get at or repair.

- Douglas Adams

Contents

List of Figures

List of Tables

Chapter 1

Introduction

1.1 Advanced High Strength Steels

Automakers today are facing a unique set of challenges. Environmental pressures to reduce carbon in the form of emissions and to improve fuel economy even in Battery Electric Vehicles (BEV) mean that lightweighting, especially of the Body-In-White (BIW), becomes increasingly important. BIW components include A, B and C pillars, door beams, front and back members and accounts for up to 28% of a vehicle's total mass. The current solution has been to "down-gauge" BIW components, *i.e.* using thinner sheet steel, in an effort to reduce overall weight. However, with using thinner steel, crash performance and rigidity must not be compromised. As a result, a large amount of research from steelmakers, automakers and academia has been devoted to the development of new classes and grades of Advanced High Strength Steels (AHSS) that satisfy the increasingly complex requirements of the automotive industry and the associated supply chains [1, 2].

AHSS is an umbrella term that comprises of three genenerations of steel development, usually in sheet format. These steels are typically >550 MPa in tensile strength and possess superior forming, bending and energy absorbing properties. The term "advanced" is used to reflect the careful alloying and thermomechanical processing necessary to achieve the superior mechanical properties in these steels [1]. The 1st generation or 1Gen AHSS relied on martensite as the strengthening phase to improve strength and formability. 1Gen AHSS include Dual Phase (DP), Transformation Induced Plasticity (TRIP) and Martensitic (MS) steels [3]. The 2nd generation of AHSS or 2Gen AHSS focused mainly on the ductility and plasticity enhancing mechanisms of the austenite phase to simultaneously improve the tensile strength and elongation compared to 1Gen AHSS. 2Gen AHSS include Austenitic Stainless Steels (Aust SS) and Twinning Induced Plasticity (TWIP) steels [4]. Finally, the 3rd generation of

AHSS or 3Gen AHSS are the most modern addition. While it has no strict definition, 3Gen AHSS are typically multi-phase steels that combine both high strength and high elongations through various strengthening and plasticity enhancing mechanisms. 3Gen AHSS include Quenching and Partitioning (Q&P) and TRIP-assisted Bainitic Ferrite (TBF) steels [5]. Many new steel alloying concepts that are currently under development but have not yet received official recognition are considered 3Gen AHSS *candidates*.

1.2 Rediscovery of medium Mn steel

Modern medium Mn steels by and large have evolved from high Mn TWIP steels. As mentioned, TWIP steels belong to the 2Gen AHSS, are fully austenitic and contain 16-30 wt% Mn. The high Mn content is necessary to firstly stabilise austenite to room temperature and secondly to raise the Stacking Fault Energy (SFE) into the deformation twinning regime. During plastic deformation, the austenite forms extremely fine deformation twins which continuously subdivide the grain, refining the dislocation mean free path in what is termed the dynamic Hall-Petch effect [6]. The TWIP effect therefore enables continuous hardening all along the stress strain curve, leading to large elongations of above 50%, high tensile strengths ($>$ 1 GPa) and also high strain hardening rates of $>$ 2 GPa [7, 8]. Therefore, during the early 2000s, TWIP steels received significant research attention as these steels were very promising materials for energy absorbing applications or for components which require large cold formabilities in both the automotive and defence industry [9, 10].

However, the high Mn content which enables the TWIP effect is also its Achilles' heel. As industrial trials began, it soon became apparent that the high Mn content was not compatible with conventional steelmaking processes. Most steelmakers and related equipment are predominantly optimised to produce 1Gen AHSS which are significantly leaner steels, containing only a maximum of 2-3 wt% Mn. The large Mn content required to produce TWIP steels also necessitated the use of high purity electrolytic Mn flake, as compared to conventionally used ferromanganese, increasing the cost of the steel significantly [11, 12]. The large alloying additions of Mn, Al and Si also made casting complex and difficult by reacting with the mould flux, increasing melt viscosity, enlarging the mushy zone and increasing the susceptibility to hot cracking [13, 14]. Mn segregation and casting defects also resulted in inhomogeneous deformation behaviour and poor hot ductility respectively [15–17]. In the light of the challenges faced by TWIP steels, industry and academia then turned their attention towards searching for a Mn-lean TWIP steel in an attempt to find the lowest amount of Mn without sacrificing

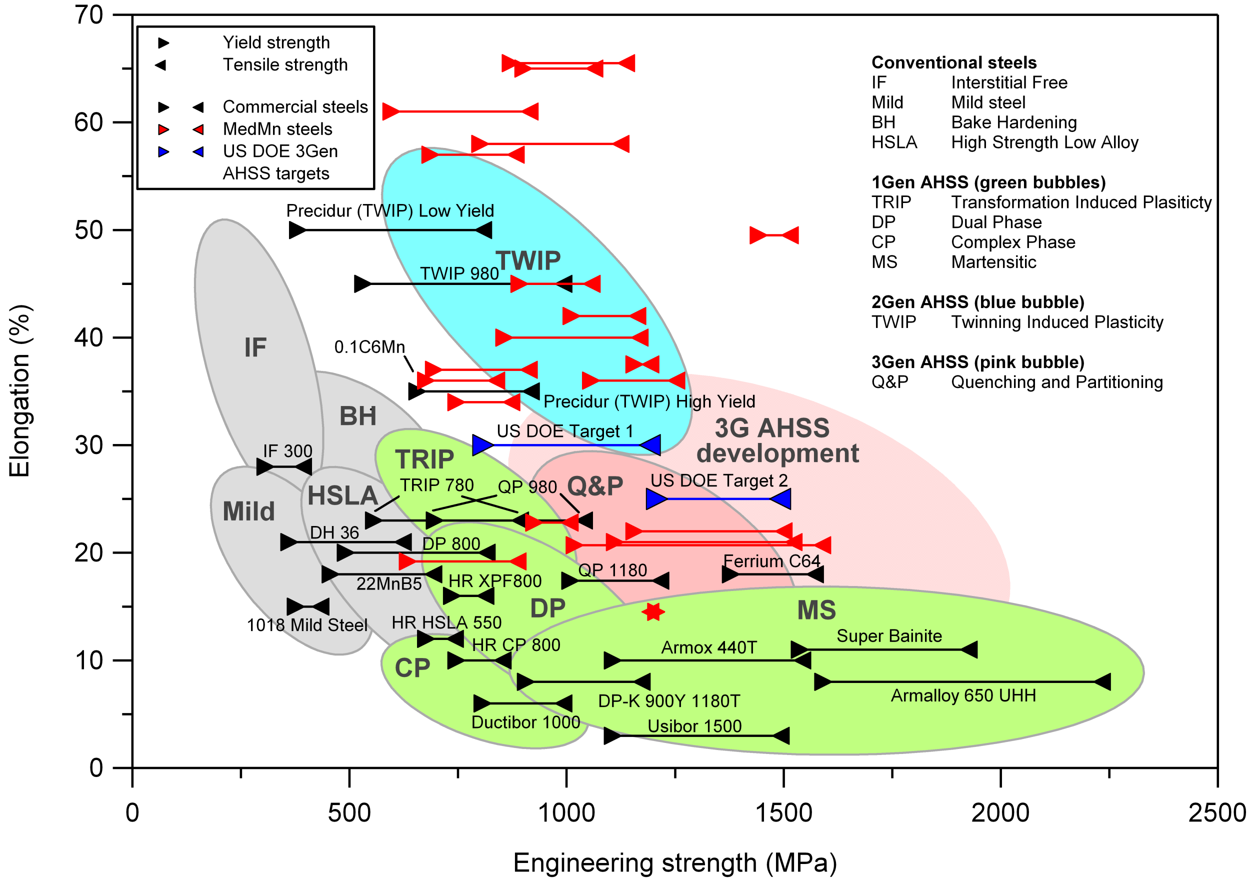

Figure 1.1: Classical "banana" diagram comparing commercial steels in black and literature medium Mn (MedMn) steels in red. US DOE Target 1: High strength, exceptional ductility steel for crash energy absorbing components. US DOE Target 2: High ductility, exceptional strength steel for anti-intrusion components. Data from [18–38].

the beneficial TWIP effect. The field of medium Mn steels was "rediscovered" as a result.

The very first medium Mn steel with composition of Fe-6Mn-0.1C was in fact developed in 1972 and is commonly attributed to Miller [39]. In the paper, Miller investigated the feasibility of Ni and Mn to lower the A_1 temperature and therefore the temperature needed to anneal a cold worked steel in the intercritical $(\gamma + \alpha)$ regime, in order to produce a stable fine grained duplex $(\gamma + \alpha)$ microstructure highly resistant to grain coarsening. Modern medium Mn steels now contain 4-12 wt% Mn and similarly have a duplex microstructure at room temperature [40, 41].

Having shifted away from TWIP steels, medium Mn steels have been the subject of intense research and development. Many researchers have now developed many novel medium Mn steels with a myriad of microstructures and tensile properties. In Figure 1.1, the classical "banana" diagram is presented, including commercial steels belonging to the three generations of AHSS, novel medium Mn steels from the literature and two US Department of Energy (US DOE) 3Gen AHSS targets [38]. It can be seen that many medium Mn steels in the literature have matched or even exceeded the tensile properties of their predecessor TWIP steels as well as the first US DOE target (target for an energy absorbing 3Gen AHSS). The combination of industrially feasible compositions and processing routes with impressive tensile properties make medium Mn steels a serious candidate for 3Gen AHSS.

1.3 Aims and motivations

Capitalising on previous work on TWIP steels in the group by Rahman *et al.* [10, 42, 43], the aim of this work was relatively simple: to develop a novel high strength high ductility TWIP-assisted medium Mn sheet steel for energy absorbing automotive applications. The novel medium Mn steel will be benchmarked in terms of tensile properties and cost against DP 800 which is the current steel used in many automotive crash absorbing members [44]. In order to achieve this aim, the following design criteria are imposed:

1. Yield strength $\geq$ 1 GPa with $\geq$ 30% elongation.
2. Mn content below 8 wt%.
3. Able to be produced with conventional steel processing methods.
4. Similar or lower alloying cost level to DP 800.

1.4 Thesis structure

This thesis follows the development of several high strength high ductility medium Mn steels. Alloy development began with DP-TWIP at 12 wt% Mn and then steadily decreasing in Mn to produce a medium Mn steel of only 5 wt% Mn. Two other high Mn steels, Kappa and TWIP NbV were also developed but not directly related to the work described in this thesis. A list of steels developed during the course of this PhD is shown in Table 1.1 although only papers (b), (c) and (e) will be presented in this thesis.

Chapter 1 briefly introduces the topic of AHSS development, highlighting the challenges faced by TWIP steel and how it led to the development of medium Mn steels.

Chapter 2 presents a literature review on the metallurgy of medium Mn steels, the deformation mechanisms and processing methods. Chapter 2 is adapted from paper (f).

Chapter 3 introduces the alloy design concept and evaluates the various tools and methods used in this work to develop novel medium Mn steels.

Table 1.1: List of steels developed during this PhD, associated Mn content and publication.

Alloy name	wt% Mn	Paper
Kappa	30	(i)
TWIP NbV	16	(g)
DP-TWIP	12	(a)
Novalloy	8	(b), (c) & (d)
Secolloy	6	NA
Triolloy	5	(e)
Quadrolloy	6	In progress

Chapter 4 investigates the deformation behaviour of Novalloy, an 8 wt% Mn medium Mn steel, and how cold rolling may enhance the TRIP effect in medium Mn steel. Chapter 4 is also presented in paper (c).

Chapter 5 then explores the scalability of Novalloy from a 400 g laboratory arc-melted ingot to a 5 kg vacuum induction melted ingot, paying attention to the effects of chemical segregation and δ-ferrite fraction on tensile properties. Chapter 5 is also presented in paper (b).

Chapter 6 introduces Triolloy, a 5 wt% Mn medium Mn steel which exihibits both the TWIP and TRIP plasticity enhancing effects. The effect of microstructure on TWIP and TRIP effects are examined. Finally, the relevance of the TWIP effect in medium Mn steels is questioned when constitutive modelling of the strain hardening curve showed little contribution to strength from twinning. Chapter 6 is also presented in paper (e).

Chapter 7 summarises the key findings from this work and suggests areas for further research.

1.5 Publications and presentations

The work conducted on the topic of medium Mn steels during the course of this PhD has been published or in preparation for publication in the following articles:

a) Kwok TWJ, Rahman KM, Xu X, Bantounas I, Kelleher JF, Dasari S, Alam T, Banerjee R, Dye D. Design of a High Strength, High Ductility 12 wt% Mn Medium Manganese Steel With Hierarchical Deformation Behaviour. *Materials Science and Engineering: A*, 2020; vol. 782 (139258). DOI: 10.1016/j.msea.2020.139258.

b) Kwok TWJ, Slater C, Xu X, Davis C, Dye D. A Scale-up Study on Chemical Segregation and the Effects on Tensile Properties in Two Medium Mn Steel Castings. *Metallurgical and Materials*

Transactions A: Physical Metallurgy and Materials Science, 2022; vol. 53, pp 585-596. DOI: 10.1007/s11661-021-06533-w.

c) Kwok TWJ, Gong P, Xu X, Nutter J, Rainforth WM, Dye D. Microstructure Evolution and Tensile Behaviour of a Cold Rolled 8 Wt Pct Mn Medium Manganese Steel. *Metallurgical and Materials Transactions A: Physical Metallurgy and Materials Science*, 2022; vol. 53, pp 597-609. DOI: 10.1007/s11661-021-06534-9.

d) X Xu, Kwok TWJ, Gong P, Dye D. Tailoring the Deformation Behaviour of a Medium Mn Steel through Isothermal Intercritical Annealing. *Materialia*, 2022; vol. 22 (101422). DOI: 10.1016/j.mtla.2022.101422.

e) Kwok TWJ, Gong P, Rose R, Dye D. The Relative Contributions of TWIP and TRIP to Strength in Fine Grained Medium-Mn Steels. *Materials Science and Engineering: A*, 2022; vol. 855 (143864). DOI: 10.1016/j.msea.2022.143864

f) Kwok TWJ, Dye D. A review of the processing, microstructure and property relationships in medium Mn steels. Submitted to International Materials Reviews.

Additional publications during the course of the PhD are shown as follows:

g) McAuliffe TP, Ackerman AK, Savitzky BH, Kwok TWJ, Danaie M, Ophus C, Dye D. 4D-STEM elastic stress state characterisation of a TWIP steel nanotwin. ArXiv:2004.03982v2, 2020.

h) Kwok TWJ, Zhai W, Peh WY, Gupta M, Fu MW, Chua BW. Squeeze Casting for the Production of Metallic Parts and Structures, in: *Encyclopedia of Materials: Metals and Alloys*, Elsevier Ltd., 2020; pp. 87-99. DOI: 10.1016/b978-0-12-819726-4.00038-7.

i) Kwok TWJ, Rahman KM, Vorontsov VA, Dye D. Strengthening κ-Carbide Steels Using Residual Dislocation Content. *Scripta Materialia*, 2022; vol. 213 (114626). DOI: 10.2139/ssrn.3994649.

The work from this PhD has been presented at the following conferences and meetings:

1. Kwok TWJ, Rahman KM, Xu X, Dye D, "Microstructure and mechanical behaviour of a 12 wt% Mn medium manganese steel", *4th High Mn Steel conference*, Aachen, Germany, 2019.
2. Kwok TWJ, Xu X, Dye D "An energy absorbing medium Mn steel for industry", *TMS*, San Diego, California, United States of America, 2020.

3. Kwok TWJ, Xu X, Gong P, Slater C, Davis C, Dye D, “How low can you go? The medium manganese limbo”, *4th Postgraduate Research Symposium on Ferrous Metallurgy*, London, United Kingdom, 2021. (Awarded 1st runners up for best presentation)

4. Kwok TWJ, Gong P, Rose R , Dye D, “A closer look at the TWIP+TRIP mechanism in medium Mn steel”, *5th Postgraduate Research Symposium on Ferrous Metallurgy*, London, United Kingdom, 2022. (Awarded best presentation)

5. Kwok TWJ, Xu X, Gong P, Slater C, Davis C, Dye D, “Tensile behaviour and martensitic transformations in a cold rolled medium Mn steel”, *TMS*, Anaheim, California, United States of America, 2022.

6. Kwok TWJ, Xu X, Gong P, Slater C, Davis C, Dye D, “A study on the deformation mechanisms and scaling up of a medium Mn steel with 8 wt% Mn”, *5th High Mn Steel conference*, Linz, Austria, 2022.

Chapter 2

Literature Review

2.1 Metallurgy of medium Mn steels

2.1.1 Evolution from high Mn to medium Mn steels

High Mn TWIP steel compositions are typically Fe-Mn-Al-Si-C, with 16-30 wt% Mn and 0.6-0.8 wt% C. The large Mn and C contents are necessary to stabilise a fully austenitic microstructure at room temperature and raise the austenite Stacking Fault Energy (SFE) into the deformation twinning regime ($\sim$ 15-40 mJ m^{-2}) [8,45]. In order to retain the fully austenitic microstructure without increasing the C content in TWIP steels, the lowest possible Mn content appears to be 12 wt% as demonstrated in a Fe-12Mn-0.6C steel by Kim *et al.* [45].

However, C can be added, to a certain degree before forming cementite, to compensate for the reduction in Mn [46]. Fully austenitic steels with Mn contents between 10-14 wt% Mn and 0.8-1.4 wt% C are also known as Hadfield steels [47], named after Sir Robert Hadfield who developed these steels in 1888 [48]. Hadfield steels have high hardness and strain hardening rates, and are therefore used in wear-resistant applications such as earth moving equipment.

When the Mn content is reduced even further, it is no longer possible to retain a stable fully austenitic microstructure at room temperature. As a result, most medium Mn steels which are also Fe-Mn-Al-Si-C type, with 4-12 wt% Mn and 0.05-0.6 wt% C, usually have a duplex ($\gamma + \alpha$) microstructure at room temperature. Due to its two phase microstructure, it is significantly easier to stabilise a fine grained microstructure as discovered in the original paper by Miller [39]. Therefore, most medium Mn steels have a significantly higher yield strength compared to TWIP steels as shown in Figure 1.1.

Another consequence of the reduced Mn content in medium Mn steels is a significantly lowered

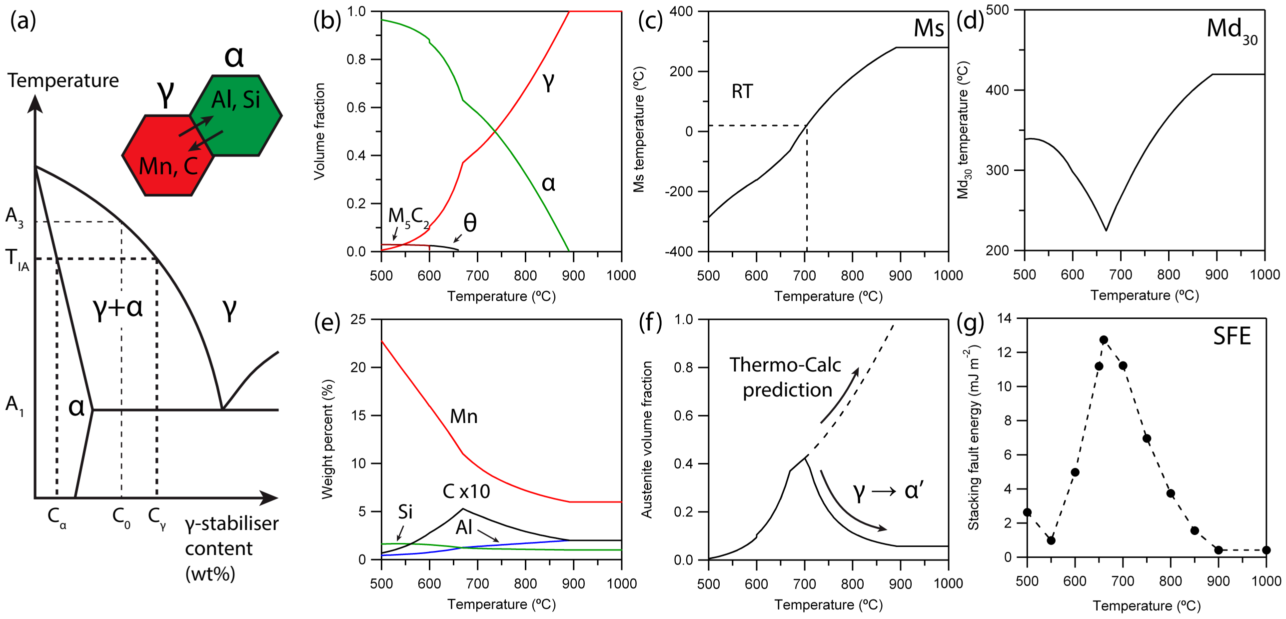

Figure 2.1: (a) Schematic phase diagram demonstrating the intercritical region between the A_1 and A_3 temperatures. C_0, C_α and C_γ are the bulk, ferrite and austenite compositions respectively. (b) Thermo-Calc property diagram of a Fe-6Mn-2Al-1Si-0.2C medium Mn steel. (c) Variation of Ms, (d) Md_{30}, (e) austenite composition, (f) expected austenite fraction at room temperature and (g) austenite SFE with IA temperature.

austenite stability and SFE. When SFE is decreased below the deformation twinning range, the $\gamma \rightarrow \varepsilon$ Transformation Induced Plasticity (TRIP) effect is activated instead of twinning [8]. Simultaneously, as the austenite stability is reduced, various transformation mechanisms such as the two-stage $\gamma \rightarrow \varepsilon \rightarrow \alpha'$ or the direct $\gamma \rightarrow \alpha'$ TRIP may be activated. If the austenite phase in medium Mn steels had the same composition as the bulk, the SFE would be too low for twinning and the austenite would be very unstable and form martensite prematurely. Therefore, in order to activate the TWIP effect or to control the TRIP effect, the austenite phase needs to be enriched in Mn and C beyond the bulk composition. Thankfully, as with most two phase alloys, it is possible to enrich the austenite phase with austenite stabilising elements such as Mn and C by heat treating the alloy in the intercritical $(\gamma + \alpha)$ temperature regime.

2.1.2 Intercritical annealing and partitioning

Central to medium Mn steel alloy development is the concept of element partitioning during an Intercritical Annealing (IA) heat treatment. From the schematic phase diagram in Figure 2.1a, the IA heat treatment can be defined as a heat treatment conducted at any temperature between the A_1 and A_3 temperature, *i.e.* the intercritical or $\gamma + \alpha$ regime. Depending on the IA temperature, the phase fraction of austenite and ferrite can be adjusted based on the lever rule. However, most researchers turn to Thermo-Calc in order to generate property diagrams for determining the equilibrium phase fractions at the intercritical temperature range. Figure 2.1b shows the property diagram of an example medium Mn steel with a composition of Fe-6Mn-2Al-1Si-0.2C using the TCFE 7.0 database. It can be seen that the A_3 temperature is 890 °C and the A_1 temperature is at 500 °C. However at 660 °C, cementite (θ) begins to precipitate and should be avoided.

Depending on the phase fraction, the composition of the austenite and ferrite phases will also be altered. Austenite stabilising elements such as Mn and C will partition to austenite, while ferrite stabilising elements such as Al and Si partition to ferrite. Based on the lever rule, a lower austenite fraction would mean that the austenite would be highly enriched in Mn and C while a high austenite fraction implies that the austenite would be more dilute. Figure 2.1e shows the composition profile of the austenite phase with temperature as simulated by Thermo-Calc. As the austenite phase fraction begins to decrease below 890 °C, austenite becomes increasingly enriched in Mn and C but depleted in Al. Below 660 °C, cementite begins to precipitate and C is lost from austenite to cementite. From the composition profile, the martensite start or Ms temperature (°C) can be calculated using an equation by Kaar *et al.* [49]:

$$Ms = 692 - 502\,[C+N]^{0.5} - 34.5\,[Mn] - 14\,[Si] + 20\,[Al] \tag{2.1}$$

where compositions are given in mass percent. From Figure 2.1c, it can be seen that if an IA temperature was chosen above 715 °C, the Ms temperature of the austenite phase would be above room temperature (20 °C). As a result, when the steel is cooled to room temperature after IA, some of the austenite would transform to α'-martensite.

The volume fraction of α'-martensite, $V_f^{\alpha'}$, can be determined using the Koistinen and Marburger equation [50, 51]:

$$1 - V_f^{\alpha'} = \exp[\beta(Ms - T_Q)] \tag{2.2}$$

where β is a constant equal to -0.011 and T_Q is the temperature below Ms to which the sample was cooled. Therefore, the expected austenite fraction at room temperature after IA is represented by Figure 2.1f. Above an IA temperature of 715 °C, the Mn and C content in the austenite phase are too low and cannot be fully stabilised to room temperature. Otherwise, the predicted austenite fraction at room temperature is the same as shown in Figure 2.1b. Therefore, in order to avoid cementite precipitation and to avoid athermal martensite transformation during cooling, the realistic IA window is only 660 - 715 °C where the room temperature austenite fraction only varies between 0.37 and 0.42.

The austenite stability against deformation induced martensitic transformation can also be calculated based on the composition. The Md_{30} temperature (°C) defined as the temperature where half of the austenite transforms to α'-martensite at a strain of 30% can be calculated using the following equation [52, 53]:

$$Md_{30} = 551 - 462[C] - 8.1[Mn] - 9.2[Si] - 1.42(-3.29 - 6.64\log_{10} d_{\gamma} - 8) \tag{2.3}$$

where d_{γ} (µm) is the austenite grain size. From Figure 2.1d, the Md_{30} temperature begins to decrease below the A_3 temperature, *i.e.* becoming more stable, as Mn and C partition into the austenite phase. However, below 660 °C, the Md_{30} temperature increases again due to the loss of C in the austenite phase. Finally, SFE can also be calculated based on the austenite composition using the method proposed by Sun *et al.* [36]. Both SFE and austenite stability, measured as either the Ms or Md_{30} temperature, will have implications on the type of plasticity enhancing mechanism in the austenite phase and will be discussed in later sections.

Therefore, Thermo-Calc can be seen to be a very useful guide in predicting equilibrium phase fractions and compositions, but the word "equilibrium" needs to be stressed. In reality, partitioning depends on factors such as the mode of transformation, diffusion kinetics and prior microstructure. The diffusion kinetics of Mn is of particular concern. Mn diffuses extremely slowly in austenite with a diffusion constant of $D_{\mathrm{Mn}}^{\mathrm{FCC}} = 2\times10^{-20}$ m^2 s^{-1} at 636 °C [54]. This is compared to ferrite or α'-martensite with a diffusion constant of $D_{\mathrm{Mn}}^{\mathrm{BCC}} = 2 \times 10^{-18}$ m^2 s^{-1} also at 636 °C [54] or another substitutional element Al which has a diffusion constant on the order of 10^{-18} m^2 s^{-1} at 600 °C in austenite [55], both of which are nearly 2 orders of magnitude faster than Mn. Mn partitioning is therefore a common difficulty in multiphase 3Gen AHSS [56]. While some researchers have developed novel processing techniques which capitalise on time dependent non-equilibrium partitioning of Mn [57, 58], it is thought that for the sake of consistency and repeatability in commercial steels, it is better to drive Mn partitioning to thermodynamic equilibrium. Two element partitioning scenarios are presented below.

Cooling from $\mathbf{A_3} \rightarrow \mathbf{T_{IA}}$

If the temperature of the steel was above the A_3 temperature and the steel was allowed to cool to the desired IA temperature T_{IA}, this might be represented industrially as the strip exiting the finishing rolls above the A_3 temperature, cooled on the run out table and coiled isothermally at T_{IA}. Using the diffusion modelling software DICTRA on a Fe-5Mn-0.15C steel, Nakada *et al.* [54] found that the entire $\gamma \rightarrow \alpha$ transformation proceeded under Partitioning Local Equilibrium (PLE) mode, controlled by the diffusion of both Mn and C in the austenite phase which was established to be a very slow process. Nakada *et al.* [54] showed that even after 50 h of IA, there was hardly any change in the ferrite fraction. This strategy of cooling from a hotter temperature to T_{IA} is therefore not recommended.

Reverting from a martensitic microstructure, room temperature → $\mathbf{T_{IA}}$

After hot rolling, most medium Mn steels, depending on the composition, can be quenched to room temperature forming a fully martensitic microstructure with lath-type athermal α'-martensite (to be covered in greater detail in section 2.3). Some of the α'-martensite can then be "reverted" back to austenite ($\alpha' \rightarrow \gamma$) by heating up from room temperature to T_{IA}. Nakada *et al.* [54] and Kamoutsi *et al.* [59] have studied the transformation mode using DICTRA and found that the growth of austenite fraction occured in three stages. In stage I, austenite grows rapidly under Negligible Partitioning Local Equilibrium (NPLE) mode, *i.e.* C diffusion only, in under a second. Austenite growth then slows relatively, transitioning to PLE mode govered by Mn partitioning in the ferrite phase, *i.e.* flux of Mn from ferrite into austenite. Interestingly, towards the end of stage II, the austenite phase fraction overshoots the equilibrium phase fraction and stage III is the shrinking of austenite to the equilibrium phase fraction, also under PLE mode but now governed by Mn partitioning in the austenite phase. The $\alpha' \rightarrow \gamma$ transformation therefore occurs relatively quickly compared to the $\gamma \rightarrow \alpha$ transformation. Souza Filho *et al.* [60] investigated the partitioning behaviour between strain induced α'-martensite and austenite and found an excellent agreement between DICTRA simulations and Atom Probe Tomography (APT) results, also confirming the PLE mode of austenite growth in α'-martensite.

Ding *et al.* [61] studied the effect of retained austenite in a martensitic microstructure on reversion kinetics and found the similar three stages of austenite growth. However, it was found that a small retained austenite fraction (< 0.1) helped increase the initial reversion kinetics by reducing the need for nucleation during initial growth but too much retained austenite slowed the overall kinetics by reducing the total nucleation sites for austenite.

It should be noted that the element partitioning in medium Mn steels is different from Q&P steels which also involve a partitioning heat treatment. In Q&P steels, element partitioning is usually conducted at a significantly lower temperature compared to medium Mn steels with the primary intent of redistributing C, rather than solute elements [62].

From an industrial standpoint, there are two main approaches to conduct IA. The first method is to conduct IA in a Continuous Annealing Line (CAL) which is also used to produce two phase steels such as DP steels. However, IA durations in a CAL are short ($\sim$ 3 min), restricting its use to hotter IA temperatures and/or medium Mn steels with prior cold work [63]. The second method is to use a Batch Annealing Furnace (BAF) for medium Mn steels requiring a lower IA temperature [64]. However, there is a minimum time associated with using BAFs at approximately 24 h. Furthermore, batch processes tend to be less productive and potentially more costly compared to continuous processes. Several diffusion models are available in the literature which will help greatly during the alloy and process design of medium Mn steels [54, 59, 65, 66].

2.1.3 Effect of common alloying elements

Manganese

Almost all steels contain some amount of Mn as it is a strong deoxidiser and also binds with S to form deformable MnS inclusions [51, 67]. Therefore, Mn is usually added up to 1 wt% for such purposes. However, in medium Mn steels, Mn is used to adjust key processing parameters and the mechanical properties of the room temperature austenite phase. From Figure 2.2a, Mn is a strong austenite stabiliser and extends the fully austenitic processing window to lower temperatures, *i.e.* depressing the A_3 temperature. This is especially useful to obtain finer prior austenite grain sizes as it facilitates lower hot rolling temperatures while still remaining fully austenitic.

Increasing the Mn content also allows more austenite to be retained at room temperature by decreasing the Ms temperature. However, it should be mentioned that most medium Mn steels have a final austenite fraction no greater than 0.5, otherwise the composition of the austenite cannot be sufficiently enriched for TWIP and/or TRIP effects. In TWIP steels, Mn was found to have a parabolic effect on SFE, decreasing SFE then increasing SFE after approximately 13 wt% [68]. However, within the range of medium Mn steels, Mn only has the effect of raising SFE of the austenite phase (Figure 2.3).

In TRIP and DP steels, $>$ 2.5 wt% Mn is avoided due to the formation of segregation-related banded structures after hot rolling [2]. However, most medium Mn steels have $>$ 4 wt% Mn which suggests that medium Mn steels may be prone to banding like DP steels. Nevertheless, Wang *et al.* [35] found minimal Mn segregation in a twin roll cast medium Mn steel (2.5 mm thickness) of composition Fe-4Mn-1.8Al-0.6Si-0.3C. This implies that newer casting technologies with faster cooling rates might alleviate the Mn segregation problem although the Mn content should be minimised as much as possible.

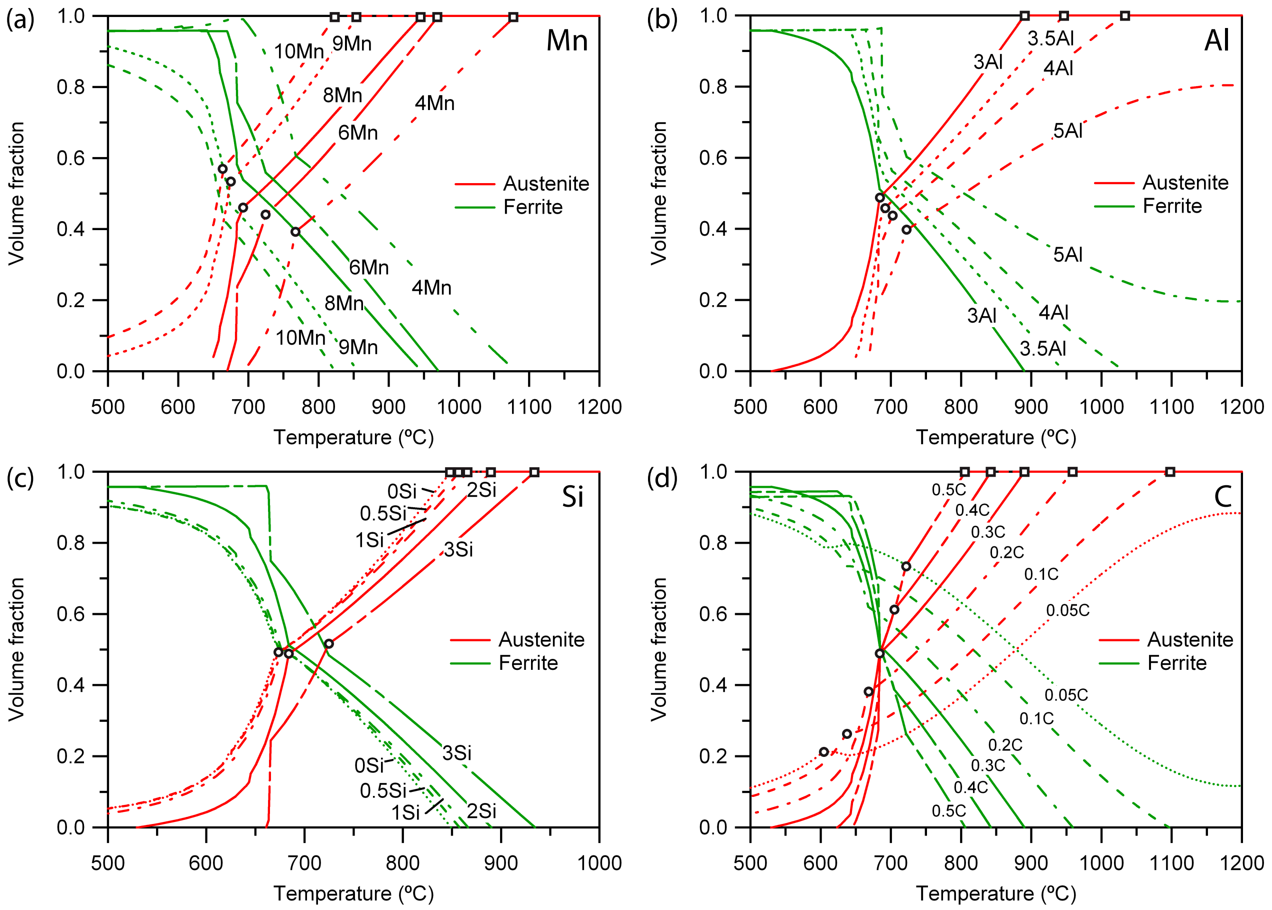

Figure 2.2: Property diagrams as simulated with Thermo-Calc with varying (a) Mn in a Fe-xMn-3Al-2Si-0.3C steel, (b) Al in a Fe-8Mn-xAl-2Si-0.3C steel, (c) Si in a Fe-8Mn-3Al-xSi-0.3C steel and (d) C in a Fe-8Mn-3Al-2Si-xC steel. N.B. Only austenite and ferrite curves shown for clarity. Open squares on the austenite curves represent the A_3 temperature and open circles represent the temperature below which cementite and other carbide species begin to form.

Aluminium

Al is a strong ferrite stabiliser and segregates to ferrite. From Figure 2.2b, Al has the effect of increasing the A_3 tempearature and more importantly, widens the intercritical regime. This helps reduce temperature sensitivity of the alloy during IA. Al also has the effect of raising the IA temperature for a given austenite volume fraction [41]. This may be beneficial as the higher temperature will aid in faster diffusion and possibly reduce the IA duration. Al is sometimes added to reduce the density of steel. Al dilates the austenite and ferrite lattice due to the larger Al atomic radius than Fe, leading to a linear reduction in density of approximately 10% with 11.5 wt% of Al [69].

However, with excessive Al additions, typically > 4-5 wt% depending on Mn and C content, the high temperature fully austenitic region will be lost. This means that the high temperature δ-ferrite phase will be stabilised to room temperature. The presence and the effects of δ-ferrite will be discussed

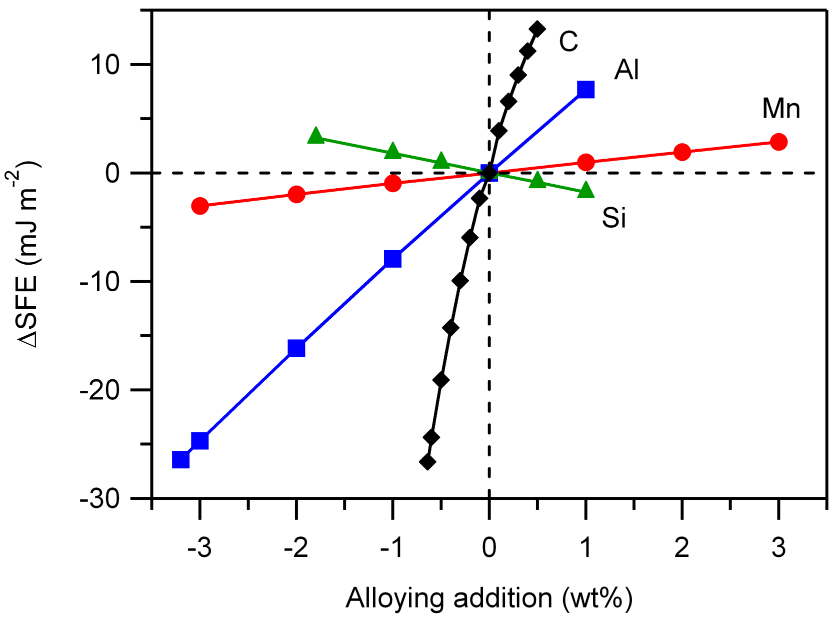

Figure 2.3: Change in SFE with different alloying additions to the austenite phase (not the bulk composition) with an initial composition of Fe-9.5Mn-3.2Al-1.8Si-0.69C-0.07V-0.03Sn [37] and SFE of 32.9 mJ m^{-2} based on the method by Sun *et al.* [36].

in a later section. If the fully austenitic region is lost through high Al additions, it can be restored by adding more Mn or C to a certain degree. However, excessive Al and C additions will cause κ-carbides to precipitate in the microstructure. If not controlled properly, κ-carbides are a deletrious phase in medium Mn steels and should be avoided [70].

Silicon

Si is a weaker ferrite stabiliser compared to Al and partitions to ferrite during intercritical annealing. From Figure 2.2c, Si does not significantly alter the A_3 temperature up to 1 wt%. Therefore, Si is usually not used primarily to adjust phase fractions and intercritical processing. However, Si is very effective in retarding cementite precipitation during cooling from either hot rolling or intercritical annealing [2, 71], allowing the austenite phase to be significantly enriched in C. Si is also a very strong ferrite solid solution strengthener [19].

While not shown in Figure 2.2c, excessive Si addition can also lead to δ-ferrite stabilisation to room temperature [36, 72]. Sun *et al.* [36] found that in a Fe-9.4Mn-3.4Si-3.2Al-0.2C medium Mn steel, the high Al and Si content in the δ-ferrite bands led to the formation of the ordered brittle B2 phase, resulting in transgranular cracking during tensile and Charpy V-notch tests. Excessive Si alloying can also lead to red scale defect during hot rolling where a eutectic compound of FeO/Fe_2SiO_4 forms on the surface of the ingot during reheating and gets pressed into the surface of the steel during hot rolling [73]. The scale is very difficult to remove during pickling and affects the subsequent galvanisability. Therefore the use of Si needs to be kept as low as possible, typically below 1 wt% [2].

Carbon

As with most steels, C is probably the most important element in medium Mn steels. C partitions to the austenite phase and has the strongest effect on lowering the A_3 temperature as shown in Figure 2.2d. C also raises the SFE (Figure 2.3) and lowers both Ms and Md_{30} temperatures. C is also a very strong austenite strengthener and produces a stronger α'-martensite after transformation.

However, there are some drawbacks if too much C is added. From Figure 2.2d, C also increases the cementite solvus, shown by the open circles. This means that only microstructures with a high austenite fraction will be cementite-free and the effective IA temperature window is shortened signficantly. As previously mentioned, when cementite particles form in the microstructure, C is lost from the austenite phase which has the adverse effect of decreasing the SFE and increasing the Md_{30} temperature (Figures 2.1d, g). Voids also tend to form around cementite particles at high strains which may act as crack nucleation sites [74]. Therefore it is best to avoid cementite formation altogether. Finally, too much C addition will negatively affect the weldability of medium Mn steels which will be covered in a later section.

Due to some of the drawbacks by excessive C addition, many researchers have kept C addtions to below 0.2 wt%. However, to enable twinning in medium Mn steels, an appreciable amount of C is needed (>0.6 wt%) in the austenite phase [7]. Therefore, most low-C medium Mn steels are TRIP-type, rather than TWIP+TRIP-type.

Carbide formers

Carbide forming elements such as Nb, Ti, V and Mo [20, 27, 28, 77–79] have been added to medium Mn steels primarily to increase the yield strength through precipitation hardening. While precipitation hardening is a potent strengthening mechanism, carbide forming elements are also very expensive and should be used judiciously.

Most studies into precipitation strengthening of medium Mn steels have been focused on the use of V as a carbide former. V has a high solubility in austenite and forms carbides at intercritical annealing temperatures, allowing for vanadium carbides (typically VC or V_4C_3) to form a relatively high density of nanoscale intragranular precipitates [80, 81]. VC precipitates have been shown to precipitate in

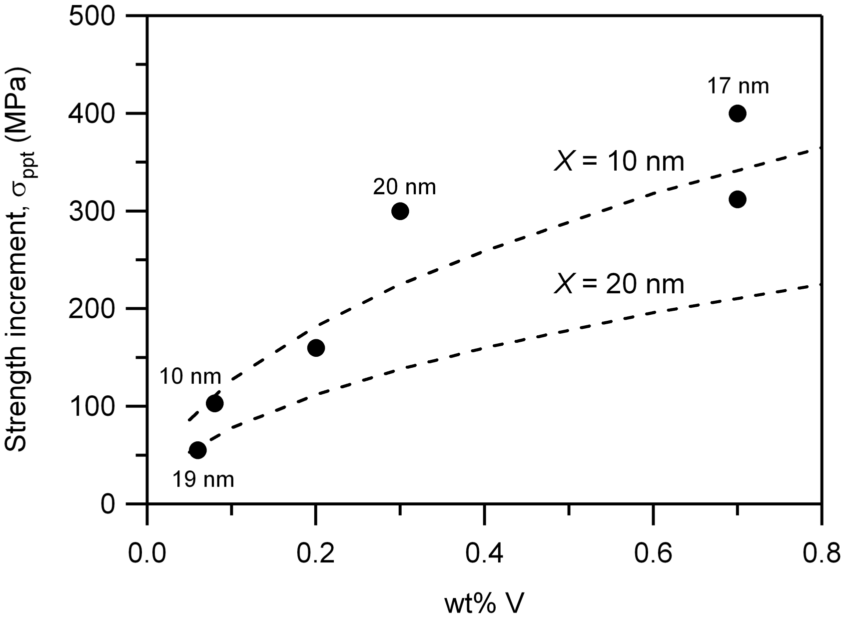

Figure 2.4: Precipitation strengthening due to V additions achieved in the literature. Mean carbide diameter given where available. Dotted lines represent the ideal strength increments when carbide diameter, X, is either 10 or 20 nm, calculated using Thermo-Calc in a Fe-8Mn-3Al-2Si-0.4C-xV steel, intercritically annealed at 750°C where $V_f^\gamma = 0.7$ and $V_f^\alpha = 0.3$ after [28]. Data from [27,28,30,37,75,76].

approximately equal amounts in both austenite and ferrite phases during IA [30,37], allowing both phases to be effectively strengthened. In order to determine the strengthening increment, σ^i_{ppt} (MPa), due to precipitation hardening in phase i, the Ashby-Orowan equation after Gladman [80] has been used by many authors [30,37] and is given as:

$$\Delta\sigma^i_{ppt} = \left(\frac{0.538\,Gbf_i^{0.5}}{X}\right)\ln\left(\frac{X}{2b}\right) \tag{2.4}$$

where G is the shear modulus ($G_\gamma = 75\,000$ MPa, $G_\alpha = 80\,000$ MPa), b is the Burgers vector ($b_\gamma = 0.250$ nm, $b_\alpha = 0.248$ nm) [22], f_i is the volume fraction of precipitates in phase i and X is the mean precipitate diameter (nm). The overall yield strength increment, $\Delta\sigma_y$ (MPa), can be determined by using a simple rule of mixtures [37]:

$$\Delta\sigma_y = \Delta\sigma^\gamma_{ppt}V^\gamma_f + \Delta\sigma^\alpha_{ppt}V^\alpha_f \tag{2.5}$$

In Figure 2.4, the ideal strength increment was calculated for a medium Mn steel of composition Fe-8Mn-3Al-2Si-0.4C-xV [28] with particle diameter of 10 and 20 nm. The VC fraction was calculated using Thermo-Calc at an IA temperature of 750 °C where $V_f^\gamma = 0.7$ and $V_f^\alpha = 0.3$. At low V concentrations (< 0.2 wt%), the literature steels appear to follow the Ashby-Orowan equation very well.

Table 2.1: Summary of the effects of various elements on key properties in medium Mn steels.

	Mn	Al	Si	C	Ref
A_3 temperature	Decrease	Increase	Increase	Decrease	-
Intercritical window	Shorten	Widen	Widen	Shorten	[36]
SFE (mJ m^{-2} / wt%)	$+1.0$	$+8.1$	-1.8	$-15.9\ [C]^2 + 32.2\ [C]$	[36]
Ms (°C / wt%)	-34.5	$+20$	-14	-502 / wt%$^{0.5}$	[49]
Md_{30} (°C / wt%)	-8.1	NA	-9.2	-462	[36, 52]
γ sol. strength (MPa / wt%)	-1.5	NA	$+23$	$+567$	[83, 84]
α sol. strength (MPa / wt%)	$+44.7$	$+70$	$+138.6$	$+5000$	[83, 84]

But at high V concentrations, there is a very large deviation beween the experimental and calculated strengths. With increasing V content, the effect of V on the non-recrystallisation temperature (T_{nr}) becomes significant [82]. Hu *et al.* [30] showed that with an addition of 0.7 wt% V, both solute and VC precipitates were able to retard both recovery and recrystallisation during intercritical rolling. Their study showed that the V-containing medium Mn steel had a 650 MPa yield strength improvement over the V-free steel processed in an identical manner. However, no more than 400 MPa was attributed to a fine dispersion of VC precipitates, the balance was from dislocation strengthening as a result from incomplete recrystallisation. Since residual stress from incomplete recrystallisation is usually undesirable from a metal forming perspective and V is a fairly expensive element in steels, V content should be kept to < 0.2 wt%.

Summary of alloying elements

As with most steels, every element in medium Mn steels is added with a purpose such as modifying the intercritical processing parameters, adjusting the austenite stability and SFE or to provide solid solution strengthening. The effects of the common alloying elements described in the above section are summarised in Table 2.1.

2.1.4 Other phases

δ-ferrite

In medium Mn steels, δ-ferrite is the first phase to form during solidification from liquid [85]. In most low carbon steels, the δ-ferrite transforms into austenite at typical reheating and hot rolling temperatures. However, in medium Mn steels, δ-ferrite can be stabilised to room temperature if the Al and Si content is sufficiently high. The presence of δ-ferrite may also indicate non-equilibrium Scheil solidification where local compositions of Al and Si due to microsegregation are able to stabilise

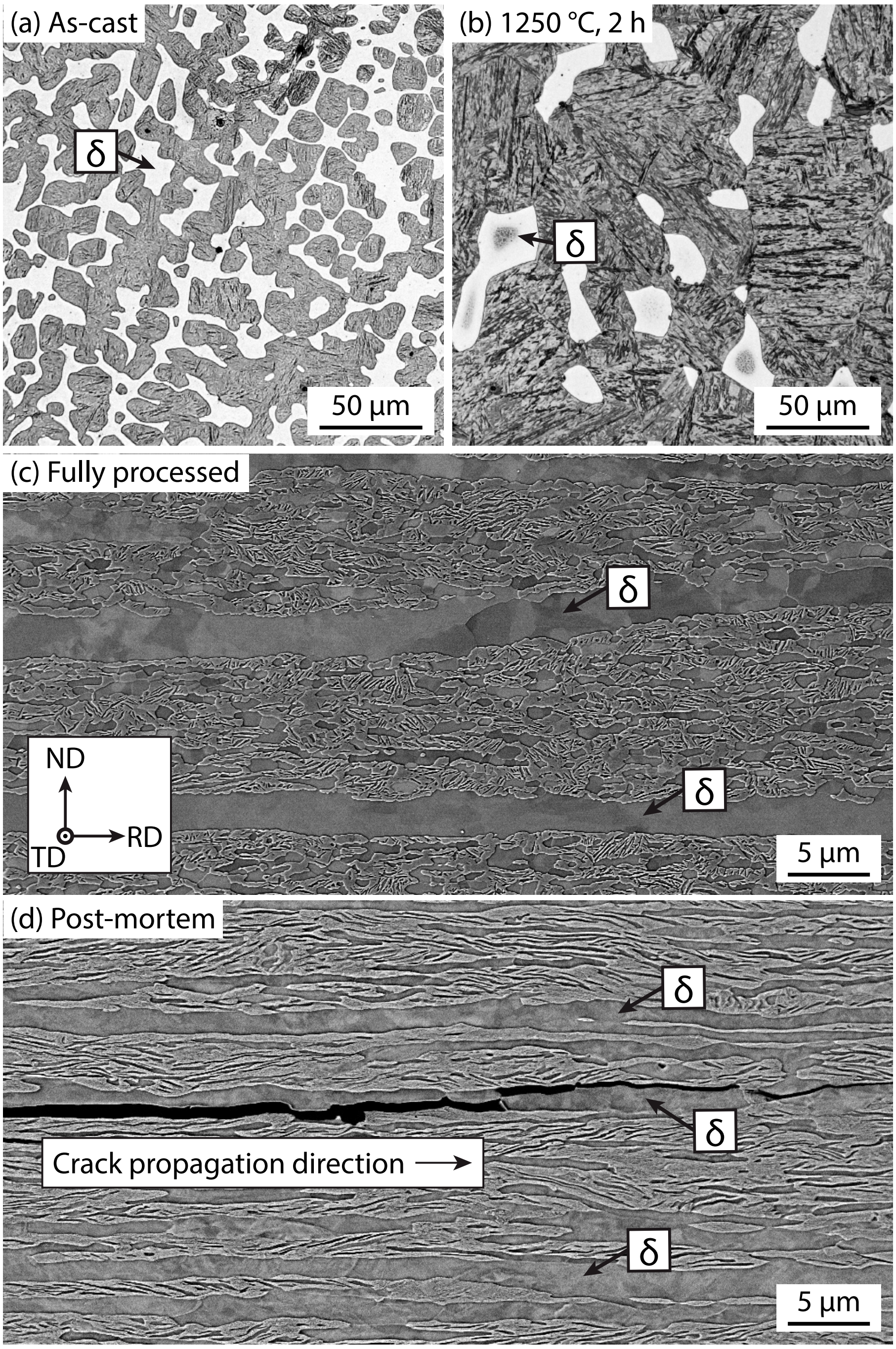

Figure 2.5: Fe-6Mn-3Al-1.5Si-0.3C medium Mn containing δ-ferrite in various conditions. Optical micrographs of (a) as-cast condition and (b) homogenised at 1250 °C, 2 h. Secondary electron micrographs of (c) after full processing, showing δ-ferrite stringers and (d) after a tensile test near the fracture surface showing a crack propagating along the interface of a δ-ferrite stringer. Tensile direction parallel to RD. Unpublished work.

δ-ferrite. If reheated for a sufficiently long time, it may be possible for microsegregation related δ-ferrite to transform into austenite [74]. However, if the alloy chemistry is such that there is no fully austenitic region (Figure 2.2b), then δ-ferrite will always be present.

While δ-ferrite and α-ferrite are both BCC and identical in terms of deformation behaviour, δ-ferrite adopts a very distinct morphology. In the as-cast state, δ-ferrite has a vermicular morphology (Figure 2.5a) at the dendrite cores. When the steel ingot is reheated, the δ-ferrite globularises (Figure 2.5b) and during rolling, the δ-ferrite grains elongate and form very long stringers in the rolling direction (Figure 2.5c).

There has been some debate as to whether δ-ferrite is beneficial or at least a benign phase rather than detrimental in medium Mn steels. On one hand, δ-ferrite does not appear to significantly affect strength [74,86] and medium Mn steels that contain δ-ferrite also do not appear to suffer from yield point elongation [87]. On the other hand, cracks are often observed at the interphase boundaries between δ-ferrite and the matrix at fracture after a tensile test (Figure 2.5d). Kim *et al.* [88] also found that the presence of coarse δ-ferrite drastically lowers the Charpy V-notch impact energy. Furthermore, if the δ-ferrite was the result of excessive Al and/or Si additions as opposed to incomplete homogenisation, Sun *et al.* [89] found that the brittle B2 ordering reaction might occur in δ-ferrite. Nevertheless, Choi *et al.* [90] argues that the interfacial cracks running along the length of the δ-ferrite boundary parallel to the tensile axis were the consequence of tensile failure rather than the cause and δ-ferrite should not be considered detrimental to the tensile properties of medium Mn steels.

2.2 Plasticity enhancing mechanisms

2.2.1 TWIP and stacking fault energy

Many researchers have been successful in activating the TWIP effect in medium Mn steels [19,30,36,98], demonstrating that it is indeed possible to retain the TWIP effect with a significantly lower Mn content. As with TWIP steels, SFE is one of the main parameters in determining the active plasticity enhancing mechanism in medium Mn steels. In Figure 2.6, the SFE and austenite stability, quantified as the Md_{30} temperature, of various literature medium Mn steels are compared. It can be seen that the steels all lie within the blue strip, this is because elements like Mn and C which increase SFE also increase the austenite stability. It is therefore difficult to alter the SFE without also changing the austenite stability, unlike in TWIP steels where the high Mn content ensures that the austenite is very stable against deformation induced martensitic transformations. It is worth noting that the high Mn TWIP steels share a similar Md_{30} as medium Mn steels but do not exhibit the TRIP effect. This highlights the limitations of austenite stability quantification which will be discussed in a later section.

Another key feature in Figure 2.6 is that at a SFE of 10 mJ m^{-2}, there appears to be a transition between TRIP only and TWIP+TRIP, *i.e.* activation of twinning. This is not far away from the

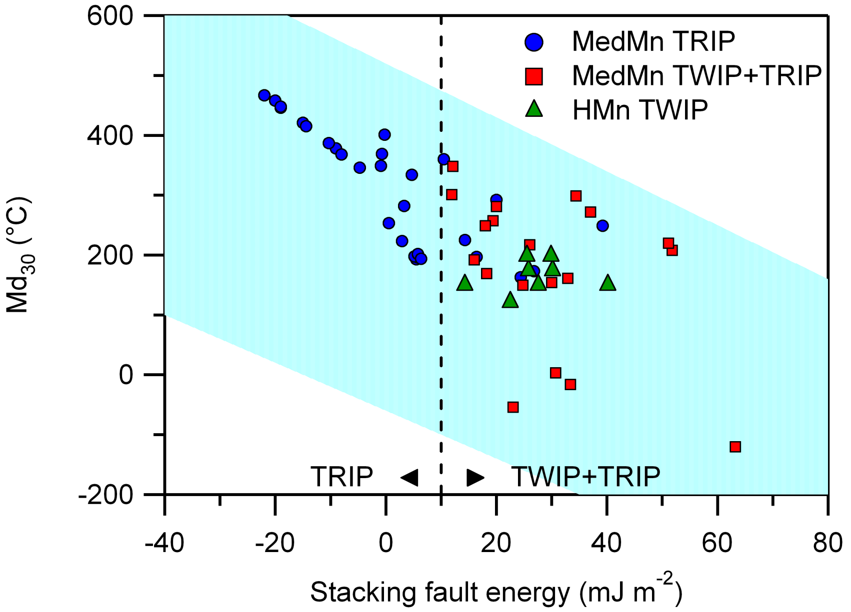

Figure 2.6: Md_{30} and SFE comparison between several medium Mn TRIP-type, TWIP+TRIP-type and High Mn (HMn) TWIP steels. An arbitrary line is drawn at SFE = 10 mJ m^{-2} where the plasticity enhancing mechanism in medium Mn steels appear to transition from TRIP to TWIP+TRIP. Data from [19, 33, 35–37, 45, 91–97]

approximate value of 15 mJ m^{-2} [8, 99] where deformation twinning becomes active in TWIP steels. However, it should also be noted that the TRIP effect is almost always active [19].

While the primary motivation behind retaining the TWIP effect in medium Mn steels is the supposed contribution to strain hardening through the dynamic Hall-Petch effect [100], there is growing evidence that even though the austenite phase in medium Mn steels can be made to twin, the TWIP effect in medium Mn steels is not as strong as compared to TWIP steels. In medium Mn steels where the austenite fraction is typically ≤ 0.5, the total strain hardening contribution from twinning is effectively halved as compared to fully austenitic TWIP steels. Since α'-martensitic transformation is unavoidable, the volume fraction of austenite available to twin decreases with increasing strain as austenite is gradually replaced by α'-martensite. Furthermore, Lee *et al.* [19] and Kwok *et al.* [97] also found that due to the fine grained nature of medium Mn steel microstructures, the capactiy for strain hardening by further grain refinement through the dynamic Hall-Petch effect was very limited. When the austenite grain size in medium Mn steels enters the submicron regime, especially in lamellar type microstructures [97], twinning was found to have nearly no effect on strain hardenability. Overall, the TWIP effect does not appear to play a significant role in the strain hardening of medium Mn steels.

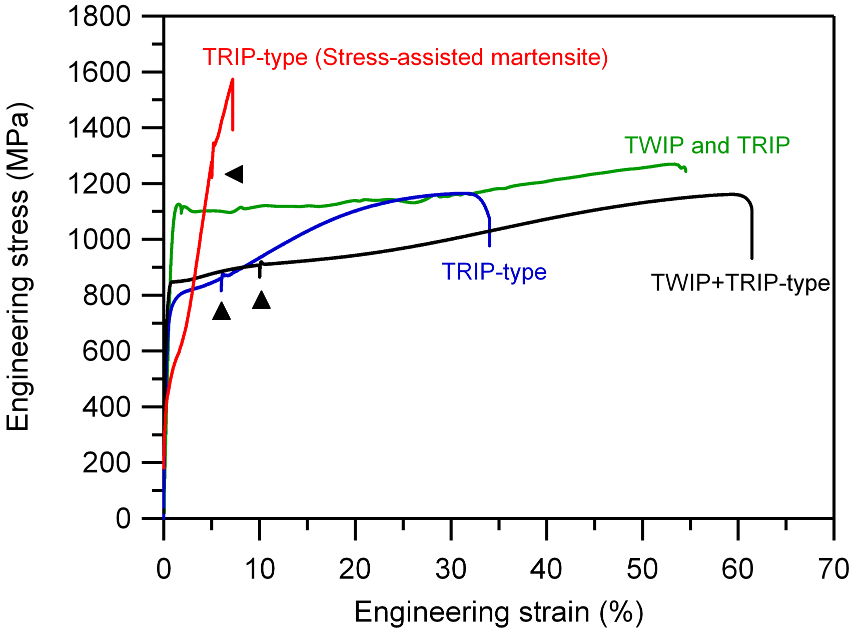

Figure 2.7: Tensile curves from different steels exhibiting different types of plasticity enhancing mechanisms. Triangles indicate the strain at which the extensometer was removed. Data from [58, 98] and unpublished work.

2.2.2 TRIP and austenite stability

Not all medium Mn steels exhibit twinning and in fact, many medium Mn steels are TRIP only. Very broadly, the TRIP effect refers to the formation of the hard α'-martensite phase in room temperature austenite during plastic deformation which then raises the strain hardening rate and delays necking [101]. High strain hardening rates and large elongations ($> 30\%$) can be achieved by controlling the TRIP effect in medium Mn steels (Figure 2.7). There are many ways to form α'-martensite, each depending on various factors such as austenite stability, grain size, presence of intragranular nucleation sites, *etc.* Nevertheless, the broad concept in developing medium Mn steels with a large ductility is to sustain a controlled evolution of α'-martensite over a large strain regime [102, 103]. Microstructurally, this means being able to continuously form small isolated grains of α'-martensite [104]. In medium Mn steels, the austenite stability can also be "tuned" to produce a range of strain harderning rates by adjusting the IA parameters [58, 105].

There are many strategies in the literature to extend the TRIP effect over a large strain regime. One strategy is to introduce a transition stage such as the two-step $\gamma \rightarrow \varepsilon \rightarrow \alpha'$ transformation [93, 106]. Intersections of two crossing ε-martensite plates are very potent nucleation sites for α'-martensite as described by Olson and Cohen [107]. Work by Field *et al.* [93, 106] showed that the two-step transformation can be enabled when the SFE is ≤ 10.5 mJ m^{-2} including negative SFEs (*i.e.* stacking faults being more stable than the FCC crystal structure). Another transition stage is the two-step $\gamma \rightarrow \gamma_{twin} \rightarrow \alpha'$ mechanism, also known as the successive TWIP+TRIP effect which will be covered in the subsequent section.

The next strategy is to create a spread in austenite stability such that the least stable austenite transforms first, ending with the most stable austenite. There have been many names given to this strategy such as spectral TRIP [103] and discontinuous TRIP [108–110]. In what has been coined spectral TRIP, Wang *et al.* [103] found that by creating a distribution of submicron austenite grain sizes, the austenite grains produced different densities of stacking faults during deformation. The smallest grains produced the highest density of stacking faults which acts as nucleation sites for α'-martensite and therefore transformed first. The slightly larger grains formed subgrains and a lower density of stacking faults and transformed later. Using grain size to create a spread in austenite stability is also shared by the discontinuous TRIP effect. From the work by Cai *et al.* [109], the discontinuous TRIP effect can be described as a burst of α'-martensite transformation in austenite grains with similar stability, which then relaxes and transfers the stress to the surrounding ferrite+austenite matrix. When the stress in the matrix rises, the least stable of the remaining austenite grains transforms to α' martensite and the process repeats. This process was demonstrated using a distribution of grain sizes [109], inhomogeneous Mn distribution between austenite grains [108] (lowest Mn content transforms first), texture [110] (austenite with lowest Schmid factor transforms first) and morphology [108] (coarse and blocky transforms first, followed by fine, globular and/or lamellar austenite). However, as its name suggests, the discontinuous TRIP effect results in a serrated stress-strain curve and is not ideal from a metal forming perspective.

The final strategy is a lot less common, it involves heavily stabilising the austenite phase, either through grain refinement [111] or chemically (*i.e.* with austenite stabilisers) [97] only allowing α'-martensite to nucleate from the austenite grain boundaries and grow in a stress-assisted manner [112]. By heavily stabilising the austenite phase, it ensures that α'-martensite does not nucleate anywhere except else apart from the interphase (γ/α) grain boundaries where the strain concentration is the highest. The growth of martensite then proceeds slowly into the austenite grain and is sustained by the stress build up at the grain boundaries which provides the driving force for transformation [97, 112]. However, it is possible to over-stabilise the austenite phase to the point where TRIP cannot occur at all and the alloy suffers from poor ductility [19, 111]. This strategy therefore represents the upper limit as to what can be achieved by varying the TRIP effect through adjusting austenite stability.

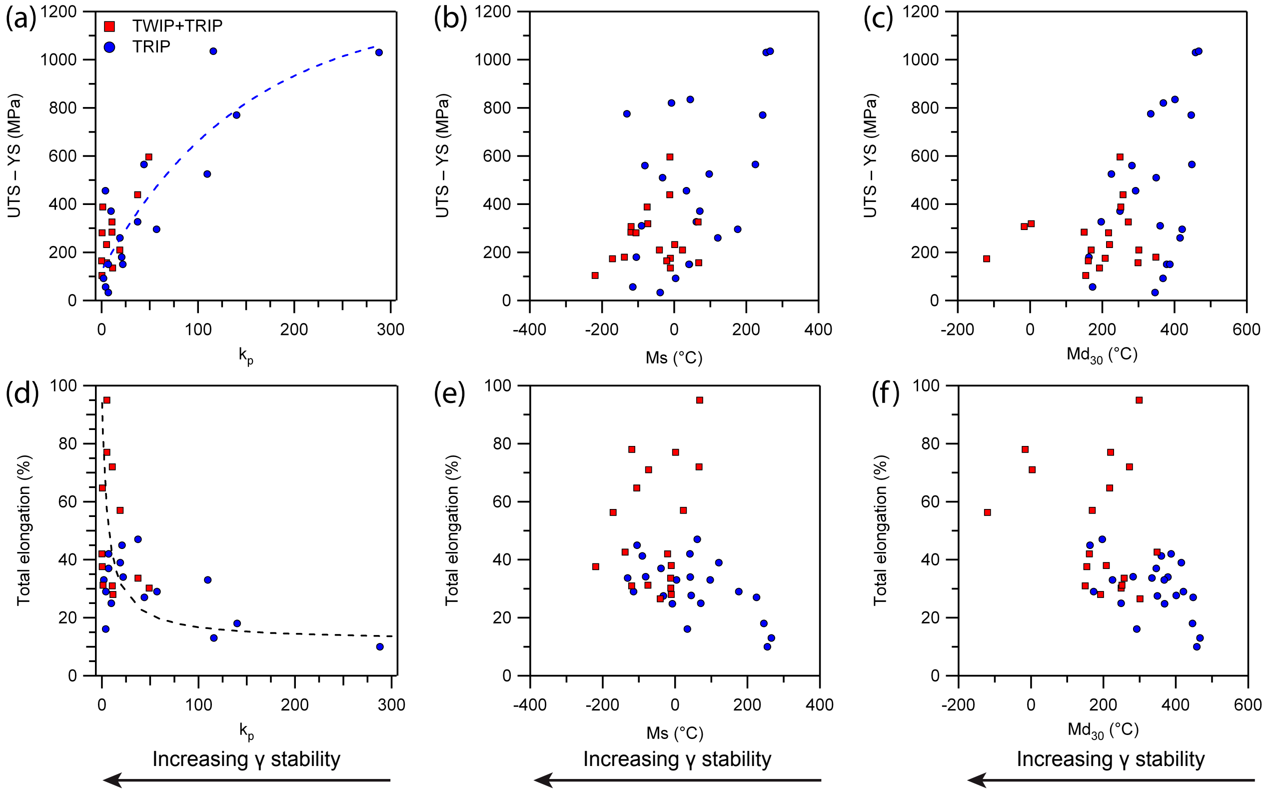

Figure 2.8: Comparison between several martensite stability parameters and tensile properties. Effect of (a) k_p, (N.B. line of best fit drawn only for TRIP-type medium Mn steels) (b) Ms and (c) Md_{30} temperatures on strain hardenability, *i.e.* difference between tensile and yield strengths. Effect of (d) k_p (N.B. line of best fit drawn for both TRIP and TWIP+TRIP medium Mn steels), (e) Ms and (f) Md_{30} temperatures on total elongation. Data from [19, 35–37, 92–94, 96, 97, 113].

Austenite fraction and stability, measurement and prediction

Austenite fraction can be measured in several different ways, these methods can be divided into electron microscopy, X-Ray Diffraction (XRD) and magnetic saturation [19, 114]. Typically, a series of interrupted tensile tests are conducted and the increasing α'-martensite fraction is measured using the abovementioned methods although *in-situ* techniques are increasingly popular. EBSD is a common electron microscope technique as it readily provides microstructure, texture and phase fraction information. However, α'-martensite and ferrite cannot be easily distinguished from each other with EBSD. Therefore, a baseline ferrite fraction at zero strain has to be obtained and any increase in ferrite or BCC fraction is then taken as α'-martensite. Other limitations of EBSD are small sampling area and an increase in non-indexed fraction at large strains which introduces significant amount of uncertainty. When using EBSD, care must be taken not to use “clean up” functions as it might obscure real features in the microstructure. XRD is an older but well established technique that can provide accurate phase fraction information by measuring the relative peak intensities of the constituent phases in the sample. The final technique, magnetic saturation, is conducted with the use of a feritscope. Magnetic saturation techniques can sample a large volume and can be conducted in-situ but needs prior calibration, usually with XRD [36,115].

To represent austenite stability, several researchers [89,94,116] have proposed using the Ludwigson-Berger austenite stability constant, k_p [117]:

$$k_p = \frac{V_{\gamma}^{-1} - V_{\gamma 0}^{-1}}{\varepsilon} \tag{2.6}$$

where $V_{\gamma 0}$ is the austenite volume fraction in the unstrained condition and V_{γ} is the austenite volume fraction at a true strain of ε, usually taken to be the failure strain to represent the total amount of transformation during a tensile test. A low k_p represents a high austenite stability and *vice versa.*

From Figures 2.8a and d, it can be seen from several TRIP-type and TWIP+TRIP-type medium Mn steels that there is a trend between k_p and strain hardenability, here measured as the difference between tensile and yield strength, and between k_p and total elongation. At low k_p or high austenite stability, Equation 2.6 suggests that either less α'-martensite is formed or formed over a larger strain, both resulting in a low strain hardenability. On the other hand, high k_p values and very low austenite stability tend to be associated with stress-assisted martensitic transformation. According to the definition by Olson and Cohen [107], stress-assisted martensitic transformation occurs below the theoretical yield point of the austenite phase and the austenite explodes with α'-martensite, resulting in extremely rapid hardening but also very poor ductility (Figure 2.7). An intermediate k_p value is therefore desired for better elongation but still retaining appreciable strain hardenability.

Unfortunately, k_p is a phenomenological parameter and there few empirical relationships that can predict the k_p value based on composition, grain size, *etc* [118]. Therefore, many researchers use other stability constants such as Ms or Md$_{30}$ (Equations 2.1 and 2.3 equations respectively) to estimate austenite stability as part of their alloy design process [30,36,119]. While many Ms and Md$_{30}$ equations that incorporate composition and grain size exist in the literature [49,52,53,120], they do not correlate well with any tensile properties, unlike k_p as shown in Figure 2.8. Austenite stability also depends on a multitude of other factors such as strain partitioning [121,122], availability of nucleation sites [123], grain morphology [124,125], shielding effects [125] and texture [108,125]. All these factors are difficult to incorporate into a single composition based equation. While calculated Ms and Md$_{30}$ parameters can be useful to compare austenite stabilities within one study, it is less helpful to compare them between studies.

2.2.3 TWIP+TRIP

As previously mentioned, it is not uncommon for TWIP and TRIP effects to occur together during plastic deformation of medium Mn steels. However, they usually occur in different grains, *i.e.* some austenite grains twin while others transform [98,126]. While the heterogeneous deformation behaviour of TWIP and TRIP in different grains can lead to large elongations (Figure 2.7), these steels generally exhibit serrated stress-strain curves *i.e.* the Portevin-Le Chatelier (PLC) effect [119,127] and is not desirable for metal forming processes. Nevertheless, TWIP and TRIP can be made to occur within the same austenite grain and has been coined the TWIP+TRIP effect by Lee and De Cooman [19,128]. Deformation *via* the TWIP+TRIP effect is more homogeneous and can also lead to significant elongations as shown in Figure 2.7. However, it should be noted that TWIP+TRIP-type medium Mn steels are not immune from PLC banding [19] although the serrations (Type A/E) occur at much higher strains [127].

The TWIP+TRIP effect can be further subdivided into the successive TWIP+TRIP and simultaneous TWIP+TRIP effects. Briefly, the successive TWIP+TRIP refers to the process where twins precede α'-martensite which forms at the twin intersections during plastic deformation, *i.e.* $\gamma \rightarrow \gamma_{twin} \rightarrow \alpha'$. This mechanism is also observed in Metastable Austenitic Stainless Steels (MASS) and is well understood [129–131]. However, Sohn *et al.* [113] first observed that twinning and transformation need not occur sequentially and can form independently from one another within the same austenite grain. Whether the medium Mn steel deforms *via* the successive or simultaneous TWIP+TRIP mechanism appears to depend solely on SFE as shown in Table 2.2 where a switch from successive to simultaneous occurs between a SFE of betwen 23-31 mJ m^{-2}. While both types of TWIP+TRIP mechanisms lead to large elongations of $> 40\%$, it is the simultaneous TWIP+TRIP that allows for a much higher elongation to failure of up to 95% as reported by Sohn *et al.* [92].

As previously mentioned, It has been shown by Lee *et al.* [19] and by Kwok *et al.* [97] that the TWIP effect has a very minimal effect on the strain hardening of fine grained TWIP+TRIP-type medium Mn steels, although the twins are needed to nucleate α'-martensite as part of the successive TWIP+TRIP effect. Therefore, the large elongation associated with TWIP+TRIP-type medium Mn steels is almost entirely due to the TRIP effect. However, the composition ranges that enable the TWIP+TRIP effect in medium Mn steels produces austenite with a signficantly higher stability than pure TRIP-type medium Mn steels, allowing for a more controlled formation of α'-martensite that leads to much higher elongations than TRIP-type medium Mn steels. Therefore, TWIP+TRIP-type

Table 2.2: Comparison of SFE and austenite stability between several literature medium Mn steels, arranged in order of increasing SFE. E − Equiaxed, L − Lamellar.

Austenite composition (wt%)	SFE (mJ m^{-2})	Ms (°C)	Md$_{30}$ (°C)	Microstructure	d_γ (µm)	TWIP+TRIP	Ref
Fe-10.3Mn-2.9Al-2.0Si-0.32C	20	15	319	E	1.5	Successive	[132]
Fe-6.6Mn-1.3Al-1.2Si-0.48C	20	88	281	E	<1	Successive	[33]
Fe-12.3Mn-2.5Al-2.4Si-0.58C	23	-144	150	E	1.2	Successive	[36]
Fe-7.3Mn-1.8Al-1.0Si-1.07C	31	-150	-1	L	1.2	Simultaneous	[97]
Fe-9.5Mn-3.2Al-1.8Si-0.69C	33	-68	161	E	4.2	Simultaneous	[37]
Fe-8.5Mn-1.9Al-1.0Si-1.10C	33	-181	-16	E	1.5	Simultaneous	[97]
Fe-10.8Mn-4.2Al-0.39C	34	-177	301	E	1.7	Simultaneous	[92]
Fe-10.2Mn-4.2Al-0.46C	37	-120	274	E	2.1	Simultaneous	[92]
Fe-11.5Mn-4.7Al-0.55C	51	-69	224	E	2.8	Simultaneous	[113]

medium Mn steels are still worth further study.

2.3 Processing and microstructure relationships

The thermomechanical processing of most medium Mn steels can be conducted in three distinct temperature regimes where $T > A_3$ *i.e.* hot processing, $A_3 < T < A_1$ *i.e.* intercritical processing and $T < A_1$ *i.e.* cold processing. In Figure 2.9, a common processing route is drawn where the medium Mn steel is hot rolled above the A_3 temperature, cooled to room temperature, cold rolled then intercritically annealed at a temperature between A_1 and A_3 to obtain the desired phase fraction and austentite properties. Many other processing strategies exist in the literature and depending on the processing history, a myriad of microstructures can be produced in medium Mn steels. This section aims to review the step-by-step microstructure evolution with various thermomechanical processing strategies.

2.3.1 Hot rolling

Most medium Mn steels in the literature are either fully austenitic or contain some amount of δ-ferrite at typical hot rolling temperatures of > 1000 °C, shown as schematic A and Aδ respectively in Figure 2.10. If the final hot rolling temperature is still within the austenitic temperature range and above the T_{nr}, then it is likely that dynamic recrystallisation would occur and the austenite grain size would be refined (microstructure B).

If the steel contains δ-ferrite, then it is likely that δ-ferrite will exist as globular grains within an austenitic matrix (microstructure Aδ). A real example is shown in Figure 2.11a-b, where an 8 wt% Mn steel was homogenised for 2 h at 1250 °C before water quenching [74]. The δ-ferrite grains can be distinguished from the matrix as the Mn depleted regions in the Mn EDS map in Figure 2.11b. After

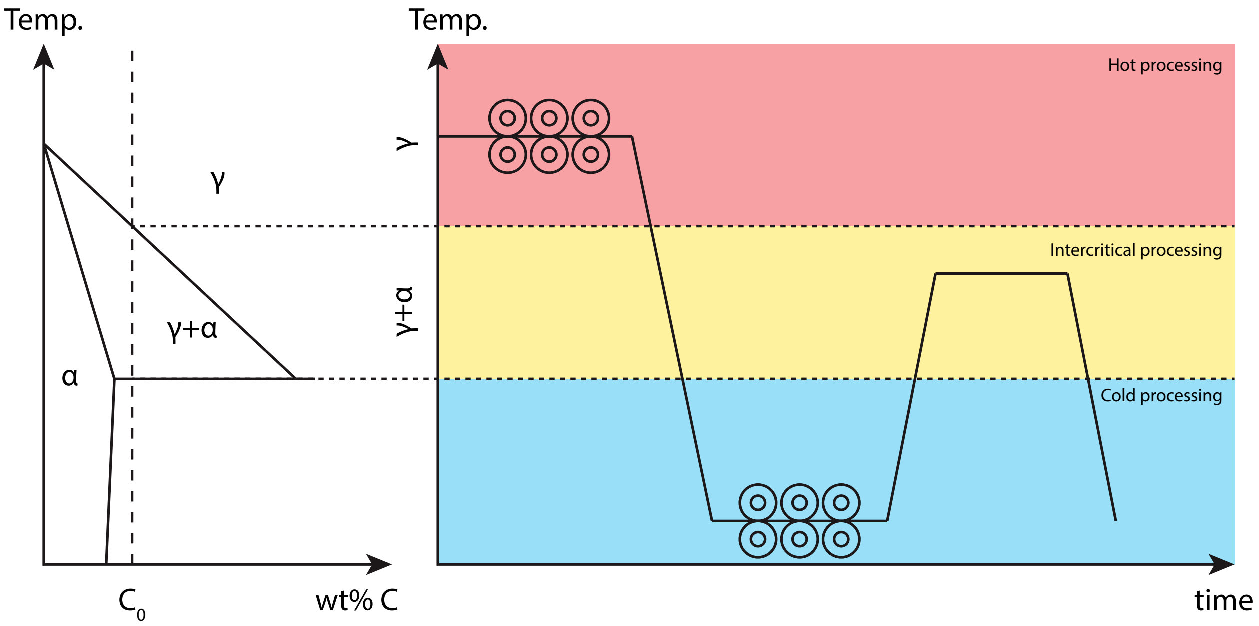

Figure 2.9: Schematic of the three main temperature regimes which correspond to the fully austenitic and intercritical regimes.

hot rolling, these δ-ferrite grains will elongate and form stringers (microstructure Bδ). In Figure 2.11c, it can be seen that the delta ferrite grains do not recrystallise and are significantly coarser compared to the fine-grained duplex matrix.

For most commercial steels, rolling takes place at decreasing temperatures where the final temperature after the last stand is below the T_{nr} temperature [133]. In medium Mn steels, the T_{nr} is usually higher than leaner AHSS, typically above 900 °C, due to the relatively higher C content [134]. When rolled below the T_{nr} temperature, the austenite grains will elongate and form pancaked austenite. However, when the rolling temperature dips below the A_3 temperature into the intercritical region, ferrite grains will begin to nucleate in the microstructure. Common nucleation sites are at austenite grain boundaries and shear bands as shown in microstructure C in Figure 2.10. In Figure 2.11d, an 8 wt% Mn steel was quenched immediately after hot rolling where the last two passes where just below the A_3 temperature. Due to the relatively high Mn and C content of the austenite phase, the austenite did not transform during quenching and effectively captures the microstructure just after the final pass. The microstructure showed elongated austenite grains and elongated ferrite grains which mainly nucleated along the austenite grain boundaries. Some finer ferrite grains can also be found within the austenite grains and most likely nucleated from other defects such as shear bands.

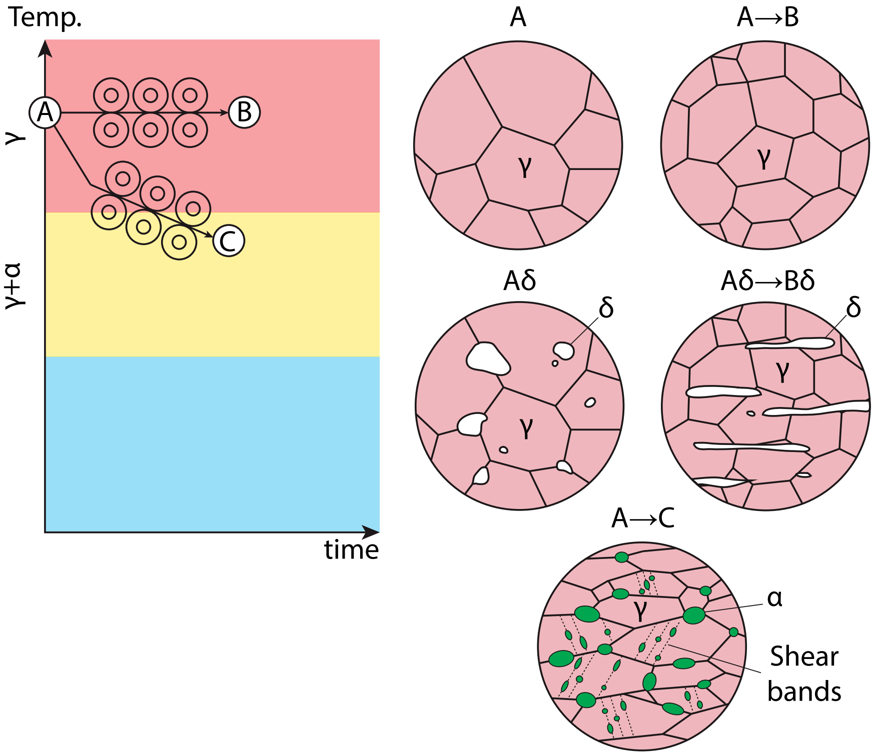

Figure 2.10: Schematic of the hot rolling stage and corresponding microstructures.

2.3.2 Cooling after hot rolling and intercritical rolling

The cooling rate after hot rolling is very important as it generally sets the foundations of the final microstructure. After the final rolling pass, the strip is usually spray quenched on the run out table either to room temperature or to the coiling temperature where it is then coiled at a constant temperature for approximately 30 min then cooled slowly within the coiler [134]. If the strip is quenched to room temperature, the microstructure will look like either microstructure D1 and D2 in Figure 2.14. When microstructures B and C are water quenched, the austenite will transform into α'-martensite and form microstructures D2 and D1 respectively. Microstructure D2 can either be entirely martensitic or contain some untransformed austenite within equiaxed prior austenite grains but microstructure D1 comprises of a small fraction of ferrite grains within a martensitic matrix. A real example of microstructures D1 and D2 are shown in Figures 2.13a and b respectively.

If the strip is coiled and cooled slowly in the coiler, a different microstructure will form. Typical coiling temperatures range from 500-600 °C which typically corresponds to the lower end of the intercritical regime in most medium Mn steels. After coiling, the strip is cooled slowly in the coiler and can be replicated to a certain degree in the laboratory by Furnace Cooling (FC). At these temperatures and durations, diffusion of Mn as well as ferrite nucleation and growth is very limited [54]. Therefore,

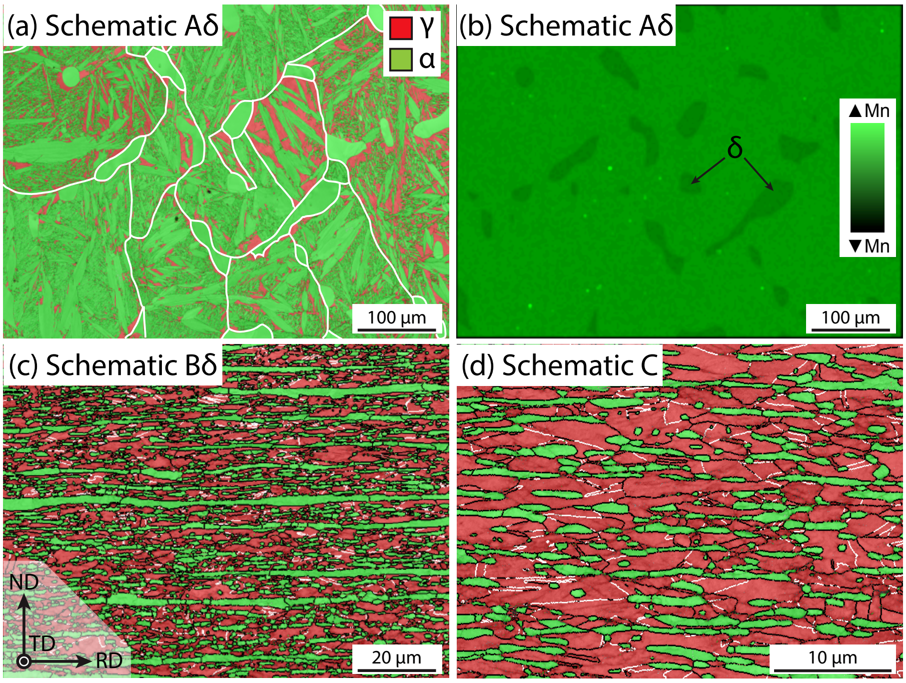

Figure 2.11: (a) EBSD PM+IQ map 8 wt% Mn steel quenched after incomplete homogenisation at 1250 °C for 2 h. White lines denote PAGBs. Green-ferrite, red-austenite. (b) Corresponding Mn-EDS map from (a) showing globular δ-ferrite grains as seen in schematic Aδ. (c) EBSD PM+IQ map of the same steel after final processing, showing how δ-ferrite grains elongate into stringers as seen in schematic Bδ. Black lines indicate HAGBs and white lines indicate austenite $\Sigma 3$ boundaries. (d) EBSD PM+IQ map of the same steel quenched after hot rolling with finish rolling temperature below A_3 temperature showing ferrite grains growing in between and within the elongated austenite grains as shown in schematic C.

it is unlikely that the phase fraction and microstructure will be significantly different before and after coiling. However, by cooling slowly in the coil box, the austenite in microstructure C gradually transforms to pearlite instead of α'-martensite. Hidalgo *et al.* [135] reported that pearlite was able to form in a Q&P steel with 4.5 wt% Mn partitioned at 500 °C. Microstructure E therefore contains globular ferrite grains (formed during hot rolling) at the PAGB in a pearlitic matrix. A real example of microstructure E is shown in Figure 2.13c where a 6 wt% Mn medium Mn steel was coiled at 600 °C and furnace cooled. The cementite lamella are clearly visible.

Instead of cooling to room temperature, the strip can be warm rolled after hot rolling. It should be mentioned that warm rolling is a relatively novel thermomechanical processing method and is not commonplace in most strip mills. Warm rolling temperatures typically lie within the intercritical temperature regime and is usually below the non-recrystallisation temperature (T_{nr}) of the steel. Since there is little recrystallisation, the austenite grains elongate in the rolling direction and form a high density of shear bands. Due to the high defect density, very fine ferrite grains will nucleate at the prior austenite grain boundaries as well as along shear bands. In some cases, austenite recrystallisation

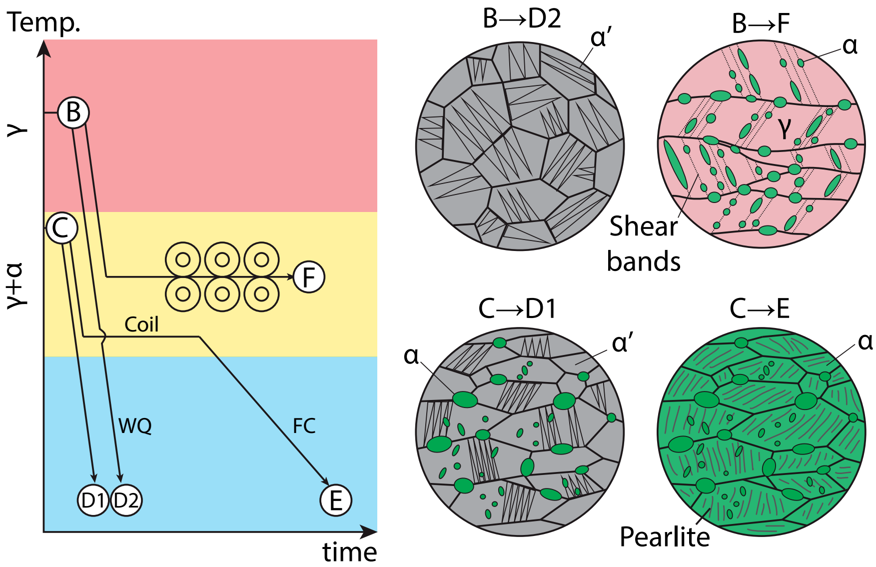

Figure 2.12: Schematic of the cooling stage after hot rolling, warm rolling stage and the corrersponding microstructures. WQ - water quench, FC - furnace cool.

is possible but only around the grain boundaries of the elongated prior austenite grains, forming a necklace-type microstructure [136] of fine ferrite and austenite grains around a highly deformed austenite core. A real example of microstructure F is shown in Figure 2.13d where the elongated prior austenite grains can be easily distinguished between layers of fine necklace ferrite and austenite grains. Very fine ferrite grains can also be observed along the diagonal shear bands.

After warm rolling, the strip is usually at its final desired thickness and can be further annealed at the warm rolling temperature to allow for recovery of the highly deformed austenite core and further element partitioning. However, very little microstructural changes occur during further annealing of the warm rolled strip.

2.3.3 Cold rolling and intercritical annealing

All medium Mn steels need a final IA heat treatment to produce the desired final phase fractions and to allow of element partitioning between the austenite and ferrite phases. If the prior microstructure was martensitic such as micstructures D1 and D2, then the IA heat treatment is also sometimes called Austenite Reverted Transformation (ART) annealing [40, 101]. Cold rolling the strip before IA greatly improves the speed of which the abovementioned processes occur but will produce only one type of microstructure. Microstructures D1, D2 and E can be cold rolled then intercritically annealed to produce microstructure I in Figure 2.15. Microstructure I is commonly described as globular or equiaxed as the cold deformation allows for recrystallisation during the IA and therefore

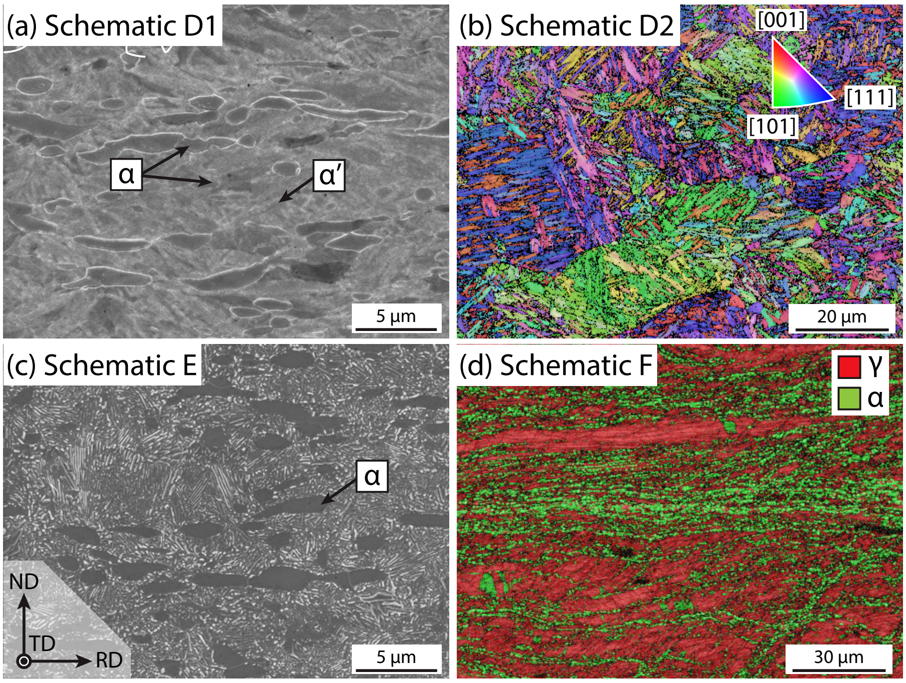

Figure 2.13: Secondary electron micrograph of a 5 wt% Mn steel (a) hot rolled then quenched showing ferrite grains at elongated PAGBs in a α'-martensitic matrix. (b) EBSD IPF-X (right) map of a hot rolled then quenched 8Mn steel showing a nearly fully α'-martensitic microstructure, after [58]. (c) The same steel from (a) but coiled at 600 °C for 30 min and furnace cooled after hot rolling showing ferrite grains at the PAGB in a pearlitic matrix. (d) EBSD phase map of a 12 Mn steel warm rolled after hot rolling showing very fine necklace austenite and ferrite grains around austenite cores. Unpublished work.

produce a homogeneous distribution of austenite and ferrite grains with a more random texture. The resulting microstructure can be extremely fine grained and as Miller [39] found in 1972, is resistant to coarsening. A real example of microstructure I is shown in Figures 2.15g-h where a hot rolled strip with microstructure E is cold rolled to a 30% thickness reduction and then intercritically annealed at 750 °C for 5 min, producing a microstructure with submicron sized austenite grains. However, it should be noted that cold rolling steels with microstructures D1 and D2 will be extremely difficult due to high rolling loads as they are both predominantly martensitic [137]. Some researchers therefore add an additional tempering heat treatment before cold rolling these microstructures [36, 119, 138].

However, if the as-coiled strip is intercritically annealed without cold rolling, then a variety of microstructures can develop as a result. When microstructure D2 is intercritically annealed, the austenite phase first nucleates in between the α'-martensite plates as a thin film which then grows in thickness [65]. The α'-martensite plates are also “tempered”, returning to BCC ferrite. The final microstructure is represented by microstructure G2 which is characterised by alternating austenite and ferrite lamella within the prior austenite grain. Microstructure G2 is often described as having a

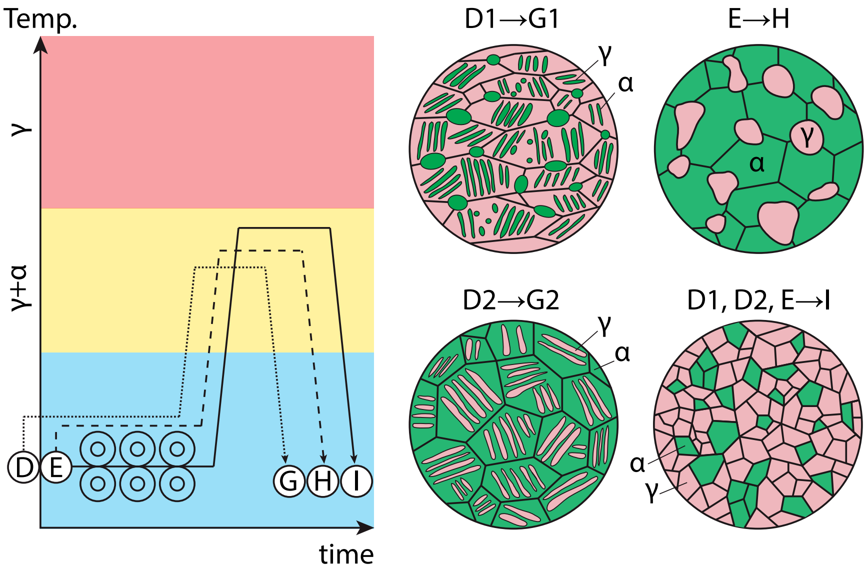

Figure 2.14: Schematic of the cold rolling stage,intercritical annealing stage and the corresponding microstructures. N.B. microstructure G1 was drawn with $V_f^\gamma > V_f^\alpha$ and G2 was drawn with $V_f^\alpha > V_f^\gamma$.

lath-like, laminated or lamellar morphology and the austenite is often termed "reverted austenite". A real example is shown in Figures 2.15c-d where the alternating lamella can be clearly observed. However, due to what has been termed the "austenite memory effect", all the austenite lamella within one prior austenite grain will adopt the same orientation, typically the original parent austenite orientation [95, 139, 140]. The exact mechanism leading to the austenite memory effect is still a subject of debate [95]. However, Liu *et al.* [140] showed that, in the absence of recrystallisation, retained austenite in between the martensite lath boundaries will grow along the lath boundaries as a film while preserving the K-S orientation relationship in order to reduce interfacial strain energy. When these austenite films impinge on each other, they will coalesce and reconstruct the prior austenite grain. The memory effect can be clearly observed in the corresponding IPF-X map in Figure 2.15d.

When microstructure D1 is intercritically annealed without cold rolling, a mixed equiaxed and lamellar microstructure will arise as shown by microstructure G1. The equiaxed grains are typically ferrite grains which formed during hot rolling in the upper intercritical temperature range while the interior of the prior austenite grain comprises of lamellar austenite and ferrite grains. An example of microstructure G1 is shown in Figures 2.15a-b. From the phase map in Figure 2.15a, the equiaxed and lamellar ferrite grains can be easily distinguished. However, like microstructure G2, the reverted austenite lamella all have the same orientation within the same prior austenite grain due to the austenite memory effect as shown in the corresponding IPF-X map in Figure 2.15b.

Finally when a pearlitic microstructure like in microstructure E is intercritically annealed, a

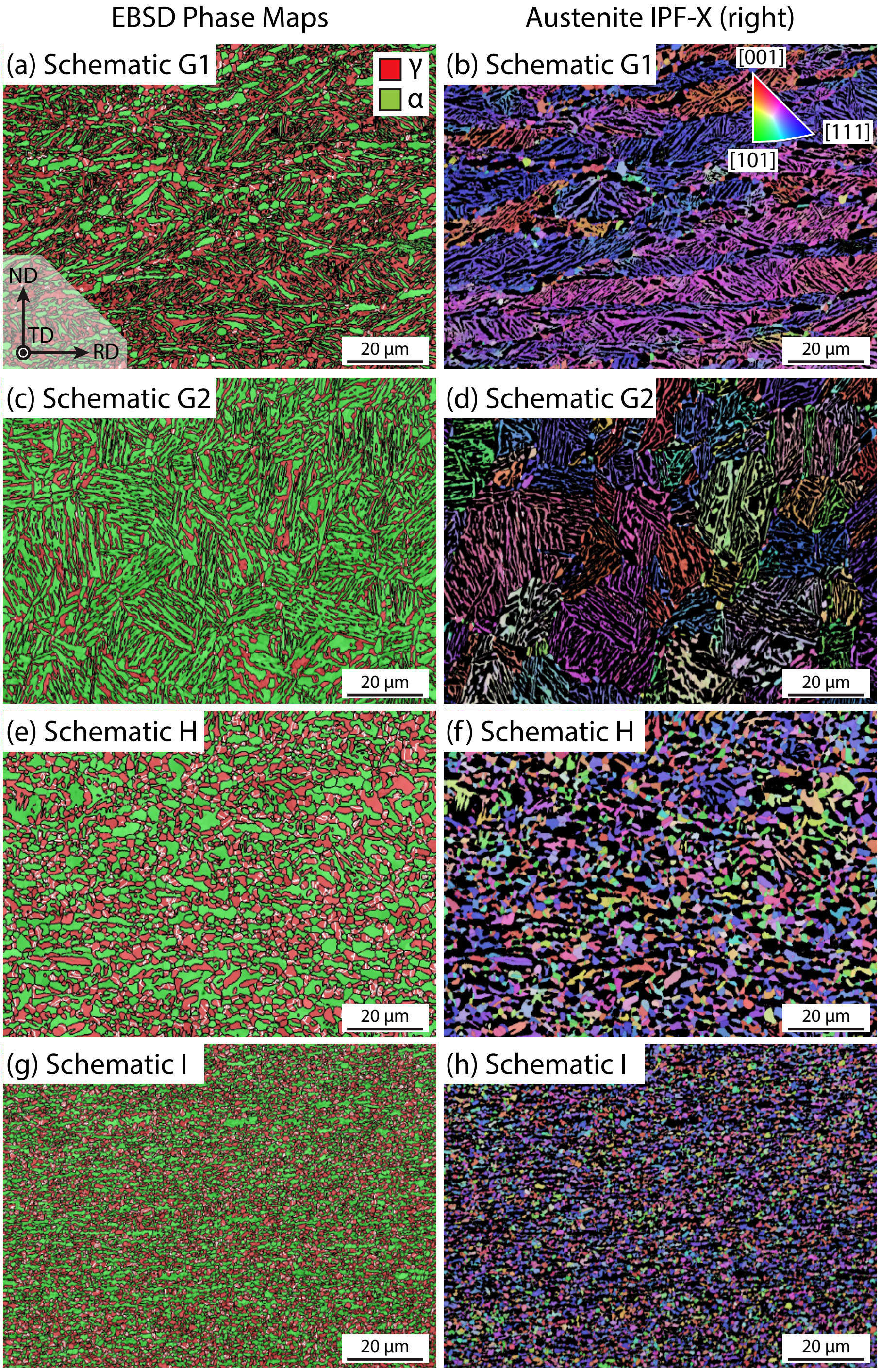

Figure 2.15: EBSD phase maps in the left column and corresponding austenite IPF-X maps in right column. (a,b) Mixed equiaxed and lamellar microstructure with equiaxed ferrite along PAGBs and lamellar structure within prior austenite grains. (c,d) Pure lamellar microstructure. (e,f) Equiaxed microstructure formed without cold rolling. (g,h) Submicron grain size achieved by cold rolling prior to IA. Unpublished work.

globular microstructure is obtained and is represented by microstructure H. It is likely that the pearlite spherodises during IA and reverts to austenite. Spherodisation and reversion can be rapid and was reported to occur within 10 min at 750 °C [97].Unlike microstructures G1 or G2, austenite reversion from spherodised pearlite does not seem to suffer from the austenite memory effect. A real example is shown in Figure 2.15e-f. In Figure 2.15f, the prior austenite grains can no longer be determined.

2.3.4 Novel heat treatments

From a steelmaking perspective, there is little flexibility in terms of modifying the hot rolling schedule due to equipment constraints. However, there is room for innovative heat treatments after hot and/or cold rolling to improve the mechanical properties of medium Mn steels. The following section aims to provide a brief overview of two of the more established novel heat treatments in the literature.

Double soaking

The double soaking concept was developed by Glover and De Moor [141–143] at the Colorado School of Mines. It primarily involves two separate heat treatments to change the initial ferritic/martensitic as-rolled microstructure to a duplex $\gamma + \alpha$ and then to a $\gamma + \alpha + \alpha'$ or $\gamma + \alpha'$ microstructure with the intention of improving the strength, hardening rate and eliminating yield point elongation.

During the first long soak or the first IA heat treatment, designed to be conducted in a BAF, the as-rolled microstructure transforms into a fine grained duplex microstructure that resembles microstructure I (Figure 2.14). The second soak is then conducted for a short duration, designed to be conducted in a CAL, at a temperature higher than the first soak. During the second soak, some of the ferrite grains transform to austenite. However the newly transformed austenite (γ_s) grains will have a different composition from the pre-existing austenite grains which formed during the first soak (γ_p). The short duration of the second soak also only allows for the partitioning of C and not Mn, therefore γ_s and γ_p will have different austenite stabilities. When the steel is quenched after the second soak, the new γ_s will transform into fresh α'-martensite while γ_p will be retained and available for the TRIP effect. The steel can also be tempered after the double soaking to restore some ductility. Double soaked and tempered medium Mn steels can have exceptionally high yield and tensile strengths of 1213 MPa and 1340 MPa respectively with appreciable ductility of 28% [142].

Two-step heat treatment

Similar to the double soaking heat treatment, the two-step heat treatment also involves using two separate heat treatments to alter the final microstructure and was developed by Steineder *et al.* [94] at Voestalpine. As mentioned previously, only one type of microstructure can arise when medium Mn steels are intercritically annealed after cold rolling, *i.e.* microstructure I (Figure 2.14). However, if a lamellar microstructure is desired, the two-step heat treatment can be used. The first step involves the full austenitisation of the cold rolled steel above the A_3 temperature for a short duration in a CAL to trigger recrystallisation and quenching to room temperature to form microstructure D2 but with a significantly finer prior austenite grain size.

The second step involves intercritical annealing the steel for a long duration in a BAF to form the final microstructure. In the work by Steineder *et al.* [94], the temperature for the first heat treatment was just below the A_3 temperaure which resulted in some globular ferrite grains forming at the PAGBs, forming a mixed microstructure similar to microstructure G1 (Figure 2.15) but with more equiaxed prior austenite grains. The two-step heat treatment can help to eliminate yield point elongation (discussed in section 2.4.2) and also has the effect of reducing anisotropy between the rolling and transverse directions due to the recrystallisation that occurs during the first heat treatment [34].

2.4 Microstructure and mechanical property relationships

Every microstructure type has a pronounced effect on the resulting mechanical properties of the medium Mn steel. This section will compare the differences in mechanical properties between the two main microstructures (*i.e.* equiaxed and lamellar) as well as some novel microstructures.

2.4.1 Yield strength

Perhaps one of the most fundamental of all microstructure - property relationships is the Hall-Petch grain size to yield strength relation given by the following equation:

$$\sigma_y = \sigma_0 + \frac{K}{\sqrt{d}} \tag{2.7}$$

where σ_0 (MPa) is the strength due to friction stress and solid solution hardening, K (MPa $\mu\text{m}^{-0.5}$) is the Hall-Petch parameter and d (µm) is the grain size. Where lamellar microstructures are concerned, d is taken as the lamella thickness [144, 145]. For this reason, medium Mn steels with lamellar microstructures tend to be slightly stronger than those with equiaxed microstructures with some exceptions. In lamellar microstructures, each lamella is extremely fine often on the order of $\sim$100 nm, depending on the initial α'-martensite lath thickness and IA duration [146] [97]. This length scale is very difficult to achieve in equiaxed microstructures without the need for heavy cold rolling and flash annealing. Depending on the degree of cold rolling reduction, IA temperature and duration, equiaxed microstructures tend to have a grain size of between 0.5 - 5 µm.

Table 2.3: Literature values of experimentally determined Hall-Petch constants (K and friction stress (σ_0). Original data from Miller [39] in the first row. N.B. Lamellar grain size determined as the lamella thickness.

σ_0 (MPa)	K (MPa µm$^{-0.5}$)	Microstructure type	Ref
501	64	Equiaxed	[39]
-	268	Equiaxed	[147]
233	332	Equiaxed	[93]
157	263	Lamellar	[144]
284	309	Lamellar	[145]

Table 2.4: Hall-Petch constants of individual phases, K_i where i denotes the phase, used in constitutuve models in the literature. N.B. Lamellar grain size determined as lamella thickness.

K_γ	K_α	$K_{\alpha'}$	Microstructure type	Ref
(MPa µm$^{-0.5}$)				
180	160	160	Equiaxed	[148]
274	573	-	Equiaxed	[19]
274	100	-	Equiaxed	[75]
449	172	-	Equiaxed	[132]
180	160	-	Lamellar	[110]
330	172	-	Both	[97]

Several authors have attempted to measure the Hall-Petch parameter in medium Mn steels including Miller [39] and have found that medium Mn steels generally obey the Hall-Petch relation even into the submicron range [147] regardless of microstructure type. Their results are shown in Table 2.3. However, there is quite a large scatter in the value of experimentally derived Hall-Petch parameters. This is likely because of different phase fractions across the different experiments. Several authors have therefore attempted to model the strength of medium Mn steels by using Hall-Petch parameters obtained from fully austenitic and ferritic steels shown in Table 2.4. While a good agreement between model and experiment was found in each case, there is still a large scatter between the Hall-Petch parameters when compared as a whole. Therefore, the only conclusion is that medium Mn steels can be effectively strengthened by grain size refinement regardless of microstructure type but the precise Hall-Petch parameters vary between experiments. Nervertheless, the ability of medium Mn steels to stabilise a fine grained microstructure [39] gives them a significant strength advantage over their predecessor TWIP steels where their inherent low yield strengths compared to other AHSS grades was a significant problem at the time [7].

2.4.2 Yield point elongation

Equiaxed microstructures tend to suffer from severe discontinuous yielding or Yield Point Elongation (YPE). YPE is characterised by a stress plateau after yielding (Figure 2.16) which can exceed 10% engineering strain in certain medium Mn steels [149] and is an undersirable feature during cold metal forming, leaving stretch marks and non-homogeneous thinning of the steel sheet. The origin of YPE in medium Mn steels is still the subject of debate and many reasons for YPE in medium Mn steels have been put forward such as phase fraction, austenite stability and the occurence of the TRIP effect [20, 149–151]. However, one of the leading theories involving grain size has been put forward by Sun *et al.* [87].

Sun *et al.* [87] describes that, generally, in order for discontinuous yielding to occur, two conditions must be satisfied. Firstly, a low density of mobile dislocations in the initial microstructure and secondly, an avalanche or rapid multiplication of mobile dislocations. Due to the nature of its processing history, equiaxed microstructures have a very low residual dislocation density due to recrystallisation during the IA heat treatment. The fine grained microstructure (∼1 µm) of most equiaxed medium Mn steels imply a large grain boundary area which can act as effective traps for mobile dislocations which form before macroscopic yielding. These two factors satisfy the first criteria for YPE. In fine grained equiaxed microstructures, especially as grain size approaches the submicron regime, the stress needed for dislocation nucleation begins to exceed that for dislocation glide due to reduced dislocation segment length and high back stresses. Therefore, when the stress for dislocation nucleation is finally reached, the immense γ/α grain boundary area due to the fine grained microstructure acts as dislocation nucleation sites and provides the avalanche of mobile dislocations, satisfying the second condition.

Sun *et al.* [87] therefore argue that the origin of YPE in equiaxed-type microstructures is predominantly due to grain size which may explain why YPE is not commonly observed in coarse δ-ferrite-containing medium Mn steels. In their experiment, YPE was reduced from approximately 4.5% to 1.5% when grain size was increased from approximately 0.7 µm to 1.2 µm. However, the work by Sun *et al.* [87] might imply that above some critical grain size, YPE can be eliminated in medium Mn steels. Unfortunately, this has yet to be shown. Interestingly, in a study by Cai *et al.* [152], a specimen with an average grain size of 350 nm showed a longer YPE than another specimen of same composition having an even finer average grain size of 130 nm. This shows that while grain size may play a significant role in influencing the yielding behaviour in medium Mn steels, there may also be other factors at work.

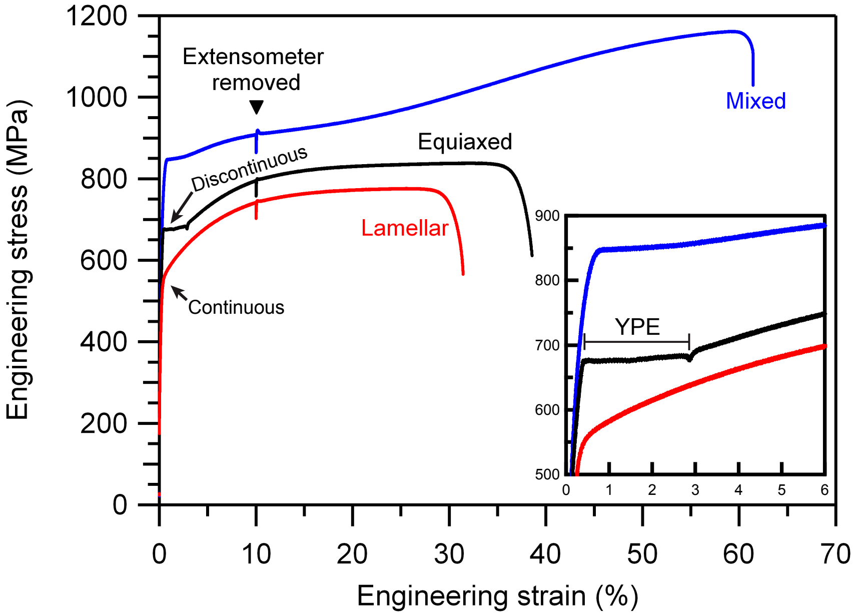

Figure 2.16: Tensile curves and yielding behaviour of a Fe-6Mn-0.2C medium Mn steel processed to produce an equiaxed microstructure and a lamellar microstructure using a two-step heat treatment (black and red respectively) and a Fe-4.3Mn-2.7Al-1.4Si-0.5C medium Mn steel processed to produce a mixed microstructure (blue). Inset: magnified view of the early yielding behaviour with the equiaxed microstructure showing discontinuous yielding with approximately 3% yield point elongation. Unpublished work.

In lamellar microstructures, the individual lamella thickness can be as fine as ∼ 100 nm but their length actually spans the entire prior austenite grain due to the austenite memory effect. Sun *et al.* [87] therefore continue to argue that due to the aspect ratio of the lamellar grains, dislocations can only realistically pile up along the slip plane parallel to the lamallae long axis, exerting a high stress at the lamella tips which act as the main sources of dislocation nucleation rather than the whole grain boundary area. Since the rate of dislocation nucleation is reduced, there can be no avalanche of mobile dislocations and therefore breaking the second condition for YPE. This result is also shared by Steineder *et al.* [94] who observed little dislocation interaction in fine equiaxed grains but dislocation cell formation along the length of lamellar grains. It may also be possible that due to the lack of true recrystallisation in lamellar microstructures, the residual dislocation density may be higher than in equiaxed microstructures, thereby breaking the first condition for a low density of mobile dislocations.

However, the literature is fairly divided as to the involvement of α'-martensite in YPE, especially when medium Mn steels begin to transform to α'-martensite immediately upon yielding. Nevertheless, it is universally agreed that TRIP occurs within the Lüders band and is therefore closely connected with YPE [87,153,154]. Many authors have therefore suggested strategies to eliminate YPE by adjusting the austenite stability [94,155]. However, Sun *et al.* [87] maintains that adjusting the austenite stability and therefore the TRIP effect only affects the Lüders band propagation (*i.e.* extends or shortens the YPE length) by altering the local work hardening rate and not its nucleation or formation. Despite the lack of consensus, it is generally agreed that to eliminate YPE in medium Mn steels, a martensitic microstructure before IA is desired [94, 156] and is also the inspiration behind the two-step heat treatment [94].

2.4.3 Charpy V-notch impact properties

Since medium Mn steels are generally designed for energy absorption, *i.e.* maximising the area under the true stress-strain curve, it is also important to investigate their impact properties since one of the primary applications is for automotive crash energy absorbing members. The best method to meausure a steel's performance in crash is through an axial drop tower test [157, 158] where the steel deforms by controlled folding and buckling. However, the drop tower test requries large amounts of steel which may not be readily available as most medium Mn steels are still in a laboratory development stage. As a proxy, some researchers turn to Charpy V-notch impact tests to measure the impact energy of medium Mn steels [88, 146, 159]. However, it is difficult to conduct a Charpy impact test on sheet steel. Most researchers therefore use sub-sized test pieces (approximately 2 mm as compared to full-sized 10 mm thickness) and normalise the result to obtain the full-sized (10 × 10 mm cross sectional area) Charpy result [146, 159]. Care must be taken when normalising the Charpy energy from sub-sized specimens, *i.e.* multiplying the Charpy energy from a 2 mm thick sub-sized specimen by five to get the equivalent result from a 10 mm thick full-sized speicmen will yield a significant over-estimation. Conversion methods to get a "true" Charpy energy as well as the toughness parameter K_{1c} do exist for other sheet steels such as DP steels [160] but none exist for medium Mn steels at the time of writing.

It is also acknowledged that Charpy V-notch impact tests may not be the most appropriate test to measure impact energy absorption for sheet steels, however it is believed on a qualitative level that improving the Charpy impact energy will also improve the crash energy absorption. Charpy V-notch tests also provide other useful information like a possible ductile-brittle transition temperature, damage and fracture mechanisms as well as notch sensitivity under high strain rates.

Han *et al.* [159] conducted a systematic analysis on the different impact properties between equiaxed and lamellar microstructures (red lines in Figure 2.17). It was found that with decreasing testing temperature, both microstructure variants showed a transition from ductile to partial quasi-cleavage to intergranular fracture. Above room temperature, the lamellar microstructure had a higer impact energy than the equiaxed microstructure which could be attributed to a higher yield strength of the

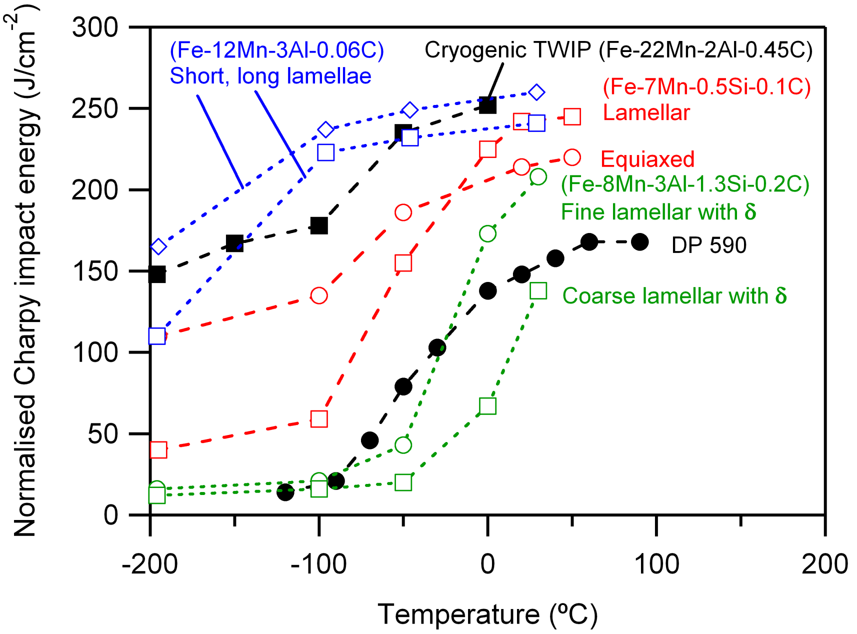

Figure 2.17: Comparison between the normalised Charpy V-notch impact energy (L-T orientation) of several medium Mn steels such as Fe-7Mn-0.5Si-0.1C (red) in its lamellar and equiaxed variants [159], Fe-12Mn-3Al-0.06C (blue) in both short and long lamellar variants [146], Fe-8Mn-3Al-1.3Si-0.2C (green) in its fine and coarse lamellar microstructures both containing δ-ferrite stringers [88], and other steels such as a cryogenic TWIP steel [66] and DP 590 [160] (black). N.B. only the Charpy samples from the cryogenic TWIP steel were full-sized. All other impact energies from other steels were normalised from sub-sized samples using different methods.

lamellar variant. However, below room temperature, the impact energy of the lamellar microstructure decreased significantly. While both microstructures failed by intergranular failure, crack propagation in the lamellar microstructure followed the coarse PAGBs rather than along the finer lamellar grains. Atom Probe Tomography (APT) revealed significant segregation of Mn and P to the PAGBs, resulting in a more brittle PAGB and easy crack propagation at cryogenic temperatures. Dutta *et al.* [146] investigated the Charpy impact properties of lamellar microstructures (blue lines in Figure 2.17) and showed that lamellar microstructures with shorter and finer lamellae consistently outperformed microstructures with longer and coarser lamellae. They concluded that it was the prior austenite grain size which was the actual determining factor where finer prior austenite grain sizes gives rise to finer lamellae and *vice versa*. The results from Han *et al.* [159] and Dutta *et al.* [146] both support the conclusion that finer prior austenite grain sizes (microstructure B in Figure 2.10) are necessary to improve the Charpy impact performance of medium Mn steels with lamellar microstructures.

Kim *et al.* [88] (green lines in Figure 2.17) also investigated the Charpy impact performance of lamellar medium Mn steels with different lamellar thicknesses and different prior austenite grain sizes but with the presence of δ-ferrite stringers in the microstructure. From Figure 2.17, their results largely agree with the rest of the literature that a finer lamellar structure arising from smaller prior austenite grains is stronger than a coarser lamellar structure. However, it cannot be said conclusively that the presence of δ-ferrite resulted in a poor Charpy impact performance compared to the results by Han *et al.* [159] and Dutta *et al.* [146]. Nevertheless, Kim *et al.* [88] concluded that the δ-ferrite phase was the primary cause for the low temperature Charpy impact performance. Through APT, they found a large build up of Mn and C at the δ-ferrite grain boundaries as well as several small carbides at the δ-ferrite grain boundaries leading to poor cohesion between the δ-ferrite grains and the matrix.

2.4.4 TWIP and TRIP effects

The ability to exhibit TWIP and/or TRIP effects is one of the unique aspects of medium Mn steel. While it has been established that the TWIP response is largely governed by the austenite SFE and the TRIP response by the austenite stability, microstructural effects also play a significant role in influencing these plasticity enhancing mechanisms.

In medium Mn steels, the TWIP effect was more commonly observed in steels with equiaxed microstructures [19, 36, 92] as compared to those with lamellar microstructures. In the few studies where twinning was observed in lamellar grains, twins were observed to propagate across the short axis of the lamella rather the long axis [35, 97]. This suggests that the mean slip length in lamellar grains is much shorter in lamellar grains compared to equiaxed grains. In TWIP steels, it is understood that decreasing the grain size raises the critical twin initiation stress [8, 42]. In a study by Kwok *et al.* [97], it was observed that twins formed at higher strains in lamellar austenite grains compared to equiaxed austenite grains. It was theorised that the significantly shorter slip length in lamellar grains raised the twin initiation stress such that twinning only occured at higher strains or stresses. Generalising this concept, if the stress needed for twinning exceeds that needed for martensitic transformation, it will be very unlikely that twins will form as TRIP will become the dominant plasticity enhancing mechanism which may explain why twinning is lamellar grains is rarely observed.

In contrast, the TRIP effect in multiphase steels is well documented [101, 121, 125, 161]. Generally, lamellar austenite is more stable than equiaxed austenite [94, 115]. However, the reason for which is not simply down to grain size or mean slip path but a combination of factors. In a study on a TRIP-assisted Q&P steel, Xiong *et al.* [162] suggested that the higher stability of lamellar austenite might be due to more effective shielding effect by the adjacent stronger ferrite lamella and a greater hydrostatic pressure on film or lamellar austenite, both factors retarding the formation of α'-martensite. A more detailed review of the effects of microstructure and grain morphology on austenite stability in

TRIP-assisted steels is provided by He [125].

2.5 Finishing

As medium Mn steels are still fairly novel and early in its development, the vast majority of the literature has been focused on developing processing techniques and investigating the tensile behaviour of medium Mn steels. However, it is important to understand that alloy design does not end with a tensile test. Steel development also involves many other factors such as formability, galvanisability and weldability, all of which may require re-optimising the base composition even if the initial tensile properties proved to be very impressive. While not a large amount of literature is available, this section aims to briefly review the current efforts in the downstream processing of medium Mn steels.

2.5.1 Galvanising

Most steels used in the automotive BIW needs to be coated for protection against corrosion and one of the best ways to protect sheet steel is galvanising. Automotive strip is commonly galvanised in a Continuous Galvanising Line (CGL) where a coil of steel is unrolled, passed through a molten zinc bath, cooled and coiled again. The CGL is a very efficient process and the steel does not spend more than 30 s in the Zn bath [163]. The gas mix, oxygen partial pressure (pO_2), dew points (temperature at which condensation of water vapour starts) and Zn bath composition can be altered to optimise the coating for different steel grades.

There have been concerns that the high Mn and Si content in medium Mn steels compared to other AHSS grades may lead to poor surface coating quality [163]. This is because Mn and Si selectively oxidise forming adherent oxides on the steel surface during intercritical annealing. When the steel is then passed through a CGL, the poor wettability between liquid Zn and the Mn and Si oxides will lead to bare spots and therefore a coating with poor quality [164, 165].

Nevertheless, McDermid's group at McMaster University have researched the galvanisability of medium Mn steels extensively and proved that it is indeed possible to galvanise medium Mn steels. Alibeigi *et al.* [166] showed that reactive wetting and the formation of a Fe-Al intermetallic layer was possible in a series of low C steels containing between 0.14 - 5.10 wt% Mn. Pourmajidian *et al.* [167] found that the addition of a 0.05 wt% of Sn and higher pO_2 atmospheres helped to increase Al uptake and the population of Fe-Al intermetallics in a Zn(Fe,Al) bath, significantly improving the reactive wetting of the steel surface. It was found that Sn decreased the surface enrichment of Mn after IA and refined the surface MnO particles. While Sn is considered a tramp element in steel, it was not found to affect the tensile properties in medium Mn steels up to 0.05 wt% [37]. Other researchers have also successfully galvanised various medium Mn steels by altering different processing parameters such as pO_2 and gas mixes [165, 168].

Interestingly, it was even proposed that IA can also be conducted in the preheating or annealing stages in a CGL before applying the Zn coating [169, 170], although the duration can be no longer than 360 s. Due to the short IA window in a CGL, it was found that a prior martensitic microstructure (microstructure D2, Figure 2.12) was preferable due to the faster austenite reversion and partitioning kinetics as compared to a cold rolled and tempered martensitic microstructure.

2.5.2 Welding and liquid metal embrittlement

Another important factor to consider is the similar and dissimilar weldability of medium Mn steels, *i.e.* to itself and to other types of steel. Of the various welding techniques, laser fusion welding and Resistance Spot Welding (RSW) are the most widely used in the automotive BIW [171]. This section will focus on the resistance spot weldability of medium Mn steels but the reader is directed to a review by Park *et al.* [172] for more information on the fusion weldability of medium Mn and high Mn TWIP steels.

Due to the relatively high Mn and C content in medium Mn steels compared to other AHSS, there have been concerns about the weldability of medium Mn steels [173]. Weldability can be quantified using the Carbon Equivalent (CE) formula using the following equation given by the American Welding Society [174]:

$$CE(wt\%) = C + \frac{Mn + Si}{6} + \frac{Cr + Mo + V}{5} + \frac{Cu + Ni}{15} \tag{2.8}$$

Generally, the higher the CE, the lower the weldability due to excessive hardening in the Fusion Zone (FZ) and Heat Affected Zone (HAZ) [175]. A CE value of $> 0.45 - 0.5$ has a “poor” weldability [51] and will require special welding processes. Unfortunately, most medium Mn steels have a high CE and initial studies have found the resistance spot weldability of medium Mn steels to be poor with very low cross tension strengths [175–177]. Jia *et al.* [178] found that the FZ in similar welds composed mainly of hard and brittle lath martensite while the austenite content in the HAZ decreased with increasing distance away from the Base Metal (BM) towards the FZ. The predominant failure mode was found to be interfacial failure which is undesirable. Mn segregation to dendrite boundaries in the FZ also creates a local region with high CE and brittleness [175, 177].

Improved cross tension strengths were observed in dissimilar welds and the failure mode changed from interfacial failure to pull-out failure which is desirable [175]. However, this was because the Mn content in the FZ was diluted by the dissimilar steel. While the joint failed by pull-out failure mode, the crack was observed to occur on the medium Mn steel side and propagated along the PAGBs in the coarse grained HAZ which were fully martensitic. Park *et al.* [176, 179] found that some toughness in the coarse grained HAZ could be restored by tempering the martensite, either by changing the weld thermal cycle or utilising a paint baking heat treatment. Stadler *et al.* [177] found that a second pulse was able to improve the cross tension strength of a similar RSW joint. The second pulse had the effect of homogenising the Mn segregation and recrystallising the grains along the edge of the FZ where cracks was observed to propagate. While remedial solutions to the seemingly poor spot weldability of medium Mn steels do exist, more research is certainly needed in this area to improve productivity and crashworthiness of the spot welded joints.

Liquid Metal Embrittlement (LME) by liquid zinc during RSW of galvanised medium Mn steel is a serious concern that is also shared by many types of AHSS [180]. LME is defined as the inter or transgranular decohesion caused by the penetration of liquid Zn into the microstructure typically along the grain boundaries, deletriously affecting tensile properties [8]. Visually, LME can be identified as cracks on the steel surface after RSW. It was found that high Mn TWIP steels were particularly sensitive to LME [181, 182], therefore there is a concern that medium Mn steels might also be as sensitive to LME. Thankfully, Razmpoosh *et al.* [183] found that medium Mn steels were significantly less prone to LME than TWIP steels during laser lap joining of a medium Mn and TWIP steel. They speculated that the increased resistance to LME might be due to the signfnicantly lower amount of γ/γ grain boundary area in medium Mn steels compared to TWIP steels. Park *et al.* [175] also did not report any LME-related cracking during their study on resistance spot weldability of galvanised medium Mn steels. That being said, medium Mn steels are not totally immune to LME [184] and more research is also needed in this area to prevent and/or mitigate LME in medium Mn steels.

2.5.3 Hole expansion

Hole expansion or stretch flangeability refers the ability of a cut-out to resist cracking when the sheet is stretched thereby increasing the radius of the cut-out [185]. Such operations are very common in automotive forming processes and it is important that medium Mn steels show a good hole expansion performance. To measure the hole expansion performance, a circular hole is punched out from a piece of sheet steel. The sheet is then clamped and a conical punch is driven into the hole, expanding the circumference of the cut out hole. The test is stopped when a through-thickness crack forms and the Hole Expansion Ratio (HER) in percent is calculated as: $(d_f - d_i)/d_i \times 100\%$, where d_f and d_i are the final and initial diameters of the cut out respectively.

Unfortunately, little is known about the hole expansion performance of medium Mn steels as very few studies have been conducted in the literature. However, it is known that the pilot medMn780 coil produced by Voestalpine has a reported HER value of approximately 30% in the punched condition which is satisfactory for BIW applications [34]. This value is not far off from 30-40% in TWIP steels [16, 186] which is encouraging.

To aid future alloy and processing design, several concepts from hole expansion tests conducted on DP and TRIP steels can be learned in order to maximise the HER in medium Mn steels. Firstly, in multiphase TRIP-assisted steels, Kashima *et al.* [187] suggested that the closer in strength between the phases the better the HER and proposed a reverted lamellar morphology without polygonal ferrite to increase stretch flangeablity. Secondly, in δ-TRIP steels, Xu *et al.* [188] also showed that a high austenite stability was beneficial for HER by reducing the amount of fresh martensite formed at the edge during punching out the initial hole for the hole expansion test. Hole expansion tests are extremely sensitive to edge effects [185] and less martensite at the rim will help to reduce the local strength mismatch between phases at the hole edge. Finally, in DP steels, microstructural damage is often observed at ferrite-martensite or martensite-martensite interfaces [189, 190]. Chen *et al.* [191] therefore theorises that in steels which contain above a certain volume fraction of martensite, the HER cannot exceed 30-40% due to the limitation of the hard martensite interface (*i.e.* α'/α or α'/α') in absorbing damage. Since medium Mn steels also accumulate damage in a similar manner [192], it is definitely of research interest if this theory applies to medium Mn steels as well.

2.6 Summary

Medium Mn steels are a metallurgically complex but exciting class of steels. Depending on composition and processing techniques, a variety of microstructures, plasticity enhancing mechanisms and therefore tensile properties can be produced. From that perspective, researchers have been very successful in developing processing techniques to produce medium Mn steels with tensile properties within the 3Gen AHSS range. Given the relatively recent "rediscovery" of medium Mn steels, researchers are still discovering new strengthening and plasticity mechanisms that can be enabled through alloying or process optimisation. The medium Mn alloy design space is vast and is certainly not exhausted yet.

However not all medium Mn steel compositions and processing methods developed in the literature are industrially feasible. Certain mechanisms and properties in medium Mn steel can only be enabled through exotic alloying or processing techniques that are not feasible or profitable in industry. This work therefore aims to develop novel medium Mn steels with a focus on industrial translation as well as to explore new plasticity mechanisms that will enhance the energy absorption capabilities of medium Mn steels.

Chapter 3

Methods

3.1 Alloy design

Alloy design by nature is a very iterative process until the desired properties are reached. The alloy design concept adopted during this work is best represented by the "washing machine of alloy design" shown in Figure 3.1. First, careful reading of the literature and simulations from Thermo-Calc are "fed" into the washing machine. Then, the "wash cycle" begins with vacuum arc melting to produce a 400 g ingot, followed by hot rolling and heat treatments to produce steel strips. Tensile specimens are then obtained from the strips to obtain their mechanical properties and to observe their deformation behaviour. Some of the post-mortem tensile specimens will then be prepared for characterisation using various microscopy techniques to understand the mechanisms underpinning the observed mechanical properties. The process is then repeated as many times as necessary until a working composition and accompanying thermomechancal process route with the desired mechanical properties is achieved.

From the previous section, it was described how the bulk composition determines the processing window where the room temperature austenite fraction can be adjusted, therefore also varying the SFE and austenite stability which governs the TWIP and/or TRIP behaviour. Generally, the requirements from the bulk chemistry are as follows:

1. Phase fractions are approximately 50% austenite and 50% ferrite.
2. The IA temperature is higher than the cementite solvus temperature.
3. Ms (after IA) is below -40 °C.
4. SFE (after IA) is between 20-30 mJ m^{-2}.

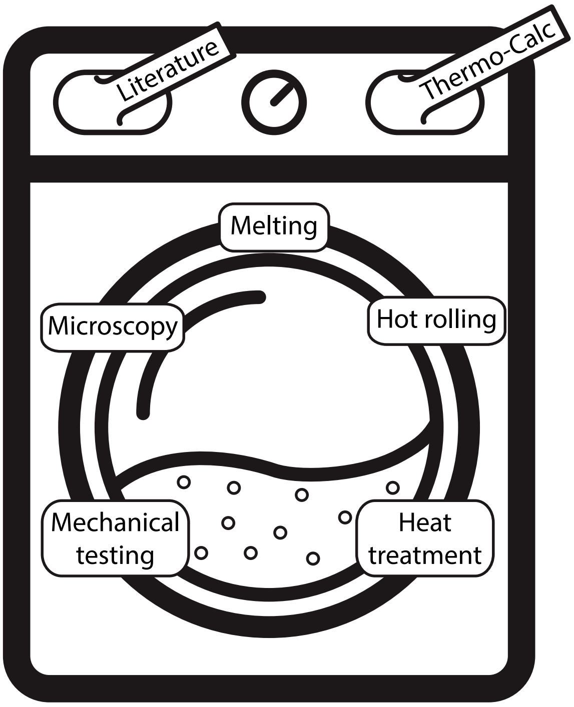

Figure 3.1: Washing machine of alloy design.

The use of Thermo-Calc with the steels database TCFE 7.0 was used extensively to generate property diagrams which provide equilibrium phase fraction information as well as composition information for each phase. Thermo-Calc has been used extensively by many authors and show reasonably good agreement [19, 41].

To determine the Ms temperature, many equations are available in the literature. However, the equation by Lee *et al.* [193] was chosen as it reflects both chemical and mechanical stabilisation (*i.e.* due to grain size) effects. The equation is given as:

$$Ms\,(^{\circ}C) = 475.9 - 335.1[C] - 34.5[Mn] - 1.3[Si] + 11.67\,\ln(d_{\gamma}) \tag{3.1}$$

where the concentration of each element is given in wt% and d_{γ} is the austenite grain size in µm. It is acknowledged that newer, more relavant Ms equations have been developed for 3Gen AHSS, such as that by Kaar *et al.* [49]. The determination of the SFE however, is more complex.

3.2 Stacking fault energy calculation

Stacking fault energy is often a contentious parameter which is both difficult to measure or calculate. Strictly speaking, a stacking fault is a planar crystal defect which occurs when a perfect dislocation splits into two Shockley partial dislocations to minimise its elastic strain energy. The Shockley partial dislocations are repulsive by nature and travel as far apart as possible, resulting in an intrinsic stacking fault bounded by the two partial dislocations [194]. Therefore, the SFE is the energy cost per unit area in creating the stacking fault. In low SFE materials such as TWIP steels, the partial dislocations can glide far apart from each other and form deformation twins if they glide on successive (111) planes [8].

There are currently two main methods to determine the SFE [68]. The first method is experimental and treats a stacking fault as a planar defect. This method requires the use of a Transmission Electron Microscope (TEM) to determine the seperation width between partial dislocations or the observation of extended dislocation nodes. The second method is a thermodynamic model which treats a stacking fault as a volumetric defect or an embryo of ϵ-martensite. The model is essentially an energy balance equation based on classical nucleation theory. The use of a TEM to determine SFE is not easily performed, inconsistent and is highly prone to error [7]. In a review by Bouaziz *et. al.* [7], the measurement of SFE in the same Hadfield steel at the same temperature yielded two SFE measurements (23 and 50 mJ m^{-2}) depending on the researcher. Therefore, the thermodynamic approach has been favoured by many researchers and great effort has been taken to develop and refine the model over the years.

The thermodynamic approach used throughout this thesis was presented by Sun *et al.* [36]. The model is an amalgamation of previous SFE models, notably those by Dumay *et al.* [91], Curtze *et al.* [195] and Saeed-Akbari *et al.* [196]. The model by Sun *et al.* [36] similarly adopts the Olson and Cohen model of expressing the SFE, Γ (mJ m^{-2}), as the change in free energy when creating a platelet of ϵ-martensite two atomic layers thick in austenite, *i.e.* a two-layer stacking fault, and can be represented by the following equation:

$$\Gamma = 2\rho(\Delta G_{chem}^{\gamma\to\epsilon} + \Delta G_{mag}^{\gamma\to\epsilon} + \Delta G_{str}^{\gamma\to\epsilon}) + 2\sigma^{\gamma/\epsilon} \tag{3.2}$$

where ρ is the molar density along the $\{111\}$ planes, $\Delta G_{chem}^{\gamma\to\epsilon}$, $\Delta G_{mag}^{\gamma\to\epsilon}$ and and $\Delta G_{str}^{\gamma\to\epsilon}$ are the chemical, magnetic and strain contributions to the molar Gibbs energy of transformation respectively. Finally, $\sigma^{\gamma/\epsilon}$ is the surface energy between austenite and ϵ-martensite taken to be 5 mJ m^{-2} [196]. The molar density ρ can be geometrically calculated according to the following equation:

$$\rho = \frac{4}{\sqrt{3}}\frac{1}{a^2 N} \tag{3.3}$$

where a is the lattice parameter which can be determined through X-Ray Diffraction (XRD) and N is Avogadro's constant. The chemical contribution to the change of molar Gibbs energy, $\Delta G_{chem}^{\gamma\to\epsilon}$

(mJ m^{-2}) can be calculated with a subregular solution model reflecting the chemical contribution per element as well as second order interactions between elements. Third order interactions were considered too small to be significant. The equation is shown as:

$$\begin{aligned}\Delta G^{\gamma\to\epsilon}_{chem} = & X_{Fe}\Delta G^{\gamma\to\epsilon}_{Fe} + X_{Mn}\Delta G^{\gamma\to\epsilon}_{Mn} + X_{Al}\Delta G^{\gamma\to\epsilon}_{Al} + X_{Si}\Delta G^{\gamma\to\epsilon}_{Si} + X_{C}\Delta G^{\gamma\to\epsilon}_{C} \\ & + X_{Fe}X_{Mn}\Delta\Omega^{\gamma\to\epsilon}_{FeMn} + X_{Fe}X_{Al}\Delta\Omega^{\gamma\to\epsilon}_{FeAl} + X_{Fe}X_{Si}\Delta\Omega^{\gamma\to\epsilon}_{FeSi} + X_{Fe}X_{C}\Delta\Omega^{\gamma\to\epsilon}_{FeC}\end{aligned} \tag{3.4}$$

where X_i is the molar fraction of each element i, $\Delta G^{\gamma\to\epsilon}_i$ is the molar Gibbs energy of each alloying element i and $\Omega^{\gamma\to\epsilon}_{ij}$ is the excess molar Gibbs energy due to mixing of elements i and j. The values of $\Delta G^{\gamma\to\epsilon}_i$ and $\Omega^{\gamma\to\epsilon}_{ij}$ can be found in the supplementary material of the work by Sun *et al.* [36]. The calculation of the magnetic contribution $\Delta G^{\gamma\to\epsilon}_{mag}$ will not be shown here but can be found in the work by Curtze *et al.* [195]. The inclusion of the strain energy term, $\Delta G^{\gamma\to\epsilon}_{str}$ (mJ), is unique to this model and is given by the following equation [197]:

$$\Delta G_{str} = \frac{11.14}{2\rho}\exp\left(\frac{-w_C}{0.56} - 3.49\right) \tag{3.5}$$

where w_C is the C content in austenite (wt%). These calculations can be done in Microsoft Excel and a spreadsheet was created, endearingly named “The TWIPulator”, to calculate the SFE based on the austenite composition obtained from Thermo-Calc. It is acknowledged that the surface energy term, $\sigma^{\gamma/\epsilon}$ is a signficant source of controversy as it can adopt values between 5-15 mJ m^{-2} and appears to be chosen arbitrarily between various SFE models, possibly resulting in very different SFE values depending on which model was used. Unfortunately, without experimental verification and advanced microscopy, the only possibility is to be consistent and the model by Sun *et al.* [36] was used throughout this thesis. A review of the various SFE calculation models and their strengths and weaknesses can be found in review papers by De Cooman *et al.* [8] and Lee *et al.* [68].

3.3 Alloy fabrication

All of the alloys produced were vacuum arc melted from pure elements in a water cooled Cu crucible. A small “button” of Fe and C, in the form of graphite, was first produced in order to prevent excessive vaporisation of elements with high vapour pressures such as Mn and Al. Due to the large difference in melting temperatures between Fe and graphite, it takes relatively long for C to fully dissolve into the molten Fe. Therefore, elements such as Mn and Al should only be introduced after the heavy melting in order to minimise time spent in the molten state. The Fe-C button would then be placed on top of the remaining pure elements in the crucible, melted down and cast into a copper mould, producing ingots measuring approximately 76 × 23 × 23 mm.

Despite best efforts to prevent element vapourisation during arc melting, it is very unlikely that the final composition in the cast ingot will be exactly the same as the nominal composition. For this reason, important development alloys or alloys for publication will be sent for external composition testing using inductively coupled plasma and inert gas fusion to determine the actual composition.

In order to reduce the hot rolling load on the pilot rolling mill and achieve the typical hot rolling thickness reductions used in industry (25-50% thickness reduction) [133], the full sized ingots were either profile rolled into a square bar or cut into bars with cross sections measuring approximately 11 × 11 mm. Hot rolling was conducted on a pilot mill with 6 inch diameter rolls at speeds between 5-10 rpm. Each bar was soaked at the first rolling temperature for a minimum of 30 min before rolling. A sizing pass was then conducted to take out as much mill spring as possible. The bar would then be rolled in approximately 5-6 passes at decreasing temperatures and decreasing reductions with a reheat in between each pass, achieving a final thickness of approximately 1.5 mm. After the final pass, the strip would be either air cooled, water quenched or returned to the furnace for a furnace cool.

3.4 Mechanical testing

From the rolled strips, tensile specimens with gauge dimensions L 19 × W 1.5 × T 1.5 mm were obtained from the rolled strips using Electrical Discharge Machining (EDM). Due to the short width of the rolled strips, only tensile specimens with the tensile axis parallel to the rolling direction could be obtained. Tensile testing was conducted on an Instron 5960 load frame with a 30 kN load cell. Tensile specimens were placed in negative grips which pull on the specimen shoulder as compared to conventional friction wedge grips which pull on the tab. This helps to ensure that only the gauge section is under tension. A clip on extensometer (12.5 mm opening) was used to measure strain during the tensile test and taken off at 10% engineering strain. The extensometer was taken off at 10% to firstly protect the extensometer in the event of premature fracture of the tensile sample and secondly, most of the samples have elongations of above 30% which is beyond the limit of the extensometer. It was also determined that at 10% elongation, all elastic flex in the load frame has been removed and the crosshead displacement can be used to accurately measure strain thereafter.

There has been some concern that the use of non-standard sub-sized tensile samples may not be representative of the bulk properties of the steel. Zheng *et al.* [198] conducted a review on miniature tensile tests and established that strength will remain unchanged if the thickness does not go below 10 grain lengths. Below this ratio, dislocation annihilation at the surface becomes significant, resulting in poor work hardening, lower strengths and ductility. Most of the steels in this work have grain sizes below 5 µm, implying that the thickness of the tensile samples used in this work is approximately 300 grain lengths which is more than sufficient to be representative of the bulk.

It is also acknowledged that the tensile sample's square cross section may introduce geometry related effects. An assessment conducted by Hanlon *et al.* [199] found that tensile properties such as yield strength, tensile strength and uniform elongation remain unchanged regardless of sample cross section although tensile samples with larger width to thickness ratios and round cross sections have larger post-uniform elongations and therefore a larger total elongation. Many of the steels developed in this work were found to have little to no post-uniform elongation. However, the lack of post-uniform elongation appears to be a feature of medium Mn steels rather than a tensile sample geometry related effect. Very little post-uniform elongation was observed even in tensile samples with the standard ASTM A50 geometry [93, 106]. Therefore, it is unlikely that the tensile properties would change significantly even if a larger tensile sample was used.

3.5 Electron Backscattered Diffraction

The use of Electron Backscattered Diffraction (EBSD) features heavily in this work to measure phase fractions. However, it is acknowledged that other methods such as X-Ray Diffraction (XRD) are more commonly used and the results are widely accepted. Unfortunately, the small size of the tensile gauge section limits the use volume dependent techniques such as XRD or magnetic saturation to determine the phase fractions in the deformed state. Therefore, only surface imaging techniques are available.

The measurement of phase fractions in multiphase steel is not a straightforward task. Jacques *et al.* [114] conducted a blind round robin assessment of six different methods, *i.e.* XRD, EBSD, optical microscopy, magnetic saturation, thermal diffusivity and laser ultrasonics, to measure retained austenite in TRIP steels and found that no particular method emerged as the "gold standard". In another study, Lee *et al.* [19] measured the ferrite content in a medium Mn steel with five different ferrite contents using EBSD, XRD, magnetic saturation and with a ferrite scope. Their results showed that the ferrite volume fraction as measured by the four methods were within ±0.05 of each other but

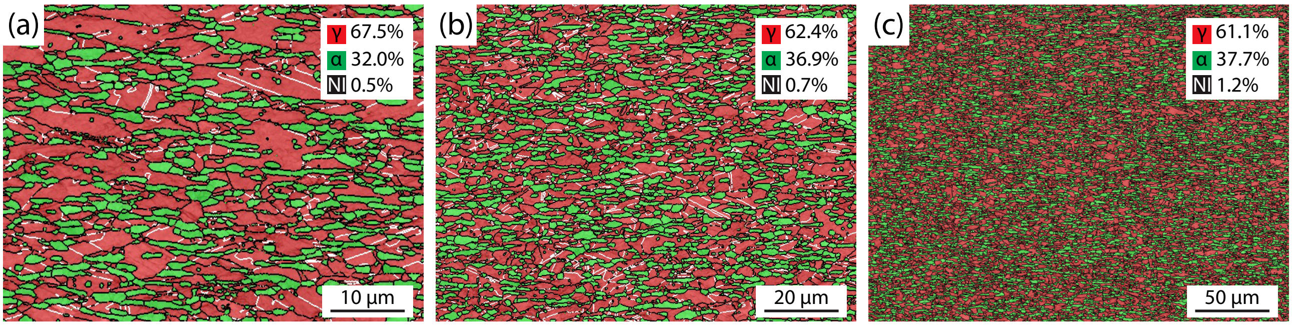

$D_\gamma = 4.1$ µm, $D_\alpha = 1.8$ µm $D_\gamma = 3.4$ µm, $D_\alpha = 2.4$ µm $D_\gamma = 3.9$ µm, $D_\alpha = 2.4$ µm

Figure 3.2: EBSD phase maps of the same steel at (a) 5000X, (b) 2500X and (c) 1000X magnification at increasing pixel sizes of 0.075 µm^2, 0.1 µm^2 and 0.15 µm^2 respectively but at similar dwell times. Black lines are the high angle grain boundaries and white lines are the austenite $\Sigma3$ boundaries. $\Sigma3$ boundaries were not shown in (c) for clarity. NI is the non-indexed fraction. D_γ and D_α are the austenite and ferrite grain sizes calculated as the equivalent circle diameter respectively.

with no method being consistently higher or lower than the other. Therefore it can be argued that there is no preferable method to measure phase fractions in medium Mn steels.

One possible weakness of EBSD is sampling error when scanned at high magnifications in order to pick out finer microstructural features. A quick illustration on how the measured phase fraction may vary with magnification is shown in Figure 3.2. At high magnifications as shown in Figure 3.2a, small intragranular ferrite grains could be observed but is lost at lower magnifications shown in Figures 3.2b-c. However, the measured phase fractions across the three magnification levels only vary by approximately 0.05, which is similar to the range of ±0.05 obtained by the aforementioned study by Lee *et al.* [19]. Therefore, this shows phase fractions obtained at high magnifications in medium Mn steels are indeed representative of the bulk steel.

Another downside of EBSD is the increase in the Non-Indexed (NI) fraction with increasing strain as severely deformed crystals do not diffract as well and therefore cannot be confidently indexed by the EBSD software. For the purposes of this work, correlative EBSD and Energy Dispersive Spectroscopy (EDS) maps of the post-mortem tensile specimens have shown that most of the NI regions were Mn-rich, suggesting that the NI regions were either highly deformed austenite or highly deformed α'-martensite. In chapter 4, the NI fraction was treated as α'-martensite but in chapter 6, it was acknowledged that the NI fraction would likely contain a mxture of both highly deformed austenite and α'-martensite. A range of phase fractions with upper and lower bounds were presented instead.

Chapter 4

Microstructure Evolution and Tensile Behaviour of a Cold Rolled 8 wt% Mn Medium Manganese Steel

4.1 Abstract

A novel medium manganese steel with composition Fe-8.3Mn-3.8Al-1.8Si-0.5C-0.06V-0.05Sn was developed and thermomechanically processed through hot rolling and intercritical annealing. The steel possessed a yield strength of 1 GPa, tensile strength of 1.13 GPa and ductility of 41%. In order to study the effect of cold rolling after intercritical annealing on subsequent tensile properties, the steel was further cold rolled up to 20% reduction. After cold rolling, it was observed that the strain hardening rate increased continuously with increasing cold rolling reduction but without a significant drop in ductility during subsequent tensile tests. The microstructural evolution with cold rolling reduction was analysed to understand the mechanisms behind this phenomena. It was found that cold rolling activated additional twinning systems which provided a large number of potent nucleation sites for strain induced martensite to form during subsequent tensile tests in what can be described as an enhanced TRIP effect.

4.2 Introduction

Medium Mn steels (4−12 wt% Mn) are an emerging class of duplex ($\gamma + \alpha$) steels that have received considerable research attention. Medium Mn steels have shown to exhibit a successive twinning and transformation induced plasticity (TWIP+TRIP) effect if the Stacking Fault Energy (SFE) and stability of the austenite phase are adjusted into the correct regime during an Intercritical Annealing (IA) heat treatment [**?**, 19]. The TWIP+TRIP effect allowed some medium Mn steels to possess large ductilities of 60−70% [19, 26, 113, 222] and therefore show great potential for use in energy absorbing applications.

Many medium Mn steels which exhibit the TWIP+TRIP effect are manufactured by a thermomechanical process composed of hot rolling followed by cold rolling and then IA. The IA is a key step where the solute elements, such as Mn, Al and Si, are able to partition into or out of the austenite phase and therefore alter the SFE and also stability. IA is greatly enhanced with prior cold rolling such that IA can be completed (*i.e.* reaching thermodynamic equilibrium) within several minutes, allowing IA to be conducted on a Continuous Annealing Line (CAL) [31] where the heating stage is usually between 2−3 minutes long. Otherwise, IA would have to be conducted in batch annealing furnaces for a minimum of several hours [38], severely reducing productivity.

One potential problem of cold rolling before IA is cracking. The hot rolled microstructure of many medium Mn steels in the literature are either partially or fully martensitic [19, 119, 139]. Therefore, a tempering step before cold rolling is usually necessary as the hot rolled strip is potentially very hard with poor ductility [36]. In conventional strip mills, hot rolled strip is usually 2−3 mm thick which then needs to be cold rolled to 1−2 mm for automotive applications. The rolling loads necessary to make the reduction in medium Mn steel can be very large as shown in a study by Buchely *et. al.* [137]. However, it is anticipated that hot rolling capabilities to produce thinner gauges will continue to improve. For example, recent advances in strip casting technology have shown that medium Mn steel can be successfully cast into 2.5 mm thick strip [35]. With this in mind, reliance on cold rolling for heavy gauge reduction can be reduced. Cold rolling can then be pushed to the end of the processing route (*i.e.* hot rolling−IA−cold rolling) where it is still useful for other purposes such as dimensional control. From an alloy design perspective, element partitioning will no longer be able to rely on cold rolling to improve partitioning kinetics. Ideally, the steel should still be able to exhibit the TWIP+TRIP effect but through a simplified hot rolling and IA thermomechanical process route without the need for cold rolling. Several medium Mn steels in the literature have successfully demonstrated this [28, 41, 139] but require IA durations between 10−30 min which may be challenging in a CAL.

Studies on IA then cold rolled medium Mn steels are relatively sparse compared to studies on cold rolled then IA steels. Sun *et. al.* [192] studied the cold rollability of high Si, δ-ferrite containing medium Mn steels and found that brittle δ-ferrite could lead to cracking during cold rolling but more importantly that the TWIP+TRIP effect greatly enhanced the amount of cold reduction without cracking as compared to another steel which only showed the TRIP effect. Wang *et. al.* [222] and Li *et. al.* [149] studied the effect of uniaxial pre-straining on the formation of Lüders type bands and concluded that pre-straining increases the dislocation density in the austenite, therefore delaying the onset of the TRIP effect which is known to cause the formation of Lüders type bands [151]. Nevertheless the effect of cold rolling on subsequent tensile behaviour and how it may affect the TWIP+TRIP effect is relatively unknown.

This study therefore aims to accomplish two points. Firstly to develop a cost effective (in terms of alloying cost and a simplified processing route) high strength medium Mn steel that exhibits the TWIP+TRIP effect through hot rolling and IA only. Secondly, to investigate the effects of cold rolling (up to 20% reduction) after IA on tensile behaviour.

4.3 Experimental

In order to minimise cost due to microalloying, a carbide optimisation study was first conducted. Three steels with different V content were arc melted from pure elements to produce a 400 g ingot with dimensions of 60 × 23 × 23 mm. The nominal composition of Fe-8.3Mn-3.8Al-1.8Si-0.5C-0.05Sn-(0, 0.04, 0.06)V in mass percent was based on a previous alloy developed by Lee and DeCooman [28]. The ingot was sectioned into 4 bars measuring 60 × 10 × 10 mm. The bars were quartz encapsulated in low pressure Ar and homogenised at 1250 °C for 24 h before quenching in water. Each bar was reheated to 1000 °C for 30 min prior to hot rolling. Thermomechanical processing was conducted in 5 passes with decreasing reductions from 1000 °C to 850 °C with a total reduction of approximately 85%. The hot rolled strips were quenched immediately after the final pass. After hot rolling, the strips were intercritically annealed at 750 °C for 5 min before being allowed to air cool. The 0.06V steel was subsequently cold rolled to 10% and 20% reduction.

Tensile samples with gauge dimensions of 19 × 1.5 × 1 mm were machined *via* Electric Discharge Machining (EDM) from the rolled strips such that the rolling direction was parallel to the tensile direction. Tensile testing was conducted at a nominal strain rate of 10^{-3} s^{-1} with an extensometer which was removed at 10% engineering strain. An extensometer was used to accurately measure the Young's modulus and early yielding behaviour but had to be removed at 10% engineering strain to prevent over-extension of the extensometer.

Secondary Electron Microscopy (SEM), Electron Backscatter Diffraction (EBSD) and Energy Dispersive Spectroscopy (EDS) were conducted on a Zeiss Sigma FE-SEM equipped with a Bruker

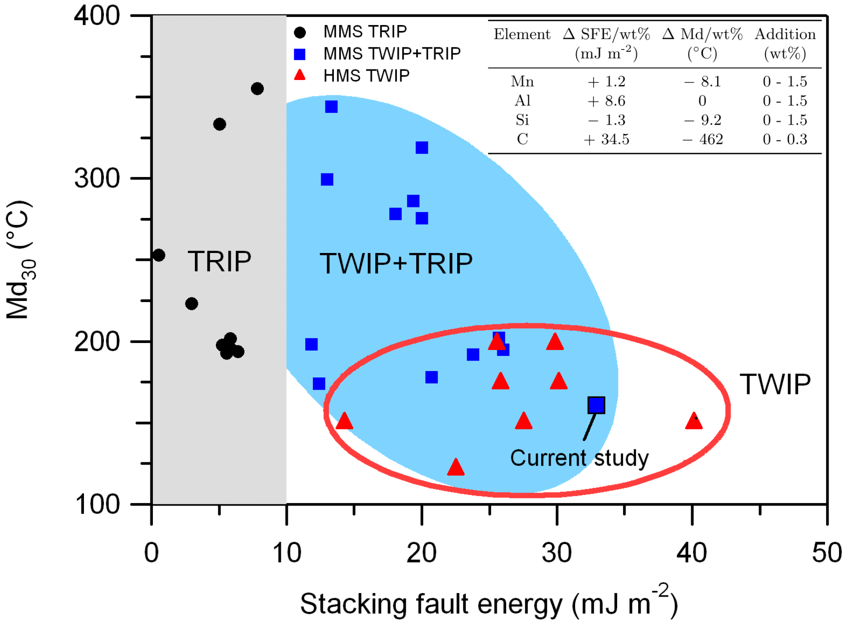

Element	Δ SFE/wt% (mJ m^{-2})	Δ Md/wt% (°C)	Addition (wt%)
Mn	+ 1.2	− 8.1	0 - 1.5
Al	+ 8.6	0	0 - 1.5
Si	− 1.3	− 9.2	0 - 1.5
C	+ 34.5	− 462	0 - 0.3

Figure 4.1: Comparison of SFE and Md$_{30}$ of the austenite phase in several Medium Mn steels (MMS) and High Mn TWIP steels (HMS) in the literature. Inset table: Change in SFE and Md$_{30}$ with different additions to austenite with an initial composition of Fe-6.55Mn-1.33Al-1.19Si-0.48C, SFE of 20 mJ m^{-2} and Md$_{30}$ of 275 °C [33]. Data from: [19, 33, 36, 45, 91, 93, 95, 132].

EBSD detector and Bruker XFlash 6160 EDS detector. Transmission Electron Microscopy (TEM) was conducted on a JEOL JEM-F200 operated at an accelerating voltage of 200 kV. Phase and orientation mapping was carried out using the NanoMEGAS ASTAR system, which uses Precession Electron Diffraction (PED) to capture EBSD-like maps in the TEM. PED patterns were collected with a precession angle of 0.7°, a precession frequency of 100 Hz and a step size of 2.5 nm. The TEM was operated with a spot size of 7 and a 10 µm condenser aperture producing a beam size of minimal diameter (<2 nm FWHM).

Samples for SEM, EBSD and EDS were mechanically ground and polished with an OP-U suspension. Samples for TEM were cut *via* EDM from heat treated blanks, mechanically ground to a thickness below 60 µm and electrolytically polished in a Struers Tenupol twin-jet electropolishing unit using a solution containing 5% perchloric acid, 35% butyl-alcohol and 60% methanol at a temperature of −40 °C.

4.4 Results

4.4.1 Alloying concept

There are many considerations to make when designing a medium Mn steel composition and its complementary thermomechanical process route. It is therefore useful to first impose several boundary conditions both in terms of composition and processing. A Mn content of 8−8.5 wt% was chosen as it represented the upper limit of what can be tolerated in conventional secondary steelmelting practice. Si content was chosen to be below 3 wt% as Si might stabilise and embrittle δ-ferrite at room temperature when added in excess [89]. Although Al can significantly reduce the density of steel [200], Al content was chosen to be kept below 4−5 wt% as Al is known to clog continuous casting nozzles [201] and form brittle κ-carbides in medium Mn steels when added in excessive amounts [200, 202]. V can also be added for carbide formation and precipitation strengthening [28, 75] but its content should ideally be kept below 0.2 wt% to minimise the alloying cost of the steel. Lastly, even though Sn is a known tramp element in steel [203], 0.05 wt% Sn was deliberately added to potentially improve the galvanisability of the steel [167].

The next step is to consider the composition of the austenite phase. Figure 4.1 shows a comparison between the stacking fault energy and stability of the austenite phase in several TRIP-type and TWIP+TRIP-type medium Mn steels as well as high Mn TWIP steels from the literature. The SFE, if not reported by the authors, was calculated according to the method by Sun *et. al.* [36]. Austenite stability, represented by Md_{30}, is defined as the temperature where half of the total austenite transforms to martensite at a strain of 30% and can be calculated according to the equation [36, 52, 53]:

$$Md_{30}(^{\circ}C) = 551 - 462C - 8.1Mn - 9.2Si - 1.42(-3.29 - 6.64\log_{10} d - 8) \tag{4.1}$$

where compositions are given in wt% and d is the grain size in µm. A combination of a moderate SFE and low Md_{30} (*i.e.* higher austenite stability) was chosen to promote twinning and a controlled TRIP effect respectively [102]. Since the TWIP+TRIP mechanism is only operative in the austenite phase, a high austenite fraction is therefore desired (≥ 0.5) for greater elongation and strain hardening rate.

The thermodynamic software Thermo-Calc is often used to provide guidance on some important processing parameters such as the optimal IA temperature, precipitation temperatures, *etc.* Inductively Coupled Plasma (ICP) and Inert Gas Fusion (IGF) were used to measure the bulk composition of the 0.06V steel and the results are shown in Table 4.1. The corresponding Thermo-Calc property diagram

Table 4.1: Bulk composition of 0.06V steel in mass percent measured by ICP, and IGF for elements marked by †.

Mn	Al	Si	C†	V	Sn	N†	P	S†
8.29	3.78	1.81	0.467	0.06	0.047	0.001	<0.005	0.003

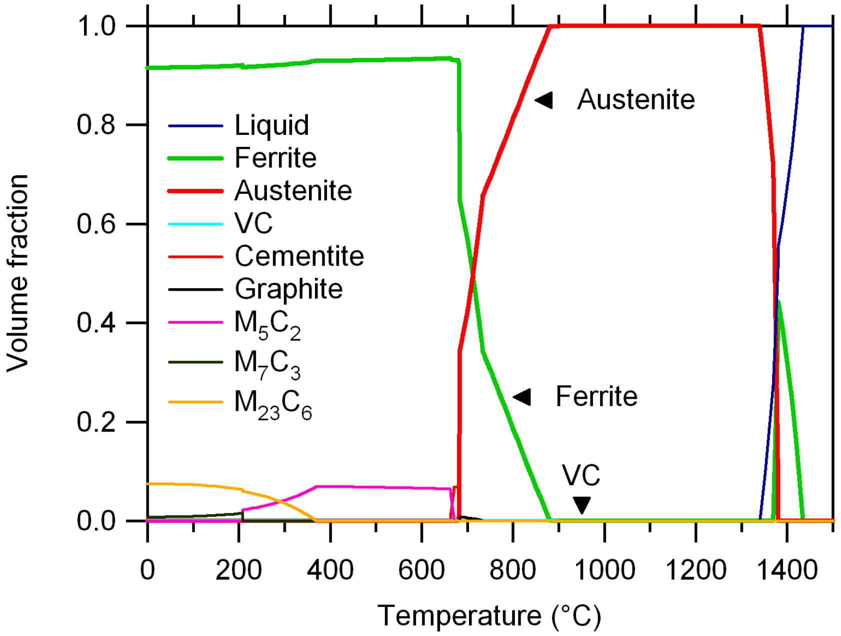

Figure 4.2: Thermo-Calc property diagram of 0.06V steel.

using the TCFE-7.0 database is shown in Figure 4.2. A wide austenitic processing window between 880−1200 °C was available for hot rolling. The δ-ferrite phase was also not expected to be present at room temperature in this alloy. VC was expected to precipitate at 940 °C while graphite and the other M_xC_y carbides were expected to precipitate at temperatures 730 °C and below. These carbides are thought to be deleterious to ductility and IA should be conducted above 730 °C to avoid the formation of these unwanted carbides. Therefore, the practical IA window was between 730−880 °C where the austenite volume fraction would vary between 0.63−1.0 respectively.

4.4.2 Tensile properties

The tensile curves of the investigated steel with different V contents in the as-annealed condition are shown in Figure 4.3. All three steels showed a high yield strength and elongation but a low strain hardening rate. The steels also showed continuous yielding with no Yield Point Elongation (YPE) and the addition of 0.05 wt% Sn did not appear to deleteriously affect overall tensile properties.

The addition of up to 0.06 wt% V resulted in an increase in yield strength from 950 to 1005 MPa but did not affect the strain hardening rate or elongation. Since the addition of 0.06 wt% V was able

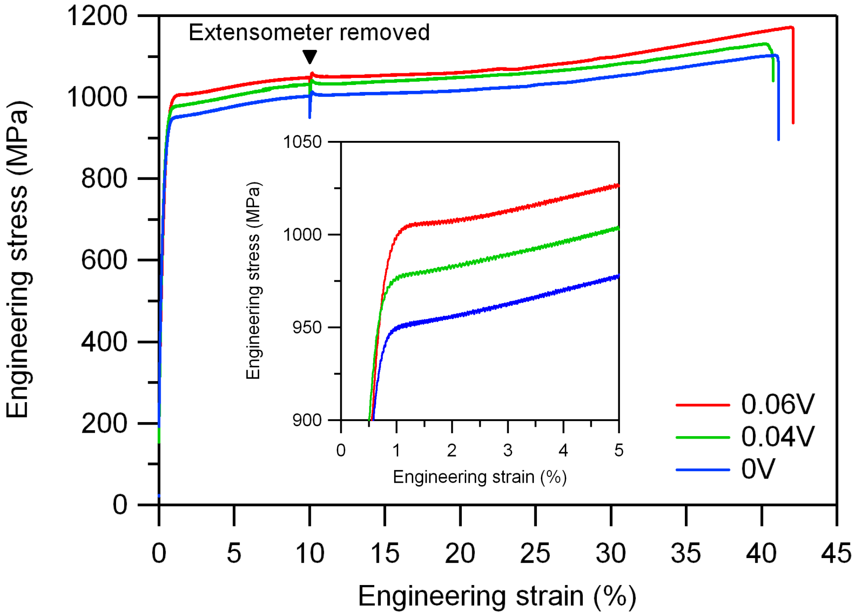

Figure 4.3: Engineering tensile curves of the investigated steel with different V content. Inset: early yielding behaviour.

to result in a GigaPascal-class steel [1], the 0.06V steel was chosen for further processing.

The 0.06V steel was further cold rolled to a reduction of 10% and 20% (hereby known as CR10 and CR20 respectively), and the resulting tensile curves are shown in Figure 4.4. In both the CR10 and CR20 samples, a pronounced YPE was observed. The presence of YPE strongly indicates that TRIP rather than TWIP was the dominant deformation mechanism at yielding [87, 98, 151, 204].

The yield strength, tensile strength and strain hardening rate increased significantly with increasing cold rolling reduction. The strain hardening rate in the as-annealed sample was not constant throughout the tensile curve, most likely due to different deformation mechanisms being active at different stages but averaged out to approximately 2 GPa. In the post-YPE section of the tensile curve, the strain hardening rate of the CR10 sample was approximately 3 GPa. However, in the CR20 sample there was a sustained hardening rate of 3.5 GPa in the post-YPE region. It is also noteworthy that both CR10 and CR20 still retained a large ductility at such high strengths. Another point of interest is the complete lack of post-uniform elongation in all the tensile samples which is also fairly common in other medium Mn steels [19, 26, 28, 33].

A summary of the tensile properties of the investigated steels is shown in Table 4.2 including the energy absorption parameter U30 which is determined as the area under the true tensile curve up to a true strain of 0.3 [98].

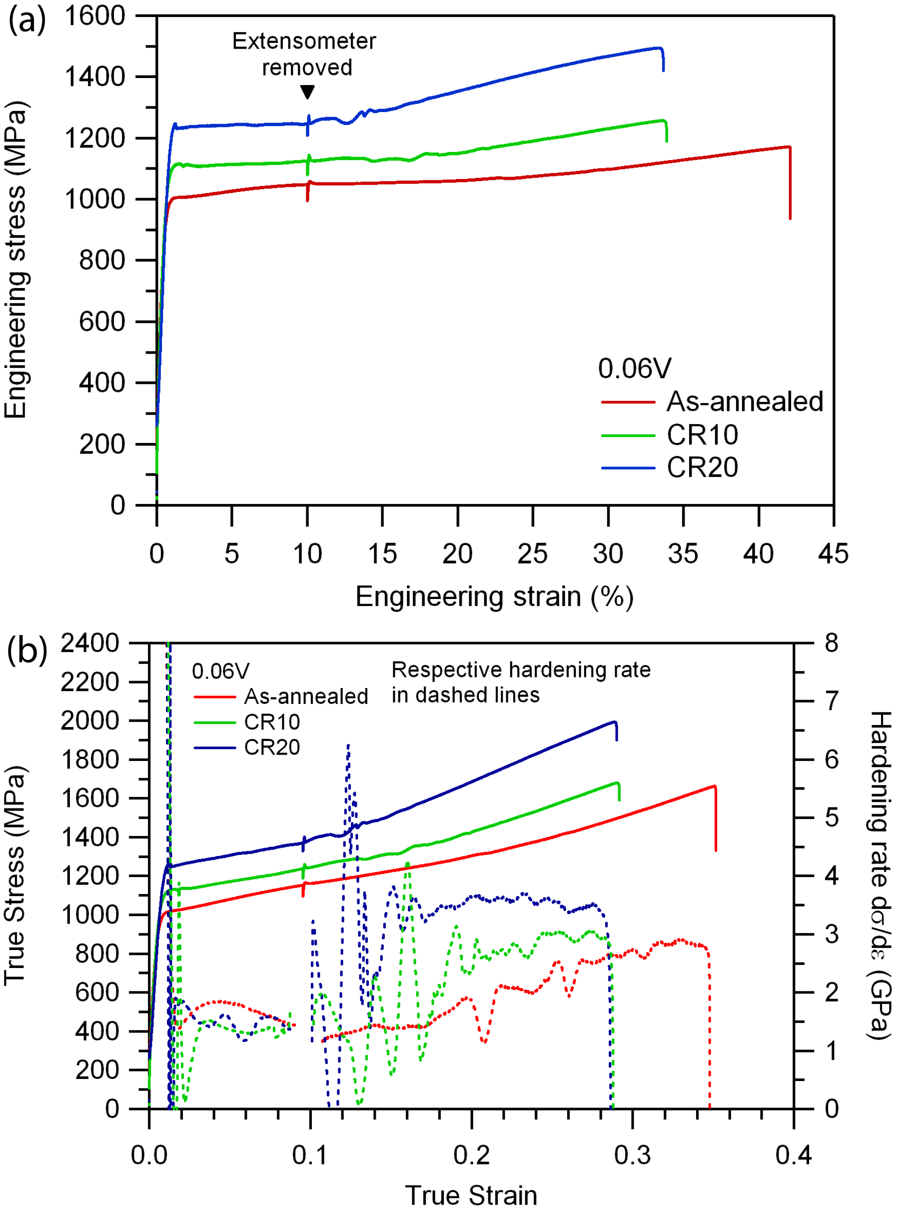

Figure 4.4: (a) Engineering tensile curves and (b) true tensile curves and hardening rate of the as-annealed and cold rolled 0.06V steel.

4.4.3 Carbide precipitation microstructure

The small strengthening increments shown in Figure 4.3 can be attributed to the increase in volume fraction of VC within the microstructure, rather than gran size refinement. In Table 4.2, the grain sizes of the 0.04V and 0.06V sample are very similar. Therefore, any increment in strength can be attributed to precipitation strengthening rather than Hall-Petch type strengthening from grain refinement. From the TEM-Bright Field (BF) micrographs in Figure 4.5, small nanometre-sized carbides can be seen in both ferrite and austenite grains and also along grain boundaries. TEM-EDS revealed them to be V-rich in composition, approximately V_4C_5 but having the cubic structure of VC (Figure 4.5c-d).

Table 4.2: Tensile properties and grain size of the investigated steels. d_γ and d_α refer to the grain size of austenite and ferrite respectively, determined as the equivalent circle diameter measured using EBSD. Note that 0.06V, CR10 and CR20 have the same composition.

Alloy	$\sigma_{0.2}$ (MPa)	σ_{UTS} (MPa)	ϵ (%)	U30 (MJ m^{-3})	d_γ (µm)	d_α (µm)
0V	950	1100	41	361	-	-
0.04V	985	1130	41	372	3.6	1.8
0.06V	1005	1170	42	379	4.2	1.8
CR10	1110	1260	34	389	-	-
CR20	1250	1490	34	445	-	-

To determine the strengthening contribution of these carbides, the Ashby-Orowan equation after Gladman [80] can be used:

$$\Delta\sigma_y^i = \left(\frac{0.538Gbf^{0.5}}{X}\right)\ln\left(\frac{X}{2b}\right) \tag{4.2}$$

where $\Delta\sigma_y^i$ is the change in yield strength of phase i (MPa), G is the shear modulus ($G_\gamma = 75\,000$ MPa, $G_\alpha = 80\,000$ MPa), b is the Burgers vector ($b_\gamma = 0.250$ nm, $b_\alpha = 0.248$ nm) [22], f is the volume fraction of carbides and X is the mean carbide diameter (nm). The overall increase in strength of the bulk alloy can be described by the rule of mixtures:

$$\Delta\sigma_y^{bulk} = \Delta\sigma_y^\alpha V_f^\alpha + \Delta\sigma_y^\gamma V_f^\gamma \tag{4.3}$$

where V_f^α and V_f^γ are the volume fractions of ferrite and austentite respectively. Image analysis of TEM micrographs in the 0.06V sample revealed that the average VC diameter was 19 ± 4 nm. VC size and distribution appeared to be fairly equal between austentite and ferrite grains. Hu *et. al.* [30] also observed VC precipitation to be approximately equal in terms of volume fraction and size between austenite and ferrite grains. The volume fraction of carbides was determined by Thermo-Calc to be 1.25×10^{-3}. Assuming an equal volume fraction of VC in both austenite and ferrite, the theoretical strength increment from the addition of 0.06 wt% V as calculated from Equations 4.2 and 4.3 was 70 MPa. However, the theoretical strength increment was slightly larger than the experimentally observed value of 55 MPa. The difference can be attributed to a slight loss of VC volume fraction to intergranular precipitates at the grain boundaries.

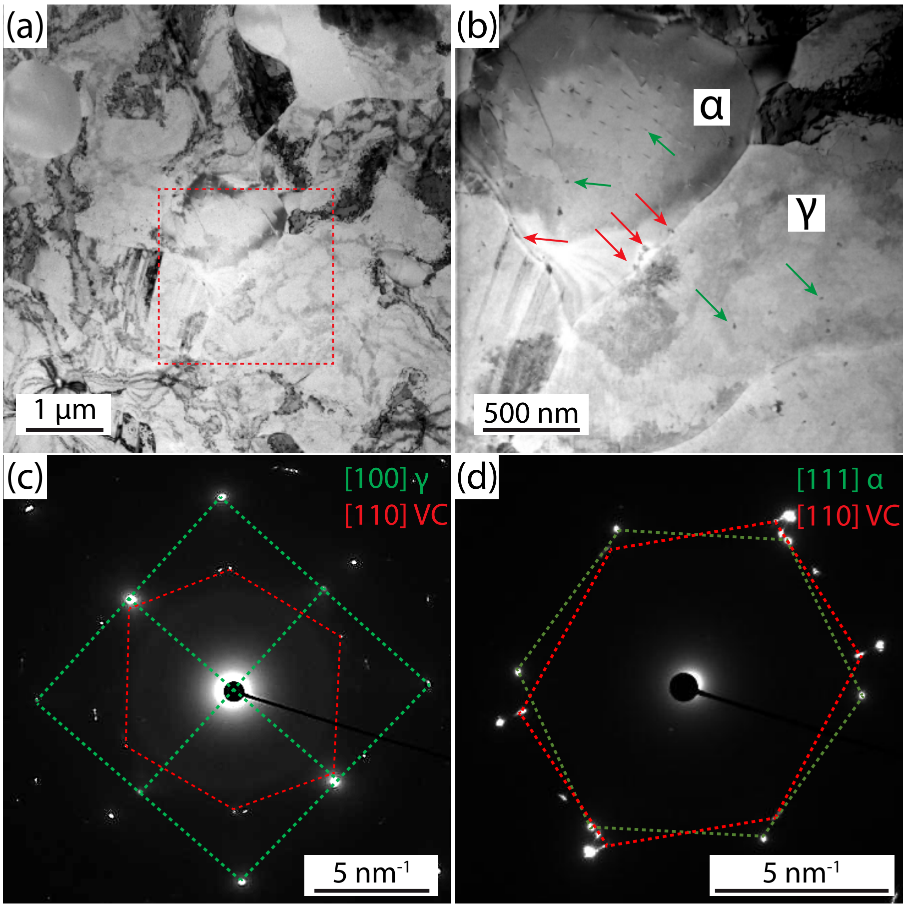

Figure 4.5: (a) TEM-BF micrograph of 0.06V as-annealed sample. (b) Magnified TEM-BF micrograph of the red square in (a) showing intergranular precipitates (red arrows) and intragranular precipitates (green arrows). Diffraction patterns obtained from (c) an austenite grain, $[100]_\gamma$ zone axis and (d) a ferrite grain, $[111]_\alpha$ zone axis.

4.4.4 EBSD observations

The EBSD maps of the as-annealed, CR10 and CR20 0.06V steel are shown in Figure 4.6 and a summary of the phase fractions is shown in Table 4.3 and Figure 4.7. The microstructure of the as-annealed sample did not resemble the typical lath-type microstructure in hot rolled, quenched and IA medium Mn steels [28]. Instead, the microstructure can be described as pancaked austenite grains with larger ferrite grains on the austenite grain boundaries and finer ferrite grains in the austenite grain interior. The phase fractions obtained were also reasonably close to that obtained by Thermo-Calc (Table 4.3) which may suggest that the equilibrium phase fraction had been attained.

The texture of the as-annealed steel is shown in Figure 4.6k-m. The steel was highly textured which is typical of steels rolled below the non-recrystallisation temperature (T_{nr}). While annealing twins could be found in multiple austenite grains, the slight curvature of the annealing twins and the lack of a recrystallisation texture imply that the as-annealed microstructure was recovered instead of

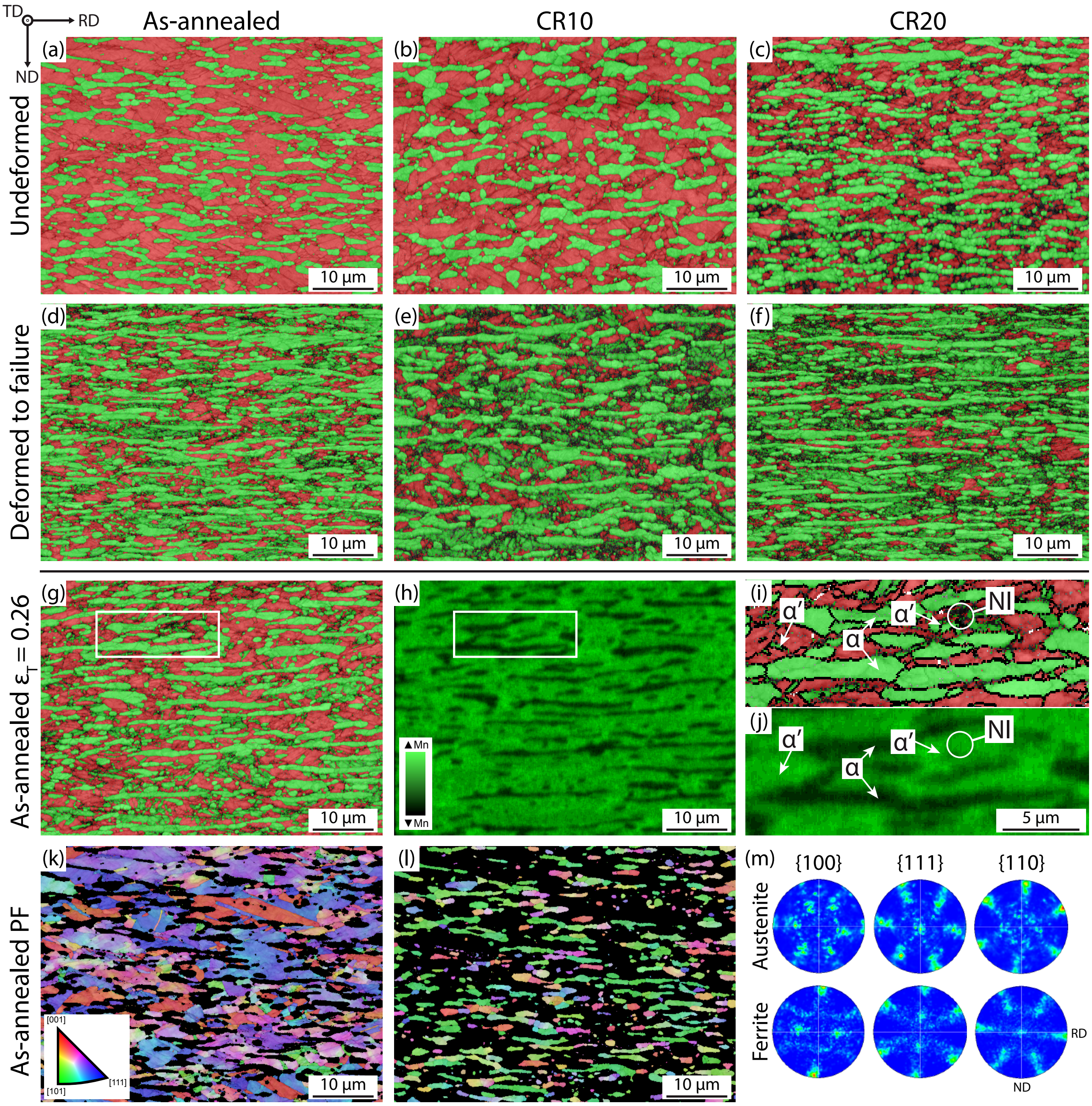

Figure 4.6: EBSD Image quality (IQ) + Phase Maps (PM) of 0.06V steel in the undeformed (a) as-annealed, (b) CR10, (c) CR20 and deformed to failure (d) as-annealed, (e) CR10, (f) CR20 conditions. EBSD IQ+PM of the (g) as-annealed 0.06V steel deformed to true strain of 0.26, red – austenite, green – ferrite or martensite. (h) Corresponding EDS-Mn map with (h). (i) Magnified region from (g) showing both ferrite and α'-martensite. High angle grain boudaries in black and austenite $\Sigma 3$ boundaries in white. (j) Corresponding magnified region from (h). (k) Austenite IPF-X, (l) ferrite IPF-X maps and (m) pole figures of the 0.06V as-annealed sample.

recrystallised and that the annealing twins formed at higher temperatures during hot rolling.

Due to the difficulty in distinguishing martensite from BCC ferrite in EBSD, the martensite fraction from any particular map was determined by summing the BCC and Non-Indexed (NI) fractions and subtracting 32.5%, where 32.5% is the sum of BCC and NI fractions in the undeformed as-annealed

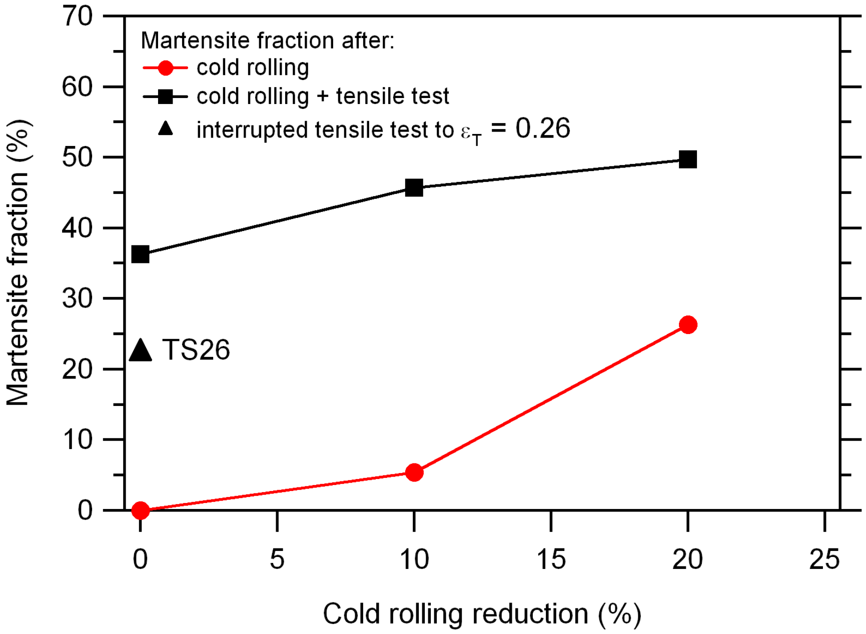

Figure 4.7: Evolution of martensite fraction with cold rolling reduction before and after a uniaxial tensile test.

sample (Figure 4.6a) and taken to be the baseline. From correlative EBSD and EDS-Mn maps in Figures 4.6i-j, most NI areas correspond to a region with high Mn concentration, *i.e.* austenite. This suggests that the NI regions were highly deformed but have the same composition as austenite and therefore may be assumed to be martensite which forms upon deformation. Nevertheless, it is acknowledged that there will be some margin of error with this indirect method of measurement.

From Figure 4.7, it is evident that the martensite fraction increased in the cold rolled samples and also in subsequent tensile tests. When cold rolled to 10% reduction (CR10), the martensite fraction increased slightly, indicating that the TRIP effect was not yet significant. However when cold rolled to 20% reduction (CR20), the martensite fraction increased signifcantly. A tensile sample made from the as-annealed steel was interupted at a true strain of 0.26, hereby known as TS26, such that it had the same equivalent strain (ϵ_{eq}) as the CR20 sample [129]. It was found that the TS26 sample had a slightly lower martensite fraction than CR20. When the cold rolled samples were tensile tested to failure, it was also found that the final martensite fraction also increased with prior cold reduction. The increase in final martensite fraction occured most significantly in the first 10% of cold rolling reduction (CR10) but began to saturate in the next 10% (CR20).

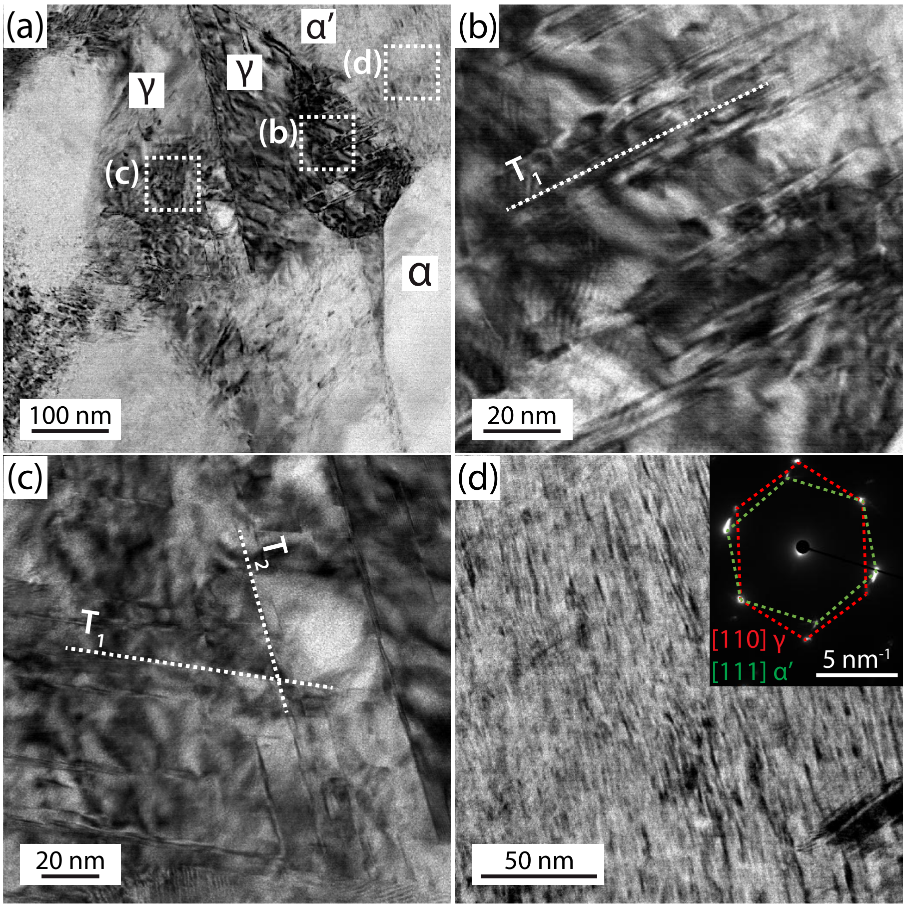

Figure 4.8: Deformation structures in CR10 sample with beam direction parallel to $[110]_{\gamma}$. (a) TEM-BF of the general microstructure. (b) STEM-BF of region b showing one active twinning system. (c) STEM- BF of region c showing two twinning systems. (d) STEM-BF of region d showing strain-induced martensite.

4.4.5 TEM observations

While EBSD is helpful in understanding the microstructural changes on a macroscopic scale, it is necessary to probe the deformation structures on a much finer scale using TEM. Figure 4.8 shows the microstructure after 10% cold rolling reduction, taken from the CR10 sample. The microstructure comprised of austenite, ferrite and also martensite. At a higher magnification, austenite twins were observed in one grain (Figure 4.8b) and two sets of twins from two twinning systems were observed in an adjacent austenite grain (Figure 4.8c). The martensite grain in Figure 4.8d had a diffraction pattern illustrating the K-S orientation relationship with the adjacent austenite grain in region (b). The martensite was therefore likely to be Strain Induced Martensite (SIM) and denoted as blocky-SIM because of its blocky morphology.

The microstructure after a 20% cold rolling reduction obtained from the CR20 sample is shown in Figure 4.9. The microstructure showed that both austenite and martensite phases had a higher

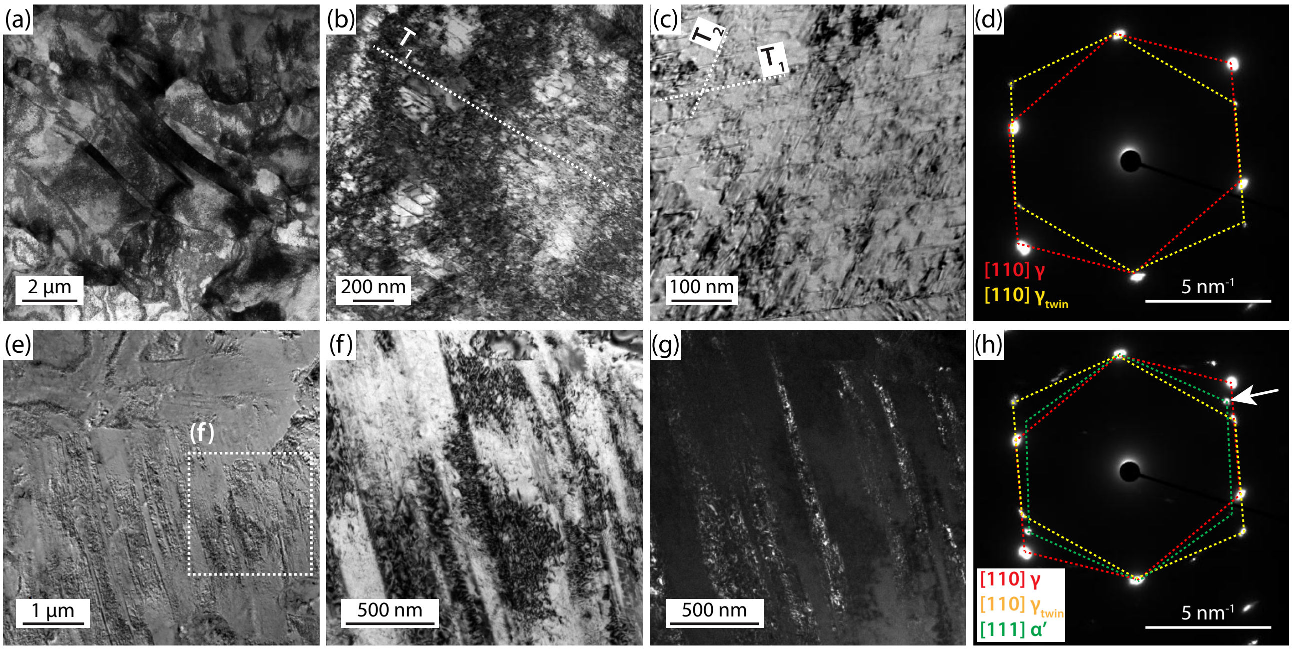

Figure 4.9: Deformation structures in CR20 sample with beam direction parallel to $[110]_{\gamma}$. (a) STEM-BF micrograph of the general microstructure. (b) STEM-BF micrograph showing one active twinning system and surrounding high dislocation density. (c) STEM-BF micrograph of a region with two active twinning systems. (d) Diffraction pattern obtained from region in (b). (e) TEM-BF micrograph of an austenite grain showing long lath-structures. (f) Magnified TEM-BF micrograph from (e). (g) TEM-Dark Field (DF) obtained from martensite spot indicated by white arrow in (h). (h) Diffraction pattern obtained from (f).

dislocation density than the CR10 sample. Austenite grains with a high density of twins from either one twinning system (Figure 4.9b) or two twinning systems (Figure 4.9c) were observed. The diffraction pattern in 4.9d was obtained from the single twinning region in Figure 4.9b. The NanoMEGAS phase map in Figure 4.10b revealed some very fine martensite grains in a region similar to Figure 4.9c containing intersecting twins from two active twinning systems. These martensite grains most likely nucleated at the twin intersections through the mechanism proposed by Olsen and Cohen [205, 206] and is widely reported in TWIP+TRIP-type medium Mn steels [19, 36].

From Figure 4.9e, a deformation structure that was not present in the CR10 sample was observed in the CR20 sample. The structure comprised of long wavy laths which spanned the entire grain. Figures 4.9f-h showed that the wavy laths were most likely kinked austenite twins which contained very fine SIM within the twin boundaries. The SIM was also found to obey the K-S orientation relationship with the parent austenite. However, according to the intersecting shear mechanism by Olson and Cohen [107], it would not be possible to nucleate martensite within a single twin. But if the twins were kinked then it might be possible that the deformation may have provided a suitable secondary shear to nucleate martensite within the twin [207, 208]. In many Metastable Austenitic Stainless

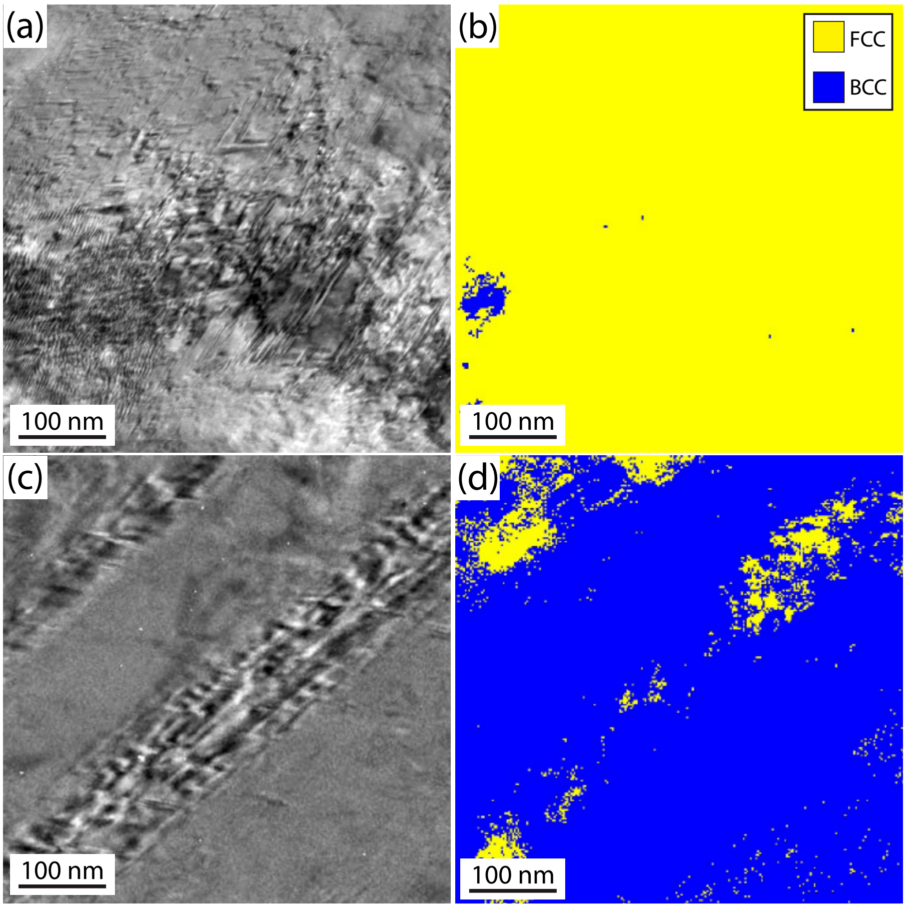

Figure 4.10: Strain-induced martensite in CR20 sample (a) TEM-BF of two twinning systems and (b) corresponding NanoMegas phase map. (c) TEM-BF of a wide twin and (d) corresponding NanoMegas phase map. Beam direction parallel to $[110]_\gamma$

Steels (MASS), martensite can also be found in curved twins without the need for an intersection with another twin [209–211]. MASS are an older class of steels which have been extensively studied. They share a large number of similarities with medium Mn steels such as the TWIP+TRIP effect and are therefore a very useful guide to the understanding of medium Mn steels. The SIM which forms at twin intersections and within curved twins shall be denoted as fine-SIM due to its small and particulate morphology.

Another grain in the CR20 sample which also contained similar wavy lath-like structures is shown in Figure 4.10c-d. However, the NanoMEGAS phase map revealed a different relationship where austenite appears to have nucleated inside a lath within a martensitic matrix. This effect was likely the result of three stages of deformation. Firstly, the formation and thickening of an austenite twin. Secondly, the nucleation of fine-SIM within the twin but not consuming the entire twin. Thirdly, the austenite matrix transforms to martensite, likely due to the growth of blocky-SIM. However, because the austenite phase within the twin was of a different orientation to the austenite matrix, it remains

Table 4.3: Phase fractions (%) of the annealed and cold rolled steels before and after tensile testing. † N.I. − Non-indexed percentage. ‡ Martensite fraction = (BCC + NI) −32 − 0.5.

	FCC	BCC	NI†	α'‡
Thermo-Calc (750 °C)	71.2	28.8	-	-
0.06V - undeformed	67.5	32	0.5	0
0.06V - deformed to 0.26	45.3	48.2	6.5	22.2
0.06V - deformed to failure	31.2	59.6	9.2	36.3
CR10 - undeformed	62.1	35.2	2.7	5.4
CR10 - deformed to failure	21.8	55.8	22.4	45.7
CR20 - undeformed	41.2	47.9	10.9	26.3
CR20 - deformed to failure	17.8	61.3	20.9	49.7

untransformed. This also shows that blocky-SIM grains in the CR20 sample were also growing with increasing cold rolling reduction.

The microstructure of the TS26 sample is shown in Figure 4.11 and was very different from the CR20 sample even though they have the same equivalent strain. Three regions from the TS26 sample were chosen in Figure 4.11 to illustrate these differences. In Region 1 (Figure 4.11a-d), large martensite plates were observed to be propagating outwards in the direction of the dashed green arrows from the interphase grain boundary marked by the dashed green line. The martensite plates appear to be able to propagate through several austenite twins in Figure 4.11b but with some distortion along the edges of the martensite plate. This suggests that twins are not a strong obstacle to the propagation of blocky-SIM which would render these twins ineffective to the future formation of fine-SIM. Intersecting twins or secondary twins from a second twinning system were not observed in the TS26 sample.

In Region 2 (Figure 4.11e-h), the martensite adopted a different morphology with a curved interface as it appears to grow into the surrounding austenite grain. Finally, in Region 3 (Figure 4.11i-k), twinned martensite or Stress-Assisted Martensite (SAM) was observed. SAM has been shown to be able to form after plastic yielding when the stress is high enough to contribute to a sufficiently large driving force for the martensitic transformation in the absence of alternative nucleation sites for SIM [107, 111, 212]. SAM was therefore likely able to form in TS26 due to a combination of a low density of twins (*i.e.* SIM nucleation sites) and high applied tensile stress (1425 MPa).

It should be noted that the martensites identified in this steel deviate slightly from the more conventional definitions of SAM and SIM. SAM is usually defined as martensite that forms under applied stress, often below the yield stress of the parent phase and nucleates on pre-existing nucleation sites. SIM is defined as martensite that forms after macroscopic yielding and nucleates on defects generated during plastic deformation [107, 213]. As a result, SAM may adopt the morphology of

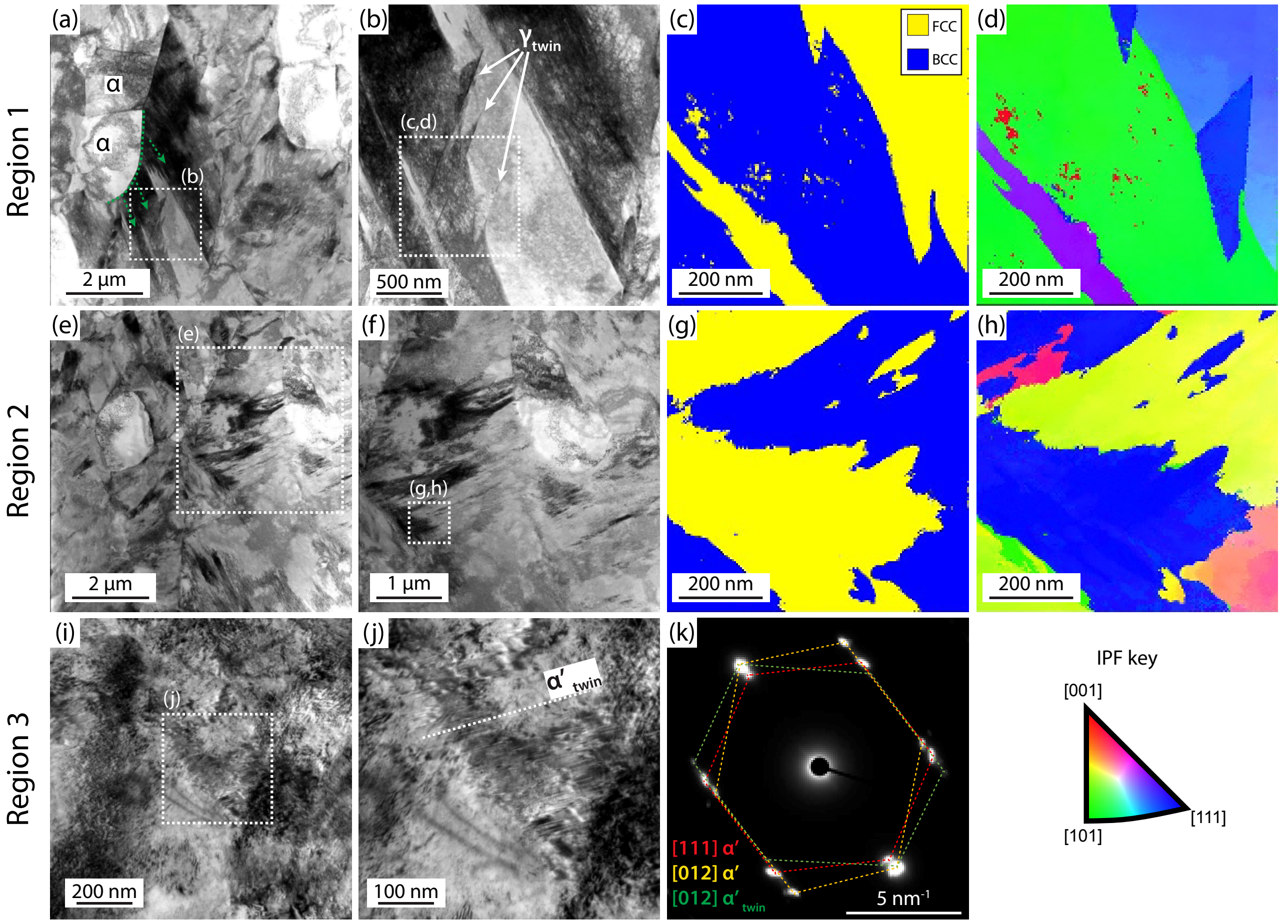

Figure 4.11: Deformation structures in TS26 sample. From region 1, (a) general microstructure (STEM-BF), (b) magnified view showing martensite and austenite twins (STEM-BF), NanoMegas (c) phase map and (d) IPF from red square in (b). From region 2, (e) general microstructure (STEM-BF), (b) magnified view of austenite and martensite regions (STEM-BF), NanoMegas (g) phase map and (h) IPF from red square in (f). From region 3, TEM-BF micrograph of (i) entirely martensitic region, (j) magnified view showing martensitic twins and (k) diffraction pattern from (j).

internally twinned plates while SIM tends to form thin laths along slip planes, twins or ϵ-martensite intersections [212]. Here, we have shown that SAM may form after yielding and also the presence of blocky-SIM which nucleates from grain boundaries instead of deformation structures.

4.4.6 Composition

The composition of each phase of the 0.06V steel was measured by SEM and TEM-EDS and compared against the Thermo-Calc simulation in Table 4.4. The C content in the austenite phase was determined by the lever rule using the phase fractions obtained by EBSD in Table 4.3 and assuming negligible C solubility in the ferrite phase.

Compositions measured by both SEM and TEM-EDS showed that Mn partitioned to austenite, whereas Al and Si partitioned to ferrite, which is well reported in the literature [214]. However, the degree of partitioning measured by SEM-EDS was much lower than TEM-EDS. This is largely due to a limitation of the large spot size of SEM-EDS in measuring the composition of a fine-grained material. The TEM-EDS results were therefore taken to be more reliable. While the compositions measured by TEM-EDS do not match up exactly with those predicted by Thermo-Calc, the degree of partitioning was such that the resulting SFE was within the known twinning regime in both high Mn TWIP steels and medium Mn steels. With reference to the Thermo-Calc simulation, the 0.06V steel was at phase equilibrium but not at composition equilibrium, most likely due to the short IA duration.

4.5 Discussion

4.5.1 Effect of cold rolling on microstructure

Table 4.4: Composition of the bulk and individual phases in the 0.06V steel measured by ICP, SEM-EDS and TEM-EDS. Uncertainties given in parantheses. †C content in SEM and TEM-EDS determined by lever rule based on phase fractions obtained from EBSD. ‡ Grain sizes calculated from the Bruker ESPRIT software.

	(wt%)						d_{grain}‡ (µm)	SFE (mJ m^{-2})	Md_{30} (°C)
	Mn	Al	Si	C†	V	Sn			
Bulk (ICP)	8.29	3.78	1.8	0.467	0.06	0.047	-	-	-
γ (Thermo-Calc)	9.38	3.69	1.98	0.7	trace	-	-	36.6	-
γ (SEM-EDS)	8.8 (0.7)	4.0 (0.6)	1.9 (0.4)	0.69	-	-	4.2	38.2	165
γ (TEM-EDS)	9.5 (0.4)	3.2 (0.1)	1.8 (0.1)	0.69	0.07 (0.03)	0.03 (0.06)	4.2	32.9	161
α (Thermo-Calc)	4.76	4.65	2.09	trace	trace	-	-	-	-
α (SEM-EDS)	7.3 (1.2)	4.2 (0.9)	1.9 (0.3)	0	-	-	1.8	-	-
α (TEM-EDS)	6.5 (0.2)	4.0 (0.1)	2.3 (0.1)	0	0.04 (0.02)	0.04 (0.08)	1.8	-	-

The TEM observations of the CR10, CR20 and TS26 samples revealed a variety of deformation structures such as twins and martensite in the microstructure. By first comparing the CR20 and TS26 sample, it is evident that the strain path, uniaxial tension in TS26 and plane strain compression in CR10 and CR20, strongly influenced the presence and density of the deformation structures. The effects of deformation mode on microstructure has been studied extensively in MASS [129,209,215–218] and largely show that as the mode of deformation changes from uniaxial to multiaxial, more slip systems and also twinning systems are activated. The same principle also appears to hold true in the investigated steel. While both CR20 and TS26 samples had the same equivalent strain, CR20 had a larger density of twins and even secondary twins (Figure 4.9) compared to TS26 which only had a low density of primary twins (Figure 4.11). This shows that cold rolling (*i.e.* plane strain compression) is able to produce a higher twin density than can be achieved under uniaxial tension. However, the lack of a high density of twins in TS26 was surprising because its SFE as calculated in Table 4.4 was well within the known twinning region of TWIP steels [8]. Nevertheless, when compared to other TWIP+TRIP-type medium Mn steels in Figure 4.1, the investigated steel had the highest SFE. This suggests that twinning kinetics in medium Mn steel are slower and may not be directly comparable with fully austenitic TWIP steels.

Twin intersection density in the microstructure is known to affect the subsequent TRIP effect by providing potent nucleation sites for SIM nucleation [19, 22, 132]. Two types of SIM were observed in the investigated steel: fine-SIM and blocky-SIM. Both fine-SIM and blocky-SIM were observed to have nucleated on defects as per the definition by Olson and Cohen [107] but were distinguished on the basis of morphology and type of nucleating defect. Fine-SIM was only observed in the CR20 sample where it nucleates at twin intersections and in curved twins (Figures 4.9 and 4.10). Fine-SIM also tends to remain within the twin boundaries even as they grow [215].

On the other hand, blocky-SIM was observed to nucleate at grain boundaries, especially interphase grain boundaries (Figures 4.8 and 4.11) and can grow to very large sizes, even consuming the entire austenite grain (Figure 4.6d-f). Blocky-SIM was observed in all three samples CR10, CR20 and TS26 suggesting that the formation of blocky-SIM was unavoidable, regardless of strain path or strain level. However, the existence of blocky-SIM at low strains, *i.e.* CR10 (Figure 4.8), suggests that grain boundaries, particularly interphase boundaries, can also act as potent nucleation sites for martensite nucleation, allowing martensite to form without the need for twin intersections, contrary to what was suggested by Lee and De Cooman [132]. This supports the observation by Sohn *et. al.* [113] that TWIP and TRIP (in the form of blocky-SIM) can occur simultaneously. During the plastic deformation of medium Mn steels, the austenite-ferrite interphase boundary experiences a large amount of strain due to the difference in operating slip systems between the two phases [87, 128]. Therefore, the large strain at the interphase grain boundaries could provide a large driving force for the nucleation of blocky-SIM.

Since twinning and martensite transformation have been shown to occur simultaneously, then TWIP and TRIP can be said to be competitive processes in the investigated alloy. At low strains (*e.g.* CR10) where the plastic mismatch between ferrite and austenite is low [128], only a small fraction of austenite has transformed in the form of blocky-SIM, allowing twins to form in the untransformed austenite. However, at higher strains (*e.g.* CR20 and TS26), a larger fraction of austenite would have transformed to blocky-SIM, with less untransformed austenite available for twinning. Cold rolling therefore promotes twin formation in the austenite before blocky-SIM begins to dominate the microstructure at higher strains, making twinning more difficult.

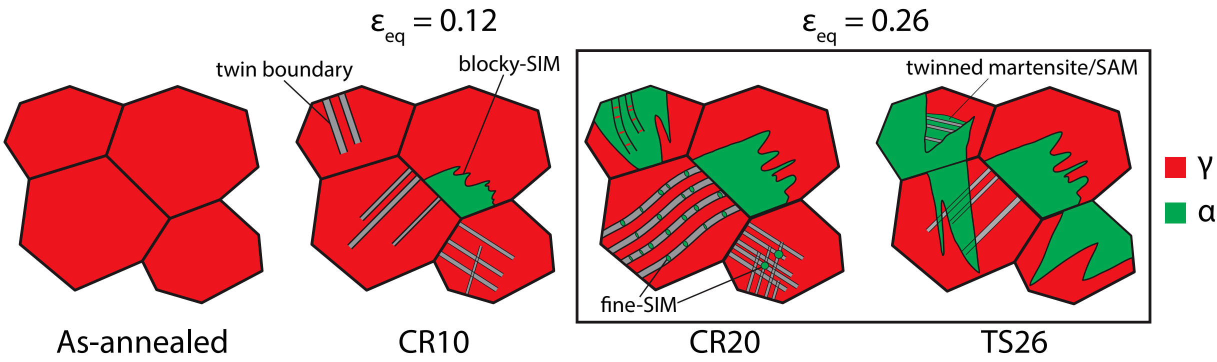

Figure 4.12: Schematic of the deformation structures in the austenite phase as seen in the various samples. CR10 showing austenite twins, as well as and blocky-SIM. CR20 showing kinked twins with fine-SIM within, intersecting twins and larger-SIM. TS26 showing only one active twinning system, extensive large-SIM and also twinned martensite (SAM).

A summary of the microstructural evolution of the austenite phase is shown in Figure 4.12. At 10% cold reduction, the austenite phase first shows twins and blocky-SIM. Secondary twins may also be present in certain grains. When cold reduction was increased to 20%, twinning becomes more extensive and numerous twin intersections have developed. Fine-SIM has started to nucleate in curved twins and at twin intersections while blocky-SIM would also have grown larger and more numerous. Alternatively, at 0.26 true tensile strain, the microstructure contains of a low density of austenite twins, a large fraction of blocky-SIM and also SAM.

It should be mentioned that the various morphologies of α'-martensites such as fine-SIM, blocky-SIM and SAM are all expected to strengthen the steel although their effectiveness and origin may differ. Fine-SIM may be considered the most effective as a distribution of fine hard particles can strengthen the austenite phase without compromising ductility. As mentioned, fine-SIM can be encouraged to form by introducing a large density of twin intersections and curved twins, both of which have been shown to be effective nucleation sites for fine-SIM. On the other hand, blocky-SIM and SAM might be considered less effective in terms of strengthening than fine-SIM because of their relatively large size. Furthermore, blocky-SIM nucleates and grows from the austenite/ferrite interphase boundary and creates a α'-martensite/ferrite interphase boundary instead which has a low damage tolerance, *i.e.* prone to forming cracks and voids at high strains due to the strength mismatch, as demonstrated in DP steels [189]. SAM is not commonly expected during plastic straining but is postulated to form at higher strains if there are a low density of nucleation sites for SIM. Therefore, little is known about post-yielding SAM but due to their blocky morphology, can be expected to behave similar to blocky-SIM.

4.5.2 Effect of cold rolling on tensile behaviour

The effect of cold rolling as explained in the previous section was to introduce a variety of deformation structures into the microstructure. When the cold rolled samples were subsequently tensile tested, these deformation structures will certainly be expected to influence the tensile behaviour. The effect of deformation twins is well known and is considered to be beneficial as it strengthens the austenite through the dynamic Hall-Petch effect [8] and also provides nucleation sites for fine-SIM [19]. Fine-SIM, especially twin intersection-type SIM, is also considered beneficial and its effect on tensile properties is well documented and modelled in both medium Mn steels and MASS [22, 132, 219, 220]. Steels which can form a higher density of twin intersections and therefore form a larger volume fraction of fine-SIM were able to exhibit higher strain hardening rates. However, the effects of blocky-SIM are not as well studied but it is postulated that because of its coarse nature, would not provide as large a benefit to strain hardening or ductility enhancement compared to fine-SIM. SAM which shares a similar blocky and coarse morphology as blocky-SIM is similarly not expected to aid in ductility enhancement [212].

From Figures 4.4 and 4.11, the as-annealed sample likely deformed *via* simultaneous TWIP and TRIP (blocky-SIM) while also forming SAM at later stages. The lack of fine-SIM and predominance of blocky-SIM in the as-annealed 0.06V steel may explain the lower strain hardening rate as compared to other medium Mn steels in the literature [19, 113, 132]. On the other hand, the cold rolled samples deformed predominantly *via* TRIP only. The YPE in the cold rolled tensile samples strongly suggests that twinning was no longer active during the early stage of deformation. It was likely that the uniaxial tensile strain was not able to activate new twinning systems nor increase twin density than what was already formed by cold rolling.

The presence of a high density of potent fine-SIM nucleation sites in the cold rolled samples indicates that during uniaxial tension, the TRIP effect would comprise of the nucleation of both fine-SIM and blocky-SIM. The additional formation of fine-SIM would greatly improve the strain hardening rate and tensile strength which was observed in Figure 4.4. Since the CR20 sample contained a higher twin density and therefore nucleation sites for fine-SIM, the strain hardening rate and tensile strength in the CR20 tensile sample was consequently higher than CR10. The higher martensite fractions in the cold rolled and tensile tested samples shown in Figure 4.7 may also be attributed to the nucleation and growth of fine-SIM that would otherwise not have formed under pure uniaxial tension. The phenomena of increased martensite fraction in cold rolled then tensile tested samples was also observed in MASS [221].

It is also noteworthy that the CR10 and CR20 tensile samples both failed at the same elongation. While the increased final martensite fraction in the cold rolled and tensile tested samples may have contributed to ductility enhancement, Sun *et. al.* [89] found that in a TWIP+TRIP-type medium Mn steel, failure was driven by void formation at α/α' interfaces, most likely due to the large plasticity mismatch between the two phases. Choi *et. al.* [90] also found that the strain gradient between α/α' interfaces resulted in interface decohesion. A similar situation may also be occuring in the CR10 and CR20 tensile samples where the interface strength was the limiting factor, since neither sample failed by necking. This failure mode in medium Mn steels may also explain the lack of post-uniform elongation in all the tensile samples in the investigated steel.

These findings suggest that the cold rolled samples were no longer TWIP+TRIP-type but deformed only *via* the TRIP mechanism. It can be viewed that by cold rolling the steel, the TWIP effect was consumed to produce an enhanced TRIP effect during subsequent uniaxial tensile testing. This implies that the strain hardening rate of medium Mn steels can be varied by simply adjusting the cold rolling reduction after the IA heat treatment. Future alloy design for cold rolled medium Mn steels should aim to reduce the SFE of the austenite to promote twinning during cold rolling and therefore increase the density of nucleation sites for fine-SIM.

4.5.3 Effect of cold rolling on yield point elongation

A study by Sun *et. al.* [87] explained why medium Mn steels with fine grained equiaxed-type microstructures typically demonstrated considerable YPE. They showed that the large austenite-ferrite interface area, due to the fine grained microstructure, provided a high density of dislocation sources leading to rapid dislocation mutiplication and therefore discontinuous yielding. While the as-annealed microstructure was also fine grained and resembled equiaxed-type microstructures, there was no true recrystallisation during intercritical annealing and it is likely that both austenite and ferrite phases still contained a high density of mobile dislocations after hot rolling, allowing for continuous yielding.

However, in the cold rolled samples the emergence of the YPE can be attributed to the TRIP effect. Gao *et. al.* [204] showed how the TRIP effect was able to sustain a large Lüders strain of 40% in a metastable austenitic stainless steel SUS304. Since the cold rolled samples contained a high density of SIM nucleation sites, the martensitic transformation would be able to provide fresh mobile dislocations and cause discontinuous yielding. This also explains why the YPE in CR20 was shorter than CR10 as the CR20 sample contains more SIM nucleation sites than CR10 which will result in a higher local strain hardening rate within the Lüders band and therefore a higher band velocity [87].

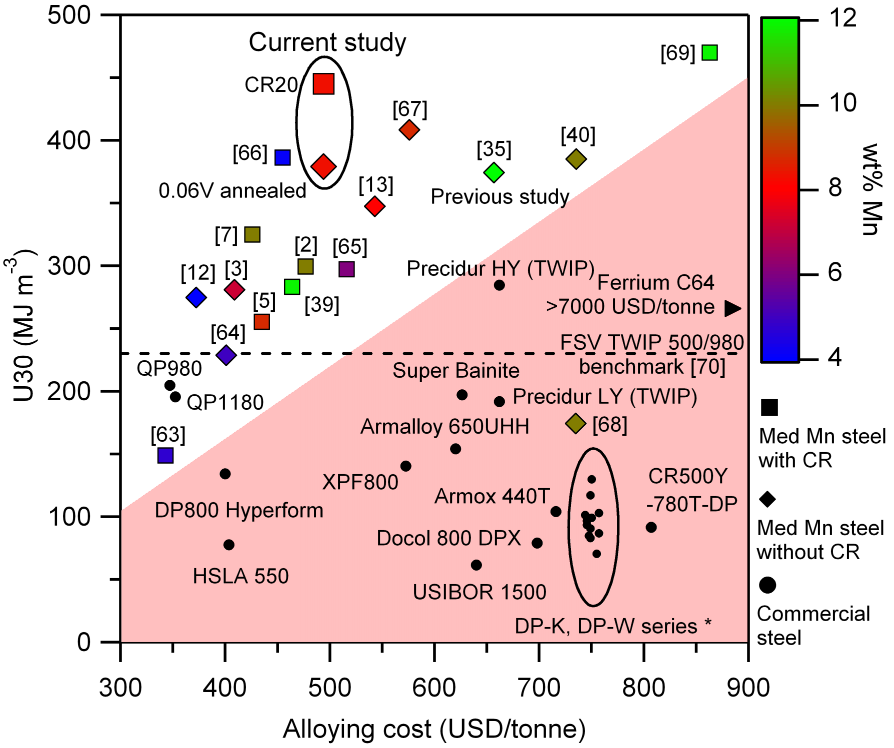

Figure 4.13: U30 diagram comparing alloying cost and energy absorption between several medium Mn steels in the literature and commerical steels. [18–27, 30, 35, 38, 41, 98, 222]. *ThyssenKrupp dual phase steels.

4.5.4 Industrial relevance

In our previous work [98], we introduced a medium Mn steel of composition Fe-12Mn-4.8Al-2Si-0.32C-0.3V and found that the high price of V greatly increased the alloying cost of the steel. Many researchers have also added V to medium Mn steels and achieved large amounts of precipitation strengthening [28, 30]. Hu *et. al.* [30] was able to improve the yield strength by 650 MPa with 0.7 wt% V through a warm rolling and IA processing route. However, relying on V for strength is a costly route. In this work, a carbide optimisation study was conducted and found that 0.06 wt% V was able to increase the yield strength by 55 MPa and sufficient to raise the yield strength of the as-annealed steel to 1 GPa.

While the thermomechanical process route was designed to resemble the production of DP steels with a CAL, it is also acknowledged that cold rolling after IA may not be compatible with a Continuous Galvanising Line (CGL) as the final cold rolling step will damage the Zn coating. Nevertheless, as medium Mn steels continue to gain industrial readiness, it is certain that a CGL will eventually be integrated into an optimised process route to produce high strength, high ductility galvanised sheet.

Figure 4.13 shows an updated figure from our previous work [98] which includes the investigated

0.06V steel, several new literature medium Mn steels and also two grades of Quenching and Partitioning (QP) steels from Baosteel. The alloying cost of novel and commercial steels were estimated based on pure metal and ferroalloy additions to steel scrap. It is acknowledged that other processing-related costs and factors also contribute to the total price of steel but it is still helpful for researchers to begin the alloy design process by attempting to minimise alloying cost. By reducing the Mn and V content from our previous alloy, the alloying cost was significantly reduced by 160 USD/tonne (prices correct as of May 2019) while maintaining a similar U30. The investigated steel in its annealed condition is price competitive with commercially available DP steels yet being two to three times more energy absorbing. When in the cold rolled condition (*i.e.* CR20), the U30 was significantly increased, presenting new opportunities for down gauging in automotive steel. This shows that a holistic alloy design concept can result in a price-competitive high strength and high energy absorbing steel.

4.6 Conclusions

The effects of cold rolling after IA were investigated in a novel steel and it was found that the tensile properties, especially the strain hardening rate, could be improved with increasing cold reduction. The microstructural evolution with increasing cold rolling reduction was investigated to understand the mechanisms behind the improvement in tensile properties. The key findings from this study are summarised as follows:

1. The microstructural evolution of deformation structures in medium Mn steels are strain path dependent. Cold rolled specimens showed higher twin densities and active secondary twin systems compared to limited twinning under uniaxial tension without prior cold rolling.

2. It is postulated that the defects introduced by cold rolling would promote the formation of fine-SIM which would lead to an increased strain hardening rate during uniaxial tension, *i.e.* an enhanced TRIP effect.

3. There is strong evidence that both TWIP and TRIP effects were occuring simultaneously during the deformation of the investigated steel, regardless of strain path.

4. By keeping the V content low (<0.2 wt%), the investigated steel is price competitive with many commercial steels but with a significantly greater energy absorption capability in terms of crush for automotive crash absorption applications.

4.7 Contribution statement

This chapter was adapted from a paper with contributions from several co-authors. In order of authorship on the paper:

TWJ Kwok - Conceptualisation, methodology, investigation, analysis, writing and visualisation.

P Gong - TEM, Nanomegas and analysis.

X Xu - Conceptualisation and supervision.

J Nutter - Nanomegas.

W M Rainforth - Proof reading.

D Dye - Conceptualisation, supervision.

Chapter 5

A Scale-up Study on Chemical Segregation and the Effects on Tensile Properties in Two Medium Mn Steel Castings

5.1 Abstract

Two ingots weighing 400 g and 5 kg with nominal compositions of Fe-8Mn-4Al-2Si-0.5C-0.07V-0.05Sn were produced to investigate the effect of processing variables on microstructure development. The larger casting has a cooling rate more representative of commercial production and provides an understanding of the potential challenges arising from casting-related segregation during efforts to scale up medium Mn steels, whilst the smaller casting has a high cooling rate and different segregation pattern. Sections from both ingots were homogenised at 1250 °C for various times to study the degree of chemical homogeneity and δ-ferrite dissolution. Within 2 h, the Mn segregation range (max $-$ min) decreased from 8.0 to 1.7 wt% in the 400 g ingot and from 6.2 to 1.5 wt% in the 5 kg ingot. Some δ-ferrite also remained untransformed after 2 h in both ingots but with the 5 kg ingot showing nearly three times more than the 400 g ingot. Micress modelling was carried out and good agreement was seen between predicted and measured segregation levels and distribution. After thermomechanical processing, it was found that the coarse untransformed δ-ferrite in the 5 kg ingot turned into coarse δ-ferrite stringers in the finished product, resulting in a slight decrease in yield strength. Nevertheless,

rolled strips from both ingots showed >900 MPa yield strength, >1100 MPa tensile strength and >40% elongation with <10% difference in strength and no change in ductility when compared to a fully homogenised sample.

5.2 Introduction

Medium Mn steels are an emerging class of steel which has shown great potential in energy absorbing applications. A medium Mn steel of composition Fe-10Mn-1.5Al-0.2Si-0.15C was developed as part of a 3rd Generation Advanced High Strength Steel (3GAHSS) development project by the U.S. Department of Energy. Termed as the "High Strength − Exceptional Ductility" steel, it had a tensile strength of 1200 MPa, elongation of 37% and could be used in the front or rear pillars of an automotive Body-In-White (BIW) to protect from front or rear impact [38].

The Mn content in these steels (4−12 wt%) is significantly lower than high Mn Twinning Induced Plasticity (TWIP) steels (16−30 wt%) and are therefore more attractive from an industrial perspective in terms of cost and ease of production. The high Mn content in TWIP steels posed many challenges to steelmakers during industrialisation efforts over the past two decades [**?**, 16]. Feasibility studies showed that Mn segregation in cast ingots led to edge cracking during hot rolling [16, 17]. It had been theorised that these problems may be avoided in medium Mn steels due to the lower Mn content. However, medium Mn steels are still relatively heavily alloyed compared to more lean steel grades such as Dual Phase (DP) steels and similar problems faced by TWIP steels may persist.

The first major problem is chemical microsegregation during casting [**?**, 64]. While the extent of segregation may not be as severe as in TWIP steels, the Mn content is still sufficiently high to be a concern. In a study on a Quenching and Partitioning (QP) steel of composition Fe-4.5Mn-1.5Si-0.3C, Hidalgo *et. al.* [135] showed that a segregation range of 2 wt% Mn resulted in different martensite fractions across the steel. This resulted in inhomogeneous strain gradients during tensile testing and premature failure. Liang *et. al.* [57] showed in another QP steel of composition Fe-3Mn-1.5Si-.25C that Mn segregation led to banding of alternate equiaxed (Mn rich) and lath (Mn depleted) type microstructures. The difference in austenite stability between grains with the two microstructures also led to strain inhomogeniety and poor ductility.

Tight composition control in medium Mn steels is important as slight variations in austenite composition may lead to different active deformation mechanisms, *i.e.* Transformation Induced Plasticity (TRIP), TWIP or TWIP+TRIP [98]. The TWIP+TRIP mechanism is usually sought after in medium Mn steels as it provides the optimal balance between strength and ductility. However, the composition window where the TWIP+TRIP mechanism is active is usually very narrow [19]. Nevertheless, Wang *et. al.* [35] showed that microsegregation in a fairly lean medium Mn steel could be avoided by twin roll casting. Their steel of composition Fe-4Mn-1.8Al-0.6Si-0.3C with a cast thickness of 2.5 mm did not show significant microsegregation and was also able to demonstrate the TWIP+TRIP effect after final processing.

The second problem is the retention of δ-ferrite to room temperature. δ-ferrite is the first phase to form during the solidification of medium Mn steels but is expected to transform to austenite at typical hot rolling and slab reheat temperatures ($<$ 1280 °C) [78, 133]. However, δ-ferrite can be stabilised to room temperature when there are excess Al or Si additions [**?**, 36]. The effect of delta ferrite varies depending on the alloy composition and desired mechanical properties. Some researchers do not consider δ-ferrite to be a problem as it does not appear to have adverse effects on tensile properties in certain alloys and may even be beneficial to ductility [**?**, 90]. However, δ-ferrite is usually not beneficial from a strength perspective as it is difficult to refine the grain size of δ-ferrite and is therefore typically weaker than the much finer austenite and α-ferrite matrix [36, 192]. When deformed to large strains, the plasticity mismatch between δ-ferrite grains and the matrix may cause interface cracking which might result in premature failure [89]. Mn segregation at the δ-ferrite interface has also been shown to reduce impact properties in medium Mn steels [88]. It is therefore important that alloy development efforts consider the size, morphology and distribution of δ-ferrite in medium Mn steels and how these factors may change during a transition from lab scale to full scale production material.

Building upon previous work on a 8 wt% Mn medium Mn steel [37], this study aims to elucidate some of the problems which may be encountered during scale up of medium Mn steels from small scale to larger scale melts with cooling rates more representative of industrial practices. In this study, two laboratory castings of different sizes and therefore different Secondary Dendrite Arm Spacings (SDAS) were produced in order to study the effect of chemical microsegregation, homogenisation duration and δ-ferrite transformation on tensile properties. It is hoped that the models developed will aid in the future development and scale up of medium Mn steels.

5.3 Experimental

Two ingots weighing 400 g (60 × 23 × 23 mm) and 5 kg (250 × 70 × 30 mm) with nominal composition Fe-8Mn-4Al-2Si-0.5C-0.07V-0.05Sn were cast using vacuum arc melting and Vacuum Induction Melting

(VIM) respectively. The choice of elements and alloying concept was described in a previous paper [37]. The 400 g ingot was prepared using pure elements and solidified in a copper mould, while the 5 kg ingot was prepared using ferroalloys and solidified in a mild steel mould. A full description of the ferroalloy compositions can be found in a previous paper [223]. The cooling rate of the 400 g ingot copper mould was estimated to be approximately 200 °C s^{-1} as given from the manufacturer (Arcast), while the cooling rate of the 5 kg mild steel mould was determined to be approximately 0.5 °C s^{-1} from previous work on DP steels [223].

Bars with dimensions 40 mm × 10 mm × 10 mm were cut *via* Electric Discharge Machining (EDM) from each ingot, quartz encapsulated and homogenised at 1250 °C for 2 h before water quenching. The bars were then hot rolled to approximately 1.5 mm in 6 passes between 1000 °C and 850 °C. The hot rolled strips were immediately water quenched after rolling and Intercritically Annealed (IA) at 750 °C for 5 min.

Tensile samples with gauge dimensions of 19 × 1.5 × 1.5 mm were cut *via* EDM with the tensile direction parallel to the rolling direction. Tensile testing was conducted at a nominal strain rate of 10^{-3} s^{-1}. Strain was measured with an extensometer from 0 to 10% engineering strain and calculated from the crosshead displacement thereafter.

Samples for microscopy were mechanically ground and polished with OP-U. Nital etchant (2% nitric acid, 98% ethanol) was used for etched samples. Scanning electron microscopy (SEM), Electron Backscatter Diffraction (EBSD) and Energy Dispersive Spectroscopy (EDS) were performed on a Zeiss-Sigma FE-SEM equipped with Bruker EBSD and XFlash 6160 EDS detectors. Image analysis was conducted using ImageJ software.

SEM-EDS grid scans were obtained over an area of 0.25 mm^2 in order to quantify the degree of segregation between the as-cast and homogenised states. 120 and 160 points in a rectangular grid were collected in the 400 g and 5 kg ingot respectively. The compositional measurements were processed according to the Weighted Interval Rank Sort (WIRS) method described by Ganesan *et. al.* [224]. The WIRS method was chosen as it was able to distinguish scatter from real element segregation trends. It first assigns a weighted value to each measurement based on the range, associated uncertainty and segregation direction of the measured element. The weighted value takes on a value between 0 and 1, where 0 represents the dendrite core and 1 represents the interdendritic region. The individual measurements are then ranked and sorted according to their weighted values.

Phase field modelling simulations were carried out using Micress 6.4 coupled with the Thermo-Calc TCFE9 and MOBFE3 databases. The model was generated using a 100×200 cell field with a scale of 1

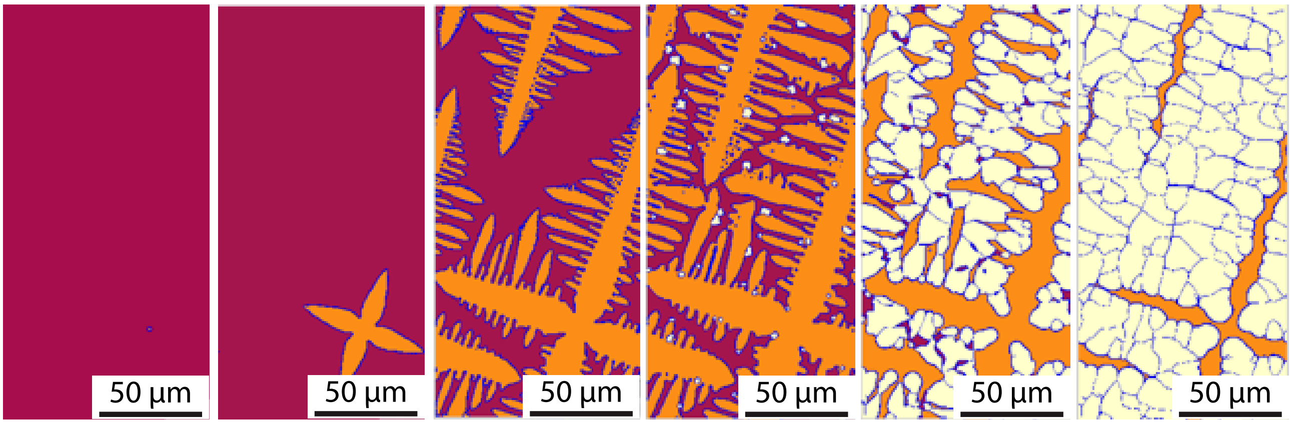

Figure 5.1: Solidification sequence as simulmated with Micress 6.4 and Thermo-Calc TCFE9 and MOBFE3 databases. Red – liquid, orange – δ-ferrite, white – austenite.

μm per pixel, using an initial condition of 1530 °C with a single seed of delta ferrite in a liquid matrix. The seed was assigned a random location and orientation. The system was then allowed to cool at specified cooling rates of 0.5, 2, 50 and 200 °C s^{-1}, with no thermal gradient applied. These cooling rates were chosen to represent the range of solidification rates seen in different casting techniques from continuous casting, 0.6 °C s^{-1}, to lab based arc melting, 200 °C s^{-1}.

Relinearisation of the phase diagram was applied every 5 °C to help resolve the solute build-up at the liquid/solid interface. A nucleation condition of the FCC structure was allowed on the BCC/liquid interface at temperature below that of the equilibrium peritectic temperature (1380 °C). The model implements a periodic/wrap around symmetry and as such any features that extend out of the right side of the image will appear from the left (the same is true in the vertical axis). Finally, a time step of 0.1/cooling rate was applied to ensure sufficient resolution at all cooling rates. A typical solidification sequence can be seen in Figure 5.1.

After conducting the solidification sequence, the output was then reapplied to Micress to apply a heat treatment. A constant temperature of 1250 °C and simulations of up to 4 hours were applied. Finally, the final phase balance and compositional distribution were exported.

5.4 Results and discussion

5.4.1 As-cast and homogenised microstructure

The bulk composition of the two ingots were measured using Inductively Coupled Plasma (ICP) and Inert Gas Fusion (IGF) and the results are shown in Table 5.1. The 400 g ingot showed a slightly lower Mn content due to the high heat input from the arc melting process, leading to excessive Mn

Table 5.1: Nominal and measured composition of the two ingots in mass percent. Compositions measured by ICP, except for elements marked by † which were measured by IGF.

	Mn	Al	Si	C†	V	Sn	N†	P	S†
Nom.	8.0	4.0	2.0	0.5	0.07	0.05	–	–	–
400 g	7.77	3.71	1.81	0.49	0.08	0.05	0.004	0.006	0.002
5 kg	8.12	3.46	1.98	0.46	0.09	0.05	0.004	0.026	0.005

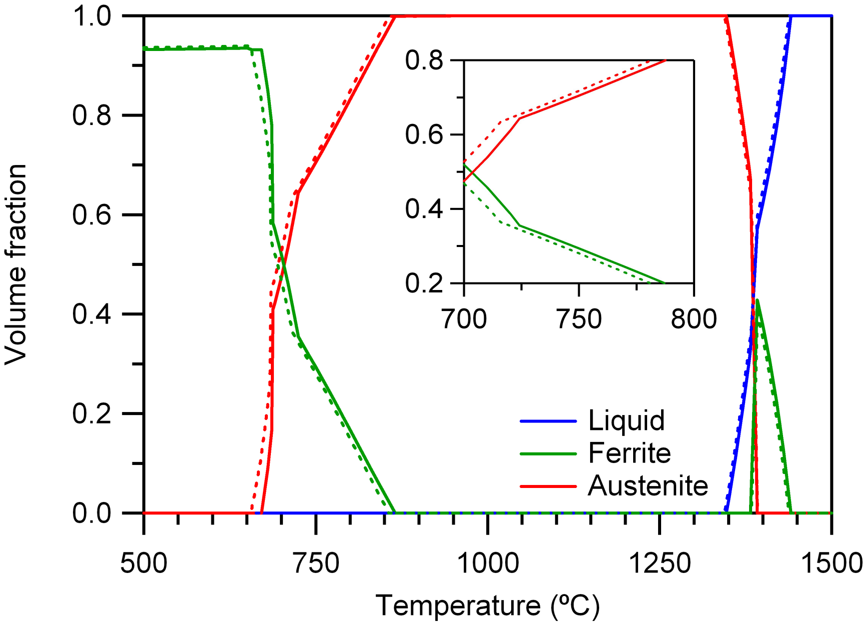

Figure 5.2: Thermo-Calc property diagram of the 400 g and 5 kg casting compositions as shown in Table 5.1 using the TCFE7 database. Only liquid, ferrite and austenite phases are shown for the sake of clarity. Solid lines – 400 g ingot, dashed lines – 5 kg ingot. Inset: magnified view of the property diagram at around 750 °C.

vapourisation. Apart from Mn, all other elements were comparable and within acceptable tolerances.

Figure 5.2 shows the property diagram of the 400 g and 5 kg steel compositions as simulated by Thermo-Calc using the TCFE7 database. Thermo-Calc is often used during the alloy design stage to give an indication of phase fractions and approximate compositions of each phase, especially within the intercritical temperature regime. In most medium Mn steels in the literature, the phases and compositions obtained during intercritical annealing are retained to room temperature [37,105,225,226]. From Figure 5.2, it can be seen that the slight differences in composition between the 400 g and 5 kg ingot did not result in a significant change in the expected phase fractions at the chosen IA temperature of 750 °C. Thermo-Calc also predicted that δ-ferrite should not be expected below 1370 °C but it was clearly observed in the as-cast micrographs of both 400 g and 5 kg ingots in Figure 5.3. From Figure 5.3, the as-cast micrographs showed δ-ferrite dendrite cores and an austenite/martensite matrix. The average SDAS was determined by measuring the number of secondary arms along several

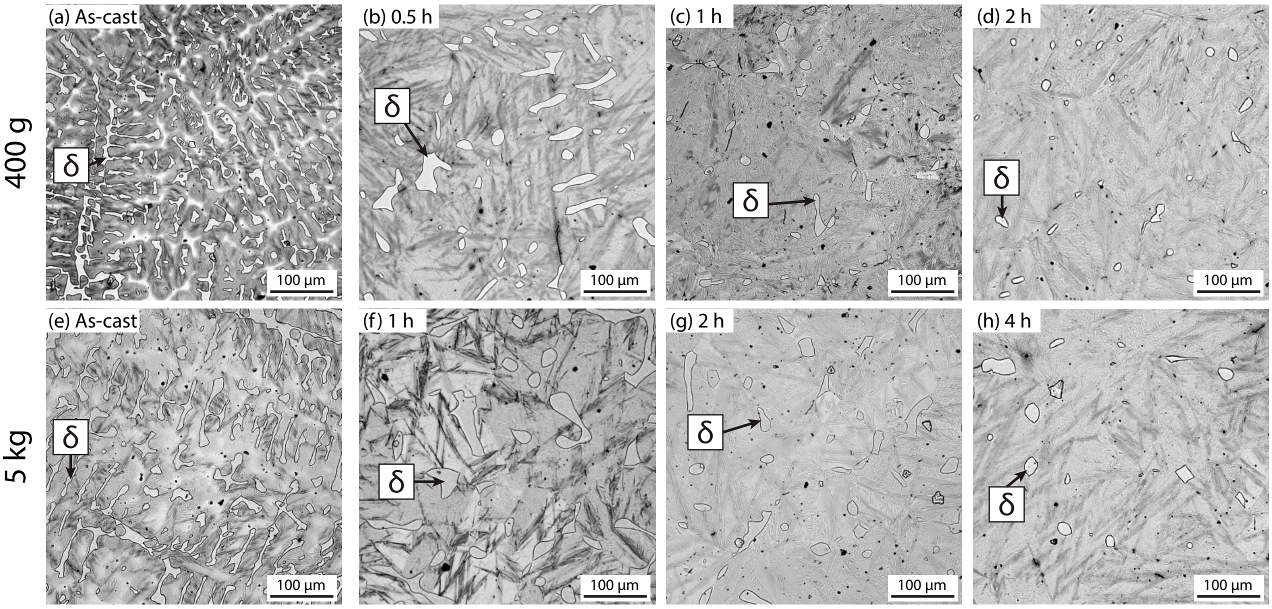

Figure 5.3: Optical micrographs of the 400 g ingot homogenised at 1250 °C for (a) 0 h, *i.e.* as-cast, (b) 0.5 h, (c) 1 h, (d) 2 h and of the 5 kg ingot homogenised at 1250 °C for (e) 0 h, *i.e.* as-cast, (f) 1 h, (g) 2 h, (h) 4 h. The microstructures all consist of δ-ferrite grains in a γ/α' matrix.

primary dendrite arms (method D by Vandersluis *et. al.* [227]) and found to be 19 ± 5 μm in the 400 g ingot and 29 ± 4 μm in the 5 kg ingot. During homogenisation, δ-ferrite was observed to spheroidise before shrinking in area. After 2 h, the δ-ferrite grains in the 400 g ingot were much smaller in size, approximately 20−25 μm wide, while the δ-ferrite grains in the 5 kg ingot were slightly larger, approximately 30−40 μm wide.

The observed microstructures were in good agreement with the Micress modelling for the two cooling rates as shown in Figure 5.4 where the size and distribution of the δ-ferrite was clearly dependent on the solidification rate. In the model, the spheroidisation of the δ-ferrite can be seen to occur during the homogenisation heat treatment with the 0.5 °C s^{-1} cooling rate showing much coarser globular δ-ferrite after 2 h.

The experimentally observed δ-ferrite area fraction as a function of homogenisation time is shown in Figure 5.5a. In the as-cast condition, both ingots had an approximate δ-ferrite area fraction of 0.25, regardless of SDAS. Within 2 h of homogenisation, which is a typical duration in an industrial reheating furnace, the area fraction decreased to 0.02 and 0.07 in the 400 g and 5 kg ingot respectively. When δ-ferrite area fraction was plotted as a function of the square root of homogenisation time, the decrease in δ-ferrite exhibits a linear trend. This suggests that the transformation of δ-ferrite to austenite at 1250 °C is a diffusion-limited process where the mean diffusion distance, x, in one dimension may be approximated as:

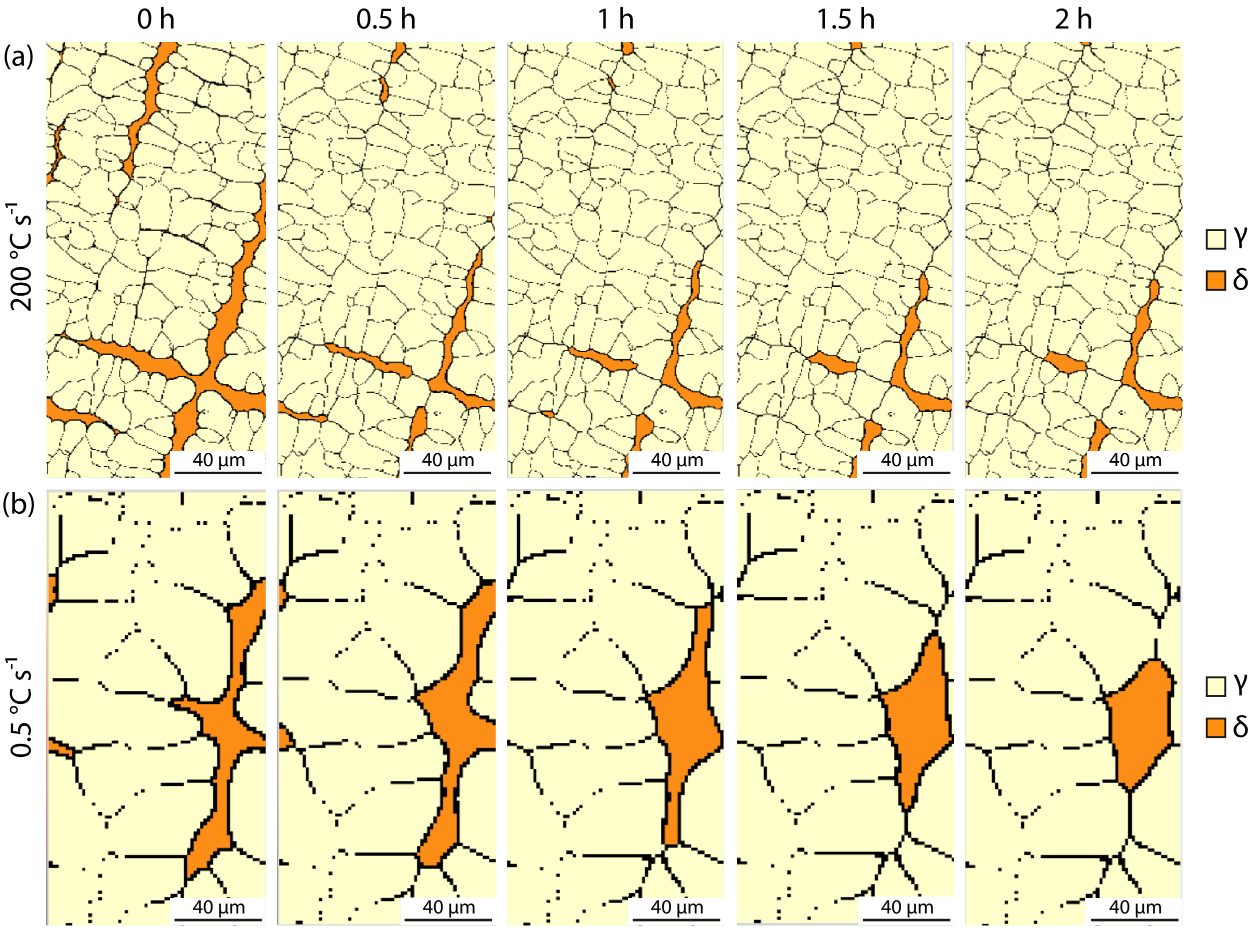

Figure 5.4: Micress simulation of the microstructure evolution during the homogenisation heat treatment at 1250 °C. Initial cast microstructures were formed from cooling rates of (a) 200 °C s^{-1}, representative of the 400 g ingot and (b) 0.5 °C s^{-1}, representative of the 5 kg ingot.

$$x \approx \sqrt{Dt} \tag{5.1}$$

where D is the diffusion coefficient and t is the time for diffusion.

When comparing the experimental results with the model (Figure 5.5b), a very good agreement can be observed. The model accurately predicts that the initial δ-ferrite fraction would be similar, regardless of cooling rate. However, it predicts a slightly lower initial area fraction than what was experimentally observed. Nevertheless, the model was able to show how the rate of δ-ferrite dissolution increases at higher cooling rates due to the much finer SDAS and therefore shorter diffusion distance. This highlights the need for full scale prototyping as small scale laboratory productions may under-predict the time necessary for homogenisation.

It is noteworthy that the model showed that the rate of homogenisation, *i.e.* δ-ferrite reduction, slows significantly at long durations ($>$ 2 h). However, it was observed experimentally that while the rate of homogenisation slowed, it was not as severe as the prediction. This was likely due to a limitation of the model being 2D and not 3D, giving one less degree of freedom for diffusion. While the impact of one less degree of freedom is negligible at short durations (< 2 h), the difference becomes more significant at longer durations.

5.4.2 Chemical segregation

Correlative EBSD and EDS maps (Figure 5.6) of the as-cast and 2 h homogenised conditions of both ingots were collected for the major alloying elements: Mn, Al and Si. In the as-cast condition of both ingots, a significant fraction of austenite was present at room temperature in the form of both untransformed and retained austenite, shown in Figures 5.6a and 5.6i. Both δ-ferrite and martensite which indexed as BCC phases were not as easily distinguished in the EBSD phase maps. However, the three phases can be identified with certainty from the EDS Mn maps (Figures 5.6b and 5.6j) which showed three distinct regions with low, medium and high concentrations of Mn. The low, medium and high Mn regions correlate with δ-ferrite, martensite/austenite and retained austenite regions respectively. Mn was therefore observed to segregate strongly to the interdendritic regions. Al similarly showed three distinct regions but with the opposite segregation direction. The high, medium and low Al regions correlated with the δ-ferrite, martensite/austenite and retained austenite regions respectively (Figures 5.6c and 5.6k). In the as-cast 400 g ingot, Si also showed three distinct regions but only the high Si regions correlated with the interdendritic regions, suggesting that Si segregates to the interdendritic region (Figure 5.6d). However, in the as-cast 5 kg ingot, Si appeared to segregate to both δ-ferrite and the interdendritic region (Figure 5.6l). The difference in Si partitioning may be due to the difference in cooling rate. At fast cooling rates observed in the 400 g ingot, Si partitions to the interdendritic region, but at slower cooling rates observed in the 5 kg ingot, there would have been sufficient time for back diffusion of Si to the δ-ferrite grains.

After 2 h, δ-ferrite was still present and easily identified as the Mn depleted regions in the EDS-Mn maps (Figures 5.6f and 5.6n). The Mn concentration of the matrix in both ingots now appear to be homogenous. The Al (Figures 5.6g and 5.6o) and Si (Figures 5.6h and 5.6p) EDS maps show that that δ-ferrite was slightly enriched in Al and Si while the matrix was homogeneous. It should also be mentioned that several alumina and silica inclusions were present in both 400 g and 5 kg ingots in the as-cast and 2 h homogenised conditions.

A more quantitative WIRS plot from EDS gridscans of the same areas in Figure 5.6 is shown in Figure 5.7. In the as-cast condition of both ingots, Mn was found to have the highest level of

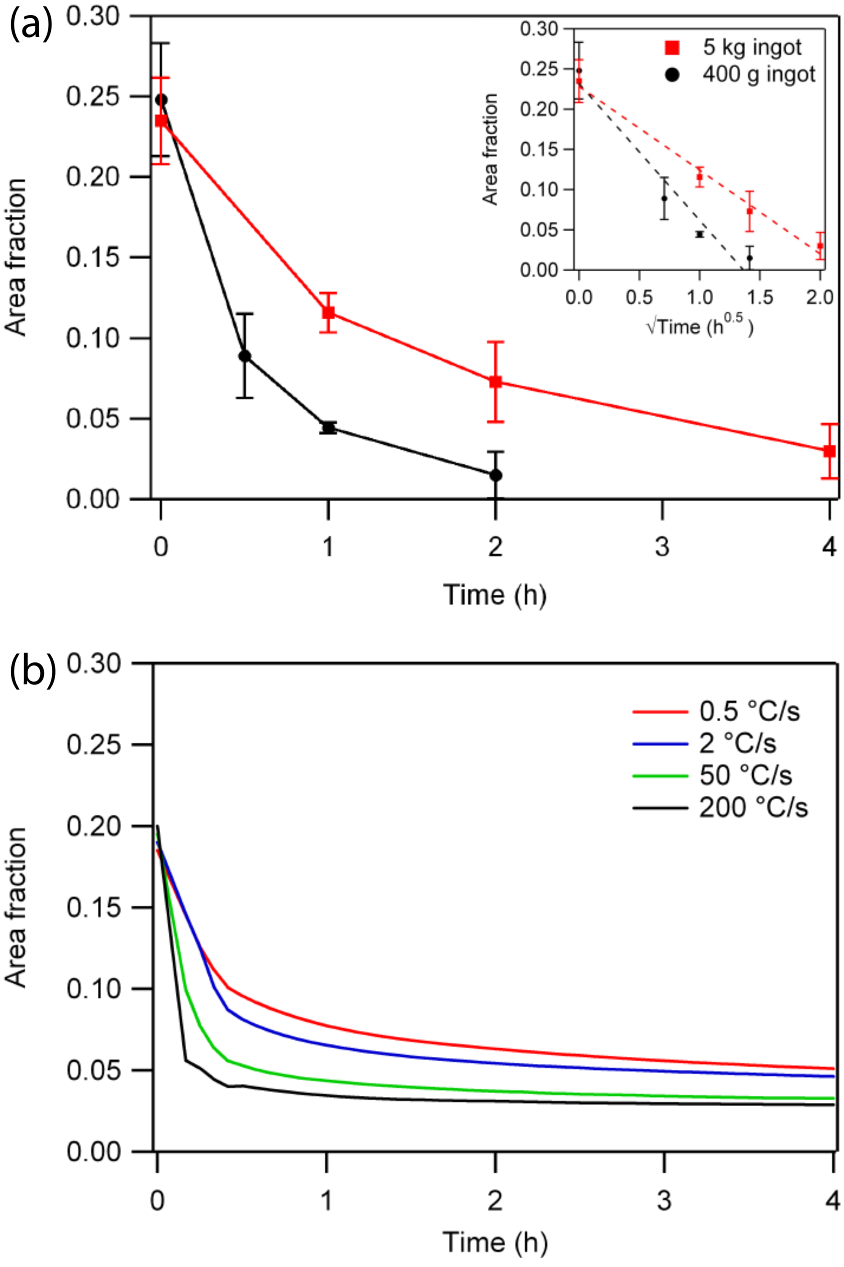

Figure 5.5: (a) Change in area fraction of δ-ferrite with homogenisation time at 1250 °C and replot as a function of the square root of time in the inset. (b) Micress simulation of the change in δ-ferrite fraction with homogenisation time at 1250 °C from ingots cast with different cooling rates..

segregation. As observed in the EDS map, Mn was found to segregate strongly to the interdendritic regions (*i.e.* high solid fraction). The degree of Mn segregation was greater in the 400 g ingot and the maximum Mn content reached as high as 14 wt%. This effect is consistent with the faster cooling rate in the 400 g ingot and therefore less time for back diffusion. At low solid fractions, a lower shelf of Mn can be observed which can be attributed to δ-ferrite.

The lower Mn shelf in both as-cast ingots corresponded with a slight increase in Al concentration confirming that Al segregates to δ-ferrite during solidification. Si did not segregate strongly in both

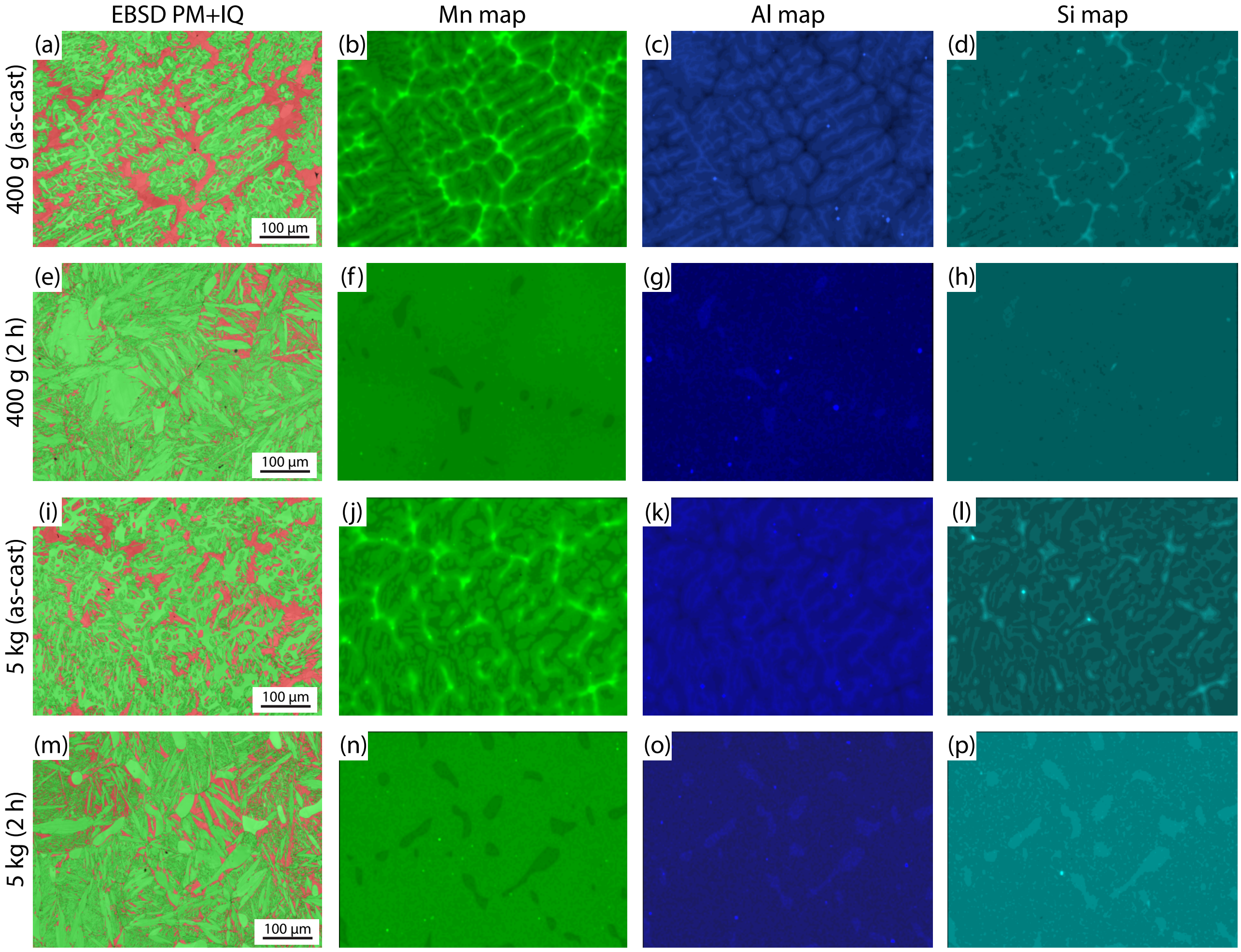

Figure 5.6: From left to right columns: EBSD phase maps and image quality (green – BCC, red – FCC), EDS-Mn, EDS-Al and EDS-Si maps of the as-cast 400 g ingot (a-d), 2 h homogenised 400g ingot (e-h), as-cast 5 kg ingot (i-l) and 2 h homogenised 5 kg ingot (m-p). For EDS maps, a brighter colour indicates a higher concentration and a darker colour indicates a lower concentration.

ingots except in the 400 g ingot where there was a slight increase in Si at the interdendritic regions.

After a 2 h homogenisation heat treatment, the Mn segregation at the interdendritic regions was mostly eliminated in both ingots. However, the lower Mn shelf was still present which corresponds to the remaining δ-ferrite. Segregation of Al and Si at the interdendritic regions were also mostly eliminated and remained fairly constant throughout the matrix.

Good agreement between modelling and experimental can be seen in Figure 5.8 where the δ-ferrite can be seen to have a similar Mn content of approximately 6 wt%. Very quickly during the homogenisation process, the Mn rich regions began to homogenise, particularly in the 400 g ingot, eliminating the smaller secondary and tertiary dendrite arms.

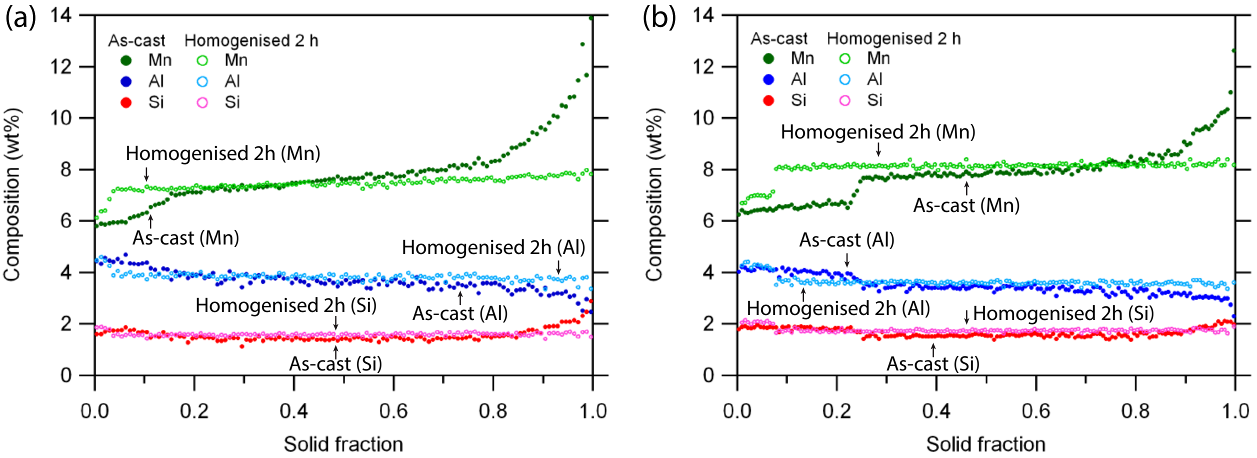

Figure 5.7: WIRS plots of the as-cast and 2 h homogenised conditions of (a) 400 g and (b) 5 kg ingots. A solid fraction of 0 represents the dendritic core regions and a solid fraction of 1 represents the interdendritic regions.

5.4.3 Tensile properties and rolled microstructure

Tensile samples were obtained from rolled and IA strips after homogenising a bar from the 400 g and 5 kg ingot for 2 h at 1250 °C, hereby known as 400 g (2 h) and 5 kg (2 h). The tensile curves are shown in Figure 5.9 together with a tensile curve obtained from previous work on a fully homogenised sample [37]. The fully homogenised sample, hereby known as 400 g (24 h), was produced using the same thermomechanical processing steps but from a 400 g ingot which was homogenised for 24 h. A summary of the tensile properties is shown in Table 5.2.

It is acknowedged that the use of sub-sized tensile samples might introduce geometry-related errors in the measured tensile properties. Unfortunately, due to the load capacity of the laboratory rolling mill, it is not possible to roll a larger bar to obtain larger tensile samples. Nevertheless, it has been shown that the yield strength, tensile strength and uniform elongation are largely independent of sample geometry [199]. Since none of the tensile samples showed any post uniform elongation in Figure 5.9, it is likely that the tensile properties in the sub-sized tensile samples will be similar to a full sized sample.

From Figure 5.9, the tensile samples from the 400 g ingots showed very similar strengths. The 400 g (24 h) sample was slightly stronger but the 400 g (2 h) sample was more ductile. The 5 kg (2 h) tensile sample was 87 MPa lower in yield strength compared to the 400 g (24 h) sample but also had slightly more ductility. All three tensile samples showed nearly identical strain hardening behaviour, strongly indicating that the TWIP+TRIP deformation mechanism was active in a similar manner across the three tensile samples in spite of the slight difference in Mn as shown in Table 5.1.

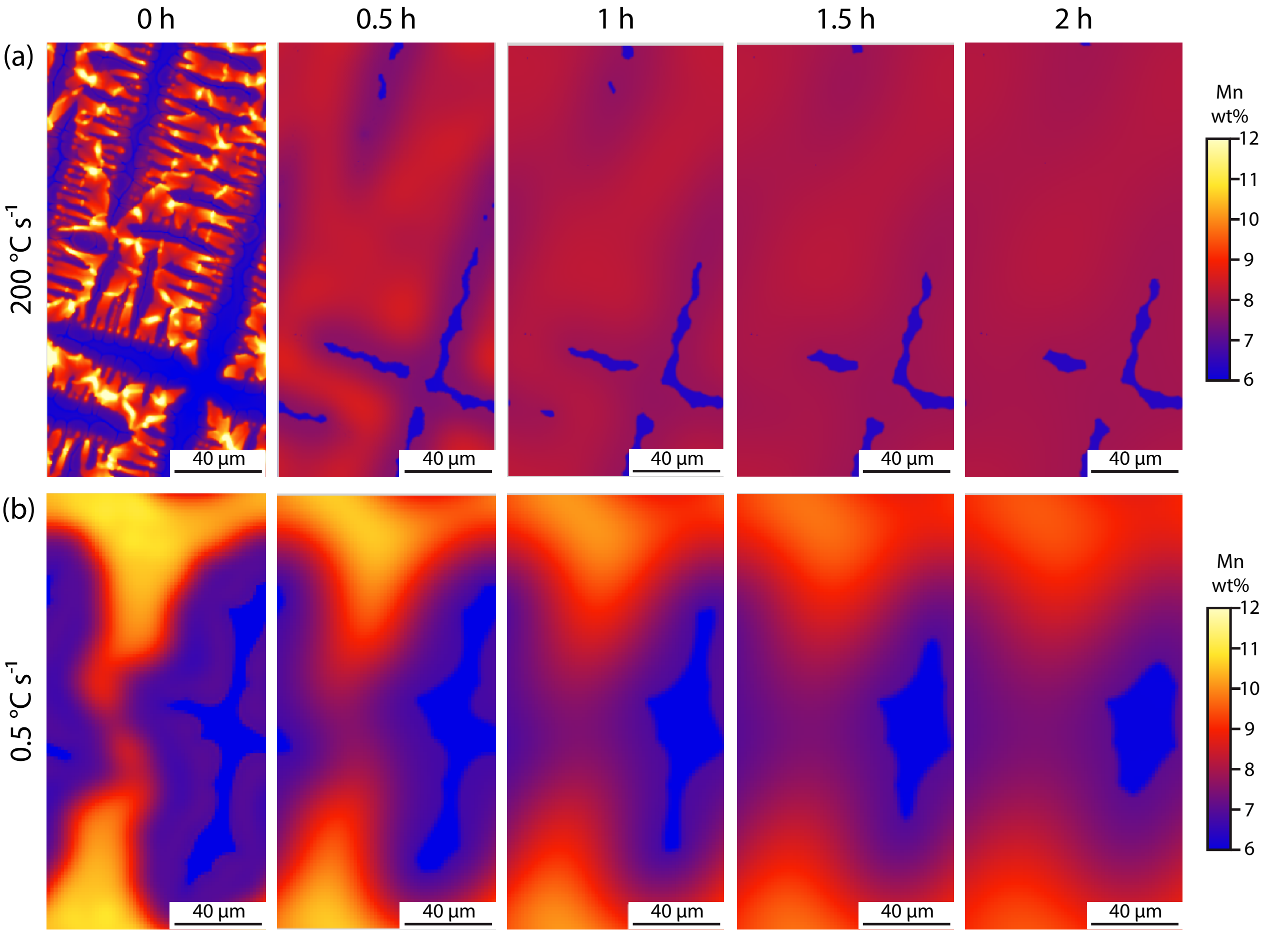

Figure 5.8: Micress segregation simulation during the homogenisation heat treatment at 1250 °C. Initial cast microstructures were formed from cooling rates of (a) 200 $^{\circ}\mathrm{s}^{-1}$, representative of the 400 g ingot and (b) 0.5 $^{\circ}\mathrm{s}^{-1}$, representative of the 5 kg ingot.

The rolled and IA microstructures of the three tensile samples are shown in Figure 5.10 and the phase fractions are shown in Table 5.3. The fully homogenised 400 g (24 h) sample (Figure 5.10c) showed fine equiaxed ferrite grains, located predominantly along the austenite grain boundaries. This accurately reflects the process route where the steel was first rolled in a temperature regime where the steel was fully austenitic and the ferrite grains were newly formed α-ferrite grains which nucleated during the final passes and the intercritical annealing heat treatment. By comparison, the 5 kg (2 h) sample showed the presence of large elongated ferrite grains which are most likely δ-ferrite stringers, consistent with the large globular δ-ferrite grains after homogenisation which became elongated during rolling. The 400 g (2 h) sample also showed the presence of δ-ferrite stringers but were shorter compared to the 5 kg (2 h) sample due to the smaller globular δ-ferrite size before hot rolling. Fine ferrite grains were also observed in the partially homogenised samples which are likely to be α-ferrite which formed in the same way as the 400 g (24 h) sample.

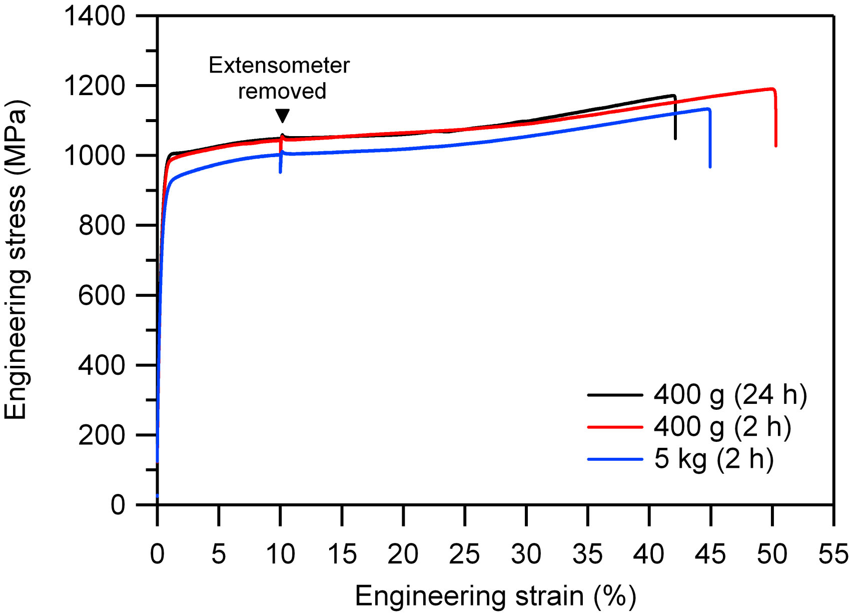

Figure 5.9: Tensile behaviour of the partially and fully homogenised rolled and IA samples.

Table 5.2: Tensile properties of the rolled strips.

	E (GPa)	σ_y (MPa)	σ_{UTS} (MPa)	ϵ (%)
400 g (24 h)	166	1005	1170	42
400 g (2 h)	175	985	1189	50
5 kg (2 h)	156	918	1133	45

The δ-ferrite fraction after rolling can be estimated by subtracting the amount of newly formed α-ferrite of the 400 g (24 h) sample from the total ferrite fraction of the 5 kg (2 h) and 400 g (2 h) rolled strips. This results in a δ-ferrite fraction of 7.2% and 4.4% respectively, which is in close agreement with the δ-ferrite fraction after the 2 h homogenisation heat treatment (Figure 5.5a) of 6.5% and 3.5% shown both experimentally and through modelling. This also shows that any remaining δ-ferrite after homogenisation will be retained to room temperature even after hot rolling.

The volume fraction and distribution of δ-ferrite can be seen to have a significant impact on tensile performance with an 87 MPa drop in yield strength when comparing the 400 g (24 h) and 5 kg (2 h) tensile sample. This phenomenon is common in dual phase steels where the spatial distribution of the second phase, such as band spacing, has been shown to have a noticeable impact on tensile performance [228]. In this medium Mn steel, the stability of δ-ferrite phase was shown to be a function of the SDAS which is determined by the casting conditions. Consequently, the size and distribution of δ-ferrite in the final microstructure would be determined by both casting condition and rolling reduction. Therefore, a finer SDAS from the cast condition will give a lower δ-ferrite fraction with a

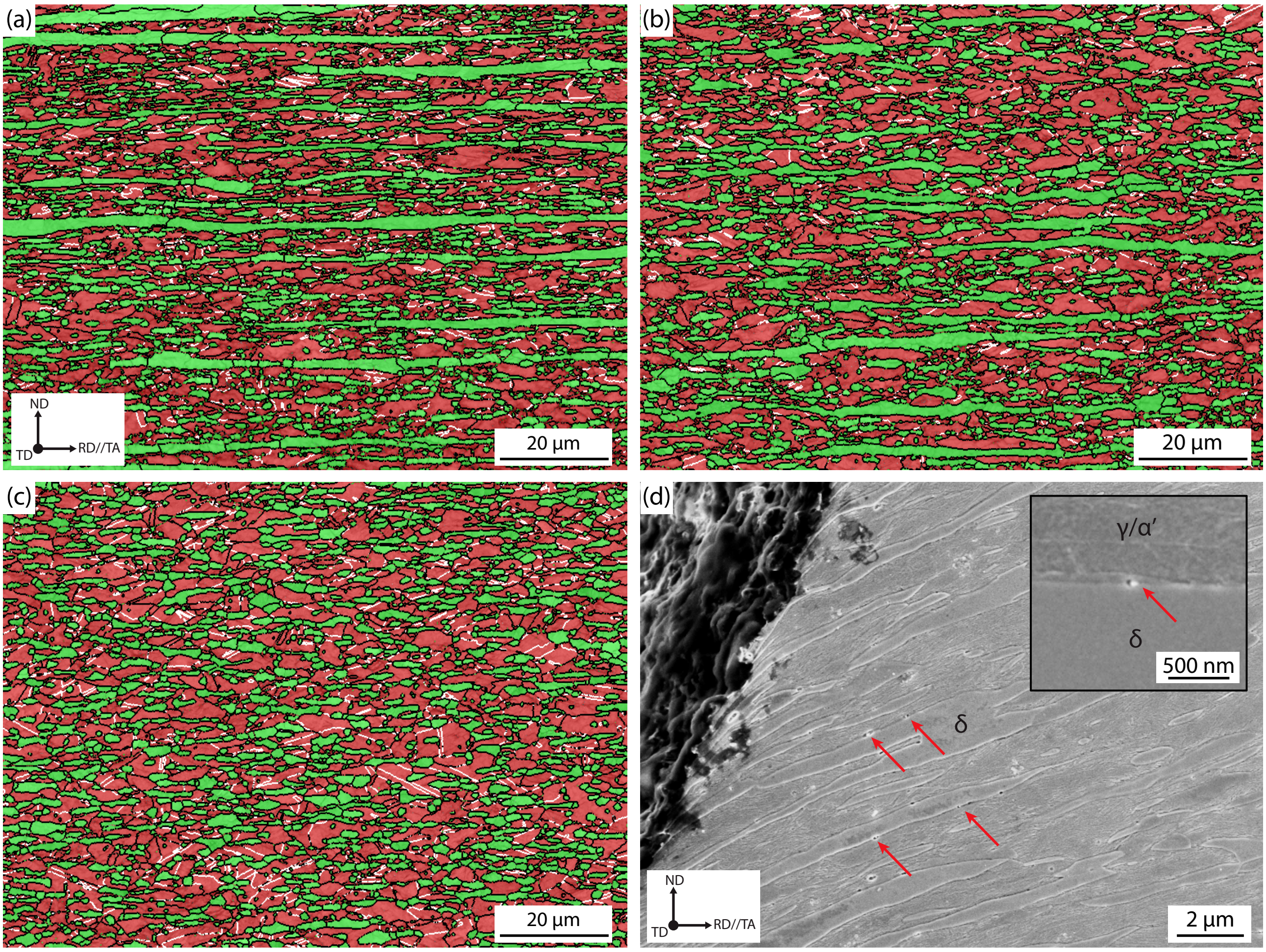

Figure 5.10: EBSD image quality and phase maps of the rolled and intercritically annealed strips from the (a) 5 kg (2 h) ingot, (b) 400 g (2 h) ingot and (c) 400 g (24 h) ingot. Red - austenite, green - ferrite. Black lines indicate grain boundaries and white lines indicate austenite Σ3 boundaries. (d) Secondary electron micrograph of a sheared edge along the fractured surface of the 5 kg (2 h) tensile specimen. Red arrows point to several nanoscale precipitates inside a void along interphase boundaries. Inset: magnified view of a precipitate along a δ-ferrite stringer.

finer band spacing and result in a stronger steel.

The relationship between casting condition and grain size distribution in the rolled strips can be seen in the Cumulative Distribution Function (CDF) plots in Figure 5.11 . Grain size was determined as the equivalent circle diameter from the EBSD data in Figure 5.10 but excluding grains which intersect the micrograph boundary. δ-ferrite grains were also excluded by first determining the percentage of δ-ferrite grains out of the total ferrite grains in Table 5.3, *i.e.* 16% and 11% of ferrite grains in the 5 kg (2 h) and 400 g (2 h) samples respectively. The ferrite grains were then sorted in decreasing size and the largest 16% and 11% of the ferrite grains were assumed to be δ-ferrite and excluded since δ-ferrite grains were consistently larger than α-ferrite grains. From Figure 5.11a, the austenite grain size CDFs were very similar. However, there was some spread in the α-ferrite grains size CDFs between the three

Table 5.3: EBSD phase fractions in % and area weighted average grain size in μm of the rolled strips as determined by the Bruker ESPRIT software. N.I. − Non indexed fraction.

	γ	α	N.I.	d_γ	d_α
5 kg (2 h)	54.3	44.1	1.6	3.6	4.0
400 g (2 h)	57.4	41.3	1.3	3.7	3.9
400 g (24 h)	62.4	36.9	0.7	3.4	2.4

rolled strips. It is noteworthy that the average α-ferrite grain size decreases slightly with increasing δ-ferrite fraction. This effect may be attributed to a lower driving force for α-ferrite grain growth during IA due to pre-existing δ-ferrite grains. Nevertheless, Figure 5.11 shows that the grain size CDFs, especially of the austenite phase, are largely independent of casting condition and δ-ferrite fraction.

From Figure 5.9, the three rolled strips had nearly identical strain hardening behaviour regardless of casting condition or δ-ferrite fraction. Since the austenite phase in all three strips had a similar grain size distribution (Figure 5.11a), this then strongly implies that the austenite phase across all three samples should have the composition, *i.e.* same Stacking Fault Energy (SFE) and stability (Md_{30}). However, the austenite phase fraction was not constant across all three samples (Table 5.3), suggesting that the composition of the austenite could not have been identical under normal circumstances. Of the alloying additions in medium Mn steel, C is able to significantly alter the SFE and Md_{30} of austenite, even in small concentrations [36, 37, 196]. Therefore, in order for the austenite phase in the partially homogenised samples to maintain the same C content as the fully homogenised sample while having a lower austenite fraction, it was likely that the excess C in the partially homogenised samples precipitated in the form of carbides along the δ-ferrite interphase boundaries (Figure 5.10d). This phenomena was not observed in the 400 g (24 h) sample where there was no δ-ferrite. The build up of C at δ-ferrite interphase grain boundaries was also observed by other researchers [88, 89].

From the post mortem 5 kg (2 h) tensile sample in Figure 5.10d, the fracture edge was observed to have sheared across the entire microstructure. Brittle transverse cleavage of δ-ferrite grains was not observed near the fracture edge nor in the gauge. Near the fracture edge, voids grew around the δ-ferrite interphase carbides but the voids remained very small and were not deemed to be a cause of fracture. Since the tensile samples which contained δ-ferrite had slightly better elongation than the 400 g (24 h) sample, it was therefore unlikely that δ-ferrite, at low fractions, would have a detrimental effect on elongation.

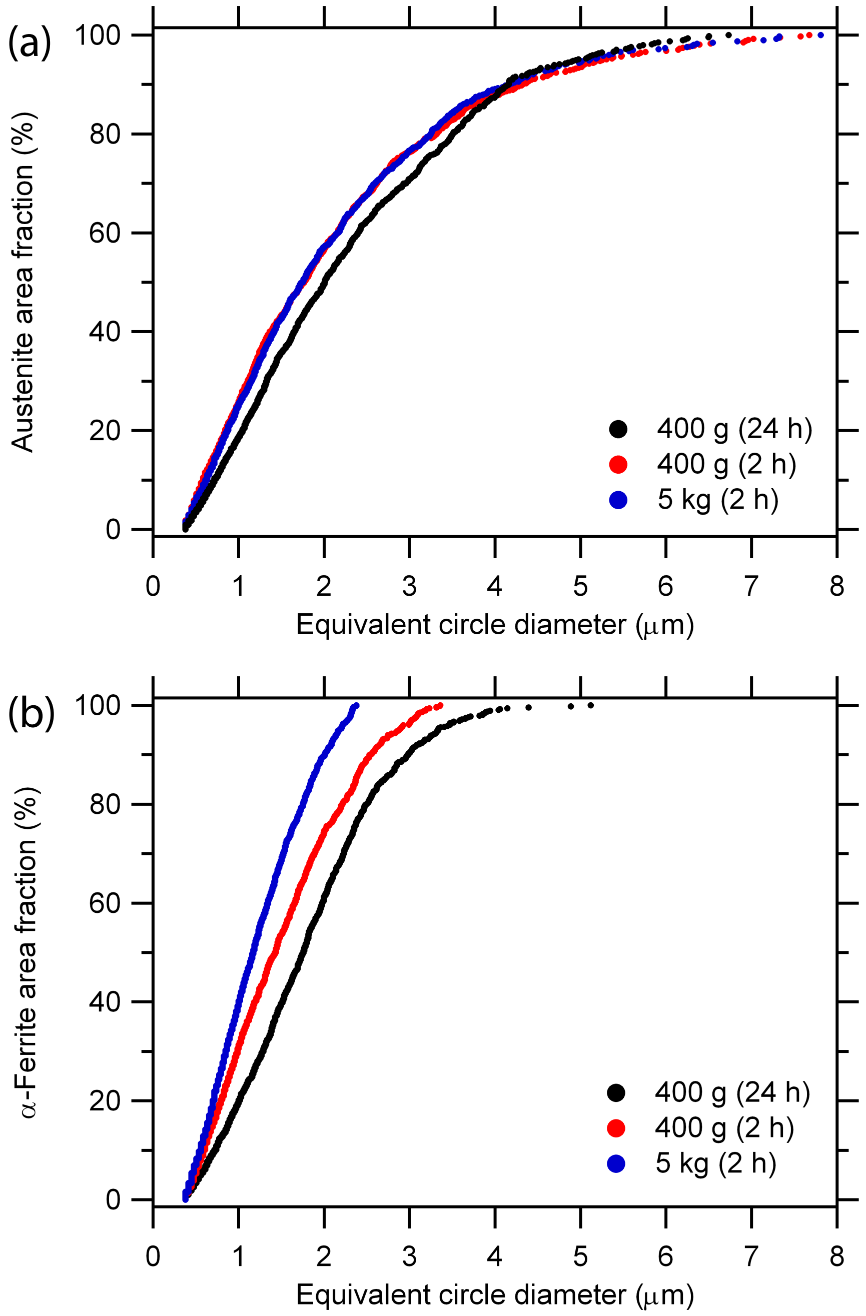

Figure 5.11: Cumulative distribution function of (a) austenite and (b) α-ferrite grain sizes across the three rolled strips.

5.4.4 Industrial relevance

It has often been assumed but not studied in detail that medium Mn steels should be less prone to chemical segregation as compared to high Mn TWIP steels [15, 229] on the basis of a significantly lower Mn content. While this was shown to be true in this study, the nature of segregation is also dependent on the process in which it was cast or produced. Since segregation is known to have a noticeable impact in medium and high Mn steels, the industrial production scale cast structure would

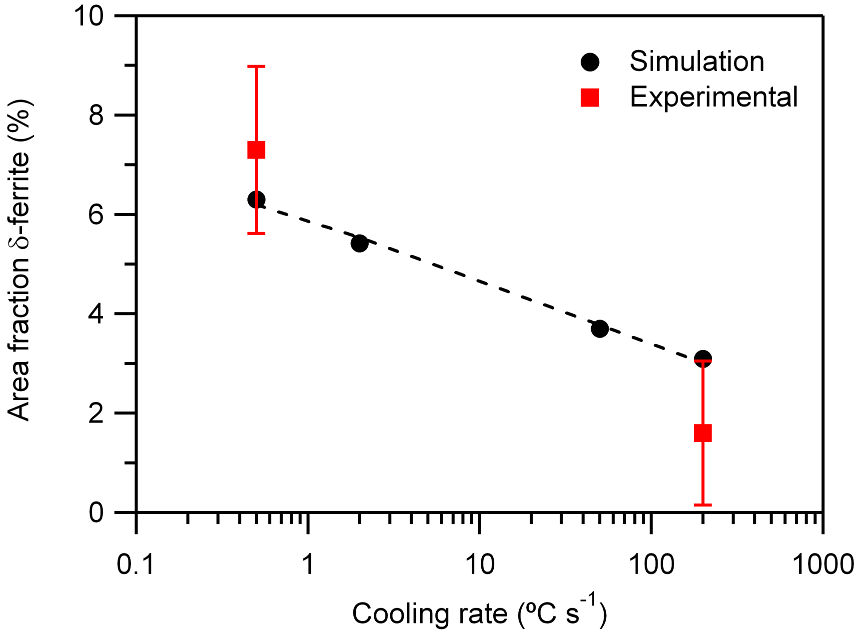

Figure 5.12: Variation of δ-ferrite after 2 h homogenisation at 1250 °C with cooling rate.

have to be replicated at a laboratory scale for a true assessment of its real-world applicability.

Two aspects of commercial production make lab scale feasibility trials difficult. Firstly, the level of rolling reduction. Commercial products are typically rolled from approximately 230 mm thick slab to 1 mm thick strip product, a reduction by more than 200 times which is difficult to attain in a lab. Secondly, the degree of chemical segregation in industrial sized slabs and the consequent effects on subsequent mechanical properties cannot be replicated through fast cooling laboratory small scale methods.

From Table 5.3 and Figure 5.11, it is evident that the scale of production has little impact on the final grain size and distribution, and as such, further rolling reduction during commercial production is not likely to refine this much more. However, this work has shown that there is a strong dependency on the casting parameters on the stability of δ-ferrite and how it manifests in the final product. Figure 5.12 shows the influence of cast cooling rate on the area fraction of δ-ferrite after 2 h homogenisation at 1250 °C. This difference has shown to have a noticeable impact on tensile properties with the slow cooled ingot showing a significant amount of δ-ferrite that forms stringers after rolling. While a 24 h homogenisation of a laboratory scale 400 g ingot would be able to demonstrate the full capability of the steel, it does not truly represent the scalability of this product. Nevertheless, the 5 kg ingot gives confidence in the scalability of the production of this steel that still combines >1100 MPa tensile strength with >40% elongation while only requiring a standard homogenisation cycle of 2 h at 1250 °C.

5.5 Conclusion

A medium Mn steel has been produced via two different processing routes. The emphasis of this work was to produce a steel with superior strength to elongation ratio while considering the full-scale production route to ensure true industrial relevance. Due to the nature of the chemical segregation of these samples, it is important that small scale production would be able to replicate some of the conditions in commercial production. This translation was aided by modelling both the solidification and homogenisation process in Micress. From this study, the following conclusions can be made:

1. The as-cast microstructure depends heavily on the solidification rate of the ingot with the 400 g fast cooling sample showing significantly finer distribution of δ-ferrite.

2. The rate of homogenisation is also dependent on the initial cast microstructure. However, a 5 kg cast that represents the cooling rates seen in commericial production showed significant reduction in δ-ferrite fraction even after a standard 2 h heat treatment.

3. Modelling has been carried out and good agreement with experiment can be seen. The modelling has revealed the trends in δ-ferrite distribution and segregation for a range of casting rates between $0.5 - 200$ °C $^{-1}$.

4. Tensile testing has shown the excellent strength to elongation ratio of the steel. While the 5 kg ingot showed a slightly lower strength, the properties were still superior compared to current commercial steels.

5. The decrease in strength in the 5 kg cast compared to the 400 g ingot can be attributed to the remnant δ-ferrite. The coarser SDAS seen in the 5 kg ingot resulted in longer diffusion distances and therefore higher amount of δ-ferrite can be seen in the final microstructure.

6. The δ-ferrite phase manifests itself as stringers in the final product. A sample of the 400 g ingot homogenised for 24 h then rolled and intercritical annealed showed no stringers and a random distribution of fine α-ferrite, providing a more efficient source of strength to the steel.

5.6 Contribution statement

This chapter was adapted from a paper with contributions from several co-authors. In order of authorship on the paper:

TWJ Kwok - Conceptualisation, methodology, investigation, analysis, writing and visualisation.

C Slater - Conceptualisation, methodology, analysis, visualisation, writing and MICRESS modelling.

X Xu - Conceptualisation and supervision.

C Davis - Conceptualisation and supervision

D Dye - Conceptualisation, methodology and supervision.

Chapter 6

The relative contributions of TWIP and TRIP to strength in fine grained medium-Mn steels

6.1 Abstract

A medium Mn steel of composition Fe-4.8Mn-2.8Al-1.5Si-0.51C (wt.%) was processed to obtain two different microstructures representing two different approaches in the hot rolling mill, resulting in equiaxed vs. mixed equiaxed and lamellar microstructures. Both were found to exhibit a simultaneous Twinning Induced Plasticity and Transformation Induced Plasticity (TWIP+TRIP) mechanism where deformation twins and α'-martensite formed independently of twinning with strain. Interrupted tensile tests were conducted in order to investigate the differences in deformation structures between the two microstructures. A constitutive model was used to find that, surprisingly, twinning contributed relatively little to the strength of the alloy, chiefly due to the fine initial slip lengths that then gave rise to relatively little opportunity for work hardening by grain subdivision. Nevertheless, with lower high-cost alloying additions than equivalent Dual Phase steels (2-3 wt% Mn) and greater ductility, medium-Mn TWIP+TRIP steels still represent an attractive area for future development.

6.2 Introduction

Medium Mn steels with Mn contents of 4-12 wt% are seeing a rise in interest as a successor to high Mn ($16 - 30$ wt% Mn) TWIP steels, named after the Twinning Induced Plasticity (TWIP) effect.

TWIP steels are fully austenitic, have large elongations of >50% and strain hardening rates of up to 3 GPa, resulting in a large amount of energy absorbed upon deformation [8–10]. However, due to the large Mn content, TWIP steels are unable to be processed using conventional secondary steelmaking processes [16, 17]. Additionally, the large Mn content has resulted in TWIP steels being significantly more expensive than other automotive strip steels [12], *e.g.* Dual Phase (DP) steels which are currently used in energy absorbing applications [3, 44]. A combination of these factors have led to limited industrial adoption of TWIP steels.

Within the past decade, many Medium Mn steels in the literature have been developed with tensile properties that exceed those of TWIP steels. By reducing the Mn content, the microstructure of medium Mn steels are now duplex ($\gamma + \alpha$). Depending on the thermomechanical processing history, a myriad of morphologies, phase fractions and distributions of the two phases can be produced. Regarding microstructure and morphology, the two most common microstructures are equiaxed and lamellar [159]. Medium Mn steels with equiaxed microstructures typically have polygonal and evenly distributed austenite and ferrite grains with a random texture. Lamellar or laminated microstructures have alternating austenite and ferrite lamellae contained within a prior austenite grain. Most medium Mn steels are either equiaxed, lamellar or both [29, 40, 159]. However, medium Mn steels with lamellar microstructures tend to be stronger, due to Hall-Petch strengthening arising from a smaller lamella thickness with some exceptions [115], and are less prone to yield point elongation [87, 94]. Nevertheless, due to industrial thermomechanical processing limitations, it is difficult to produce a microstructure that is entirely equiaxed or lamellar. The first medium Mn steel produced on an industrial scale by Voestalpine in Linz had a mixed lamellar and equiaxed microstructure [34].

In addition to the many types of microstructures that can be produced in medium Mn steels, many different plasticity enhancing mechanisms, on top of dislocation glide, can be activated in the austenite phase. By reducing the Mn content compared to high Mn TWIP steels, the stability of the austenite phase is lowered greatly such that stress-assisted or strain induced martensitic transformation is possible, *i.e.* the Transformation Induced Plasticity (TRIP) effect. Additionally, if the Stacking Fault Energy (SFE) can be raised into the twinning regime (15-35 mJ m^{-2}) through element partitioning during an Intercritical Annealing (IA) heat treatment, the TWIP effect may also be activated [19, 37]. Most literature medium Mn steels are either pure TRIP-type or TWIP+TRIP-type [40, 41].

Many medium Mn steels in the literature have exhibited both TWIP and TRIP behaviour but they often occur in different austenite grains, *e.g.* coarse austenite deforming *via* TRIP and fine austenite deforming *via* TWIP [98, 126, 230]. This means that the austenite grains do not deform homogeneously and such steels often exhibit serrations in the strain hardening curve. Therefore, the combined TWIP+TRIP effect, which occurs in a single austenite grain, is of particular interest as it allows for homogeneous deformation, sustained hardening during deformation and elongations in excess of 40% [19, 36, 37, 92, 113, 230]. However, the interplay between TWIP and TRIP can be very different. Lee *et al.* [19, 132] identified the successive TWIP+TRIP effect in a steel with austenite composition Fe-10.3Mn-2.9Al-2.0Si-0.32C. It was found that the austenite phase first formed twins and subsequently strain induced martensite at the twin intersections. This successive TWIP+TRIP effect led to a two-stage hardening behaviour where the first stage was twinning dominated and the second stage was transformation dominated. Sohn *et. al.* [92, 113] seperately indentified a slightly different mechanism where twins and martensite formed concurrently and independently within an austenite grain during deformation. In their steel with austenite composition of Fe-11.5Mn-4.74Al-0.55C, the simultaneous TWIP+TRIP effect led to a multi-stage hardening behaviour and an exceptional 77% total elongation.

Between the successive and simultaneous TWIP+TRIP mechanisms, the successive mechanism is more widely reported [19, 33, 36, 132] and is also the more commonly accepted mechanism of Strain Induced Martensite (SIM) nucleation and growth in Metastable Austenitic Stainless Steels (MASS) such as 304 and 301 [104, 107, 131]. The steel benefits from a high strain hardening rate (> 1.5 GPa) because of two powerful plasticity enhancing mechanisms operating after each other. In the simultaneous mechanism, however, the twinning and transformation kinetics appear to be very slow, providing just enough hardening to avoid necking [113]. Nevertheless, it allowed for a very steady engineering stress up to the failure strain of 77%, signifcantly larger than medium Mn steels which exhibit the successive TWP+TRIP mechanism (40-50%).

It is still uncertain what factors determine whether the austenite phase deforms *via* successive or simultaneous TWIP+TRIP although factors such as microstructure, SFE and austenite stability are likely to play a large role [37, 110, 147]. Furthermore, most medium Mn steels shown to exhibit the TWIP+TRIP effect originate from equiaxed microstructures, *i.e.* polygonal austenite grains. Not much is known how the TWIP+TRIP effect occurs in lamellar or mixed microstructures. This study therefore aims to explore the effect of microstructure on the interplay between TWIP and TRIP mechanisms and therefore their relative contributions. This would be achieved by producing two types of microstructures with similar austenite volume fraction and composition and examining how the various deformation structures evolve with strain. It is hoped that the increased understanding of the various types of deformation mechanisms in medium Mn steel will be useful in aiding future alloy

Table 6.1: Composition of the bulk steel in mass % as measured by ICP and IGF for elements marked by †.

Fe	Mn	Al	Si	C†	N†	P	S†
Bal	4.77	2.75	1.51	0.505	0.003	<0.005	0.002

design and cold metal forming processes.

6.3 Experimental

A steel ingot of dimensions 70 × 23 × 23 mm was produced *via* vacuum arc melting. The bulk composition shown in Table 6.1 was measured using Inductively Coupled Plasma (ICP) and Inert Gas Fusion (IGF). In order to simulate an industrial reheating cycle, the ingot was homogenised in a vacuum tube furnace at 1250 °C for 2 h and allowed to furnace cool to room temperature. The ingot was then reheated to 1100 °C and rough rolled at the same temperature from 23 to 12 mm thickness in 4 passes and water quenched. The rough rolled ingot was then split along the long axis into two bars *via* Electric Discharge Machining (EDM). The bars were then reheated to 1000 °C and finish rolled from 12 mm to 1.5 mm thick strip in six passes with a finish temperature of 850 °C. One strip was water quenched immediately after the last pass, while the another strip was cooled to 600 °C and held for 30 min to simulate the coiling process and finally furnace cooled to room temperature. Both strips were then intercritically annealed at 750 °C for 10 min. The final samples produced either by furnace cooling or water quenching will be referred to as FC and WQ respectively.

Tensile samples with gauge dimensions 19 × 3 × 1.5 mm were machined from both strips *via* EDM, such that the tensile direction was parallel to the rolling direction. Tensile testing was subsequently conducted on an Instron load frame with a 30 kN load cell at a nominal strain rate of 10^{-3} s^{-1}.

Samples for Electron Backscattered Diffraction (EBSD) were mechanically ground and polished with an OPU polishing suspension. Samples for Transmission Electron Microscopy (TEM) and Transmission Kikuchi Diffraction (TKD) were prepared by mechanically thinning a 3 mm disk of material to below 90 µm in thickness and subsequently electrolytic polished using a twin-jet electropolisher with a solution containing 5% perchloric acid, 35% butyl-alcohol and 60% methanol at a temperature of −40 °C.

EBSD was conducted on a Zeiss Sigma FEG-SEM equipped with a Bruker EBSD detector. TEM and Energy Dispersive Spectroscopy (TEM-EDS) was conducted on on a JEOL JEM-F200 operated at an accelerating voltage of 200 kV. Transmission Kikuchi Diffraction (TKD) was conducted on a JEOL 7900 FEG-SEM.

A constitutive model based on the work by Lee *et al.* [19, 75, 132] and Latypov *et al.* [148] was modified and used to model the plastic behaviour of the FC and WQ conditions. A full description of the model can be found in the Appendix and is available on GitHub [231].

6.4 Results

6.4.1 Tensile properties

The tensile behaviour of the FC and WQ steels are shown in Figure 6.1 and the tensile properties are summarised in Table 6.2. From Figure 6.1a, it can be seen that both FC and WQ steels have very high strengths (>800 MPa) and exceptional ductility (>70%). The WQ steel had a higher yield and tensile strength but the FC steel had a slightly longer elongation. The inset in Figure 6.1a showed that the WQ steel had a very short yield point elongation of approximately 2% strain.

When the Strain Hardening Rate (SHR) was obtained by differentiating the true stress-strain curve, it can be seen that they possessed a very similar shape, similar to many medium Mn steels [19, 28, 132] and MASS [104, 232–234] that exhibit the successive TWIP+TRIP effect. Four hardening stages can be identified. At stage I, *i.e.* the onset of plastic deformation, both SHR curves showed a rapid decrease, reaching a local minima at approximately 0.02 true strain before bouncing back rapidly to the first peak between 0.04 and 0.05 true strain. At stage II, the SHR then decreases to a saddle point and at stage III it rises again slowly to the second peak. Finally, at stage IV the SHR decreases up to failure. While the shape of the SHR curves may be similar, the strain at which the first peak, saddle point and second peaks occur as well as its value differ slightly between the FC and the WQ steel. To investigate the microstructural evolution at these three unique points, interrupted tensile tests were conducted up to the corresponding strains for the FC and WQ steel. The as-annealed and interrupted tensile samples are henceforth named FC0, FC4, FC20, FC60 for the FC steel and WQ0, WQ5, WQ13, WQ50 for the WQ steel where the digits represent the engineering strain to which they were tested, rounded to the nearest percent.

6.4.2 Microstructure

EBSD Image Quality and Phase Maps (IQ+PM) of the FC and WQ steels at varying strain are shown in Figure 6.2. In the as-annealed condition, FC0 showed a largely equiaxed microstructure (Figure 6.2a). It was likely that the cementite in the pearlite matrix globularised and transformed into austenite during the IA, while WQ0 adopted a mixed equiaxed + lamellar microstructure. The lamellar regions

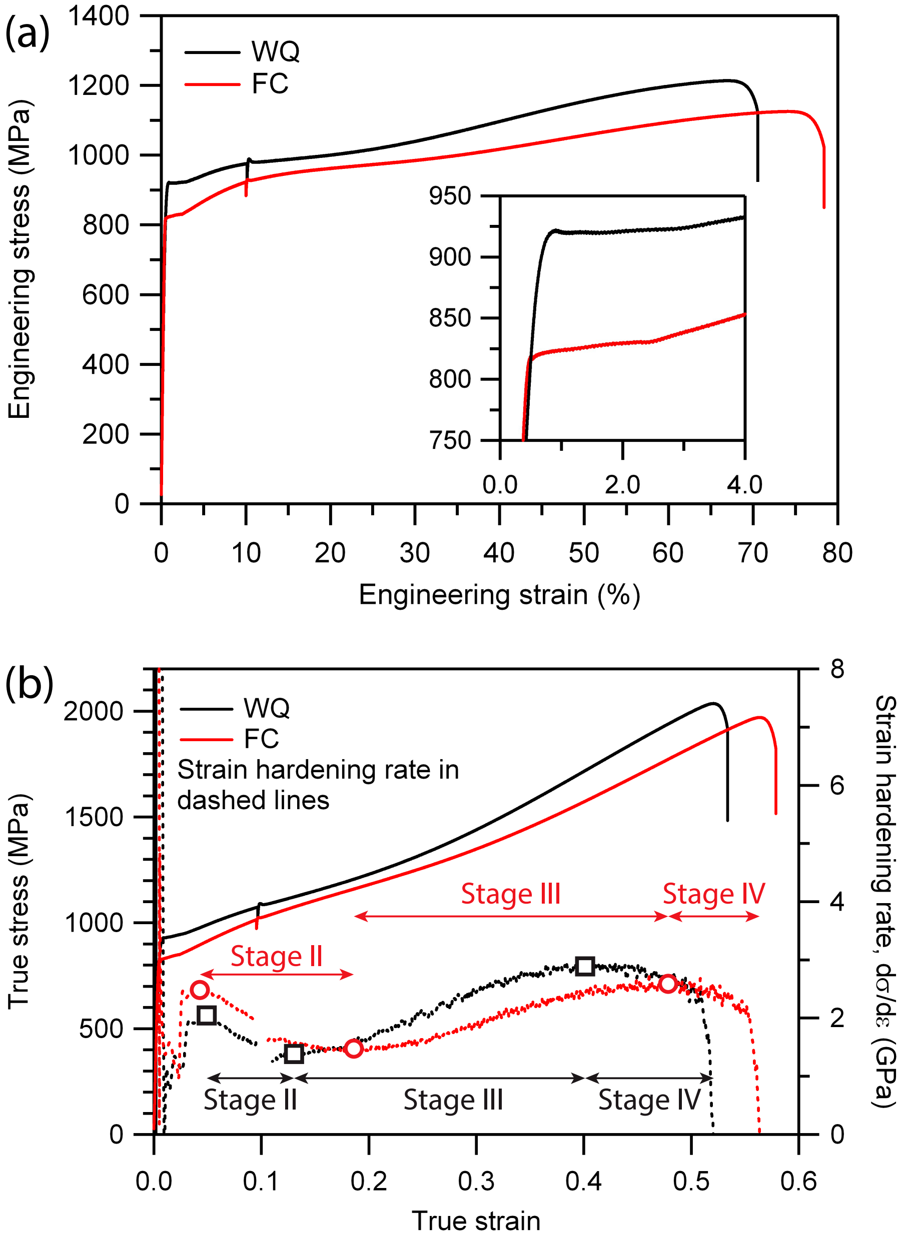

Figure 6.1: (a) Engineering stress strain curves. Inset: early yielding behaviour. (b) True stress strain curves and strain hardening rate. Open red circles and black squares indicate true strains where interrupted tests were conducted. Stage I of the hardening rate was not labelled for clarity but refers to the true strain range between the onset of plastic deformation and the beginning of Stage II. N.B. extensometer was removed at 10% strain.

arose when austenite nucleated in between martensite laths, while the equiaxed regions formed due to some degree of recrystallisation of martensite, predominantly around the PAGBs.

With increasing strain, it was observed that the austenite fraction began to decrease after the first peak, indicating that the TRIP effect was operative in both FC and WQ steels. However, due to the increasing Non-Indexed (NI) fraction at higher strain levels, there was some uncertainty in the calculated martensite fraction, which indexes as BCC in EBSD. It is acknowledged that the NI

Table 6.2: Summary of tensile properties. E - Young's modulus, $\sigma_{0.2}$ - 0.2% proof stress, MPa% - UTS $\times$ ε.

	E (GPa)	$\sigma_{0.2}$ (MPa)	UTS (MPa)	ε (%)	MPa% ($\times 10^3$)
FC	205	818	1125	78	87.8
WQ	193	895	1214	71	86.2

regions are typically either martensite or deformed austenite. Therefore, an upper and lower limit was established in Figures 6.2k-l where the upper martensite limit was obtained if the entire NI fraction was treated as martensite and the lower martensite limit was obtained if the entire NI fraction was treated as austenite and *vice versa* for the austenite upper and lower limits.

Between the as-annealed condition and the first peak, there was no transformation in both FC and WQ steels, suggesting that an incubation strain was needed for the TRIP effect. Subsequently, with increasing strain, the martensite fraction in the WQ steel increased at a higher rate compared to the FC steel with a larger final fraction at the failure strain. In the FC steel, both ferrite and austenite grains were observed to elongate in the tensile direction while in the WQ steel, the lamellar regions were also observed to elongate but additially rotating and orienting themselves parallel to the tensile direction at the failure strain.

While EBSD was able to provide macroscopic insights into the microstructural evolution, it was necessary to probe the finer deformation structures using TEM. Figure 6.3 shows the microstructure of the FC and WQ steel in the as-annealed condition under STEM-BF. The as-annealed FC microstructure showed an equiaxed microstructure with a low dislocation density. On the other hand, the as-annealed WQ microstructure showed a lamellar microstructure with average lamella width of 290 nm. A relatively larger number of dislocations were observed in the WQ microstructure. Han *et al.* [115] also found that the ferrite phase in lamellar type microstructures had a higher dislocation density than equiaxed ferrite due to the lack of recrystallisation during IA. While the FC microstructure was not obtained *via* cold rolling and recrystallising, the multiple phase transformations during coiling, furnace cooling and IA were likely able to eliminate any residual dislocation density after hot rolling.

Stage I: zero strain to first peak

At stage I, there was no transformation (Figure 6.2) and almost no twinning in samples FC4 and WQ5. From Figure 6.4, it was observed that dislocation multiplication was occuring in the austenite and ferrite phases in both the FC and WQ conditions. In FC4, multiple Stacking Faults (SFs) were

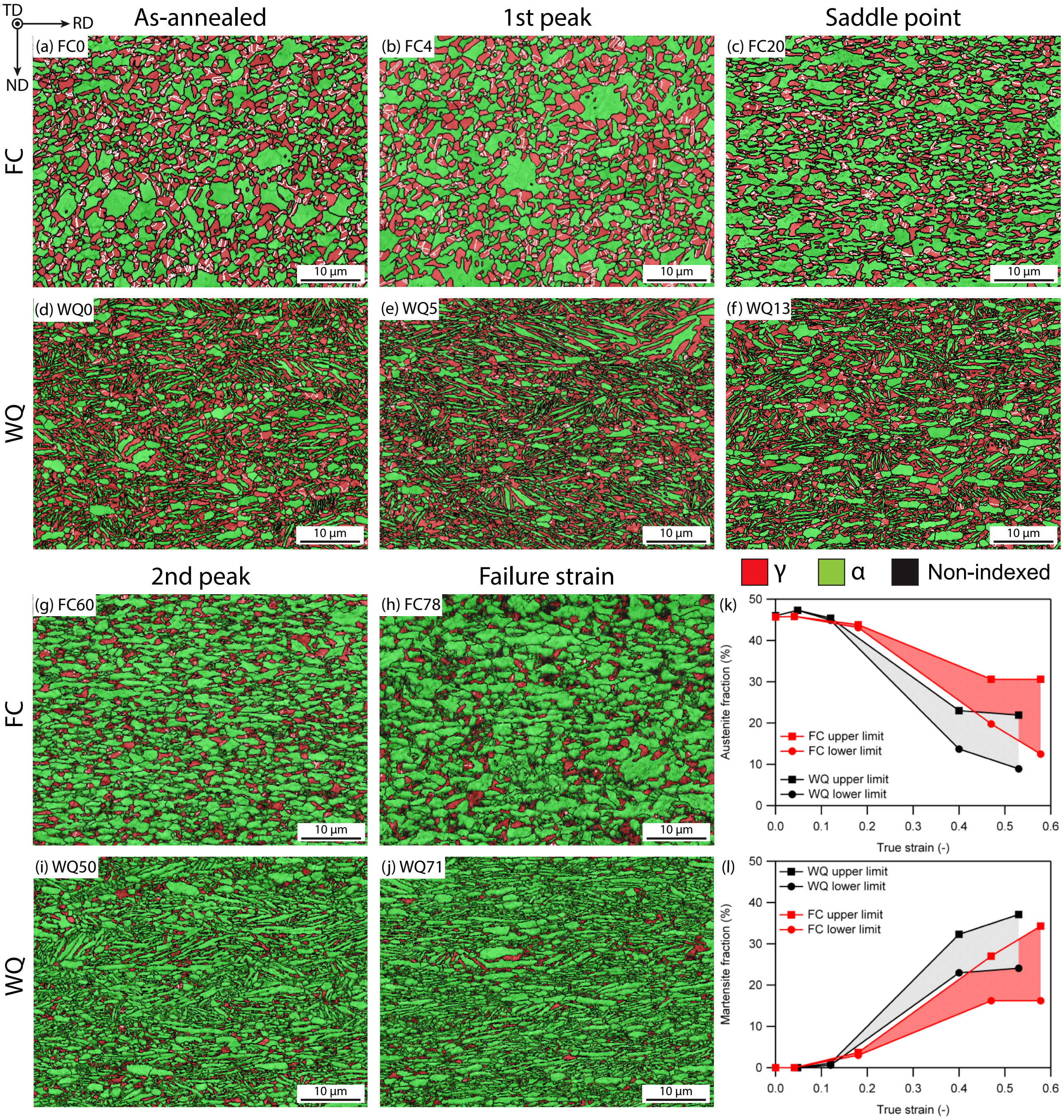

Figure 6.2: EBSD image quality and phase maps of (a) FC0, (b) FC4, (c) FC20, (d) WQ0, (e) WQ5, (f) WQ13, (g) FC60, (h)FC78, (i) WQ50, (j) WQ71. Red – austenite, green – ferrite/α'-martensite, black – non-indexed fraction. Black lines indicate High Angle Grain Boundaries (HAGBs) and white lines indicate austenite $\Sigma3$ boundaries, *i.e.* annealing twin boundaries. (k) Summary of the change in austenite and (l) α'-martensite phase fractions with true strain.

observed growing from austenite and annealing twin boundaries. In WQ5, SFs were also observed but only in the more globular austenite grains. In the lamellar grains however, no SFs were observed. Instead, dislocations were emitted from the interphase boundaries and also seen to be piling up across the width of certain lamellar grains. The higher density of SFs in FC4 may also explain why the SHR

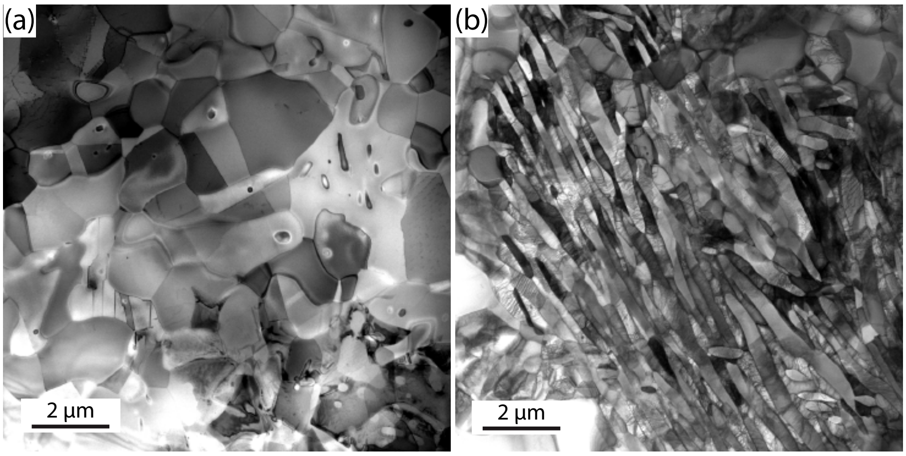

Figure 6.3: STEM-BF images of (a) FC and (b) WQ in the as-annealed condition.

at the first peak was higher than WQ5.

In many fine grained equiaxed medium Mn steels, the first peak is the result of yield point elongation [33, 132]. Sun *et al.* [87] have shown that this was because of a rapid dislocation generation from the large amount of γ/α interfaces in a relatively dislocation free microstructure. Lamellar microstructures typically exhibit continuous yielding due to a higher dislocation density within the lamellar grains, as seen in Figure 6.3b. However, because WQ was a mixed microstructure, combining both equiaxed and lamellar regions, a short yield point elongation was still present.

Stage II: first peak to saddle point

Figure 6.5 shows the microstructures of FC20 and WQ13 at the SHR saddle point. In FC20, some austenite grains were observed to have one set of twins, while others were observed to have two. Figure 6.5a shows an austenite grain with twins growing out from the grain boundary while stacking faults were growing in the other twinning direction. The SFs appear to have either nucleated from the grain boundary or from the first twins. In another austenite grain in FC20 as shown in Figures 6.5b-c, two twinning systems were clearly operating as also shown in the diffraction pattern where two sets of twinning spots were observed. According to the successive TWIP+TRIP mechanism described by Lee *et al.* [19, 128], α'-martensite at twin intersections should be observed at this strain. However, additional diffration spots associated with martensite transformation were not observed at the twin intersections in FC20. High Resolution TEM (HR-TEM) of the twin intersections also showed no martensite at the twin intersections.

In WQ13, there was very limited twinning compared to FC20. In Figure 6.5e, only a small twinned region could be found and was not located in a lamellar region. In Figures 6.5f-g, several thin laths of

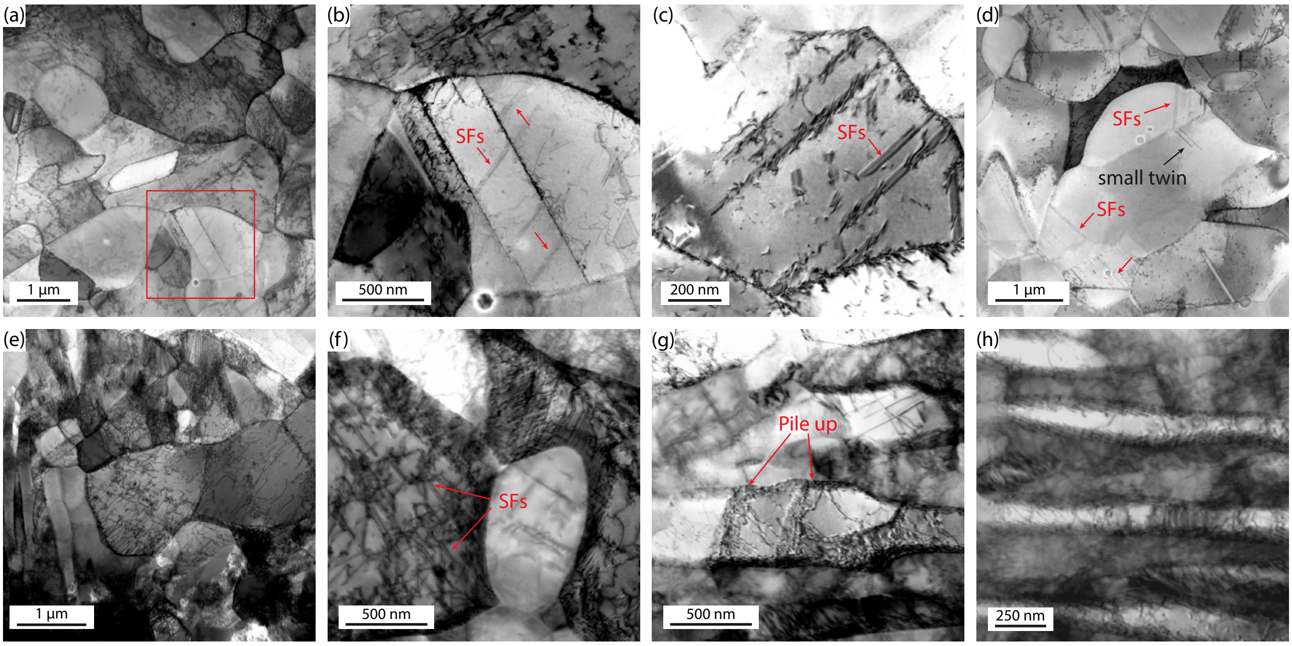

Figure 6.4: STEM-BF of (a-d) FC4 and (e-h) WQ5 at the first SHR peak. (a) General microstructure of FC steel, (b) magnified view of red square in (a) showing stacking faults inside an austenite grain and its annealing twin. (c) Stacking faults in a separate austenite grain. (d) Stacking faults (red arrows) emitted from a grain boundary terminating at a subgrain boundary and small twins (black arrow) emitted from the subgrain boundary. (e) General microstructure of WQ steel, (f) partial dislocations within an equiaxed austenite grain. (g) Dislocation pile up across a lamellar grain. (h) Dislocations emitted from interphase boundaries of lamellar grains.

martensite were found in an austenite grain adjacent to a lamellar region. The diffraction pattern in Figure 6.5h showed that the martensite laths had a Kurdjumov-Sachs orientation relationship (KS-OR) with the parent austenite. Thin martensite laths were also observed by Lee *et al.* [28] in a lamellar medium Mn steel.

Stage III & IV: saddle point to second peak to failure

At the second SHR peak, the TEM micrographs of FC60 and WQ50 are shown in Figure 6.6. In FC60, many twinned austenite grains could be observed such as the one shown in Figure 6.6a. With increased magnification. Much finer but shorter twins were observed within the grain interior (Figure 6.6b) and when the magnification was increased further, several short twins from the second twinning system could be observed (Figure 6.6c). This suggests that twinning continued to occur even up to 60% strain in the FC steel. In another austenite grain as shown in Figure 6.6d, twin thicknening was observed which has often been found in TWIP steels at large strains [235] and was also observed by Sohn *et al.* [113] in a medium Mn steel.

In WQ50, a large number of twinned lamellar austenite grains were observed. This suggests that in

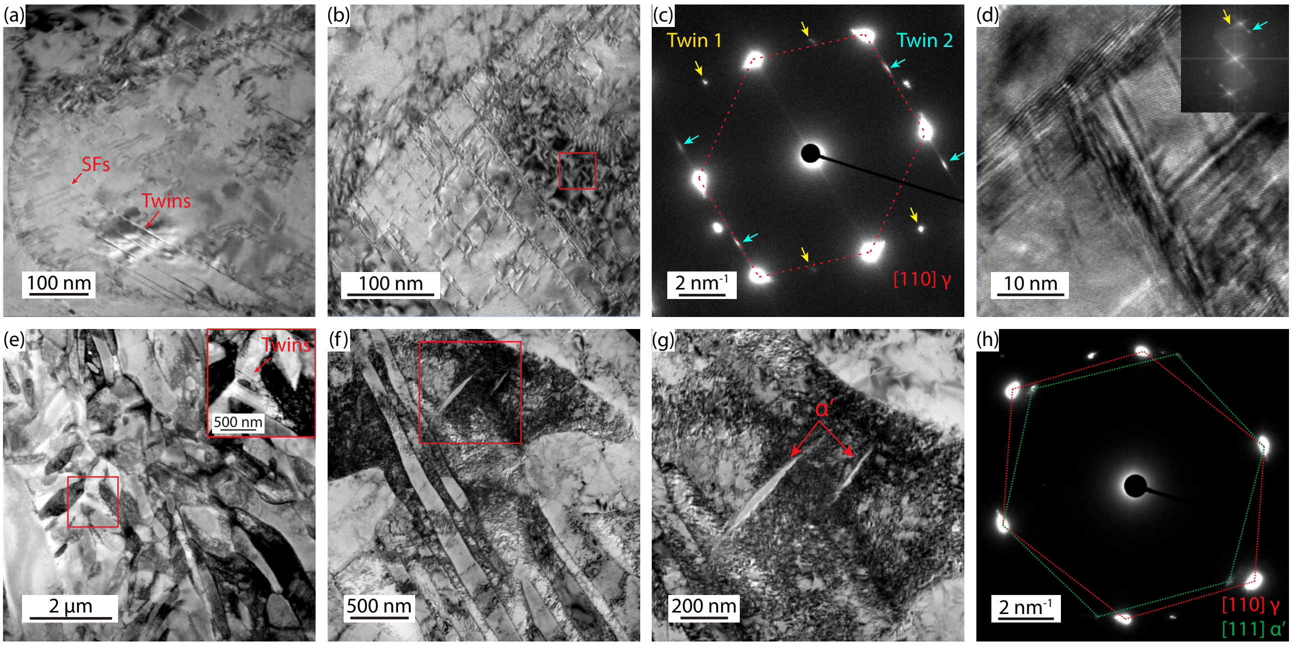

Figure 6.5: TEM micrographs of (a-d) FC20 and (e-h) WQ13 steels at their respective SHR saddle points. TEM-BF of (a) twins in one twinning direction and SFs in the other direction, (b) two twinning systems in an austenite grain. (c) Diffraction pattern obtained from the austenite grain in (b) showing twinning spots from two systems. (d) HR-TEM of red square in (b) showing twin intersection. Inset: pseudo-diffraction pattern of $[110]_\gamma$ showing twinning spots. (e) STEM-BF mmicrograph of the general microstructure of WQ steel with very limited twinning. (f) TEM-BF micrograph of thin α'-martensite laths nucleating in deformed austenite. (g) TEM-BF micrograph of the red square in (f). (h) Diffraction pattern obtained from (g) showing austenite and α'-martensite with the KS-OR.

WQ, twinning was more active in stage III compared to stage II. Figure 6.6a shows a lamellar austenite grain with twins that grew across the grain. Further magnification revealed secondary twins at the tip of the lamellar grain. However, the diffraction pattern from the tip still showed that there was no α'-martensite at the twin intersections. Nevertheless, in another grain (Figures 6.6g-h), martensite laths were observed growing from the grain boundary across a twinned lamellar austenite grain in the same direction as the twins.

While TEM has effectively revealed the twinned structures in both FC and WQ steels, it was difficult to identify martensitic regions. For this reason, TKD was conducted on the TEM foils from FC60 and WQ50. The resulting data is shown in Figure 6.7. In the FC60 sample (Figures 6.7a-c), a deformed equiaxed austenite grain with a curved annealing twin (outlined in white) could be observed from the Band Contrast (BC) and FCC IPF-Z maps. From the BCC IPF-Z map (Figure 6.7c), BCC regions were observed within the outlined austenite grain. These BCC grains were observed to be within 5° of the KS-OR with the parent austenite grain and were therefore different variants of α'-martensite. These blocky α'-martensite grains appear to have first nucleated from the austenite grain boundaries

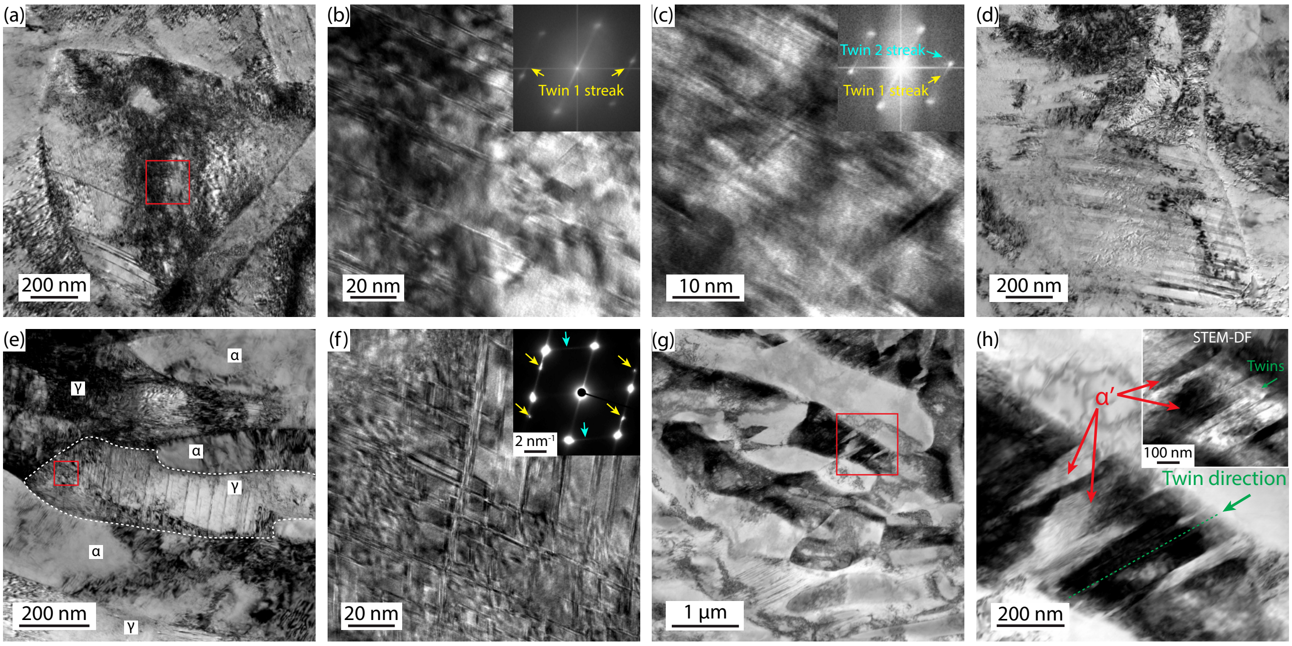

Figure 6.6: TEM micrographs of (a-d) FC60 and (e-h) WQ50 at their respective second SHR peaks. TEM-BF of (a) a deformed austenite grain demonstrating long twins near the bottom. HR-TEM micrographs of (b) magnified area of the red square in (a) demonstrating shorter and thinner twins, inset: pseudo-diffraction pattern of $[110]_\gamma$ demonstrating twinning streaks, (c) further magnification of (b) revealing short twins from the second twinning system, inset: pseudo-diffraction pattern of $[110]_\gamma$ demonstrating two twinning streaks. (d) TEM-BF of an austenite grain showing thick twins. TEM-BF of (e) lamellar region in WQ50 showing heavily twinned austenite grains and the highlighted austenite grain having a larger twin density at the lamella tip, (f) magnified image from red square in (e) showing two active twinning systems. Inset: diffraction pattern of the twinned region. Yellow arrows point to primary twin spots, cyan arrows point to secondary twin streaks. Beam parallel to $[110]_\gamma$. STEM-BF of (g) another lamellar region and (h) magnified image from red square in (g) showing α'-martensite growing across a twinned austenite lamella in the twinning direction. Inset: STEM-DF of (h) highlighting the twins.

and then from each other, suggesting that α'-martensite growth was limited and nucleation may have occured continuously with increasing strain. The limited growth may explain why size of the blocky α'-martensite grains remained very small. However, it cannot be said that the α'-martensite observed in Figure 6.7 only formed during stage III, it is likely that some α'-martensite also formed during stage II.

In the WQ50 sample (Figures 6.7d-f), the austenite grains before transformation were more easily identified as the dark grey, *i.e.* more deformed regions in the BC map (Figure 6.7d). This is also confirmed in Figure 6.7e where the untransformed austenite lie within the dark grey regions. In Figures 6.7e-f, four areas of interest are highlighted. In area 1, the arrows point to α'-martensite grains with a lath morphology which were observed growing across austenite lamellae as observed in WQ13 (Figures 6.5f-h). However, this morphology was an exception rather than the rule as similar lath martensite

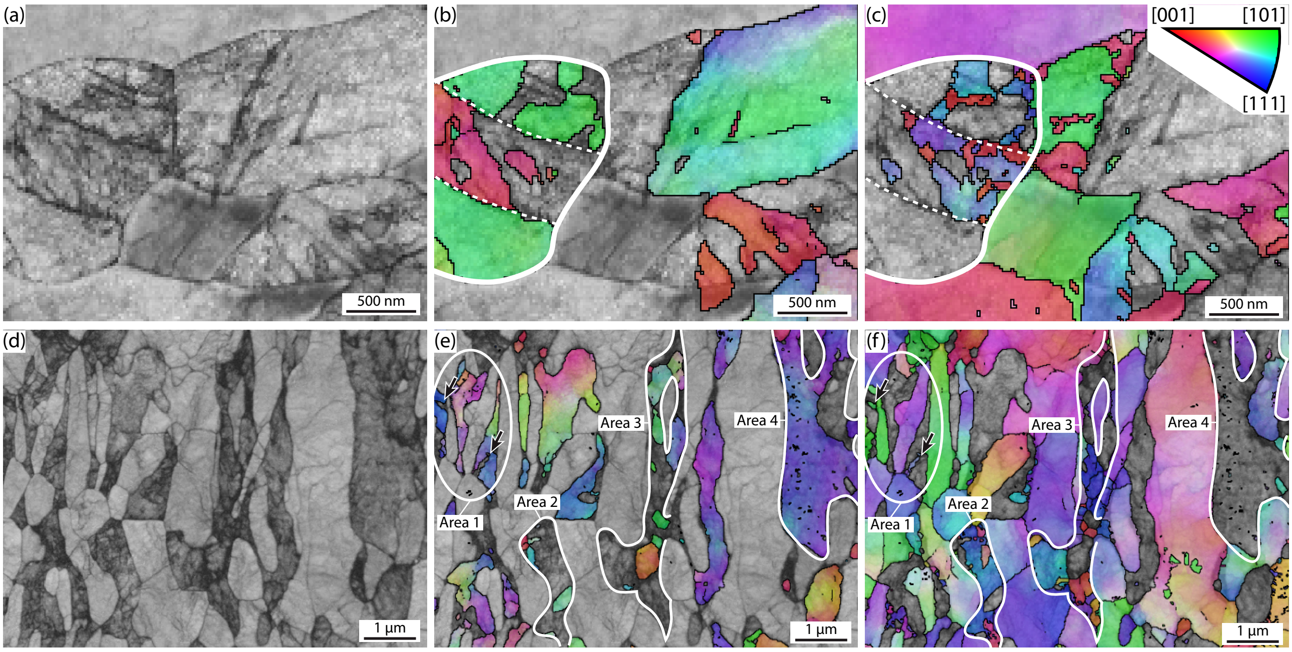

Figure 6.7: TKD micrographs of (a-c) FC60 and (d-f) WQ50. (a) Band contrast, (b) FCC IPF-Z map and (c) BCC IPF-Z map of FC60 sample. (d) Band contrast, (e) FCC IPF-Z map and (f) BCC IPF-Z map in WQ50 sample. Z-direction points out of the page. Black lines indicate HAGBs.

morphologies were not commonly observed elsewhere. It is also worth noting that the three austenite lamellae contained in area 1 remained largely untransformed even up to 50% strain. In area 2, the outlined region was likely a globular prior austenite grain but was elongated at 50% strain. The prior austenite grain was mostly transformed with only a few pockets of austenite left. In the BCC IPF-Z map in Figure 6.7f, several small martensite grains were observed at the prior austenite grain boundary in a similar manner as described in FC60. However, the prior austenite grain was mostly dominated by a single martensite grain with [111] direction out of the page. In area 3, the outlined prior austenite grain was similarly partially transformed to martensite. In the more bulbous region near the bottom left, a single martensite grain with [111] direction out of the page also dominated the region. However, at the bottom tip and along the length of the lamellar grain, the austenite grain transformed into relatively equally sized submicron martensite grains. Finally, in area 4, the untransformed austenite grain contained several extremely fine intragranular martensite grains. These martensite grains were significantly finer and do not appear to have nucleated from a grain boundary in the same manner as in the aforementioned three areas. It is therefore possible that these fine martensite grains are of the twin-twin intersection variety which forms in the successive TWIP+TRIP mechanism.

Finally at stage IV, comparing the EBSD phase maps in Figures 6.2g-l, the austenite phase still continued to transform to martensite. However, stage IV is characterised as a strain region of decreasing

Table 6.3: TEM-EDS measurements in mass percent of alloying elements in each phase in the FC0 and WQ0 samples, balance being Fe. Standard error given in paranthesis. d_{grain} calculated as the equivalent circle diameter from EBSD, except for * which is the average austenite lamellar width in WQ0. N.B. the morphology of the grains in FC0 and WQ0 samples are equiaxed and lamellar respectively. † C content determined by lever rule assuming negligible C content in ferrite.

	Mn	Al	Si	C†	V_f	d_{grain} (µm)	SFE (mJ m^{-2})	Ms (°C)	Md$_{30}$ (°C)
Bulk (ICP)	4.77	2.75	1.41	0.505	-	-	-	-	-
γ FC0	8.49 (0.37)	1.89 (0.05)	0.95 (0.04)	1.10	0.46	1.5	33.4	-181	-16.1
γ WQ0	7.30 (0.60)	1.80 (0.10)	1.00 (0.11)	1.07	0.47	1.2	30.7	-133	5
						0.3*	30.7	-150	-0.6
α FC0	4.77 (1.90)	2.41 (0.11)	1.39 (0.16)	0	0.54	3.0	-	-	-
α WQ0	3.92 (0.05)	2.25 (0.12)	1.37 (0.07)	0	0.53	1.3	-	-	-

SHR (Figure 6.1b), suggesting that both twin and martensite fractions were both approaching saturation until both steels failed by necking, *i.e.* $\sigma = d\sigma/d\varepsilon$.

6.4.3 Composition

The composition of austenite and ferrite in both FC and WQ steels were measured using TEM-EDS. The results are shown in Table 6.3. The C content in austenite was determined by using the lever rule, assuming negligible C solubility in ferrite. The SFE was calculated according to the method proposed by Sun *et al.* [36]. *Md$_{30}$*, defined as the temperature where half of the austenite transforms to martensite at a strain of 30% was calculated according to the following equation [52, 53]:

$$Md_{30}(°C) = 551 - 462C - 8.1Mn - 9.2Si - 1.42(-3.29 - 6.64\log_{10} d_\gamma - 8) \tag{6.1}$$

where compositions are given in mass % and d_γ is the austenite grain size in µm. A higher Md$_{30}$ indicates lower austenite stability against strain induced martensitic transformation and *vice versa.* The Ms temperature, defined as the temperature where athermal martensite begins to form upon rapid cooling from austenite, was calculated according to the following equation [193]:

$$Ms(°C) = 475.9 - 335.1C - 34.5Mn - 1.3Si + 11.67\ln(d_\gamma) \tag{6.2}$$

A higher Ms indicates lower austenite stability against athermal martensitic transformation and *vice versa.* Both Md$_{30}$ and Ms have been used to qualitatively determine the stability of austenite against strain induced martensitic transformation.

Comparing the austenite compositions between the FC and WQ states in Table 6.3, it can be seen that the FC condition had a slightly higher Mn content while the other elements remained relatively equal. This may be attributed to the additional coiling and furnace cooling steps during the processing of the FC condition which provided additional time for Mn to partition out of ferrite and into the cementite phase. During the IA step, the cementite then globularised and transformed into austenite with an enriched Mn content compared to the WQ condition. The difference in Mn content resulted in a slightly higher SFE and lower Md_{30} and Ms for FC.

The SFE of FC and WQ steels were both within the predicted twinning regime of TWIP steels [8] and also medium Mn steels [37]. On the other hand, because of the large C content in both steels (> 1 wt%), the Md_{30} and Ms temperatures were very low, suggesting that the austenite was very stable. In medium Mn steels, Lee *et al.* [19] demonstrated that it was possible to overstabilise the austenite phase such that the TRIP effect no longer becomes operative. While the TRIP effect was clearly observed in both FC and WQ, the high austenite stability would certainly have an effect on the nucleation and growth of α'-martensite grains.

6.4.4 Modified constitutive model

After examining the microstructural evolution with strain using EBSD, TEM and TKD, it is evident that it was the simultaneous, rather than the successive TWIP+TRIP mechanism that was active in both FC and WQ conditions as α'-martensite grains were not observed at twin intersections and have mostly nucleated at austenite grain boundaries. Microstructural examination also showed that the evolution of deformation structures such as twins and α'-martensite were very different between FC and WQ conditions. The different twinning kinetics theoretically should have resulted in a clear difference in strain hardening profiles between the FC and WQ conditions. However, from Figure 6.1b, the strain hardening rate curves between FC and WQ conditions showed a very similar profile.

In order to reconcile the seemingly conflicting observations between the tensile properties and microstructure evolution, a constitutive model developed by Lee *et al.* [19,75,132] was used to determine if the tensile properties in Figure 6.1 could be reproduced given the microstructural data from Figures 6.2–6.7 and *vice versa.* Since the constitutive model was initially developed for medium Mn steels that exhibited the successive TWIP+TRIP mechanisms, two key changes were made in order to accomodate the simultaneous TWIP+TRIP mechanism. Firstly, equations responsible for the evolution of martensite fraction with strain were replaced with a single Avrami equation [236–238] which also effectively uncouples the dependence of TRIP on TWIP. Secondly, following the findings of Latypov *et al.* [148], the strength of the α'-martensite phase was approximated to be constant with strain. The

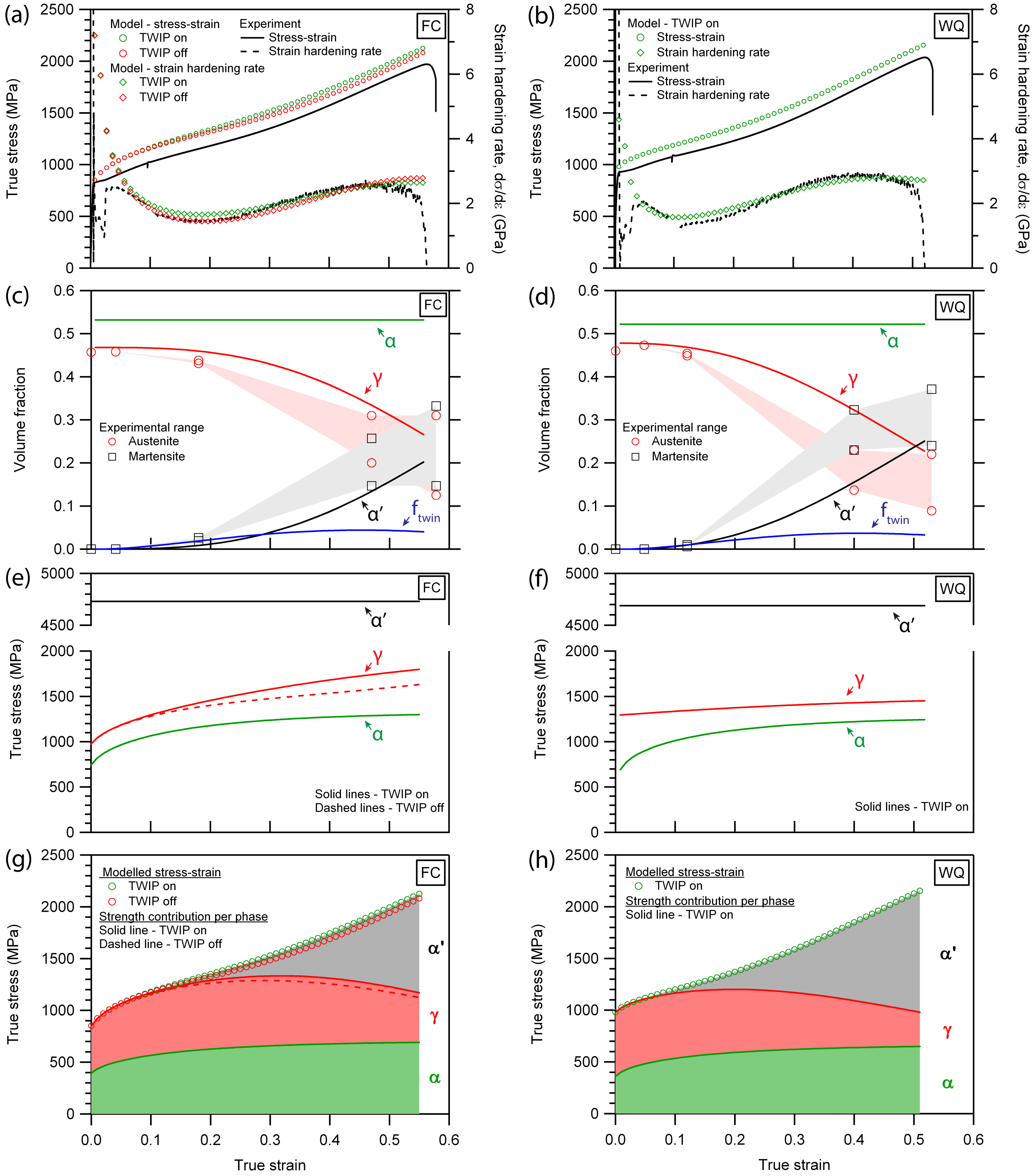

Figure 6.8: Experimental and modelled tensile curves of the (a) FC and (b) WQ conditions. Experimental and modelled changes in phase fraction with strain of the (c) FC and (d) conditions. Twin fraction, f_{twin}, refers to the fraction of twins in austenite multiplied by the austenite fraction. Component stress-strain curves of the individual phases of the (e) FC and (f) WQ conditions. Cumulative contributions to global strength from the individual phases in the (g) FC and (h) WQ conditions. N.B. Modelled TWIP off curves for the WQ condition were not shown for clarity as they were nearly identical to TWIP on curves. TWIP on and off curves are very similar in FC condition and nearly identical in WQ condition due to limited dislocation storage ability at slip lengths on the micron and submicron level.

results from the modified constitutive model are shown in Figure 6.8.

From Figure 6.8a, a good agreement between the model and experimental stress-strain and SHR curves was observed for the FC condition. A slight overprediction was observed in the modelled stress-strain curve but can be attributed to the model assuming continuous yielding and not accounting for the slight yield point elongation in the FC condition. From Figure 6.8c, the predicted austenite and α'-martensite phase fractions were shown to be in reasonable agreement with the experimental ranges as determined using EBSD in Figure 6.2. This largely confirms the validity of the modified constitutive model for modelling the simultaneous TWP+TRIP mechanism in equiaxed-type microstructures.

However, the same model did not work as well when applied to the WQ condition. In Figure 6.8b the model appears to show a good fit with the SHR curve, however the predicted α'-martensite fraction fell short of the experimentally determined range at a true strain of 0.4 in Figure 6.8d. This was largely attributed to the mixed equiaxed and lamellar grain morphology in the WQ condition which might have led to a more complex strain partitioning mechanism that might not be best represented with the current equations. Nevertheless, the model was able to reasonably predict the initial and final martensite fractions in the WQ condition.

Since TWIP and TRIP mechanisms have been uncoupled in the modified constitutive model, it is possible to model the plastic response without the TWIP effect. In Figure 6.8a, both modelled stress-strain and SHR curves are shown with the TWIP effect turned on or off. Remarkably, there was no significant loss in strain hardening even with the TWIP effect turned off. In the WQ condition (Figure 6.8b), there was almost no difference whether the TWIP effect was turned on or off. Therefore the modelled stress-strain and SHR curves with TWIP off were not shown in Figure 6.8b.

The component stress-strain curves in the FC and WQ conditions are shown in Figures 6.8e-f respectively. In the FC condition, the TWIP effect was observed to strengthen the austenite phase by 167 MPa at the failure strain. However, this strength was reduced to only 44 MPa when the loss of austenite volume fraction to α'-martensite transformation was taken into account as seen in Figure 6.8g. From Figure 6.8f, the austenite phase was not observed to strain harden significantly in the WQ condition, largely due to the close competiton between dislocation multiplication and annihilation arising from the short lamella thickness. The lack of any difference in strength between the TWIP on and off conditions in WQ was likely due to the severe reduction in the dislocation storage rate in the austenite grains due to the already very fine lamella widths [239]. Therefore, further refinement of the grain size through the dynamic Hall-Petch effect [8] due to twinning proved to be ineffective in improving the strength of the austenite phase in the WQ condition.

By multiplying the component strength by the respective volume fraction of each phase, the cumulative contribution to global strength from each phase with strain can be obtained and is shown in Figures 6.8g-h. It can be seen that the strength contribution from the TWIP effect is dwarfed by the TRIP effect. The strength from the α'-martensite phase contributes to nearly 50% of the UTS in the FC condition and more than 50% of the UTS in the WQ condition.

6.5 Discussion

6.5.1 α'-martensite nucleation and growth

In order to attain a sustained high SHR and large elongations in TRIP-assisted steels, it is necessary to continuously form fine α'-martensite in a steady manner over a wide strain range [102,103]. A common strategy is to create a spread in austenite stability *via* grain size distribution [103], inhomogeneous Mn composition [108] or texture [110]. This leads to a spectral TRIP [103] or discontinous TRIP effect [108,110,222] where transformation begins and ends with the least and the most stable austenite grains respectively.

In both FC and WQ conditions, the austenite phase was chemically very stable against α'-martensitic transformation due to the high Mn and C content (Table 6.3). Chatterjee *et al.* [112] showed that with such a high C content, formation of Strain-Induced Martensite (SIM) would be highly improbable. However, an applied stress can provide an additional mechanical driving force, ΔG_{mech}, for Stress-Assisted Martensite (SAM) transformation [240,241]. In medium Mn steels, it is known that strain and therefore stress localises at the interphase boundaries during deformation due to the strength mismatch between austenite, ferrite and α'-martensite [128]. The high stress localisation was likely to have been able to provide a sufficiently high mechanical driving force for SAM to nucleate at austenite grain boundaries as observed in Figures 6.5, 6.6 and 6.7. Grain boundary SAM nucleation was also observed by Yen *et al.* [111] in a medium Mn steel with a submicron grain size. The stress-assisted nature of α'-martensite nucleation may explain why an incubation strain was observed (Figure 6.2l) as it would be necessary to build up a critical local stress at the austenite grain boundaries. However, the stress field at the grain boundary would decay rapidly towards the interior of the parent austenite grain and the driving force for SAM transformation would similarly diminish. The highly local stress concentration may explain why the α'-martensite grains in both FC and WQ were very small as α'-martensite cannot grow past the stress field. With additional deformation, α'-martensite grains with favourable orientations with stress will grow (areas 2 and 3 in Figure 6.7), whereas repeated nucleation of α'-martensite nucleating on top of each other will occur (Figures 6.7b-c). The phenomenon of α'-martensite only being able to nucleate and grow within local stress concentrations keeps the α'-martensite grains small and greatly extends the strain regime where TRIP occurs.

6.5.2 Effects of microstructure on TWIP and TRIP

The effects of grain size on twinning and martensitic transformation in austenite are well studied. In TWIP steels, there is an impression that grain size reduction generally increases the twinning stress [8]. However, in many studies, reducing the grain size to 1-5 µm does not appear to negatively affect tensile properties and elongation, although it is acknowledged that the twinning stress was increased [42, 242]. From Table 6.3, the grain size, measured as the equivalent circle diameter, of FC and WQ conditions were not significantly different. However, from Figures 6.5 and 6.6 it was observed that extensive twinning occured in stage II and III for FC but mostly in stage III for WQ. In WQ, twins were observed to propagate across the width of the lamellar grains (Figures 6.6e-h), implying that the lamellar width (approximately 300 nm) should be considered rather than the equivalent circle diameter. Since the austenite lamellar width in the WQ condition was significantly finer than that of the equiaxed grain diameter in FC, the twinning stress in the WQ condition would be much higher and would explain why twinning in lamellar austenite grains was delayed to a later stage compared to equiaxed austenite grains.

In TRIP-assisted steels, it is well known that a decreasing grain size has a strong mechanical stabilisation effect on austenite, inhibiting the formation of α'-martensite [113, 193, 243]. Additionally, blocky or equiaxed austenite is generally less stable than film or lamellar austenite in medium Mn steels [124, 125]. Therefore, it should follow that the WQ samples would form less α'-martensite than the FC samples at a similar strain since the lamellar width of the WQ samples was much finer than the grain size in the FC samples. However, from Figure 6.2l, there was more α'-martensite in the WQ sample than in the FC sample at failure, going against conventional wisdom. In this alloy, the austenite phase of both FC and WQ conditions were chemically very stable, dominating the mechanical stability term due to grain size refinement in Equation 6.2, as seen in Table 6.3. The effect of relative grain size difference on austenite stability between the equiaxed grain diameter in FC samples and the lamella grain width in WQ samples were therefore not expected to be significant. However, α'-martensite nucleation was shown to be restricted to the austenite grain boundaries where there is a local concentration of stress. In the WQ samples, the lamellar grain morphology has a larger grain boundary area to volume ratio and therefore able to provide a larger number of nucleation sites for α'-martensite to form. Therefore, it was likely that α'-martensite was able to nucleate more easily in the WQ samples, resulting in a higher α'-martensite fraction at failure. However, it is acknowledged that a simple explanation cannot fully capture the complexity of α'-martensitic transformation in WQ. In Figures 6.7d-f, the fine austenite lamella in Area 1 and a wide lamellar austenite grain in Area 4 had different surface area to volume ratios yet both remained largely untransformed, suggesting that other effects such as texture, Schmid factors and stress shielding were possibly also involved [110,121,124,125]. Nevertheless, in this alloy with a very high austenite stability where the formation of α'-martensite was nucleation-limited, grain boundary area to volume ratio would have certainly played a significant role among the other factors known to contribute to α'-martensite transformation.

6.5.3 Strain hardening behaviour and constitutive modelling

Perhaps the most striking observation from the modified constitutive model in Figure 6.8 was the lack of strengthening contribution from the TWIP effect, especially in the WQ condition. Through the original constitutive model developed for successive TWIP+TRIP medium Mn steel, Lee and De Cooman [19] showed that the TWIP effect was less effective in small austenite grains and concluded that strengthening from the TRIP effect was more pronounced compared to the TWIP effect. In this study, a similar conclusion was reached for the FC steel with an equiaxed microstructure. However, this study extends the concept to include the simultaneous TWIP+TRIP mechanism and for lamellar microstructures which showed a nearly complete lack of contribution to strengthening from the TWIP effect.

Given the lack of strengthening from the TWIP effect, it is therefore unsurprising that the observed differences in twinning kinetics in FC and WQ conditions did not result in a significant difference in the strain hardening behaviour. Instead, the strain hardening behaviour was dominated by the TRIP effect. Furthermore, since both FC and WQ conditions were found to share a similar α'-martensite nucleation and growth mechanism, it is reasonable to expect the strain hardening profiles to be very similar.

Since the TWIP effect does little in terms of strength for medium Mn steels, it is probably better to not pursue the TWIP+TRIP effect in alloy design. In order to enable the TWIP+TRIP effect, a relatively high SFE and austenite stability is needed [37]. This is enabled by a combination of either low Mn and high C (current alloy), or high Mn and low C. If the TWIP effect can be forgone during alloy design, it would be possible to enable low to medium Mn and low C (3-6 wt% Mn, 0.05-0.2 wt% C) compositions that exhibit the TRIP effect only. Such low Mn, low C compositions have been increasingly termed lean medium Mn steels [244], and are desirable in terms of lower segregation after casting [74], better weldability [245], processability, *etc.* However, it is worth noting that while the TWIP effect does little for TWIP+TRIP-type medium Mn steels, the tensile properties still tend to be better in terms of elongation than in pure TRIP-type medium Mn steels [19, 58, 92, 113]. The higher Mn and C contents necessary for the TWIP+TRIP effect also stabilises the austenite phase and prolongs the TRIP effect to significantly higher strains. Therefore, the alloy chemistry surrounding TWIP+TRIP-type medium Mn steels is still worth further study, although less focus might be given to the TWIP effect. It may also be of research interest to determine if the TWIP effect may have other benefits in terms of ductility or performance at high strain rates.

6.6 Conclusion

The effects of microstructure on the TWIP+TRIP mechanism were examined in a 5Mn-0.5C type medium Mn steel in two conditions representing different processing strategies in the steel mill. In the first, furnace cooling after hot rolling was employed (FC), as in a coiler; and in the other, water quenching (WQ) on the run-out bed. Both were then intercritically annealed, as on a continuous annealing line. These produced steels with similar initial austenite compositions and phase fractions but with equiaxed vs mixed equiaxed+lamellar microstructures, respectively.

1. Both FC and WQ conditions showed superior mechanical properties and the simultaneous TWIP+TRIP plasticity enhancing mechanism was identified to be operative in both conditions regardless of microstructural form.

2. A novel α'-martensite nucleation and growth mechanism in high C austenite was proposed. Stress-assisted α'-martensite was able to nucleate at the austenite grain boundaries due to the high stress concentration during deformation. The α'-martensite is unable to grow beyond the stress field into the parent austenite grain due to the high chemical stability and therefore remains small. The continuous formation and slow growth of α'-martensite grains greatly extends the strain regime where TRIP is operative and allows for large elongations to failure.

3. The shorter austenite lamella width in the WQ samples compared to the austenite grain diameter in the FC samples resulted in a shorter mean free path for twinning. This raised the critical twinning stress such that extensive twinning was only observed at higher strains in the WQ sample.

4. A modified constitutive model was developed and found to have a good fit with the experimental data. The model also showed that the TWIP effect did not provide significant strengthening in the FC condition and almost no strengthening in the WQ condition. However, this does not exclude the possibility that the TWIP effect may nevertheless provide ductility advantages over TRIP-only steels.

6.7 Contribution statement

This chapter was adapted from a paper with contributions from several co-authors. In order of authorship on the paper:

TWJ Kwok - Conceptualisation, methodology, investigation, analysis, writing and visualisation.

P Gong - TEM, TKD and analysis.

R Rose - Methodology and MATLAB modelling.

D Dye - Conceptualisation and supervision.

6.8 Appendix

To model the simultaneous TWIP+TRIP effect in the FC and WQ conditions, we follow the constitutive modelling work of Lee *et al.* [19, 75, 132] and Latypov *et al.* [148]. This work similarly applies the iso-work assumption to model the strain partitioning between austenite, ferrite and martensite. The iso-work assumption can be expressed as:

$$\sigma_\gamma d\varepsilon_\gamma = \sigma_\alpha d\varepsilon_\alpha = \sigma_{\alpha'} d\varepsilon_{\alpha'} \tag{6.3}$$

where σ_γ, σ_α and $\sigma_{\alpha'}$ are the flow stresses of austenite, ferrite and α'-martensite respectively and $d\varepsilon_\gamma$, $d\varepsilon_\alpha$ and $d\varepsilon_{\alpha'}$ are the incremental strains of austenite, ferrite and α'-martensite respectively. The global applied strain can therefore be expressed as a rule of mixtures:

$$d\varepsilon = f_\gamma d\varepsilon_\gamma + f_\alpha d\varepsilon_\alpha + f_{\alpha'} d\varepsilon_{\alpha'} \tag{6.4}$$

where f_γ, f_α and $f_{\alpha'}$ are the phase fractions of austenite, ferrite and α'-martensite respectively. Stresses were calculated by incrementally increasing true strain and updating the dislocation densities using the local gradient of dislocation density as a function of strain. To calculate strain partitioning, iso-work constraints were applied by using a trust-region-dogleg algorithm, a refined Newton's method in MATLAB. The model was implemented in MATLAB and is available online [231].

To begin, the flow stress, σ, of FC and WQ was assumed to obey the law of mixtures:

$$\sigma = \sigma_\gamma f_\gamma + \sigma_\alpha f_\alpha + \sigma_{\alpha'} f_{\alpha'} \tag{6.5}$$

The flow stress of each phase, σ_i, where i denotes austenite, ferrite or α'-martensite, can be described as:

$$\sigma_i = \sigma_i^{YS} + A M_i \mu_i b_i \sqrt{\rho_i} \tag{6.6}$$

where σ_i^{YS} is the yield strength, A is a constant equal to 0.4, M_i is the Taylor factor, μ_i is the shear modulus, b_i is the magnitude of the Burger's vector and ρ_i is the stored dislocation density of phase i. The yield strength of each phase was determined by summing the solid solution and grain size strengthening contributions through the following equation:

$$\sigma_i^{YS} = \sigma_i^s + \frac{K_i}{\sqrt{d_i}} \tag{6.7}$$

where σ_i^s is the solid solution strength, K_i is the Hall-Petch parameter and d_i is the grain size of phase i. The austenite Hall-Petch parameter by Rahman *et al.* [42] was used in place of original value used by Lee and De Cooman [132] as it was found to give a better fit. Additionally, the austenite lath width in the WQ sample was used for d_γ rather than the ECD grain size in Table 6.3. The solid solution strength of each phase was calculated according to the following empirical equations [83, 84]:

$$\sigma_\gamma^s = 567(X_C^\gamma) - 1.5(X_{Mn}^\gamma) + 23(X_{Si}^\gamma) \tag{6.8}$$

$$\sigma_\alpha^s = 5000(X_C^\alpha) + 44.7(X_{Mn}^\alpha) + 138.6(X_{Si}^\alpha) + 70(X_{Al}^\alpha) \tag{6.9}$$

$$\sigma_{\alpha'}^s = 413 + 1720(X_C^\gamma) \tag{6.10}$$

where X_j^i is the concentration of element j, in mass percent, in phase i. The evolution of dislocation density with strain, $\frac{d\rho_i}{d\epsilon_i}$, was determined by calculating the rate of dislocation storage and annihilation in each phase using the Kocks-Mecking model given as [1]:

$$\frac{d\rho_i}{d\varepsilon_i} = M\left(\frac{P_i}{b_i\Lambda_i} + \frac{k_1^i}{b_i}\sqrt{\rho_i} - k_2^i\rho_i\right) \tag{6.11}$$

where P_i is a coefficient related to the grain size, Λ_i is the dislocation mean free path, k_1^i is the dislocation storage coefficient and k_2^i is the dislocation annihilation coefficient of phase i. Here, we decided to treat the α'-martensite grains as undeformable particles and set $k_1^{\alpha'}$ and $k_2^{\alpha'}$ to zero. The term P_i is defined as the probability for a dislocation to not be absorbed into a grain boundary [239] and is given as:

$$P_i = exp\left[-\left(\frac{d_i^c}{d_i}\right)^3\right] \tag{6.12}$$

where d_c^i is a critical grain size of phase i, below which the rate of dislocation annihilation at the grain boundaries is larger than the rate of dislocation storage and *vice versa.* The dislocation mean free path of ferrite, Λ_α, and α'-martensite, $\Lambda_{\alpha'}$, was assumed to be equal to the average grain size. However, for the austenite phase, the dislocation mean free path, Λ_γ was determined as:

$$\Lambda_\gamma = \left(\frac{1}{d_\gamma} + \frac{1}{\lambda_T}\right)^{-1} \tag{6.13}$$

where λ_T is the mean twin spacing and is given as the following equation:

$$\lambda_T = 2c_T\frac{1-f_T}{f_T} \tag{6.14}$$

where c_T is the twin thickness and f_T is the volume fraction of twins. The evolution of twin volume fraction with strain can be expressed as:

$$f_T = f_\gamma f_0[1-\exp(-\alpha\varepsilon)]^m \tag{6.15}$$

where f_0 is the twin saturation volume fraction, α is the coefficient associated with the formation of a twin nucleus when perfect dislocations intersect and m is the exponent associated with the probability of perfect dislocations intersecting. Finally, since the evolution of α' martensite with strain no longer relies on the prior formation of twins, a simple Avrami equation [236–238] was used to describe the evolution of martensite fraction with strain:

---

[1] It should be noted that Equation 6.11 contained a typographical error in the original reference [19]. We have verified this with the authors of that paper and rectified this in the current paper.

$$f_{\alpha'} = (1 - f_{\alpha})(1 - \exp(-a\varepsilon^{b})) \tag{6.16}$$

where a and b are Avrami constants. Since precise measurement of martensite fraction was not possible, the Avrami constants were fitted by minimising the χ^2 of the modelled and experimental strain hardening data using a gradient search. Values for the parameters used for the model are given in Table 6.4 and 6.5.

Table 6.4: Table of parameter values used in the constitutive model after the work by Lee and De Cooman [19].

	Units	Austenite	Ferrite	Martensite
μ_i	GPa	75	75	80
K_i	MPa µm$^{-0.5}$	330 [42]	172 [246]	0
b_i	Å	2.50	2.48	2.48
k_1	-	0.006 [148]	0.0065 [148]	0
k_2	-	2 [148]	2 [148]	0
d_i^c	µm	1.5 [75]	2.1 [75]	2.1 [75]
ρ_{ini}	m^{-2}	10^{12}	10^{12}	10^{15}
α	-	3.5	-	-
m	-	2	-	-
f_0	-	0.2 [100]	-	-
M	-	3.06	2.95	3.06

Table 6.5: Table of experimental and fitting parameters used in the constitutive model.

	Units	Austenite	Ferrite	Martensite
c_T	nm	30	-	-
d_i (FC)	µm	1.5	3.0	0.2
d_i (WQ)	µm	0.3	1.3	0.2
a (FC)	-	-	-	3.3
a (WQ)	-	-	-	3.7
b (FC)	-	-	-	3.1
b (WQ)	-	-	-	2.5

Chapter 7

Conclusions

The primary goal of this work was to develop a novel TWIP-assisted medium Mn steel with 1 GPa yield strength and a minimum of 30% ductility. This goal was achieved with the development of Novalloy with 8 wt% Mn. Since the thermomechanical processing of Novalloy did not involve cold rolling, the possibility of utilising cold rolling as the final processing step to produce cold rolled grades of medium Mn steel was investigated. In Chapter 4, the differences in tensile behaviour between the as-annealed and cold rolled Novalloy samples were compared. It was found that twinning in medium Mn steels was strain path dependent where plane strain compression *i.e.* cold rolling produced a significantly higher twin density and activated multiple twinning systems compared to uniaxial tension at the same equivalent strain. When the cold rolled samples were subsequently tested in uniaxial tension, it was observed that the total transformation ratio increased with increasing cold rolling reduction. It was postulated that the increasing density of twin intersections introduced during cold rolling contributed to the higher transformation ratio by acting as potent nucleation sites for α'-martensite during subsequent tensile testing. Nevertheless, the low twin density under uniaxial tension was surprising, suggesting that Novalloy might have been too highly alloyed. Another observation which warranted further study was the introduction of a significant yield point elongation in the cold rolled specimens as current theories into the origins of yield point elongation in medium Mn steels are not able to sufficiently explain the emergence of yield point elongations in cold rolled medium Mn steels.

In order to demonstrate the industrial scalability of Novalloy over TWIP steels, a homogenisation study was conducted in Chapter 5. It was found that the cooling rate and therefore SDAS had an effect on the time needed to fully transform δ-ferrite grains to austenite during a simulated slab reheating cycle at 1250 °C. After reheating for 2 h, it was found that some δ-ferrite grains still remained untransformed. Nevertheless, Mn segregation to the interdendritic regions have been mostly eliminated. The experimental observations regarding solidification sequence, Mn segregation and δ-ferrite transformation were also reproduced using the MICRESS modelling software to facilitate future alloy design.

Having learned from Chapters 4 and 5, Triolloy was fabricated with a significantly lower Mn, Al and Si content. In Chapter 6, the twinning response was improved and δ-ferrite was able to be fully eliminated within a reheating cycle of 1250 °C for 2 h. When Triolloy was manufactured under two different thermomechanical processing concepts to produce a mixed lamellar+equiaxed and a fully equiaxed microstructure, it was found that the strain hardening behaviour was remarkably similar. Further examination showed that the twinning kinetics were very different between the two microstructures and was most likely due to the difference in dislocation mean free path between the diameter of an equiaxed grain (1-2 µm) and the thickness of a lamellar grain ($\sim$ 300 nm). However, they both shared the same stress-assisted α'-martensite nucleation and growth mechanism. Constitutive modelling of the strain hardening rate revealed a surprising conclusion that the contribution to strengthening from the TWIP effect was negligible compared to the TRIP effect. This finding questions the initial premise of designing a TWIP-assisted medium Mn steel. Nevertheless, the alloying chemisty that enables twinning also extends the TRIP effect over a long strain regime which still makes these steels a substantial improvement over equivalent DP steel grades.

A summary of the medium to high Mn steel development is presented in Figure 7.1. In order to improve industrial scalability, the Mn content has been lowered successively from 16 wt% in high Mn TWIP steels to 5 wt% in Triolloy which was the final alloy design iteration as part of this work. As the Mn content decreases, it was generally observed that the yield strength also decreases, largely due to a loss in solid solution strengthening. However, the steels with reduced Mn contents are not any less ductile, owing to the effective tuning of SFE and austenite stability to produce the maximum TWIP and/or TRIP response at any Mn content.

While several novel steels and strategies to maximise elongation have been developed over the course of the PhD, it is acknowledged that several limitations and caveats exist. Firstly, tensile testing was conducted predominantly on sub-sized tensile specimens. While it has been shown that for a sufficiently small grain size, the use of sub-sized tensile specimens is indeed representative of full-sized specimens [247], it is still necessary to conduct tensile testing on a full sized tensile specimen in accordance to ASTM standards. This will allow a fair one-to-one comparison with other commercial sheet steels. Secondly, constitutive modelling described in chapter 6 can be improved. While the

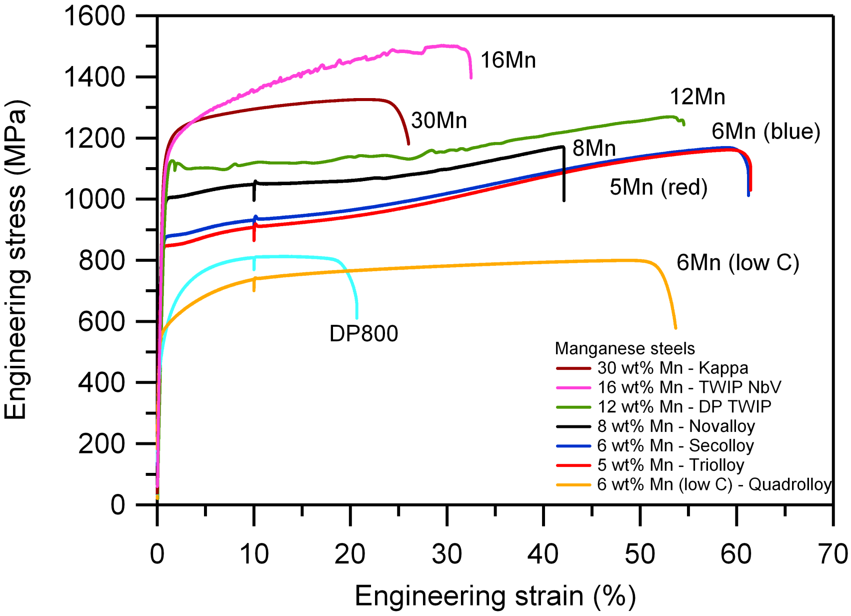

Figure 7.1: Tensile curves of all medium and high Mn steels developed during the PhD.

constitutive model was developed and verified by De Cooman and co-workers [19,148], it is acknowledged that many fitting parameters have been used. Therefore, a better model could be developed which captures the strain partitioning between austenite and ferrite in both the equiaxed and lamellar type microstructures. Such models will no doubt extend its use to metal forming processes involving medium Mn steel.

7.1 Suggestions for futher study

As previously mentioned in Chapter 2, steel alloy development does not end with an impressive tensile curve. Many other downstream processes have to be considered as well. A key and pressing topic that requires more research attention is the poor resistance spot weldability of medium Mn steels. Most spot welded medium Mn steels form a fully martensitic fusion zone which is brittle and susceptible to interfacial failure [175]. The carefully balanced phase fractions and element partitioning in the base metal are also destroyed in the heat affected zone [178]. The combination of many factors such as the brittle fusion zone and an off-balance heat affected zone have resulted in poor cross tension strengths. While novel techniques such as double pulse spot welding can improve the cross tension strengths [177], most medium Mn steels cannot be spot welded by conventional methods as things stand, hindering its uptake as an automotive steel.

To address this problem, a new alloy, Quadrolloy, was produced with 6 wt% Mn and a significantly lower C content. From Figure 7.1, Quadrolloy (6Mn low C) has the same yield strength and tensile strength as DP 800 but with a significantly larger elongation likely due to an extended TRIP effect. Furthermore, because of its lower C content, Quadrolloy is expected to have the highest weldability among the previously developed medium Mn steels. Similar and dissimilar spot welding trials with DP 800 will be undertaken in order to better understand the causes for poor weldability and then to design strategies to improve the cross tension strength of medium Mn steel resistance spot welds.

Other downstream process that requires attention is LME and hydrogen embrittlement. As mentioned in section 2.5.2, preliminary studies into LME have shown that medium Mn steels are significantly more resistant to LME compared to TWIP steels. However, more evidence needs to be gathered to determine if LME is a significant issue in medium Mn steels that warrants further study and remedial action from an alloy design perspective. Hydrogen embrittlement is another problematic issue affecting many high strength steels [248]. Early studies have shown that medium Mn steels are indeed susceptible to and suffer from hydrogen embrittlement [249, 250]. However, studies in this area are sparse and certainly deserves more attention.

Other than downstream processes, many other scientific questions remain unanswered. The origin of yield point elongation in medium Mn steels still remains under debate and a consensus within the community has not yet been reached. The TRIP effect in medium Mn steel also appears to be slightly different from other TRIP-assisted steels. Medium Mn steels are able to exhibit many different types of martensite morphologies as shown in Chapter 4 but their origins, strain-induced or stress-assisted, are still not yet clear. It is therefore important to further understand the TRIP effect to maximise the tensile capabilities of medium Mn steels. In-situ tensile experiments can be conduted in a SEM to investigate the evolution of martensitic structures with strain as well as strain partitioning behaviour in samples which exhibit the yield point elongation. High strain rate testing also needs to be conducted since medium Mn steels are designed for crash energy absorption. Finally, constitutive modelling on medium Mn steels which have mixed equiaxed+lamellar or lamellar microstructures needs to be improved. Given that lamellar microstructures do not suffer from yield point elongation, the steel industry is looking to scale up medium Mn steels with lamellar microstructures. Therefore, better models needs to be developed that also apply to medium Mn steels with lamellar microstructures.

Bibliography

[1] Keeler S, Kimchi M, J Mooney P. Advanced High-Strength Steels Apllication Guidelines Version 6.0. Tech. rep., WorldAutoSteel, 2017.

[2] Rana R, Singh S. Automotive Steels: Design, Metallurgy, Processing and Applications, Woodhead Publishing, 2016.

[3] Billur E, Altan T. Three generations of advanced high strength steels for automotive applications, Part I. *Stamping Journal*, 2013; pp. 16–17.

[4] Billur E, Dykeman J, Altan T. Three Generations of Advanced High-Strength Steels for Automotive Applications, Part II. *Stamping Journal*, 2014; pp. 12–13.

[5] Billur E, Altan T. Three Generations of Advanced High-Strength Steels for Automotive Applications, Part III. *Stamping Journal*, 2014.

[6] Allain S, Chateau JP, Bouaziz O, Migot S, Guelton N. Correlations between the calculated stacking fault energy and the plasticity mechanisms in Fe-Mn-C alloys. *Materials Science and Engineering A*, 2004; vol. 387-389 (1-2 SPEC. ISS.), pp. 158–162.

[7] Bouaziz O, Allain S, Scott CP, Cugy P, Barbier D. High manganese austenitic twinning induced plasticity steels: A review of the microstructure properties relationships. *Current Opinion in Solid State and Materials Science*, 2011; vol. 15, pp. 141–168.

[8] De Cooman BC, Estrin Y, Kim SK. Twinning-induced plasticity (TWIP) steels. *Acta Materialia*, 2018; vol. 142, pp. 283–362.

[9] De Cooman BC, Chin K-g, Kim J. High Mn TWIP Steels for Automotive Applications. In M Chiaberge (Ed.), New Trends and Developments in Automotive System Engineering, chap. 6, pp. 101–128, IntechOpen, 2011.

[10] Rahman KM, Vorontsov VA, Dye D. The dynamic behaviour of a twinning induced plasticity steel. *Materials Science and Engineering A*, 2014; vol. 589, pp. 252–261.

[11] Horvath CD. Advanced steels for lightweight automotive structures. In P Mallick (Ed.), Materials, Design and Manufacturing for Lightweight Vehicles, chap. 2, pp. 39–95, Elsevier Ltd, 2021.

[12] Elliott R, Coley K, Mostaghel S, Barati M. Review of Manganese Processing for Production of TRIP/TWIP Steels, Part 1: Current Practice and Processing Fundamentals. *JOM*, 2018; vol. 70 (5), pp. 680–690.

[13] Cho JW, Yoo S, Park MS, Park JK, Moon KH. Improvement of Castability and Surface Quality of Continuously Cast TWIP Slabs by Molten Mold Flux Feeding Technology. *Metallurgical and Materials Transactions B: Process Metallurgy and Materials Processing Science*, 2017; vol. 48, pp. 187–196.

[14] Zhuang C, Liu J, Li C, Tang D. Study on high temperature solidification behavior and crack sensitivity of Fe-Mn-C-Al TWIP steel. *Scientific Reports*, 2019; vol. 9 (15962).

[15] Wietbrock B, Bambach M, Seuren S, Hirt G. Homogenization strategy and material characterization of high-manganese TRIP and TWIP steels. *Materials Science Forum*, 2010; vol. 638-642, pp. 3134–3139.

[16] Bausch M, Frommeyer G, Hofmann H, Balichev E, Soler M, Didier M, Samek L. Ultra high-strength and ductile FeMnAlC light-weight steels. Tech. rep., Luxembourg, 2013.

[17] Bleck W, Phiu-on K, Heering C, Hirt G. Hot workability of as-cast high manganese-high carbon steels. *Steel Research International*, 2007; vol. 78 (7), pp. 536–545.

[18] Sohn SS, Song H, Jo MC, Song T, Kim HS, Lee S. Novel 1.5 GPa-strength with 50%-ductility by transformation-induced plasticity of non-recrystallized austenite in duplex steels. *Scientific Reports*, 2017; vol. 7 (1255).

[19] Lee S, De Cooman BC. Annealing Temperature Dependence of the Tensile Behavior of 10 pct Mn Multi-phase TWIP-TRIP Steel. *Metallurgical and Materials Transactions A: Physical Metallurgy and Materials Science*, 2014; vol. 45, pp. 6039–6052.

[20] Lee D, Kim JK, Lee S, Lee K, De Cooman BC. Microstructures and mechanical properties of Ti and Mo micro-alloyed medium Mn steel. *Materials Science and Engineering A*, 2017; vol. 706, pp. 1–14.

[21] De Cooman BC, Lee SJ, Shin S, Seo EJ, Speer JG. Combined Intercritical Annealing and Q&P Processing of Medium Mn Steel. *Metallurgical and Materials Transactions A: Physical Metallurgy and Materials Science*, 2017; vol. 48, pp. 39–45.

[22] Lee S, Woo W, de Cooman BC. Analysis of the Tensile Behavior of 12 pct Mn Multi-phase (α + γ) TWIP + TRIP Steel by Neutron Diffraction. *Metallurgical and Materials Transactions A: Physical Metallurgy and Materials Science*, 2016; vol. 47, pp. 2125–2140.

[23] Luo H, Dong H. New ultrahigh-strength Mn-alloyed TRIP steels with improved formability manufactured by intercritical annealing. *Materials Science and Engineering A*, 2015; vol. 626, pp. 207–212.

[24] Shao C, Hui W, Zhang Y, Zhao X, Weng Y. Microstructure and mechanical properties of hot-rolled medium-Mn steel containing 3% aluminum. *Materials Science and Engineering A*, 2017; vol. 682, pp. 45–53.

[25] He BB, Huang MX. Strong and ductile medium Mn steel without transformation-induced plasticity effect. *Materials Research Letters*, 2018; vol. 6 (7), pp. 365–371.

[26] Hu B, Luo H. A strong and ductile 7Mn steel manufactured by warm rolling and exhibiting both transformation and twinning induced plasticity. *Journal of Alloys and Compounds*, 2017; vol. 725, pp. 684–693.

[27] Zhu Y, Hu B, Luo H. Influence of Nb and V on Microstructure and Mechanical Properties of Hot-Rolled Medium Mn Steels. *Steel Research International*, 2018; vol. 89 (1700389).

[28] Lee S, De Cooman BC. Tensile behavior of intercritically annealed ultra-fine grained 8% Mn multi-phase steel. *Steel Research International*, 2015; vol. 86 (10), pp. 1170–1178.

[29] Li J, Song R, Li X, Zhou N, Song R. Microstructural evolution and tensile properties of 70 GPa·% grade strong and ductile hot-rolled 6Mn steel treated by intercritical annealing. *Materials Science and Engineering A*, 2019; vol. 745, pp. 212–220.

[30] Hu B, He BB, Cheng GJ, Yen HW, Huang MX, Luo HW. Super-high-strength and formable medium Mn steel manufactured by warm rolling process. *Acta Materialia*, 2019; vol. 174, pp. 131–141.

[31] Lee S, Lee SJ, Santhosh Kumar S, Lee K, De Cooman BC. Localized deformation in multiphase, ultra-fine-grained 6 Pct Mn transformation-induced plasticity steel. *Metallurgical and Materials Transactions A: Physical Metallurgy and Materials Science*, 2011; vol. 42, pp. 3638–3651.

[32] Lee H, Chul M, Su S, Zargaran A, Hyun J, Kim NJ, Lee S. Novel medium-Mn (austenite + martensite) duplex hot-rolled steel achieving 1.6 GPa strength with 20 % ductility by Mn-segregation- induced TRIP mechanism. *Acta Materialia*, 2018; vol. 147, pp. 247–260.

[33] Lee S, Lee K, De Cooman BC. Observation of the TWIP+TRIP Plasticity-Enhancement Mechanism in Al-Added 6 Wt Pct Medium Mn Steel. *Metallurgical and Materials Transactions A: Physical Metallurgy and Materials Science*, 2015; vol. 46, pp. 2356–2363.

[34] Steineder K, Stahl V, Krizan D, Kaar S, Hebesberger T. Development of Third Generation Advanced High Strength Steels for Automotive Applications. In 19th International Scientific Conference Transfer 2018. 2018 .

[35] Wang H, Zhang Y, Ran R, Wang Y, Kang J, Li Y, Misra RD, Yuan G, Wang G. A medium-Mn steel processed by novel twin-roll strip casting route. *Materials Science and Technology*, 2019; vol. 35 (10), pp. 1227–1238.

[36] Sun B, Fazeli F, Scott C, Brodusch N, Gauvin R, Yue S. The influence of silicon additions on the deformation behavior of austenite-ferrite duplex medium manganese steels. *Acta Materialia*, 2018; vol. 148, pp. 249–262.

[37] Kwok TWJ, Gong P, Xu X, Nutter J, Rainforth WM, Dye D. Microstructure Evolution and Tensile Behaviour of a Cold Rolled 8 Wt Pct Mn Medium Manganese Steel. *Metallurgical and Materials Transactions A: Physical Metallurgy and Materials Science*, 2022; vol. 53, pp. 597–609.

[38] Savic V, Hector L, Singh H, Paramasuwom M, Basu U, Basudhar A, Stander N. Development of a Lightweight Third-Generation Advanced High-Strength Steel (3GAHSS) Vehicle Body Structure. *SAE International Journal of Materials and Manufacturing*, 2018; vol. 11, pp. 303–313.

[39] Miller RL. Ultrafine-grained microstructures and mechanical properties of alloy steels. *Metallurgical and Materials Transactions B*, 1972; vol. 3, pp. 905–912.

[40] Ma Y. Medium-manganese steels processed by austenite-reverted-transformation annealing for automotive applications. *Materials Science and Technology*, 2017; vol. 33 (15), pp. 1713–1727.

[41] Lee YK, Han J. Current opinion in medium manganese steel. *Materials Science and Technology*, 2015; vol. 31 (7), pp. 843–856.

[42] Rahman KM, Vorontsov VA, Dye D. The effect of grain size on the twin initiation stress in a TWIP steel. *Acta Materialia*, 2015; vol. 89, pp. 247–257.

[43] Rahman KM, Jones NG, Dye D. Micromechanics of twinning in a TWIP steel. *Materials Science and Engineering A*, 2015; vol. 635, pp. 133–142.

[44] Olsson K, Gladh M, Hedin JE, Larsson J. Microalloyed high-strength. *Advanced Materials and Processes*, 2006; vol. 164 (8), pp. 44–46.

[45] Kim JK, De Cooman BC. Stacking fault energy and deformation mechanisms in Fe-xMn-0.6C-yAl TWIP steel. *Materials Science and Engineering A*, 2016; vol. 676, pp. 216–231.

[46] Tofaute W, Linden K. Transformations in solid state of manganese steels containing 1.2% C and 17% Mn. *Archiv für das Eisenhüttenwesen*, 1936; (10), pp. 515–524.

[47] Sabzi M, Farzam M. Hadfield manganese austenitic steel: A review of manufacturing processes and properties. *Materials Research Express*, 2019; vol. 6 (10).

[48] Hadfield RA. Some newly discovered properties of Iron and Manganese. *Minutes of the Proceedings of The Institution of Civil Engineers*, 1888; vol. 93 (1888), pp. 61–75.

[49] Kaar S, Steineder K, Schneider R, Krizan D, Sommitsch C. New Ms-formula for exact microstructural prediction of modern 3rd generation AHSS chemistries. *Scripta Materialia*, 2021; vol. 200 (113923).

[50] Koistinen DP, Marburger RE. A general equation prescribing the extent of the austenite-martensite transformation in pure iron-carbon alloys and plain carbon steels. *Acta Metallurgica*, 1959; vol. 7 (1), pp. 59–60.

[51] Bhadeshia HKDH, Honeycombe R. Steels and Properties, Butterworth-Heinemann, 2017, 4th ed.

[52] Angel T. Formation of martensite in austenitic stainless steels. *Journal of the Iron and Steel Instiitute*, 1954; vol. 5, pp. 165–175.

[53] Nohara K, Ono Y, Ohashi N. Composition and Grain Size Dependencies of Strain-induced Martensitic Transformation in Metastable Austenitic Stainless Steels. *Tetsu-To-Hagane/Journal of the Iron and Steel Institute of Japan*, 1977; vol. 63 (5), pp. 772–782.

[54] Nakada N, Mizutani K, Tsuchiyama T, Takaki S. Difference in transformation behavior between ferrite and austenite formations in medium manganese steel. *Acta Materialia*, 2014; vol. 65, pp. 251–258.

[55] Gómez M, Medina SF. Role of microalloying elements in the microstructure of hot rolled steels. *International Journal of Materials Research*, 2011; vol. 102 (10), pp. 1197–1207.

[56] De Moor E, Kang S, Speer JG, Matlock DK. Manganese Diffusion in Third Generation Advanced High Strength Steels. *Proceedings of the International Conference on Mining, Materials and Metallurgical Engineering*, 2014; .

[57] Liang J, Zhao Z, Tang D, Ye N, Yang S, Liu W. Improved microstructural homogeneity and mechanical property of medium manganese steel with Mn segregation banding by alternating lath matrix. *Materials Science and Engineering A*, 2018; vol. 711, pp. 175–181.

[58] Xu X, Kwok TWJ, Gong P, Dye D. Tailoring the Deformation Behaviour of a Medium Mn Steel through Isothermal Intercritical Annealing. *Materialia*, 2022; vol. 22 (101422).

[59] Kamoutsi H, Gioti E, Haidemenopoulos GN, Cai Z, Ding H. Kinetics of Solute Partitioning During Intercritical Annealing of a Medium-Mn Steel. *Metallurgical and Materials Transactions A: Physical Metallurgy and Materials Science*, 2015; vol. 46, pp. 4841–4846.

[60] Souza Filho IR, Kwiatkowski da Silva A, Sandim MJR, Ponge D, Gault B, Sandim HRZ, Raabe D. Martensite to austenite reversion in a high-Mn steel: Partitioning-dependent two-stage kinetics revealed by atom probe tomography, in-situ magnetic measurements and simulation. *Acta Materialia*, 2019; vol. 166, pp. 178–191.

[61] Ding R, Dai Z, Huang M, Yang Z, Zhang C, Chen H. Effect of pre-existed austenite on austenite reversion and mechanical behavior of an Fe-0.2C-8Mn-2Al medium Mn steel. *Acta Materialia*, 2018; vol. 147, pp. 59–69.

[62] Speer JG, De Moor E, Findley KO, Matlock DK, De Cooman BC, Edmonds DV. Analysis of microstructure evolution in quenching and partitioning automotive sheet steel. *Metallurgical*

and Materials Transactions A: Physical Metallurgy and Materials Science, 2011; vol. 42, pp. 3591–3601.

[63] Lee S, Lee SJ, De Cooman BC. Austenite stability of ultrafine-grained transformation-induced plasticity steel with Mn partitioning. *Scripta Materialia*, 2011; vol. 65, pp. 225–228.

[64] Rana R. Special issue on 'Medium manganese steels'. *Materials Science and Technology*, 2019; vol. 35 (17), pp. 2039–2044.

[65] Mueller JJ, Hu X, Sun X, Ren Y, Choi K, Barker E, Speer JG, Matlock DK, De Moor E. Austenite formation and cementite dissolution during intercritical annealing of a medium-manganese steel from a martensitic condition. *Materials and Design*, 2021; vol. 203 (109598).

[66] Lee J, Sohn SS, Hong S, Suh BC, Kim SK, Lee BJ, Kim NJ, Lee S. Effects of Mn Addition on Tensile and Charpy Impact Properties in Austenitic Fe-Mn-C-Al-Based Steels for Cryogenic Applications. *Metallurgical and Materials Transactions A: Physical Metallurgy and Materials Science*, 2014; vol. 45, pp. 5419–5430.

[67] Campbell J. Complete Casting Handbook: Metal Casting Processes, Metallurgy, Techniques and Design: Second Edition, Butterworth-Heinemann 2015, 2nd ed.

[68] Lee YK, Lee SJ, Han J. Critical assessment 19: stacking fault energies of austenitic steels. *Materials Science and Technology*, 2016; vol. 32 (1), pp. 1–8.

[69] Frommeyer G, Brüx U. Microstructures and Mechanical Properties of High-Strength Fe-Mn-AI-C Light-Weight TRIPLEX Steels. *Steel Research International*, 2006; vol. 77 (9-10), pp. 627–633.

[70] Chen S, Rana R, Haldar A, Ray RK. Current state of Fe-Mn-Al-C low density steels. *Progress in Materials Science*, 2017; vol. 89, pp. 345–391.

[71] Kozeschnik E, Bhadeshia HKDH. Influence of silicon on cementite precipitation in steels. *Materials Science and Technology*, 2008; vol. 24 (3), pp. 343–347.

[72] Wang Z, Xu J, Yan Y, Li J. The influence of microstructure on the mechanical properties and fracture behavior of medium Mn steels at different strain rates. *Materials*, 2019; vol. 12 (4228).

[73] Fukagawa T, Okada H, Maehara Y. Mechanism of Red Scale Defect Formation in Si-added Hot-rolled Steel Sheets. *ISIJ International*, 1994; vol. 34 (11), pp. 906–911.

[74] Kwok TWJ, Slater C, Xu X, Davis C, Dye D. A Scale-up Study on Chemical Segregation and the Effects on Tensile Properties in Two Medium Mn Steel Castings. *Metallurgical and Materials Transactions A: Physical Metallurgy and Materials Science*, 2022; vol. 53, pp. 585–596.

[75] Lee S, Estrin Y, De Cooman BC. Constitutive modeling of the mechanical properties of V-added medium manganese TRIP steel. *Metallurgical and Materials Transactions A: Physical Metallurgy and Materials Science*, 2013; vol. 44, pp. 3136–3146.

[76] He BB, Huang MX. Simultaneous Increase of Both Strength and Ductility of Medium Mn Transformation-Induced Plasticity Steel by Vanadium Alloying. *Metallurgical and Materials Transactions A: Physical Metallurgy and Materials Science*, 2018; vol. 49, pp. 1433–1438.

[77] Han Y, Shi J, Xu L, Cao WQ, Dong H. TiC precipitation induced effect on microstructure and mechanical properties in low carbon medium manganese steel. *Materials Science and Engineering A*, 2011; vol. 530, pp. 643–651.

[78] Vázquez PJC, Pacheco-Cedeño JS, Ramos-Azpeitia MO, Garnica-González P, Garibay-Febles V, Moreno-Palmerin J, Cruz-Rivera JdJ, Hernández-Rivera JL. Casting and constitutive hot flow behavior of medium-mn automotive steel with nb as microalloying. *Metals*, 2020; vol. 10 (206).

[79] Pan HJ, Cai MH, Ding H, Huang HS, Zhu B, Wang YL, Zhang YS. Microstructure evolution and enhanced performance of a novel Nb-Mo microalloyed medium Mn alloy fabricated by low-temperature rolling and warm stamping. *Materials and Design*, 2017; vol. 134, pp. 352–360.

[80] Gladman T. Precipitation hardening in metals. *Materials Science and Technology*, 1999; vol. 15, pp. 30–36.

[81] Baker TN. Processes, microstructure and properties of vanadium microalloyed steels. *Materials Science and Technology*, 2009; vol. 25 (9), pp. 1083–1107.

[82] Kaikkonen PM, Somani MC, Karjalainen LP, Kömi JI. Flow stress behaviour and static recrystallization characteristics of hot deformed austenite in microalloyed medium-carbon bainitic steels. *Metals*, 2021; vol. 11 (138).

[83] De Cooman BC, Speer JG. Fundamentals of Steel Product Physical Metallurgy, AIST, 2011.

[84] Speich G, Warlimont H. Yield strength and transformation substructure of low-carbon martensite. *Journal of the Iron and Steel Instititue*, 1968; vol. 206 (4), pp. 385–392.

[85] Wang W, An Z, Luo S, Zhu M. In-situ observation of peritectic solidification of Fe-Mn-Al-C steel with medium manganese. *Journal of Alloys and Compounds*, 2022; vol. 909 (164750).

[86] Wang Z, Xu J, Li J. Mechanical properties and fracture behaviors of medium-Mn steels with and without delta-ferrite for different intercritical annealing times. *Materials Characterization*, 2021; vol. 172 (110730).

[87] Sun B, Ma Y, Vanderesse N, Varanasi RS, Song W, Bocher P, Ponge D, Raabe D. Macroscopic to nanoscopic in situ investigation on yielding mechanisms in ultrafine grained medium Mn steels: Role of the austenite-ferrite interface. *Acta Materialia*, 2019; vol. 178, pp. 10–25.

[88] Kim MT, Park TM, Baik KH, Choi WS, Choi PP, Han J. Crucial microstructural feature to determine the impact toughness of intercritically annealed medium-Mn steel with triplex-phase microstructure. *Acta Materialia*, 2019; vol. 164, pp. 122–134.

[89] Sun B, Palanisamy D, Ponge D, Gault B, Fazeli F, Scott C, Yue S, Raabe D. Revealing fracture mechanisms of medium manganese steels with and without delta-ferrite. *Acta Materialia*, 2019; vol. 164, pp. 683–696.

[90] Choi H, Lee S, Lee J, Barlat F, De Cooman BC. Characterization of fracture in medium Mn steel. *Materials Science and Engineering A*, 2017; vol. 687, pp. 200–210.

[91] Dumay A, Chateau JP, Allain S, Migot S, Bouaziz O. Influence of addition elements on the stacking-fault energy and mechanical properties of an austenitic Fe-Mn-C steel. *Materials Science and Engineering A*, 2008; vol. 483-484, pp. 184–187.

[92] Sohn SS, Song H, Kwak JH, Lee S. Dramatic improvement of strain hardening and ductility to 95% in highly-deformable high-strength duplex lightweight steels. *Scientific Reports*, 2017; vol. 7 (1927).

[93] Field DM, Qing J, van Aken DC. Chemistry and Properties of Medium-Mn Two-Stage TRIP Steels. *Metallurgical and Materials Transactions A: Physical Metallurgy and Materials Science*, 2018; vol. 49, pp. 4615–4632.

[94] Steineder K, Krizan D, Schneider R, Béal C, Sommitsch C. On the microstructural characteristics influencing the yielding behavior of ultra-fine grained medium-Mn steels. *Acta Materialia*, 2017; vol. 139, pp. 39–50.

[95] Luo H, Shi J, Wang C, Cao W, Sun X, Dong H. Experimental and numerical analysis on formation of stable austenite during the intercritical annealing of 5Mn steel. *Acta Materialia*, 2011; vol. 59, pp. 4002–4014.

[96] Li X, Song R, Zhou N, Li J. An ultrahigh strength and enhanced ductility cold-rolled medium-Mn steel treated by intercritical annealing. *Scripta Materialia*, 2018; vol. 154, pp. 30–33.

[97] Kwok TWJ, Gong P, Rose R, Dye D. The relative contributions of TRIP and TWIP to strength in fine grained medium-Mn steels. *arXiv:2204.05388 [cond-mat.mtrl-sci]*, 2022; .

[98] Kwok TWJ, Rahman KM, Xu X, Bantounas I, Kelleher JF, Daswari S, Alam T, Banerjee R, Dye D. Design of a High Strength, High Ductility 12 wt% Mn Medium Manganese Steel With Hierarchical Deformation Behaviour. *Materials Science & Engineering A*, 2020; vol. 782 (139258).

[99] Kim CW, Kwon SI, Lee BH, Moon JO, Park SJ, Lee JH, Hong HU. Atomistic study of nano-sized κ-carbide formation and its interaction with dislocations in a cast Si added FeMnAlC lightweight steel. *Materials Science and Engineering A*, 2016; vol. 673, pp. 108–113.

[100] Bouaziz O, Allain S, Scott C. Effect of grain and twin boundaries on the hardening mechanisms of twinning-induced plasticity steels. *Scripta Materialia*, 2008; vol. 58, pp. 484–487.

[101] Bleck W, Guo X, Ma Y. The TRIP Effect and Its Application in Cold Formable Sheet Steels. *Steel Research International*, 2017; vol. 88 (1700218).

[102] Herrera C, Ponge D, Raabe D. Design of a novel Mn-based 1 GPa duplex stainless TRIP steel with 60 % ductility by a reduction of austenite stability. *Acta Materialia*, 2011; vol. 59, pp. 4653–4664.

[103] Wang MM, Tasan CC, Ponge D, Raabe D. Spectral TRIP enables ductile 1.1 GPa martensite. *Acta Materialia*, 2016; vol. 111, pp. 262–272.

[104] Talonen J, Nenonen P, Pape G, Hänninen H. Effect of strain rate on the strain-induced γ α-martensite transformation and mechanical properties of austenitic stainless steels. *Metallurgical and Materials Transactions A: Physical Metallurgy and Materials Science*, 2005; vol. 36, pp. 421–432.

[105] Li ZC, Li XJ, Mou YJ, Misra RD, Ding H, He LF, Li HP. Tuning austenite stability in a medium Mn steel and relationship to structure and mechanical properties. *Materials Science and Technology*, 2020; vol. 36 (12), pp. 1308–1317.

[106] Field DM, Garza-Martinez LG, Van Aken DC. Processing and Properties of Medium-Mn TRIP Steel to Obtain a Two-Stage TRIP Behavior. *Metallurgical and Materials Transactions A: Physical Metallurgy and Materials Science*, 2020; vol. 51, pp. 4427–4433.

[107] Olson GB, Cohen M. A mechanism for the strain-induced martensitic transformations. *Journal of the Less-Common Metals*, 1972; vol. 28, pp. 107–118.

[108] Li ZC, Misra RD, Cai ZH, Li HX, Ding H. Mechanical properties and deformation behavior in hot-rolled 0.2C-1.5/3Al-8.5Mn-Fe TRIP steel: The discontinuous TRIP effect. *Materials Science and Engineering A*, 2016; vol. 673, pp. 63–72.

[109] Cai ZH, Ding H, Misra RD, Ying ZY. Austenite stability and deformation behavior in a cold-rolled transformation-induced plasticity steel with medium manganese content. *Acta Materialia*, 2015; vol. 84, pp. 229–236.

[110] Xu YB, Zou Y, Hu ZP, Han DT, Chen SQ, Misra RD. Correlation between deformation behavior and austenite characteristics in a Mn-Al type TRIP steel. *Materials Science and Engineering A*, 2017; vol. 698, pp. 126–135.

[111] Yen HW, Ooi SW, Eizadjou M, Breen A, Huang CY, Bhadeshia HKDH, Ringer SP. Role of stress-assisted martensite in the design of strong ultrafine-grained duplex steels. *Acta Materialia*, 2015; vol. 82, pp. 100–114.

[112] Chatterjee S, Bhadeshia HKDH. Transformation induced plasticity assisted steels: Stress or strain affected martensitic transformation? *Materials Science and Technology*, 2007; vol. 23 (9), pp. 1101–1104.

[113] Sohn SS, Choi K, Kwak JH, Kim NJ, Lee S. Novel ferrite-austenite duplex lightweight steel with 77% ductility by transformation induced plasticity and twinning induced plasticity mechanisms. *Acta Materialia*, 2014; vol. 78, pp. 181–189.

[114] Jacques PJ, Allain S, Bouaziz O, De A, Gourgues AF, Hance BM, Houbaert Y, Huang J, Iza-Mendia A, Kruger SE, Radu M, Samek L, Speer J, Zhao L, van der Zwaag S. On measurement

of retained austenite in multiphase TRIP steels results of blind round robin test involving six different techniques. *Materials Science and Technology*, 2009; vol. 25 (5), pp. 567–574.

[115] Han J, Lee SJ, Jung JG, Lee YK. The effects of the initial martensite microstructure on the microstructure and tensile properties of intercritically annealed Fe-9Mn-0.05C steel. *Acta Materialia*, 2014; vol. 78, pp. 369–377.

[116] Kaar S, Krizan D, Schneider R, Sommitsch C. Impact of Si and Al on Microstructural Evolution and Mechanical Properties of Lean Medium Manganese Quenching and Partitioning Steels. *Steel Research International*, 2020; vol. 91 (2000181).

[117] Ludwigson D, Berger J. Plastic behaviour of metastable austenitic stainless steels. *J. Iron Steel Inst*, 1969; vol. 207 (1), pp. 63–69.

[118] Samek L, De Moor E, Penning J, De Cooman BC. Influence of alloying elements on the kinetics of strain-induced martensitic nucleation in low-alloy, multiphase high-strength steels. *Metallurgical and Materials Transactions A: Physical Metallurgy and Materials Science*, 2006; vol. 37, pp. 109–124.

[119] Sun B, Vanderesse N, Fazeli F, Scott C, Chen J, Bocher P, Jahazi M, Yue S. Discontinuous strain-induced martensite transformation related to the Portevin-Le Chatelier effect in a medium manganese steel. *Scripta Materialia*, 2017; vol. 133, pp. 9–13.

[120] Field DM, Baker DS, Van Aken DC. On the Prediction of α-Martensite Temperatures in Medium Manganese Steels. *Metallurgical and Materials Transactions A: Physical Metallurgy and Materials Science*, 2017; vol. 48, pp. 2150–2163.

[121] Zhang S, Findley KO. Quantitative assessment of the effects of microstructure on the stability of retained austenite in TRIP steels. *Acta Materialia*, 2013; vol. 61, pp. 1895–1903.

[122] Ryu JH, Kim DI, Kim HS, Bhadeshia HKDH, Suh DW. Strain partitioning and mechanical stability of retained austenite. *Scripta Materialia*, 2010; vol. 63, pp. 297–299.

[123] Wang J, Van der Zwaag S. Stabilization mechanisms of retained austenite in transformation-induced plasticity steel. *Metallurgical and Materials Transactions A: Physical Metallurgy and Materials Science*, 2001; vol. 32, pp. 1527–1539.

[124] Chiang J, Boyd JD, Pilkey AK. Effect of microstructure on retained austenite stability and tensile behaviour in an aluminum-alloyed TRIP steel. *Materials Science and Engineering A*, 2015; vol. 638, pp. 132–142.

[125] He B. On the factors governing austenite stability: Intrinsic versus extrinsic. *Materials*, 2020; vol. 13 (3440).

[126] He BB, Luo HW, Huang MX. Experimental investigation on a novel medium Mn steel combining transformation-induced plasticity and twinning-induced plasticity effects. *International Journal of Plasticity*, 2016; vol. 78, pp. 173–186.

[127] Field DM, Van Aken DC. Dynamic Strain Aging Phenomena and Tensile Response of Medium-Mn TRIP Steel. *Metallurgical and Materials Transactions A: Physical Metallurgy and Materials Science*, 2018; vol. 49, pp. 1152–1166.

[128] Lee S, Woo W, De Cooman BC. Analysis of the Plasticity-Enhancing Mechanisms in 12 pctMn Austeno-ferritic Steel by In Situ Neutron Diffraction. *Metallurgical and Materials Transactions A: Physical Metallurgy and Materials Science*, 2014; vol. 45, pp. 5823–5828.

[129] Nakada N, Ito H, Matsuoka Y, Tsuchiyama T, Takaki S. Deformation-induced martensitic transformation behavior in cold-rolled and cold-drawn type 316 stainless steels. *Acta Materialia*, 2010; vol. 58, pp. 895–903.

[130] Shen YF, Li XX, Sun X, Wang YD, Zuo L. Twinning and martensite in a 304 austenitic stainless steel. *Materials Science and Engineering A*, 2012; vol. 552, pp. 514–522.

[131] Tian Y, Gorbatov OI, Borgenstam A, Ruban AV, Hedström P. Deformation Microstructure and Deformation-Induced Martensite in Austenitic Fe-Cr-Ni Alloys Depending on Stacking Fault Energy. *Metallurgical and Materials Transactions A: Physical Metallurgy and Materials Science*, 2017; vol. 48, pp. 1–7.

[132] Lee S, De Cooman BC. Tensile Behavior of Intercritically Annealed 10 pct Mn Multi-phase Steel. *Metallurgical and Materials Transactions A*, 2014; vol. 45, pp. 709–716.

[133] Panigrahi BK. Processing of low carbon steel plate and hot strip-an overview. *Bulletin of Materials Science*, 2001; vol. 24 (4), pp. 361–371.

[134] Lenard JG. Primer on Flat Rolling, Elsevier, 2007, 2nd ed.

[135] Hidalgo J, Celada-Casero C, Santofimia MJ. Fracture mechanisms and microstructure in a medium Mn quenching and partitioning steel exhibiting macrosegregation. *Materials Science and Engineering A*, 2019; vol. 754, pp. 766–777.

[136] Ponge D, Gottstein G. Necklace formation during dynamic recrystallization: Mechanisms and impact on flow behavior. *Acta Materialia*, 1998; vol. 46 (1), pp. 69–80.

[137] Buchely MF, Field DM, Van Aken DC. Analysis of Hot- and Cold-Rolled Loads in Medium-Mn TRIP Steels. *Metallurgical and Materials Transactions B: Process Metallurgy and Materials Processing Science*, 2019; vol. 50, pp. 1180–1192.

[138] Song H, Yoo J, Kim SH, Sohn SS, Koo M, Kim NJ, Lee S. Novel ultra-high-strength Cu-containing medium-Mn duplex lightweight steels. *Acta Materialia*, 2017; vol. 135, pp. 215–225.

[139] Kim MT, Park TM, Baik KH, Choi WS, Han J. Effects of cold rolling reduction ratio on microstructures and tensile properties of intercritically annealed medium-Mn steels. *Materials Science and Engineering A*, 2019; vol. 752, pp. 43–54.

[140] Liu L, Yang ZG, Zhang C, Liu WB. An in situ study on austenite memory and austenitic spontaneous recrystallization of a martensitic steel. *Materials Science and Engineering A*, 2010; vol. 527, pp. 7204–7209.

[141] Glover A, Gibbs PJ, Liu C, Brown DW, Clausen B, Speer JG, De Moor E. Deformation behavior of a double soaked medium manganese steel with varied martensite strength. *Metals*, 2019; vol. 9 (761).

[142] Glover A, Speer JG, De Moor E. Tempering and Austempering of Double Soaked Medium Manganese Steels. *Frontiers in Materials*, 2021; vol. 7 (622131).

[143] Speer J, Rana R, Matlock D, Glover A, Thomas G, De Moor E. Processing Variants in Medium-Mn Steels. *Metals*, 2019; vol. 9 (771).

[144] Wang C, Cao W, Shi J, Huang C, Dong H. Deformation microstructures and strengthening mechanisms of an ultrafine grained duplex medium-Mn steel. *Materials Science and Engineering A*, 2013; vol. 562, pp. 89–95.

[145] Zhang R, Cao W, Peng Z, Shi J, Dong H, Huang C. Intercritical rolling induced ultrafine microstructure and excellent mechanical properties of the medium-Mn steel. *Materials Science and Engineering A*, 2013; vol. 583, pp. 84–88.

[146] Dutta A, Park TM, Nam JH, Lee SI, Hwang B, Choi WS, Sandlöbes S, Ponge D, Han J. Enhancement of the tensile properties and impact toughness of a medium-Mn steel through the homogeneous microstrain distribution. *Materials Characterization*, 2021; vol. 174 (110992).

[147] Zhang Y, Wang L, Findley KO, Speer JG. Influence of Temperature and Grain Size on Austenite Stability in Medium Manganese Steels. *Metallurgical and Materials Transactions A: Physical Metallurgy and Materials Science*, 2017; vol. 48, pp. 2140–2149.

[148] Latypov MI, Shin S, De Cooman BC, Kim HS. Micromechanical finite element analysis of strain partitioning in multiphase medium manganese TWIP+TRIP steel. *Acta Materialia*, 2016; vol. 108, pp. 219–228.

[149] Li ZC, Ding H, Misra RD, Cai ZH. Deformation behavior in cold-rolled medium-manganese TRIP steel and effect of pre-strain on the Lüders bands. *Materials Science and Engineering A*, 2017; vol. 679, pp. 230–239.

[150] Luo H, Dong H, Huang M. Effect of intercritical annealing on the Lüders strains of medium Mn transformation-induced plasticity steels. *Materials and Design*, 2015; vol. 83, pp. 42–48.

[151] Zhang M, Li L, Ding J, Wu Q, Wang YD, Almer J, Guo F, Ren Y. Temperature-dependent micromechanical behavior of medium-Mn transformation-induced-plasticity steel studied by in situ synchrotron X-ray diffraction. *Acta Materialia*, 2017; vol. 141, pp. 294–303.

[152] Cai MH, Zhu WJ, Standford N, Pan LB, Chao Q, Hodgson PD. Dependence of deformation behavior on grain size and strain rate in an ultrahigh strength-ductile Mn-based TRIP alloy. *Materials Science and Engineering A*, 2016; vol. 653, pp. 35–42.

[153] Wang XG, Wang L, Huang MX. Kinematic and thermal characteristics of Lüders and Portevin-Le Châtelier bands in a medium Mn transformation-induced plasticity steel. *Acta Materialia*, 2017; vol. 124, pp. 17–29.

[154] Callahan M, Hubert O, Hild F, Perlade A, Schmitt JH. Coincidence of strain-induced TRIP and propagative PLC bands in Medium Mn steels. *Materials Science and Engineering A*, 2017; vol. 704, pp. 391–400.

[155] Cai ZH, Jing SY, Li HY, Zhang KM, Misra RD, Ding H, Tang ZY. The influence of microstructural characteristics on yield point elongation phenomenon in Fe-0.2C-11Mn-2Al steel. *Materials Science and Engineering A*, 2019; vol. 739, pp. 17–25.

[156] Luo H, Dong H, Huang M. Effect of intercritical annealing on the Lüders strains of medium Mn transformation-induced plasticity steels. *Materials and Design*, 2015; vol. 83, pp. 42–48.

[157] Ratte E, Leonhardt S, Bleck W, Franzen M, Urban P. Energy absorption behaviour of austenitic and duplex stainless steels in a crash box geometry. *Steel Research International*, 2006; vol. 77 (9-10), pp. 692–697.

[158] Quadfasel A, Teller M, Madivala M, Haase C, Roters F, Hirt G. Computer-aided material design for crash boxes made of high manganese steels. *Metals*, 2019; vol. 9 (772).

[159] Han J, da Silva AK, Ponge D, Raabe D, Lee SM, Lee YK, Lee SI, Hwang B. The effects of prior austenite grain boundaries and microstructural morphology on the impact toughness of intercritically annealed medium Mn steel. *Acta Materialia*, 2017; vol. 122, pp. 199–206.

[160] Chao YJ, Ward JD, Sands RG. Charpy impact energy, fracture toughness and ductile-brittle transition temperature of dual-phase 590 Steel. *Materials and Design*, 2007; vol. 28, pp. 551–557.

[161] Suh DW, Kim SJ. Medium Mn transformation-induced plasticity steels: Recent progress and challenges. *Scripta Materialia*, 2017; vol. 126, pp. 63–67.

[162] Xiong XC, Chen B, Huang MX, Wang JF, Wang L. The effect of morphology on the stability of retained austenite in a quenched and partitioned steel. *Scripta Materialia*, 2013; vol. 68, pp. 321–324.

[163] Mintz B. Hot dip galvanising of transformation induced plasticity and other intercritically annealed steels. *International Materials Reviews*, 2001; vol. 46 (4), pp. 169–197.

[164] Pourmajidian M, McDermid JR. Selective Oxidation of a 0.1C-6Mn-2Si Third Generation Advanced High-Strength Steel During Dew-Point Controlled Annealing. *Metallurgical and Materials Transactions A: Physical Metallurgy and Materials Science*, 2018; vol. 49, pp. 1795–1808.

[165] Kyoung RJ, Cho L, Jong HO, Myoung SK, Ki CK, De Cooman BC. Surface Selective Oxide Reduction During the Intercritical Annealing of Medium Mn Steel. *Metallurgical and Materials Transactions A: Physical Metallurgy and Materials Science*, 2017; vol. 48, pp. 3635–3641.

[166] Alibeigi S, Kavitha R, Meguerian RJ, McDermid JR. Reactive wetting of high Mn steels during continuous hot-dip galvanizing. *Acta Materialia*, 2011; vol. 59, pp. 3537–3549.

[167] Pourmajidian M, McDermid JR. On the reactive wetting of a medium-Mn advanced high-strength steel during continuous galvanizing. *Surface and Coatings Technology*, 2019; vol. 357, pp. 418–426.

[168] Chen Z, He Y, Zheng W, Wang H, Zhang Y, Li L. Effect of hot-dip galvanizing process on selective oxidation and galvanizability of medium manganese steel for automotive application. *Coatings*, 2020; vol. 10 (1265).

[169] Bhadhon KMH, Wang X, McNally EA, McDermid JR. Effect of Intercritical Annealing Parameters and Starting Microstructure on the Microstructural Evolution and Mechanical Properties of a Medium-Mn Third Geration Advance High Strength Steel. *Metals*, 2022; vol. 12 (356).

[170] Pallisco DM, McDermid JR. Mechanical property development of a 0.15C-6Mn-2Al-1Si third-generation advanced high strength steel using continuous galvanizing heat treatments. *Materials Science and Engineering A*, 2020; vol. 778 (139111).

[171] Pouranvari M, Marashi SPH. Critical review of automotive steels spot welding: process, structure and properties. *Science and Technology of Welding and Joining*, 2013; vol. 18 (5), pp. 361–403.

[172] Park G, Jeong S, Lee C. Fusion Weldabilities of Advanced High Manganese Steels: A Review. *Metals and Materials International*, 2021; vol. 27, pp. 2046–2058.

[173] Wang C, Li X, Han S, Zhang L, Chang Y, Cao W, Dong H. Warm Stamping Technology of the Medium Manganese Steel. *Steel Research International*, 2017; vol. 1700360, pp. 1–6.

[174] O'Brien A, Guzman C (Eds.). Welding Handbook, vol. 4, American Welding Society, Miami, 2011, 9th ed.

[175] Park G, Kim K, Uhm S, Lee C. A comparison of cross-tension properties and fracture behavior between similar and dissimilar resistance spot-weldments in medium-Mn TRIP steel. *Materials Science and Engineering A*, 2019; vol. 752, pp. 206–216.

[176] Park G, Uhm S, Lee C. Effects of in-situ post-weld heat treatment on the microstructure and mechanical properties of the coarse-grained heat-affected zone in a resistance spot weld in medium Mn TRIP steel. *Materials Science and Engineering A*, 2020; vol. 788 (139477).

[177] Stadler M, Schnitzer R, Gruber M, Steineder K, Hofer C. Influence of the cooling time on the microstructural evolution and mechanical performance of a double pulse resistance spot welded medium-mn steel. *Metals*, 2021; vol. 11 (270).

[178] Jia Q, Liu L, Guo W, Peng Y, Zou G, Tian Z, Zhou YN. Microstructure and tensile-shear properties of resistance spot-welded medium Mn steel. *Metals*, 2018; vol. 8 (48).

[179] Park G, Kim K, Uhm S, Lee C. Remarkable improvement in resistance spot weldability of medium-Mn TRIP steel by paint-baking heat treatment. *Materials Science and Engineering A*, 2019; vol. 766 (138401).

[180] WorldAutoSteel. Combined reports - AHSS implementation solutions: liquid metal embrittlement study. Tech. rep., WorldAutoSteel, 2020.

[181] Beal C, Kleber X, Fabregue D, Bouzekri M. Liquid zinc embrittlement of twinning-induced plasticity steel. *Scripta Materialia*, 2012; vol. 66, pp. 1030–1033.

[182] Kang H, Cho L, Lee C, De Cooman BC. Zn Penetration in Liquid Metal Embrittled TWIP Steel. *Metallurgical and Materials Transactions A: Physical Metallurgy and Materials Science*, 2016; vol. 47, pp. 2885–2905.

[183] Razmpoosh MH, Biro E, Chen DL, Goodwin F, Zhou Y. Liquid metal embrittlement in laser lap joining of TWIP and medium-manganese TRIP steel: The role of stress and grain boundaries. *Materials Characterization*, 2018; vol. 145, pp. 627–633.

[184] Murugan SP, Kim J, Kim J, Wan Y, Lee C, Jeon JB, Park YD. Role of liquid Zn and α-Fe(Zn) on liquid metal embrittlement of medium Mn steel: An ex-situ microstructural analysis of galvannealed coating during high temperature tensile test. *Surface and Coatings Technology*, 2020; vol. 398 (126069).

[185] Comstock RJ, Scherrer DK, Adamczyk PD. Hole expansion in a variety of sheet steels. *Journal of Materials Engineering and Performance*, 2006; vol. 15 (6), pp. 675–683.

[186] Chen L, Kim JK, Kim SK, Kim GS, Chin KG, De Cooman BC. Stretch-flangeability of high Mn TWIP steel. *Steel Research International*, 2010; vol. 81 (7), pp. 552–568.

[187] Kashima T, Yuri T, Sugimoto KI, Hashimoto S. Effect of initial microstructures before annealing on ductility of TRIP-aided steel sheets. *Tetsu-To-Hagane/Journal of the Iron and Steel Institute of Japan*, 2003; vol. 89 (5), pp. 609–615.

[188] Xu X, Xu BY, Chen P, Liu RD, Wang GD, Yi HL. Effect of austenite stability on the hole expansion behavior of δ-TRIP steels. *Materials Today Communications*, 2020; vol. 24 (101034).

[189] Levy BS, Gibbs M, Van Tyne CJ. Failure during sheared edge stretching of dual-phase steels. *Metallurgical and Materials Transactions A: Physical Metallurgy and Materials Science*, 2013; vol. 44, pp. 3635–3648.

[190] Tsipouridis P, Werner E, Krempaszky C, Tragl E. Formability of high strength dual-phase steels. *Steel Research International*, 2006; vol. 77 (9-10), pp. 654–667.

[191] Chen X, Jiang H, Cui Z, Lian C, Lu C. Hole expansion characteristics of ultra high strength steels. *Procedia Engineering*, 2014; vol. 81, pp. 718–723.

[192] Sun B, Fazeli F, Scott C, Yan X, Liu Z, Qin X, Yue S. Critical role of strain partitioning and deformation twinning on cracking phenomenon occurring during cold rolling of two duplex medium manganese steels. *Scripta Materialia*, 2017; vol. 130, pp. 49–53.

[193] Lee SJ, Park KS. Prediction of martensite start temperature in alloy steels with different grain sizes. *Metallurgical and Materials Transactions A: Physical Metallurgy and Materials Science*, 2013; vol. 44, pp. 3423–3427.

[194] Christian J. A theory of the transformation in pure cobalt. *Proceedings of the Royal Society A*, 1951; vol. 206 (1084), pp. 51–64.

[195] Curtze S, Kuokkala V. Dependence of tensile deformation behavior of TWIP steels on stacking fault energy, temperature and strain rate. *Acta Materialia*, 2010; vol. 58, pp. 5129–5141.

[196] Saeed-Akbari A, Imlau J, Prahl U, Bleck W. Derivation and variation in composition-dependent stacking fault energy maps based on subregular solution model in high-manganese steels. *Metallurgical and Materials Transactions A: Physical Metallurgy and Materials Science*, 2009; vol. 40, pp. 3076–3090.

[197] Lee SJ, Han J, Lee CY, Park IJ, Lee YK. Elastic strain energy induced by epsilon martensitic transformation and its contribution to the stacking-fault energy of austenite in Fe-15Mn-xC alloys. *Journal of Alloys and Compounds*, 2014; vol. 617, pp. 588–596.

[198] Zheng P, Chen R, Liu H, Chen J, Zhang Z, Liu X, Shen Y. On the standards and practices for miniaturized tensile test A review. *Fusion Engineering and Design*, 2020; vol. 161 (112006).

[199] Hanlon DN, Van Bohemen SM, Celotto S. Critical Assessment 10: Tensile elongation of strong automotive steels as function of testpiece geometry. *Materials Science and Technology*, 2015; vol. 31 (4), pp. 385–388.

[200] Chen S, Rana R, Haldar A, Ray RK. Current state of Fe-Mn-Al-C low density steels. *Progress in Materials Science*, 2017; vol. 89, pp. 345–391.

[201] Vermeulen Y, Coletti B, Blanpain B, Wollants P, Vleugels J. Material evaluation to prevent nozzle clogging during continuous casting of Al killed steels. *ISIJ International*, 2002; vol. 42 (11), pp. 1234–1240.

[202] Song H, Kwon Y, Sohn SS, Koo M, Kim NJ, Lee BJ, Lee S. Improvement of tensile properties in (austenite+ferrite+κ-carbide) triplex hot-rolled lightweight steels. *Materials Science and Engineering: A*, 2018; vol. 730, pp. 177–186.

[203] Zhang X, Ma G, Liu M, Li Z. Removal of residual element tin in the ferrous metallurgy process: A review. *Metals*, 2019; vol. 9 (834).

[204] Gao S, Bai Y, Zheng R, Tian Y, Mao W, Shibata A, Tsuji N. Mechanism of huge Lüders-type deformation in ultrafine grained austenitic stainless steel. *Scripta Materialia*, 2019; vol. 159, pp. 28–32.

[205] Olson GB, Cohen M. A mechanism for the strain-induced nucleation of martensitic transformations. *Journal of the Less-Common Metals*, 1972; vol. 28, pp. 107–118.

[206] Olson GB, Cohen M. A General Mechanism of Martensitic Nucleation- Part II. FCC —,-BCC and Other Martensitic Transformations. *Metallurgical Transactions A*, 1976; vol. 7, pp. 1905–1914.

[207] Bogers AJ, Burgers WG. Partial dislocations on the {110} planes in the B.C.C. lattice and the transition of the F.C.C. into the B.C.C. lattice. *Acta Metallurgica*, 1964; vol. 12, pp. 255–261.

[208] Higo Y, Lecroisey F, Mori T. Relation between applied stress and orientation relationship of α martensite in stainless steel single crystals. *Acta Metallurgica*, 1974; vol. 22, pp. 313–323.

[209] Tsakiris V, Edmonds DV. Martensite and deformation twinning in austenitic steels. *Materials Science and Engineering A*, 1999; vol. 273-275, pp. 430–436.

[210] Tian Y, Borgenstam A, Hedström P. Comparing the deformation-induced martensitic transformation with the athermal martensitic transformation in Fe-Cr-Ni alloys. *Journal of Alloys and Compounds*, 2018; vol. 766, pp. 131–139.

[211] Chen M, Terada D, Shibata A, Tsuji N. Identical area observations of deformation-induced martensitic transformation in SUS304 austenitic stainless steel. *Materials Transactions*, 2013; vol. 54 (3), pp. 308–313.

[212] Maxwell PC, Goldberg A, Shyne JC. Stress-Assisted and strain-induced martensites in FE-NI-C alloys. *Metallurgical Transactions*, 1974; vol. 5, pp. 1305–1318.

[213] Sinha AK. Physical Metallurgy Handbook, McGraw-Hill, 2003.

[214] Hu B, Luo H, Yang F, Dong H. Recent progress in medium-Mn steels made with new designing strategies, a review. *Journal of Materials Science and Technology*, 2017; vol. 33, pp. 1457–1464.

[215] Murr LE, Staudhammer KP, Hecker SS. Effects of Strain State and Strain Rate on Deformation-Induced Transformation in 304 Stainless Steel: Part II. Microstructural Study. *Metallurgical Transactions A*, 1982; vol. 13, pp. 627–635.

[216] Beese AM, Mohr D. Effect of stress triaxiality and Lode angle on the kinetics of strain-induced austenite-to-martensite transformation. *Acta Materialia*, 2011; vol. 59, pp. 2589–2600.

[217] Sohrabi MJ, Naghizadeh M, Mirzadeh H. Deformation-induced martensite in austenitic stainless steels: A review. *Archives of Civil and Mechanical Engineering*, 2020; vol. 20 (124).

[218] Shrinivas V, Varma SK, Murr LE. Deformation-induced martensitic characteristics in 304 and 316 stainless steels during room-temperature rolling. *Metallurgical and Materials Transactions A*, 1995; vol. 26, pp. 661–671.

[219] Lebedev AA, Kosarchuk VV. Influence of phase transformations on the mechanical properties of austenitic stainless steels. *International journal of plasticity*, 2000; vol. 16, pp. 749–767.

[220] Martin S, Wolf S, Martin U, Krüger L, Rafaja D. Deformation Mechanisms in Austenitic TRIP/TWIP Steel as a Function of Temperature. *Metallurgical and Materials Transactions A: Physical Metallurgy and Materials Science*, 2016; vol. 47, pp. 49–58.

[221] Milad M, Zreiba N, Elhalouani F, Baradai C. The effect of cold work on structure and properties of AISI 304 stainless steel. *Journal of Materials Processing Technology*, 2008; vol. 203, pp. 80–85.

[222] Wang JJ, Hui WJ, Xie ZQ, Zhang YJ, Zhao XL. Influence of pre-strain on microstructural characteristics and tensile deformation behaviour of a cold-rolled Al-containing medium Mn steel. *Journal of Materials Science*, 2020; vol. 55, pp. 5296–5310.

[223] Zhu Y, Slater C, Connolly S, Farrugia D, Davis C. Rapid alloy prototyping for strip steel development : DP800 steel case study. *Ironmaking & Steelmaking*, 2021; vol. 48 (5), pp. 493–504.

[224] Ganesan M, Dye D, Lee PD. A technique for characterizing microsegregation in multicomponent alloys and its application to single-crystal superalloy castings. *Metallurgical and Materials Transactions A: Physical Metallurgy and Materials Science*, 2005; vol. 36, pp. 2191–2204.

[225] Lee S, De Cooman BC. On the selection of the optimal intercritical annealing temperature for medium Mn TRIP steel. *Metallurgical and Materials Transactions A: Physical Metallurgy and Materials Science*, 2013; vol. 44, pp. 5018–5024.

[226] Farahani H, Xu W, van der Zwaag S. Prediction and Validation of the Austenite Phase Fraction upon Intercritical Annealing of Medium Mn Steels. *Metallurgical and Materials Transactions A: Physical Metallurgy and Materials Science*, 2015; vol. 46, pp. 4978–4985.

[227] Vandersluis E, Ravindran C. Comparison of Measurement Methods for Secondary Dendrite Arm Spacing. *Metallography, Microstructure, and Analysis*, 2017; vol. 6, pp. 89–94.

[228] Slater C, Davis C. Near Net Shape Casting: Is It Possible to Cast Too Thin? *Metallurgical and Materials Transactions B: Process Metallurgy and Materials Processing Science*, 2020; vol. 51, pp. 2532–2541.

[229] Reitz J, Wietbrock B, Richter S, Hoffmann S, Hirt G, Friedrich B. Enhanced homogenization strategy by electroslag remelting of high-manganese TRIP and TWIP steels. *Advanced Engineering Materials*, 2011; vol. 13 (5), pp. 395–399.

[230] Lee CY, Jeong J, Han J, Lee SJ, Lee S, Lee YK. Coupled strengthening in a medium manganese lightweight steel with an inhomogeneously grained structure of austenite. *Acta Materialia*, 2015; vol. 84, pp. 1–8.

[231] Rose R, Kwok TWJ. TWIP-TRIP constitutive modelling. *GitHub Repository*, 2022. Available at: https://github.com/RoryRose/TRIP_TWIP_constituative_modelling.git

[232] Talonen J. Effect of strain induced alpha'-martensite transformation on mechanical properties of metastable austenitic stainless steels. Ph.D. thesis, Helsinki University of Technology, 2007.

[233] Kovalev A, Jahn A, Weiß A, Scheller PR. Characterization of the TRIP/TWIP effect in austenitic stainless steels using Stress-Temperature-Transformation (STT) and Deformation-Temperature-Transformation (DTT) Diagrams. *Steel Research International*, 2011; vol. 82 (1), pp. 45–50.

[234] Choi JY, Hwang SW, Ha MC, Park KT. Extended strain hardening by a sequential operation of twinning induced plasticity and transformation induced plasticity in a low Ni duplex stainless steel. *Metals and Materials International*, 2014; vol. 20 (5), pp. 893–898.

[235] Mahajan S, Chin GY. Formation of Deformation Twins in F.C.C. Crystals. *Acta Metallurgica*, 1973; vol. 21, pp. 1353–1363.

[236] Avrami M. Kinetics of phase change. I: General theory. *The Journal of Chemical Physics*, 1939; vol. 7, pp. 1103–1112.

[237] Avrami M. Kinetics of phase change. II Transformation-time relations for random distribution of nuclei. *The Journal of Chemical Physics*, 1940; vol. 8, pp. 212–224.

[238] Avrami M. Granulation, phase change, and microstructure kinetics of phase change. III. *The Journal of Chemical Physics*, 1941; vol. 9, pp. 177–184.

[239] Bouaziz O, Estrin Y, Bréchet Y, Embury JD. Critical grain size for dislocation storage and consequences for strain hardening of nanocrystalline materials. *Scripta Materialia*, 2010; vol. 63, pp. 477–479.

[240] Das A, Chakraborti PC, Tarafder S, Bhadeshia HKDH. Analysis of deformation induced martensitic transformation in stainless steels. *Materials Science and Technology*, 2011; vol. 27 (1), pp. 366–370.

[241] Das A. Crystallographic variant selection of martensite at high stress/strain. *Philosophical Magazine*, 2015; vol. 95 (20), pp. 2210–2227.

[242] Gutierrez-Urrutia I, Zaefferer S, Raabe D. The effect of grain size and grain orientation on deformation twinning in a Fe-22wt.% Mn-0.6wt.% C TWIP steel. *Materials Science and Engineering A*, 2010; vol. 527, pp. 3552–3560.

[243] Yang HS, Bhadeshia HKDH. Austenite grain size and the martensite-start temperature. *Scripta Materialia*, 2009; vol. 60, pp. 493–495.

[244] Kaar S, Krizan D, Schneider R, Sommitsch C. Impact of Si and Al on Microstructural Evolution and Mechanical Properties of Lean Medium Manganese Quenching and Partitioning Steels. S*Steel Research International* 2020; vol. 91 (2000181).

[245] Qi X, Du L, Hu J, Misra RDK. Enhanced Impact Toughness of Heat Affected Zone in Gas Shield Arc Weld Joint of Low-C Medium-Mn High Strength Steel by Post-Weld Heat Treatment. *Steel Research International*, 2018; vol. 89 (1700422).

[246] Harding J. The effect of grain size and strain rate on the lower yield stress of pure iron at 288K. *Acta Metallurgica*, 1969; vol. 17, pp. 949–958.

[247] Zhang L, Harrison W, Yar MA, Brown SGR, Lavery NP. The development of miniature tensile specimens with non-standard aspect and slimness ratios for rapid alloy prototyping processes *Journal of Materials Research and Technology*, 2021; vol. 15, pp. 1830–1843.

[248] Bhadeshia HKDH. Prevention of Hydrogen Embrittlement in Steels. *ISIJ International*, 2016; vol. 56 (1), pp. 24–36.

[249] Sun B, Krieger W, Rohwerder M, Ponge D, Raabe D. Dependence of hydrogen embrittlement mechanisms on microstructure-driven hydrogen distribution in medium Mn steels. *Acta Materialia*, 2020; vol. 183, pp. 313–328.

[250] Cho L, Kong Y, Speer JG, Findley KO. Hydrogen embrittlement of medium Mn steels *Metals*, 2021; vol. 11 (2), 358.